Crustal Structure, Fault Kinematics and Seismicity Statistics in the Kumaun-Nepal Himalaya

THESIS

Submitted in partial fulfillment of the requirements for the degree of

DOCTOR OF PHILOSOPHY

by

Himanshu Verma
(ID No. 2019PHXF0415P)

Under the Supervision of

Prof. Sumanta Pasari

and Co-Supervision of

Prof. Kuo-En Ching

BITS Pilani
Pilani | Dubai | Goa | Hyderabad | Mumbai

BIRLA INSTITUTE OF TECHNOLOGY AND SCIENCE PILANI

2024

"Success is not final, failure is not fatal: it is the courage to continue that counts."

- Winston Churchill

BIRLA INSTITUTE OF TECHNOLOGY & SCIENCE, PILANI

CERTIFICATE

This is to certify that the thesis titled, **"Crustal Structure, Fault Kinematics and Seismicity Statistics in the Kumaun-Nepal Himalaya"** submitted by **Mr. Himanshu Verma**, ID No. **2019PHXF0415P** for the award of Ph.D. of the Institute embodies original work done by him under our supervision.

Signature of the Supervisor
Name : **PROF. SUMANTA PASARI**
Designation : **Associate Professor**
Department of Mathematics
Birla Institute of Technology & Science,
Pilani, Pilani Campus
Date: __/__/____

Signature of the Co-Supervisor
Name : **PROF. KUO-EN CHING**
Designation: **Associate Professor**
Department of Geomatics
National Cheng Kung University,
Taiwan
Date: __/__/____

Dedicated to
My Beloved Father

Acknowledgements

A journey is undoubtedly smoother when you have companions. During my Ph.D. journey, I've been fortunate to have the company and support of numerous individuals. I am profoundly grateful to all those who have contributed to the successful completion of this doctoral journey, which would not have been possible without their unwavering support, guidance, and encouragement.

Firstly, I would like to extend my heartfelt gratitude to my supervisor, Prof. Sumanta Pasari, for his mentorship, insightful guidance, and invaluable feedback throughout the entire research process. His expertise and dedication have been instrumental in shaping the direction of this thesis. He has not only been a guide in academia but also a source of motivation during the challenging phases. His belief in my potential has encouraged me to strive for higher standards. The collaborative atmosphere he fostered in our interactions has been instrumental in broadening my perspectives.

I also express my sincere gratitude to my co-supervisior Prof. Kuo-En Ching for his guidance and encouragements. I am grateful for the opportunity to learn under his mentorship. I truly appreciate his dedication to my intellectual growth, his willingness to invest time and effort, and his role as a constant pillar of support.

I am also thankful to all the professors of the Department of Mathematics of BITS Pilani, Pilani Campus, for their guidance and valuable suggestions in my research work. I feel fortunate to have my Doctoral Advisory Committee (DAC) members, Prof. Rakhee and Prof. Rajesh Kumar, for their insightful discussions and valuable suggestions that have significantly enriched the quality of this work.

I am grateful to Prof. Bhupendra Kumar Sharma (Former Head of the Department), and Prof. Devendra Kumar, Head of the Department of Mathematics, for their unwavering support. I extend my acknowledgment to all the faculty members, staff and research scholars for their valuable assistance and cooperation throughout my research journey.

With great reverence, I express my gratitude to Prof. V. Ramgopal Rao (Vice Chancellor), Prof. Sudhirkumar Barai (Director), Prof. M.B. Srinivas (Dean, AGSRD), and Prof.

Shamik Chakraborty (Associate Dean, AGSRD) for providing necessary facilities.

I express my gratitude to Dr. Yogendra Sharma (National Cheng-Kung University, Taiwan) for engaging in insightful discussions on seismic hazard along the Himalayan arc and for providing continuous support and encouragement throughout my Ph.D. journey. Additionally, I extend my appreciation to Dr. Eric O. Lindsey from the University of New Mexico for his valuable comments and suggestions regarding our research on integrating GPS and InSAR observations along the Himalaya.

I want to express my gratitude to my parents, Late Mohan Lal and Mrs. Gayitri Devi, for showering me with boundless love and unwavering encouragement, which have been like a deep well of inspiration. Their invaluable guidance and wisdom have significantly shaped my academic journey. I would like to extend my appreciation to my brother, Ajay Verma, whose unwavering belief in me has been essential for completing this journey. I also express my gratitude to my uncles (mama), Sitaram Kashyap and Mahender Kashyap, for their continual motivation and support, which has served as an endless source of inspiration, propelling me forward in my studies. The steadfast support of my cousins, Harish and Ankit, has been a constant anchor, offering solace during the challenges and triumphs of this journey.

I thanks my colleagues and fellow researchers, Dr. Deepak, Dr. Pallav, Dr. Sugandha, Dr. Komal Deswal, Dr. Barkha, Dr. Sonali, Dr. Komal, Mrs. Meghana, and Mr. Parveen whose engaging discussions and camaraderie have fostered an environment conducive to intellectual growth. I must also acknowledge the invaluable contributions of Komal and Meghana, without whom I could not have completed this thesis. Their engaging discussions, shared meals, and enjoyable distractions provided much-needed respite from my research and helped rejuvenate my mind. Additionally, I extend my thanks to my seniors, Dr. Neha and Dr. Sarita, and my juniors, including Ms. Sakshi Shukla, Ms. Sonu Devi, Ms. Sharmila Devi, and Mr. Shekhar, for their assistance on numerous occasions throughout this journey.

I must acknowledge the financial support provided by CSIR/UGC, which enabled me to carry out this research effectively and efficiently. This journey has been a collective

effort, and I am humbled by the support I have received. My deepest gratitude goes to each and every individual who has played a role, no matter how small, in helping me reach this milestone.

Place: BITS Pilani, Pilani Campus

Date: __/__/____ **Himanshu Verma**

Abstract

The Himalayas, the world's youngest and tallest mountain range, formed as a result of the ongoing collision between the Indian and Eurasian tectonic plates. This collision leads the Himalaya to accumulate elastic strain energy over the years, which is subsequently released in terms of earthquakes. To this end, some notable Himalayan earthquakes in the past century include the Kangra earthquake on April 4, 1905 (M_w 7.8), the Bihar-Nepal earthquake on January 15, 1934 (M_w 8.4), the Assam earthquake on August 15, 1950 (M_w 8.6), the Kashmir earthquake on October 8, 2005 (M_w 7.6), and the most recent April 25, 2015 Gorkha earthquake (M_w 7.8). However, there are several spatial segments along the active Himalayan seismic belt that are probably mature now to experience one or more large to great earthquakes, where the accumulated elastic strain energy has been partially released or not released. Therefore, a large event in recent times would cause enormous damage to the increasing population and growing infrastructure in Himalaya and its adjoining Indo-Gangetic region. Consequently, understanding present-day seismic hazard and identifying the regions with high seismic potential are inevitable along the Himalaya.

Seismic hazard analysis of a region typically relies on two main types of data: satellite-based measurements such as GPS and InSAR data, and earthquake data comprising hypocentral details, slip location, magnitude, and origin time. While the former is often used to depict crustal structure, fault kinematics, and associated earthquake potential, the latter aids in time and space clustering and corresponding seismic hazard analysis. These analyses usually fall into two categories: theory-driven physical models describing tectonic dynamics and data-driven empirical models based on earthquake statistics. A combination of these two techniques is often recommended for a comprehensive seismic hazard analysis in a defined region.

In light of the above scenario, the present thesis focuses on the contemporary seismic hazard analysis using a combination of GPS, InSAR, and earthquake data in the Kumaun-Nepal Himalaya. The research design outlined in the thesis is structured as follows.

Chapter 1 provides an overview and rationale of the thesis, along with the primary objective and scope of the thesis. Chapter 2 lays the groundwork of the thesis by examining the study area and available datasets, including GPS velocity field, InSAR velocity field, integrated velocity field, and earthquake data. Chapters 3 to 5 are in a sense the core of the thesis, for which the obtained results are directly relevant to the seismic hazard evaluation. Specifically, Chapter 3 deals with the estimation of spatial distribution of earthquake potential through an "area-based" approach along four different sections of the study area. Chapter 4 analyzes fault kinematics and slip distribution of the MHT, and subsequently estimates earthquake potential through a "fault-based" approach. Chapter 5 carries out probabilistic earthquake recurrence modeling and natural time analysis to estimate the conditional probability of large-sized earthquakes and the current state of developing earthquake cycles at several city regions, respectively. Finally, Chapter 6 summarizes the research outcomes of the thesis, accompanying relevant future scopes.

To achieve the overall research goal, the first task is to integrate GPS and InSAR data to derive a high-resolution velocity field. This high-resolution velocity field is utilized to estimate contemporary seismic moment budget in the Kumaun Himalaya and three spatial sections in the Nepal Himalaya. For this, (i) three types of geodetic strain, namely dilatational, maximum shear, and rotational strain are calculated; subsequently, (ii) geodetic and seismic moment rates are computed using the estimated strain tensor and compiled earthquake data, respectively; and, (iii) a section-wise seismic moment budget is derived through a comparison between geodetic and seismic moment rates over the study region. The findings reveal that the strain rate is not homogeneous over the study region. Particularly, along the MCT, higher strain rates are observed. The associated seismic moment budget, the mismatch between geodetic and seismic moments, provides an earthquake potential of M_w 8.1 in the Kumaun, M_w 8.5 in the western Nepal, M_w 7.9 in the central Nepal, and M_w 8.1 in the eastern Nepal.

After an area-based earthquake potential estimation, the next task is to carry out crustal structure and fault kinematics of the MHT in Kumaun-Nepal region. For this, twenty arc-normal profiles are selected based on integrated velocity patterns. Then, a Bayesian

inversion model is employed to calculate the spatial distribution of slip rates and fault geometry over these twenty profiles. Subsequently, the estimated slip rates are used to calculate section-wise slip deficit rates, moment deficit rates, and associated earthquake potential. The results indicate that the study area exhibits consistent fault parameters, with dip angles ranging from 25.0° to 32.0°, locking depths between 6.2 km and 10.2 km, and fault depths from 12.1 km to 14.3 km. To note, slip rates of the MHT vary within each section, namely 19.1 in Kumaun, 15.5 mm/yr in western Nepal, 13.8 mm/yr in central Nepal, and 12.4 mm/yr in eastern Nepal. The inferred slip rate of the MHT corresponds to a slip deficit of 16.5 mm/yr in the Kumaun, 13.3 mm/yr in the western Nepal, 11.3 mm/yr in the central Nepal, and 10.9 mm/yr in the eastern Nepal, implying an earthquake potential of M_w 8.2, M_w 8.4, M_w 8.2, and M_w 8.3, respectively. Overall, the findings regarding earthquake potential using area-based and fault-based approaches suggest that each section of the study area has the potential to produce great earthquake(s) in the near future.

After geodetic investigation, the subsequent task is to derive seismicity statistics for an empirical hazard analysis in the Kumaun-Nepal region. For this, earthquake "forecasting" based on interevent times and earthquake "nowcasting" based on interevent counts (natural times) are performed. The overall flow of earthquake forecasting includes (i) earthquake data compilation, (ii) interevent time modeling corresponding to successive large events ($M_w \geq 6.5$) through several reference probability distributions, and, finally (iii) computation of conditional probability and hazard function curves for a set of elapsed and residual times. Results reveal that (i) the best-fit comes from lognormal, exponential, and exponentiated Weibull, and (ii) the estimated cumulative and conditional probability of a $M_w \geq 6.5$ event in the study region reach 0.90–0.95 in the next 12–22 years (2035–2045) and 25–36 years (2048–2059), respectively. On the other hand, seismic nowcasting involves (i) tabulation of "natural time" counts, counts of $4.0 \leq M_w < 6.0$ earthquakes between two successive large events ($M_w \geq 6.0$), (ii) deriving natural time seismicity statistics through several reference probability distributions, and, finally (iii) computing earthquake potential score (EPS) at several city regions to realize the current progression

of regional earthquake cycle. The findings highlight that (i) the seismicity in the study region reveals natural time Weibull statistics and (ii) the EPS values (0%–100%) for 30 city regions lie in the range of 77% to 98%. Higher values of EPS for most of these cities including Kathmandu indicate that they have reached their rear end in the seismic cycle of large earthquakes. Therefore, the empirical hazard analysis discussed above demands attention of the disaster management authorities in Kumaun-Nepal Himalaya.

In summary, the present thesis examines the integrated velocity field, strain distribution, fault characteristics, slip distribution, seismic moment budget, earthquake recurrence modeling, and natural time analysis to conclude that each section of the Kumaun-Nepal Himalaya is capable of experiencing a great earthquake in the near future. Overall, the thesis findings inevitably contribute to a better understanding of the contemporary seismic hazard in the Kumaun-Nepal Himalaya, consequently aiding in social policy-making, insurance strategies, urban planning, and various other practical applications for the end-users.

Contents

List of Abbreviations

Sr. No.	Abbrevation	Stands for
1	AIC	Akaike Information Criterion
2	BPT	Brownian passage-time
3	CDF	Cumulative Distribution Function
4	DHR	Delhi-Haridwar Ridge
5	EDF	Empirical Distribution Function
6	EPS	Earthquake Potential Score
7	FIM	Fisher Information Matrix
8	FZR	Faizabad Ridge
9	GACOS	Generic Atmospheric Correction Online Service
10	GCMT	Global Centroid Moment Tensor
11	GeMR	Geodetic Moment Rate
12	GNSS	Global Navigation Satellite System
13	GPS	Global Positioning System
14	IGP	Indo-Gangetic Plain
15	IGS	International GNSS Service
16	IMD	India Meteorological department
17	InSAR	Interferometric Synthetic Aperture Radar
18	ISC	International Seismological Centre
19	ITRF	International Terrestrial Reference Frame
20	K-S	Kolmogorov–Smirnov
21	LOS	Line of Sight
22	MBT	Main Boundary Thrust
23	MCMC	Markov Chain Monte Carlo
24	MCT	Main Central Thrust

25	MFT	Main Frontal Thrust
26	MHT	Main Himalayan Thrust
27	MIDAS	Median Interannual Difference Adjusted for Skewness
28	MIT	Massachusetts Institute of Technology
29	MLE	Maximum Likelihood Estimation
30	MSR	Munger-Saharsa Ridge
31	NGL	Nevada Geodetic Laboratory
32	NTA	Natural Time Analysis
33	PPD	Posterior Probability Distribution
34	RINEX	Receiver Independent Exchange Format
35	SAR	Synthetic Aperture Radar
36	SBAS	Small Basline Subset
37	SeMR	Seismic Moment Rate
38	SLR	Satellite Laser Ranging
39	STD	South Tibetan Detachment
40	TEQC	Translation, Editing, and Quality Check
41	UPS	Uninterrupted Power Supply
42	USGS	United States Geological Survey
43	VLBI	Very Long Baseline Interferometry

List of Tables

List of Figures

Chapter 1

Introduction

The art of proposing a question must be held of higher value than solving it.

— Georg Cantor

This chapter presents a general overview and motivation of the thesis work. The chapter discusses the evolution and tectonic setting of the Himalaya along with its major fractures (thrusts), subsequent seismicity, and seismic gaps. It also includes the primary objective and the scope of the present research work. A chapter-wise roadmap of the thesis is also presented towards the end of this chapter.

Contents

1.1 Overview and motivation

The continent-continent collision, an enduring phenomenon in the geological annals of our planet, has bestowed upon us some of the most awe-inspiring mountain ranges on Earth. Among these, the collision between Indian and Eurasian plates stands as a monumental geological event, unfolding over the course of 55 million years. This extraordinary collision has given rise to the formidable Himalaya, a range that continues to rise and evolve to this day. The Himalayas, with their towering peaks and dynamic geology, constitute one of the world's most active and iconic mountain chains. Over the centuries, this majestic range has not only shaped the landscape but also witnessed a devastating history of seismic events, leaving an indelible mark on the history of our planet with its legacy of powerful earthquakes.

The ongoing convergence of the Indian and Eurasian plates controls seismic activity along the Himalayan arc [1, 2]. This convergence causes the Himalayan arc to accumulate significant stress, which is eventually released through small to great earthquakes, usually at a shallow to intermediate depth [3–5]. To this end, some notable devastating earthquakes along the Himalaya include the Kangra earthquake on April 4, 1905 (M_w 7.8), the Bihar-Nepal earthquake on January 15, 1934 (M_w 8.4), the Assam earthquake on August 15, 1950 (M_w 8.6), the Kashmir earthquake on October 8, 2005 (M_w 7.6), and the most recent April 25, 2015 Gorkha earthquake (M_w 7.8) [6–8]. Considering the fact that a series of significant earthquakes have damaged the Himalayan arc in the past, does the area still have a substantial potential of experiencing another large-scale disaster in the near future? Here this question is addressed through a comprehensive seismic hazard analysis using geodetic and earthquake data in the Kumaun and Nepal Himalaya.

In seismic hazard analysis, the data that are available for the study of crustal deformation and earthquake inter-arrival times, primarily fall into two categories. The first type of the data is satellite-based measures of surface deformation, including Global Positioning System (GPS) and Interferometric Synthetic Aperture Radar (InSAR) products [9–12]. The second type is the earthquake data that includes hypocentral information from cata-

logs, the location of initial slip, the magnitude of the eventual earthquake, and the origin time [13–15]. While the former is often used to describe the underlying crustal structure, strain distribution, fault kinematics, and thereby earthquake potential based on the seismic moment budget in a defined region [9–12], the later is used for earthquake interevent time analysis, space-time clustering of seismic events, pattern informatics and thereby earthquake hazard estimation in a geographic area [13–15]. Consequently, these approaches of seismic hazard analysis may be classified into two fundamental types, theory-driven physical models (i.e., fault and/or area based models) and data-driven statistical models (i.e., area based models) [9–15]. The physical models aim to describe the dynamics of the underlying tectonic forces and stresses to the observed displacements at the Earth's surface [9–12, 16], whereas the statistical models assume some form of a probability distribution of the earthquake occurrence process, and then attempt to define the parameters in terms of observable [13–15]. A combination of these two techniques is often recommended for comprehensive seismic hazard analysis in a region.

In geodesy-based seismic hazard analysis, GPS and InSAR products have already demonstrated their effectiveness in quantifying tectonic deformation at several active regions [17–23]. While the ground-based GPS technique provides dense time series of accurate positions at a limited number of points, the space-based InSAR technique can provide dense spatial coverage at a limited number of epochs. The GPS technique is capable of accurately measuring three-dimensional positions with a notably higher level of accuracy in the horizontal dimension compared to the vertical [24], whereas InSAR methods can quantify deformations in the line of sight (LOS) direction with high precision ranging from mm to cm [25, 26]. As a consequence, these two geodetic methods complement one another in crustal deformation monitoring and their integration enables a uniform spatio-temporal range for higher spatial and temporal resolution than any of them alone [27–31].

In light of the above discussion, the present thesis primarily focuses on the contemporary seismic hazard analysis using a combination of GPS, InSAR, and earthquake data along the Kumaun and Nepal Himalaya (Figure 1.1). For this, (i) the GPS and InSAR data

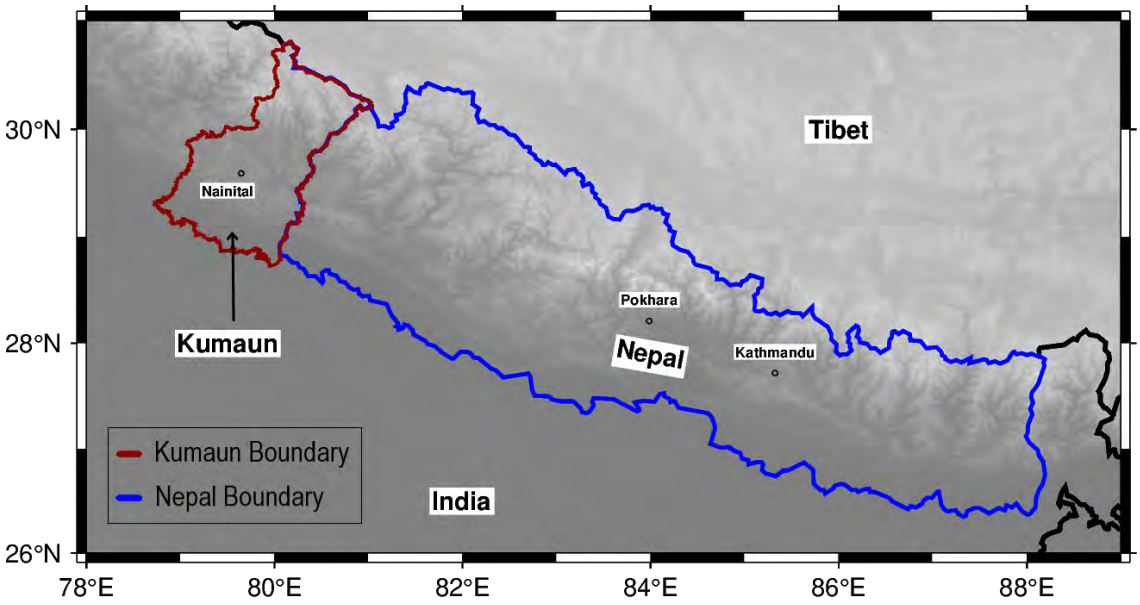

Figure 1.1: Geographic location of the Kumaun-Nepal Himalaya region.

are integrated to obtain high-resolution integrated velocities in the study area (Chapter 2); then, (ii) the integrated velocities are employed to compute the rate of interseismic strain buildup in the region (Chapter 3); subsequently, (iii) a section-wise seismic moment budget is calculated based on moment accumulation and moment release in the study area (Chapter 3); then, (iv) the slip rate and fault parameters are estimated using integrated velocity field to determine whether the fault is presently locked or interseismically active (Chapter 4), and, at last, (v) probabilistic earthquake recurrence modeling and natural time analysis have been carried out to estimate the conditional probability of large-sized earthquakes and the current state of developing earthquake cycle at several city regions, respectively (Chapter 5). The subsequent sections detail the evolution of the Himalaya and its classification.

1.2 Evolution of the Himalaya

During the late Paleozoic and early Mesozoic eras, there was a supercontinent, named Pangaea, which began to fragment around 200 million years ago (Figure 1.2) [32–34]. As a result, around 71 million years ago, the Indian subcontinent embarked on a northward drift towards the Eurasian plate (Figure 1.2) [32–34]. This marked the inception of Himalayan

narrative. The Indian Plate's relentless northward movement culminated in a monumental collision with the Eurasian Plate, setting up the stage of the Himalayan range [33, 35, 36]. This collision led to intense compression, crustal thickening, and the emergence of initial Himalayan foothills. Due to this enormous continent-continent collision, the Himalaya continues to evolve, resulting in the intense seismic activity along the region.

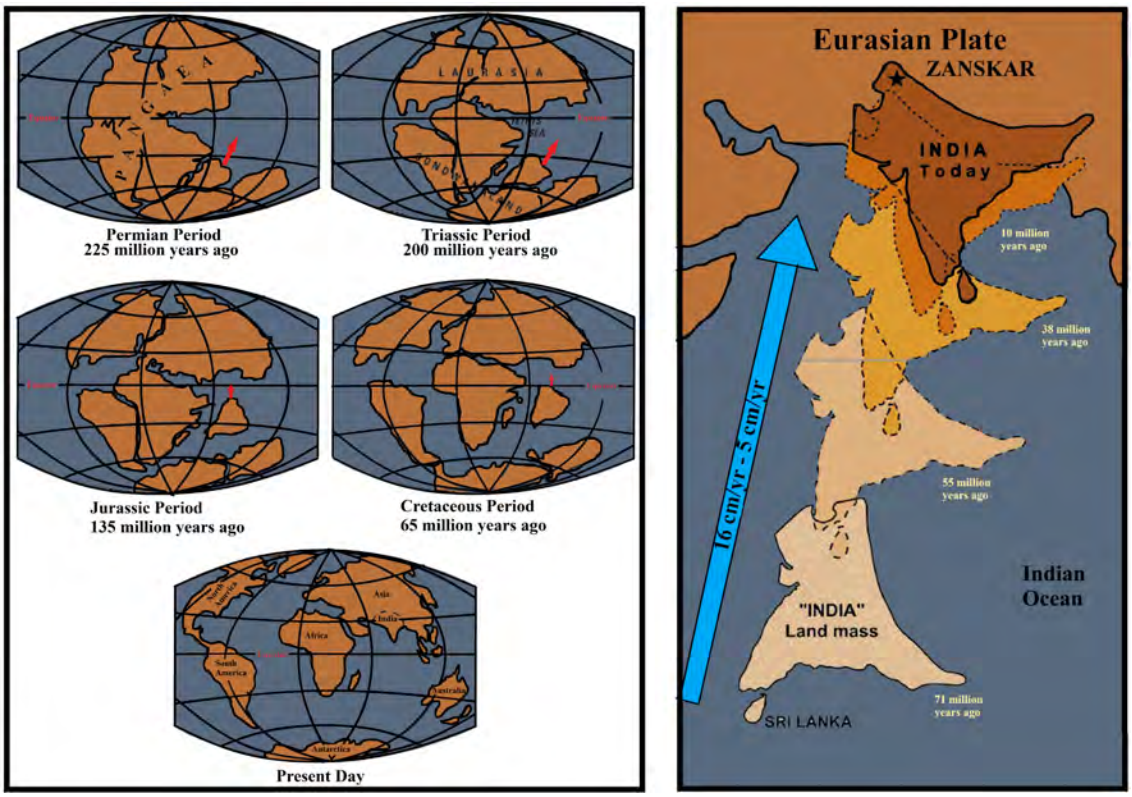

Figure 1.2: The left panel illustrates the disintegration of Pangaea into separate continents, while the right panel depicts the continuous movement of the Indian plate towards the Eurasian plate (source: www.usgs.gov).

As the Himalayan arc was formed due to the continuous convergence between the Indian and Eurasian plates, it exhibits long-term evidence of thrusting and layering [37–39]. Previous studies suggest that the Indian plate heading towards the Eurasian plate at a rate of 40–50 mm/yr, resulting in the folding, faulting, and uplift of geological features [2, 34, 40, 41]. The megathrust of the Himalaya absorbs around half of this convergence between the Indian and Eurasian plates, leading to a history of small to large earthquakes in the

region [42].

1.3 Tectonic or longitudinal classification

The Himalaya is one of the youngest and tallest mountain ranges globally. It stretches for about 2400 km in length and varies in width from $\sim$ 240 km to $\sim$ km kilometers [2, 43]. The range has an arched shape, bending southwards with distinct turns at its western and eastern ends [44]. This shape is mainly due to the Indian plate moving northward and pushing the Himalayan rocks southwards over the Indo-Gangetic basin in the foothills [45, 46]. Significantly, the Himalayan arc is notable for the lateral continuity of its major tectonic events, marking a prominent aspect of its geological evolution.

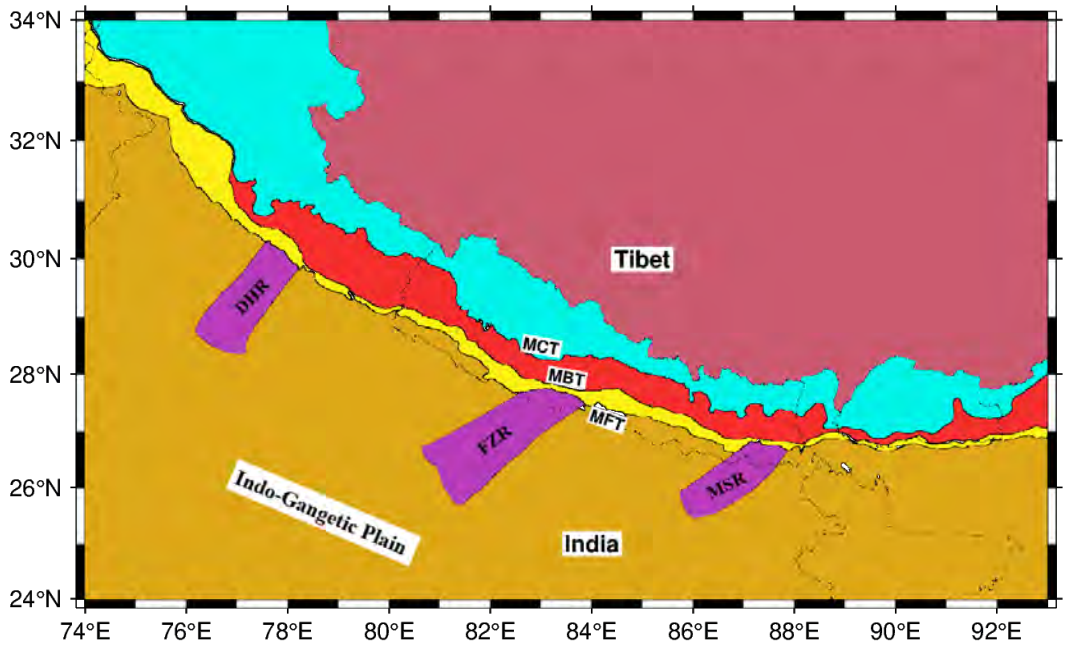

Figure 1.3: Geological map of the Himalaya. Abbreviations are as follows: MCT, Main Central Thrust; MBT, Main Boundary Thrust; MFT, Main Frontal Thrust; and STD, South Tibetan Detachment; DHR, Delhi-Haridwar Ridge; FZR, Faizabad Ridge; MSR, Munger-Saharsa Ridge.

The Himalayan region is split into three side-by-side mountain ranges: the Siwalik Himalaya (or Outer Himalaya), the Lesser Himalaya (or Lower Himalaya), and the Higher Himalaya (or Greater Himalaya) (Figure 1.3). Each of these parts of the Himalaya has

its own unique types of rocks and layers. They are separated from one another by large geological faults. The South Tibetan Detachment (STD) separates the Higher Himalayan ranges from the Tibetan sedimentary (Figure 1.3). The Main Boundary Thrust (MBT) is the Lesser Himalaya's southernmost limit, whereas the Main Central Thrust (MCT) is the border between the Greater and Lesser Himalayas (Figure 1.3). The Main Frontal Thrust (MFT) detaches the Indo-Gangetic Plains and the Siwalik Himalaya (Figure 1.3) [47–49]. These primary faults are believed to converge underneath the Himalaya into a basal thrust fault, known as the Main Himalayan Thrust (MHT) (Figure 1.3).

1.3.1 Higher Himalaya

The formation of the Higher Himalaya occurred through a ductile extrusion process during the earlier Miocene, approximately 23 million years ago. This region, also known as the 'Central Crystalline Axis' of the Himalayan region, signifies the central point of the mountain-building process [2]. It encompasses a lofty mountain range with perpetual snow cover, with elevations ranging from 3,000 m to as high as 8,849 m. Notable peaks in this range include Kedarnath (6,700 meters), Badarinath (7,138 m), and Nanda Devi (7,817 m) in India, as well as Mount Everest (8,849 meters), Kanchenjunga (8,586 m), and Annapurna I (8,091 m) in Nepal [2]. This region has experienced multiple phases of deformation, occurring in a north-to-south direction, and is associated with the MCT, which brought the Higher Himalayas atop the Lower Himalayas [50]. The rocks found in the Higher Himalaya include paragneiss, schist, migmatite, and orthogneiss.

1.3.2 Lesser Himalaya

The Lesser Himalaya, within the broader geological context, occupies a critical position in the tectonic framework of the Himalayan region. This region is situated to the south of the Higher Himalaya and north of the Siwalik Himalaya [2]. This region is characterized by its relatively lower altitude compared to the towering peaks of the Higher Himalaya. It features a diverse and picturesque landscape, with rolling hills, terraced fields, dense forests, and charming hill stations. A lot of the Lesser Himalaya's peaks are covered in

thick layers of snow all year. It forms a pivotal transition zone where significant tectonic interactions occur. The Lesser Himalaya bears the imprints of the ongoing collision between the Indian and Eurasian plates [44]. As compression intensified in the vicinity of the MCT, the meta-sedimentary rocks underwent significant pressure, leading to the formation of tight folds. Consequently, these folds tilted, sometimes overturning and toppling over in the fold-thrust belt. This geological process resulted in the creation of a duplex region characterized by a series of stacked lithotectonic units [44, 51, 52]. As the exhumation process proceeded along the MCT, both Higher Himalaya and Lesser Himalaya rocks underwent late-stage retrograde metamorphism [53]. Additionally, the rock formations of the Lesser Himalaya were further thrust southwards over the Siwalik terrane along the MBT.

1.3.3 Siwalik Himalaya

To the south of the MBT lies the Sub-Himalaya, commonly known as the Siwalik Hills [2]. These hills form the southern boundary of the Himalayan Mountain range and exhibit a youthful topography (Figure 1.3). Parallel to the Lesser and Higher Himalaya, this mountain range has an average height between 600 m and 1,220 m and a width between 10 km and 48 km. Along the MBT, the thrust sheets of the Lesser Himalaya extend farther south, resulting in the fragmentation of the Himalayan terrain into a series of multiple faults [2, 52]. The Sub-Himalayan area primarily consists of sediments eroded from the rugged northern mountains. Within the Siwalik basin itself, frequent reversals in the sequence of sedimentary layers have occurred due to thrusting activities. The intensity of thrusting diminishes gradually from the northeast to the southwest, where the Siwalik hills are characterized by broad, open folds dissected by high-angle reverse faults heading north [54]. The Siwalik terrain consists of varying proportions of sandstone, mudstone, and conglomerates within its different stratigraphic layers [55]. As a result of prolonged deformation along the Siwalik range, certain geological features such as pop-up structures (for instance, the Shillong Plateau), fault remnants, and piggyback basins (including the Dehra Dun, Rapti-Dang Dun, Kota-Pawalgarh Dun, Pinjor Dun, Hetauda Dun, Chitwan

Dun, and Deukhuri Dun) have taken shape [56, 57].

1.3.4 Indo-Gangetic Plain

The entire Himalayan mountain range has been pushed southward over the Indo-Gangetic Plain (IGP) along the MFT (Figure 1.3) [47]. This expansive and continuously deepening foreland basin has formed due to the compressional forces generated within the under-thrusting plate as a consequence of the collision between the Indian and Eurasian plates [58, 59].

The alluvial deposits carried by the Sindhu, Ganga, and Brahmaputra river systems collectively shape the Sindhu-Ganga-Brahmaputra Plain, also known as the IGP. This foreland basin represents a significant geological feature of the Indian subcontinent, covering an extensive area of approximately 250,000 km^2 [60]. The fluvial deposits along the Himalayan front reach thicknesses of approximately 6 km, gradually diminishing toward the south [2, 61]. Within the IGP, three prominent ridges exist, namely Delhi-Haridwar Ridge (DHR), Faizabas Ridge (FZR), and Munger-Saharsa Ridge (MSR) (Figure 1.3) [43, 52]. This foreland basin serves as the habitat for more than 200 million people, diverse wildlife, and lush forests. It is important to note that the seismic activity in the IGP fore-deep is not as pronounced as in the Himalayan arc [62].

1.4 Longitudinal classification

Along the length of the Himalayan arc, it can be further categorized into three larger sections: the northwest Himalaya (approximately 71°E to 80°E, covering the Kashmir Sector, Himachal region, and Garhwal-Kumaun region), the central Himalaya (approximately 80°E to 89°E, covering western Nepal, central Nepal, and eastern Nepal), and the northeast Himalaya (approximately 89°E to 97°E, covering Sikkim, Darjeeling, Bhutan, and Arunachal Himalaya) (Figure 1.4). These regions are traversed by the major thrust faults of the Himalayan arc, namely MCT, MBT, and MFT [2, 63]. Furthermore, all three of these regions have a history of experiencing devastating earthquakes in the past.

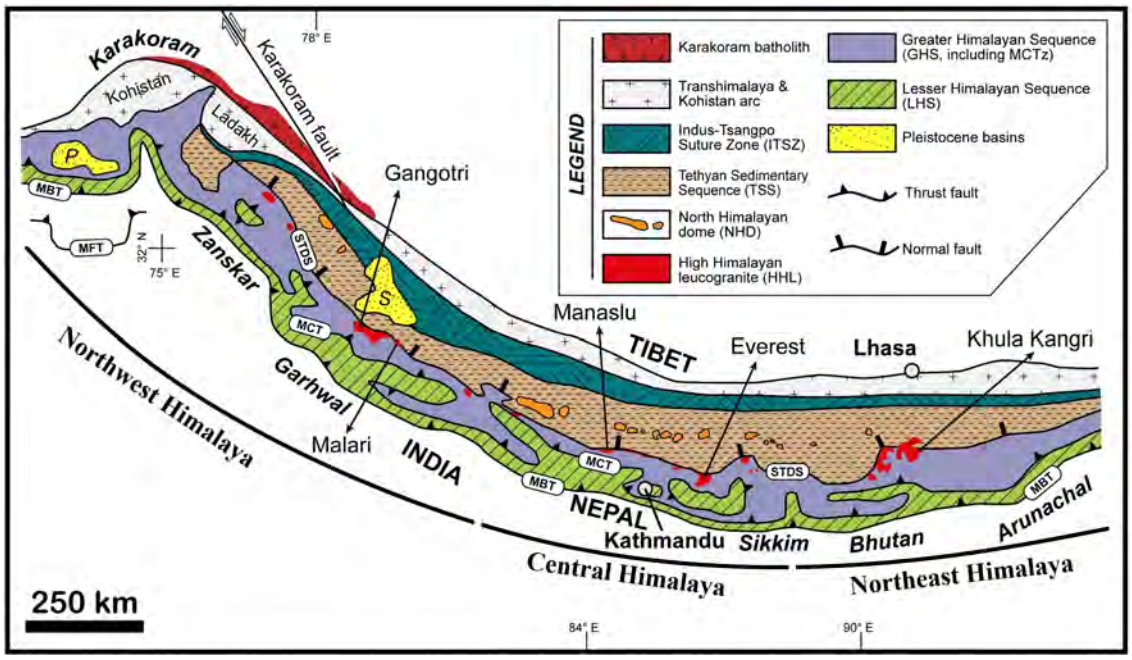

Figure 1.4: A schematic representation of the geological layout of the Himalayan arc, delineating its primary units, classification, and tectonic boundaries (modified after Carosi et al. (2018) [64]).

1.4.1 Northwest Himalaya

The northwest Himalaya encompasses several distinct geological features, forming a complex landscape. The northeastern mountain sequence, situated at elevations ranging from approximately 800 to 2000 m, consists of early to late Tertiary sedimentary rocks sourced from the Siwalik mountains. These rocks have been intricately folded and deformed by the action of mega thrusts [41, 65, 66]. In the Kashmir and Himachal region within the northwest Himalaya, the MBT and MCT are not well-defined, though there are indications of imbricate faults in the area (Figure 1.4) [2]. On the other hand, in the Garhwal-Kumaun Himalaya, the region between the MBT and MCT widens to over 80 km, and both of these thrusts exhibit several surface exposures [2]. Additionally, the southernmost frontal thrust, known as the MFT, marks the boundary between Quaternary fluvial deposits of the IGP and the Janauri anticline [48, 67–69]. This region experienced some significant events, namely the 1905 Kangra, and the 2005 Kashmir earthquakes. The extensive subducting DHR could potentially exert an influence on seismic events in this

region [9]. The DHR serves as an extension of the Aravalli mountain belt and extends beneath the Himalayan arc. This extension may be linked to lower magnitude seismic activity [70].

1.4.2 Central Himalaya

The central Himalaya region encompasses both Nepal Himalaya and southern Tibet (Figure 1.4). Here, the Siwalik group forms a folded Cenozoic piedmont region [44]. This region exhibits a distinct demarcation of the megathrust system of the Himalaya (Figure 1.4) [2]. The Higher Himalaya, within this area, consists of a stratigraphic succession of approximately 10 km, comprising crystalline rocks and sedimentary rocks with fossils [71, 72].

Notably, the world's highest peak, Mount Everest (approximately 8,849 m), is situated in this region. The Lesser Himalaya in this part comprises sedimentary and metasedimentary rocks of Precambrian to Miocene age, which lack fossils [61]. Furthermore, the central Himalaya includes the FZR, which acts as a subsurface extension of the Bundelkhand massif [70]. Evidence of low-magnitude seismic activity is apparent from a densely installed seismic network along this ridge [12]. The FZR separates the Gandak depression to the east from the Sarda depression to the west [70]. The central Himalaya has been the epicenter of numerous significant seismic events throughout its history, including 1100 Nepal ($M_w \sim 8.4$), 1505 Lo Mustang ($M_w \sim 8.2$), 1833 Bihar-Nepal (M_w 7.5), 1934 Bihar-Nepal (M_w 8.0), and the most recent 2015 Gorkha (M_w 7.8) event [6–8, 73–77].

1.4.3 Northeast Himalaya

The northeastern Himalayan region and its surrounding areas exhibit intricate tectonic behavior characterized by elevated seismic activity (Figure 1.4). This region falls within seismic zones IV and V on India's seismic zonation map [78]. The frontal part of the northeastern Himalaya, situated along the Brahmaputra Basin, is wedged between the Himalayan arc and the Indo-Burmese arc [79]. Over the years, this region has witnessed two significant seismic events, namely the 1897 Shillong earthquake (M_w 8.0) and the

1950 Assam earthquake (M_w 8.2), in addition to several major earthquakes in the last century. One of the distinguishing characteristics of the northeast Himalaya is its location between two major tectonic arcs: the Himalayan arc to the north and the Indo-Burmese arc to the south [80]. This geological arrangement has contributed to the region's complex tectonic behavior and seismicity. The 1897 Shillong earthquake occurred in proximity to the Shillong plate, which is an uplifted horst block formed during the Cenozoic era. It became geologically isolated from peninsular India due to the deposition of Tertiary Ganges-Brahmaputra fluvial sediments [80].

1.5 The Himalayan Megathrust System

The Himalayan megathrust system is a critical geological feature that plays a central role in shaping the Himalayan mountain range and contributing to seismic activity in the region. It consists of a network of fault zones associated with the collision and convergence of

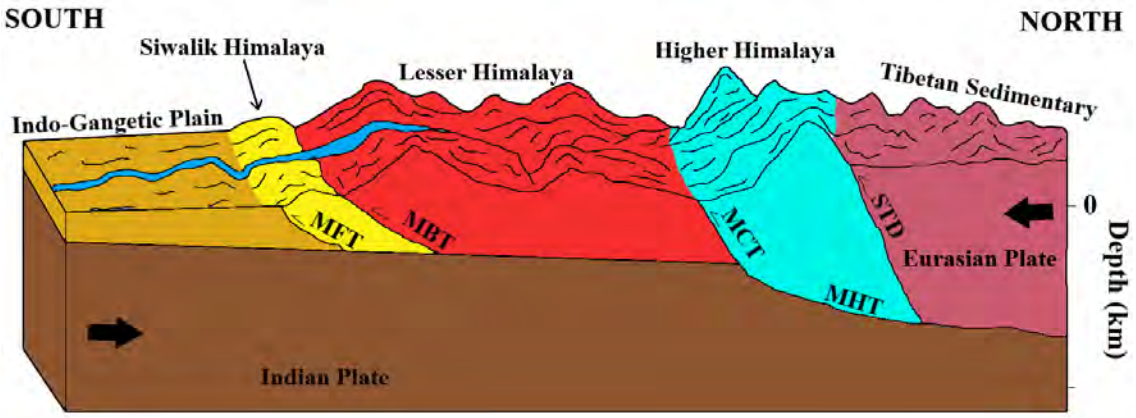

Figure 1.5: The Himalayan arc in schematic cross-section. Abbreviations are as follows: MCT, Main Central Thrust; MBT, Main Boundary Thrust; MFT, Main Frontal Thrust; and MHT, Main Himalayan Thrust;

the Indian and Eurasian tectonic plates. These thrust faults have developed due to the north-south convergence of the Indian and Eurasian continental plates over ∼50 million years (Figure 1.5) [2]. Due to this ongoing collision, the Himalayan arc is renowned for being one of the most seismically active regions worldwide. As the Indian plate steadily

advances northward, the sedimentary crustal layer undergoes intricate folding, continuous buckling, and eventually fractures into distinct tectonic segments through faulting and thrusting processes [2]. This persistent collision has given rise to three major active thrust systems: the Main Central Thrust (MCT), the Main Boundary Thrust (MBT), and the Main Frontal Thrust (MFT), accompanied by various imbricate branching faults and out-of-sequence faults (Figure 1.3) [2, 48, 57, 81]. Furthermore, these three megathrusts are believed to converge onto a basal detachment plane known as the Main Himalayan Thrust (MHT), where the Indian plate subducts beneath the Eurasian plate (Figure 1.5) [44, 82].

1.5.1 Main Frontal Thrust

The MFT is positioned along the southern margin of the Himalayan collision zone and is thought to accommodate a significant portion, ranging from 50% to 100%, of the overall shortening occurring across the Himalaya [74]. This fault is the most recently formed major structural discontinuity and runs parallel to the Himalayan mountain ranges, effectively separating the outermost Siwalik Himalaya from the IGP (Figure 1.5). The active thrusting along the MFT has elevated the Siwalik hills to heights approximately ranging from 500 m to 1000 m above the neighboring Indo-Gangetic plain [47, 48]. It is considered to be a blind fault due to its limited surface exposures [48, 83]. Over the Quaternary period, the MFT has displayed activity, resulting in various alterations to the region's more recent geological, geomorphological, and drainage features. The MFT has a northward dip of around 15° to 35° and is associated with a long-term slip rate estimated at roughly 8 to 10 mm/yr, although there are considerable uncertainties in this measurement, ranging from 3 to 7 mm/yr [67, 72].

1.5.2 Main Boundary Thrust

The MBT constitutes a significant north-dipping thrust fault, typically inclined at angles between 30° and 50°, positioned beneath the Lesser Himalayan rocks (Figure 1.5). It played a role in the Cenozoic shortening of the upper Indian Plate and presently delineates

the structural and orographic boundary between the Outer and Lesser Himalayas. The MBT exhibits characteristics of a brittle fracture [44]. The MBT is notably well-exposed throughout the entire central Himalaya and can even be discerned in aerial photographs. In the Kumaun Himalaya region, the MBT has experienced rotational and strike-slip movements during the Holocene period [52]. The distance between the MFT and MBT ranges from approximately 30 km to 80 km in the northwest Himalaya, largely due to the presence of substantial reentrant features in the MBT [2].

1.5.3 Main Central Thrust

The MCT stands as a prominent geological fault within the Himalayan wedge, extending along the Himalayan arc. It exhibits a dip of approximately 12° to 35° degrees northward (Figure 1.5) [2, 84]. Topographically, the MCT is evident as a significant elevation change, ranging from approximately 3000 m to 5000 m. Functioning as a ductile shear zone, it plays a crucial role in the placement of the high-grade Higher Himalayan crystalline complex above the lower-grade to unmetamorphosed Lesser Himalayan sequence. The activity of the MCT remains a subject of debate. Nakata (1989) [48] suggested dormancy based on carbon dating of Quaternary deposits along the northwest Himalaya. Conversely, Ponraj et al. (2010) [85] proposed possible activity, citing significant geodetic strain rates and microseismic activity in the MCT zone along the Kumaun Himalaya. Additionally, seismic clusters of moderate-sized earthquakes have been observed along the MCT in the Higher Himalaya [86].

1.5.4 Main Himalayan Thrust

The megathrust system in the Himalaya, including the MCT, MBT, and MFT, is believed to converge underneath the Himalaya into a basal thrust fault, known as the MHT (Figure 1.5) [2, 61, 87]. The MHT acts as an interface between the descending Indian plate and the overlying Himalayan structures [44, 61]. Its configuration resembles a flat-ramp-flat structure, with the mid-crustal ramp dipping at an angle of about 5° to 15° in the northward direction [11, 12, 73, 88–90]. This ramp section of the MHT has been associated with

numerous significant Himalayan earthquakes [11, 12, 41, 61, 88, 89].

Previous geodetic investigations [e.g., [11, 73, 90–92] have indicated that the deeper portion of the MHT exhibits creeping behavior, which refers to slow, continuous fault activity due to crustal deformation. The shallower part, including the MFT, is locked with a slip deficit rate of approximately 14 to 18 mm/yr. This accumulated deficit rate, amassed over the course of a century, poses the potential for triggering a major Himalayan earthquake in the future [5, 11, 93].

1.6 Central seismic gap

The concept of seismic gaps, forming the basis of the seismic gap hypothesis, is rooted in the principles of the "elastic rebound theory" [94]. According to this theory, the ongoing stress resulting from the motion of tectonic plates along a fault or plate boundary gradually leads to the accumulation of strain energy. This energy builds up until it surpasses the strength of the rocks involved [94]. Eventually, this accumulated strain energy is released during earthquakes, causing the rocks to return to their original shape [94]. In the context of the Himalayan region, the identification of seismic gaps is crucial. These gaps are regions that have not witnessed significant seismic activity despite their high hazard potential. Notably, three distinct seismic gaps have been identified in the Himalayan arc based on the spatial distribution of past major earthquakes and the extended periods of quiescence in these highly vulnerable segments. These seismic gaps are known as the Kashmir seismic gap, central seismic gap, and Assam seismic gap [95–98].

The central seismic gap refers to the seismic gap between the rupture zones of two great earthquakes, namely the 1905 Kangra and 1934 Bihar-Nepal earthquakes [7, 96, 97]. Previous studies [6, 10, 16, 99] observed that the Kumaun Himalaya, and western Nepal (sections of the central seismic gap) could produce a great earthquake as neither the Kumaun Himalaya nor western Nepal has ruptured in the previous 200 to 500 years. However, the notion of this suggested seismic gap is a topic of extensive debate [3, 100]. This debate arises due to the occurrence of two substantial historical earthquakes in this region, in AD 1505 and 1803.

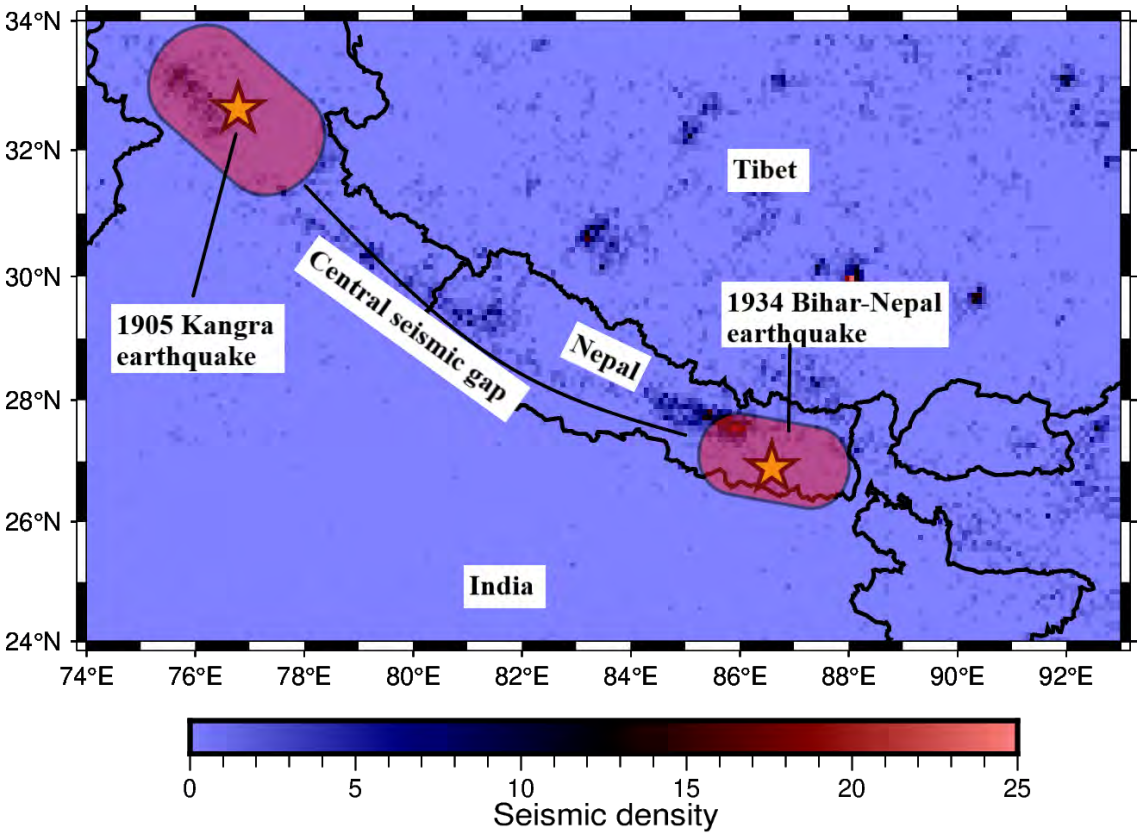

Figure 1.6: Epicentral locations and the rupture extents of the 1905 Kangra earthquake and the 1934 Bihar-Nepal earthquake.

1.7 Objective of the thesis

The primary objective of this thesis is to assess the ongoing crustal deformation during the interseismic period and consequently to re-evaluate the contemporary seismic hazards in the Kumaun and Nepal Himalaya. To accomplish this primary objective, four specific sub-objectives have been framed below.

1. To derive the most updated high-resolution integrated velocity field for the study region

2. To estimate a section-wise seismic moment budget and corresponding earthquake potential in the Kumaun and Nepal Himalaya

3. To characterize the fault kinematics (e.g., distribution of dip-angle, fault depth,

locking depth, rake angle, and slip rate) of the Main Himalayan Thrust (MHT) in the study region

4. To perform probabilistic earthquake recurrence modeling and seismic nowcasting in the study area

1.8 Scope of the thesis

This section delineates various scopes and related work elements to achieve the research objective:

1. GPS data collection from the regional network comprising 22 GPS sites in the Kumaun Himalaya.

2. Processing the accrued GPS data using the GAMIT-GLOBK suite of post-processing software to generate position time-series and velocity vectors.

3. Combining regional velocity vectors with published data (26 GPS velocity datasets) using a seven-parameter Helmert transformation in the Kumaun Himalaya.

4. Similarly, combining 46 NGL-based GPS velocity vectors with published data (31 GPS velocity datasets) in the Nepal Himalaya.

5. Estimating InSAR-based ascending and descending LOS velocities across the Kumaun and Nepal Himalaya via LiCSAR processing toolbox.

6. Integrating GPS and InSAR-derived velocities to create a high-resolution integrated velocity field along the Kumaun and Nepal Himalaya.

7. Compiling a seismic catalog by collating data from several sources including ISC, USGS, IMD, and other published works.

8. Calculating dilatation, maximum shear, and rotational strain rates across the Kumaun and Nepal Himalaya using the high-resolution integrated velocity field.

9. Deriving geodetic moment rates from strain tensors and seismic moment rates from earthquake database, and comparing these rates across the Kumaun and three spatial segments of Nepal to calculate the seismic moment budget.

10. Assessing slip rates and fault geometry of the MHT over the Kumaun and Nepal Himalaya using a Bayesian fault inversion model.

11. Deriving conditional probability curves (hazard function curves) for different combination of elapsed times and residual times.

12. Carrying out natural time seismicity statistics and computing earthquake potential scores for several city regions embedded in the study region.

13. Identifying the regions of high seismic hazard regions by employing both theory-driven geodetic modeling and data-driven empirical statistical analysis.

1.9 Organization of the thesis

The present thesis delves into seismic hazard analysis through the utilization of geodetic data (GPS and InSAR) and earthquake data over the Kumaun and Nepal Himalaya. The thesis comprises six distinct chapters.

Chapter 1 provides a theoretical exploration of the Himalayan arc, encompassing its evolutionary history, tectonic characteristics, subregions, and notable seismic gaps. Additionally, this chapter outlines the objective of the thesis and offers a concise roadmap for the subsequent sections.

Chapter 2 delves into an in-depth presentation of the study area of this thesis. It comprehensively covers various datasets utilized throughout the research including GPS data, InSAR data, the integrated velocity field, and earthquake data.

Chapter 3 is dedicated to calculating the distribution of strain rates and the associated seismic moment budget. This involves a comparative analysis between the accumulated geodetic moment rates derived from strain rates and the released seismic moment rates

obtained from earthquake data. This assessment spans across the Kumaun Himalaya and three distinct spatial sections of the Nepal Himalaya.

Chapter 4 focuses on determining the spatial patterns of slip rates and fault geometry along the MHT using a Bayesian fault inversion model across 20 arc-normal profiles within the Kumaun and Nepal Himalaya. It concludes by computing the earthquake potential based on the derived slip deficit rates.

In Chapter 5, a data-driven area-based methodology comprising earthquake forecasting (interevent time modeling) and earthquake nowcasting (natural time analysis) is provided. While the empirical forecasting technique aims to statistically assess the conditional probability of future large earthquakes, the seismic nowcasting method aims to indirectly determine the current progression of regional earthquake cycle at several city locations.

Finally, Chapter 6 encapsulates the essence of the thesis work, emphasizing its primary contributions and offering insights into potential future directions for research.

Chapter 2

Study Area and Dataset

"Every data point has a story to tell,
and every dataset is a chapter in the book of knowledge."
— Nate Silver

In order to assess seismic hazards, a good understanding of the study area and relevant dataset is crucial. To this end, the chapter offers valuable perspectives to the seismotectonic setting of the study area, used geodetic and earthquake data, and a summary of previous crustal deformation studies in the region. It also includes an overview of the geodetic data, especially GPS and InSAR, by detailing their composition, data collection, and processing techniques. The combination of GPS and InSAR velocities enables a high-resolution integrated velocity field of the study region. Similarly, a number of procedures and pictorial representations of earthquakes is provided for studying the earthquake data characteristics. This includes epicentral distributions of earthquakes, homogeneity in magnitude, magnitude-frequency plot, magnitude-time graph, and cross-sectional views along longitude and latitude. This chapter essentially serves as a pre-requisite for the following chapters. For example, the high-resolution integrated velocity field is an inevitable input parameter for Chapters 3 and 4 to determine strain rate, seismic moment budget, and fault kinematics along the study area. Similarly, the compiled earthquake data, both homogenized and complete, is an important parameter for Chapters 3 to 5 to estimate seismic moment rate, earthquake potential, interevent time modeling (earthquake forecasting), and

nowcast score calculation (earthquake nowcasting) for several city regions embedded in the study area.

Contents

Parts of this chapter have been published/submitted in the following refereed publications:

H. Verma, S. Pasari, Y. Sharma, K. E. Ching. "High-resolution velocity and strain rate fields in the Kumaun Himalaya: An implication for seismic moment budget". *Journal of Geodynamics* 160 (2024) 102023 (SCI).

H. Verma, S. Pasari, and Y. Sharma. "Tectonic deformation along the Delhi-Haridwar Ridge revealed by InSAR observations: Preliminary results". In: *2021 IEEE International India Geoscience and Remote Sensing Symposium (InGARSS)*. IEEE, 2021, pp. 181–184 (Scopus).

H. Verma, Y. Sharma, and S. Pasari. "Synthetic aperture radar interferometry to measure earthquake-related deformation: A case study from Nepal". In: *Disaster Management in the Complex Himalayan Terrains.* Springer, 2022, pp. 133–140.

H. Verma, Y. Sharma, K. E. Ching, S. Pasari. "Contemporary seismic moment budget along the Nepal Himalaya derived from high-resolution InSAR and GPS velocity field". *Acta Geophysica* (2024) (in print, SCIE).

2.1 Introduction

In the pursuit of understanding contemporary seismic hazards and interseismic crustal deformation, a comprehensive assessment of the study area and dataset becomes paramount. Although the entire Himalayan arc is recognized to be an earthquake prone zone, this thesis purposefully concentrates on the Kumaun and Nepal Himalaya due to the shortage of time and manpower.

The Kumaun Himalaya, the eastern part of the northwest Himalaya, stands out to be an area with high seismic potential as the region is in a seismic quiescence phase for the last 200 to 500 years [16, 99]. Nevertheless, during the last several decades, the Kumaun Himalaya has experienced many small-sized earthquakes with a few strong events. Analyses of focal mechanism solutions for these earthquakes in the region indicate thrusting tectonic activity [101, 102]. The geophysical measurements in the Kumaun Himalaya revealed a high conductive zone beneath the Higher Himalaya which coincides with the mid-crustal microseismicity belt [103]. Although there has been no recorded megathrust earthquake in the Kumaun Himalaya, its surrounding regions have experienced two significant events on September 1, 1803 and June 6, 1505 in Uttarakhand Himalaya [5]. However, there is no evidence of surface fault scarps from these earthquakes in the Kumaun Himalaya [104, 105]. Nonetheless, paleoseismological studies have preserved evidence of at least one great earthquake that occurred between 1222 and 1422 in the same region [106, 107]. The estimated magnitude of this earthquake is greater than $M_w \sim 8.4$, confirming the region's potential to accumulate enough elastic strain energy to produce megathrust earthquakes in the future. Therefore, it is believed that the Kumaun Himalaya region may produce large-sized powerful earthquakes in future, closing the spatio-temporal seismic gap. In light of the above discussion, it is important to determine the present-day crustal deformation throughout the Kumaun Himalaya to re-assess seismic hazard scenario in the area.

On the other hand, the Nepal Himalaya (also known as the central Himalaya) is one of the world's most seismically active intercontinental colliding tectonic region that has

experienced many deadly earthquakes in past. Some of these notable events are the 1100 Nepal ($M_w \sim 8.4$), 1255 Kathmandu ($M_w \sim 7.8$), 1344 Mechi ($M_w \sim 7.9$), 1408 Nepal-Tibet ($M_w \sim 8.2$), 1505 Lo Mustang ($M_w \sim 8.2$), 1681 Kosi ($M_w \sim 8.0$), 1767 Bagmati ($M_w \sim 7.9$), 1833 Bihar-Nepal (M_w 7.5), 1934 Bihar-Nepal (M_w 8.0), and the most recent 2015 Gorkha (M_w 7.8) event [6–8, 73–77]. Nonetheless, there may be latent seismic energy beneath the Nepal Himalaya that is yet to be released, potentially resulting in a significant earthquake in the near future. Previous studies [e.g., 11, 12, 16, 108] have suggested that the moment deficit rate along the Nepal Himalaya is high. As a result, the Nepal Himalaya holds significant importance in the context of seismic hazards.

To assess the present-day seismic hazards in the Kumaun and Nepal Himalaya regions, a vast array of datasets and methods is required. For this, (i) GPS and InSAR velocities are derived and subsequently combined to obtain a high-resolution integrated velocities over the Kumaun and Nepal Himalaya and (ii) the earthquake dataset is acquired from several open source and published data to understand different characteristics of earthquake data. The derived integrated velocity field will be utilized to estimate the present day strain rate distribution, seismic moment budget, and fault kinematics along the Kumaun and Nepal Himalaya in Chapters 3 and 4. On the other hand, the complied earthquake dataset will be used to calculate seismic moment rate and earthquake potential, and to perform earthquake forecasting and nowcasting in Chapters 3 to 5.

2.2 Study area

The study region of this thesis encompasses both Kumaun and Nepal Himalaya (Figure 2.1). In the study region, there are four distinct lithotectonic units: the Siwalik Himalaya, Lesser Himalaya, Higher Himalaya, and Tethys Himalaya. These units are separated by four intracrustal boundary thrust/fault systems (Figure 2.1). The Siwalik Himalaya, characterized by sedimentary rocks, occupies the southernmost expanse of the Himalayas. Northwards from the Siwalik Himalaya lies the Lesser Himalaya, distinguished by its metamorphic rock composition. Progressing further north, the Higher Himalaya lies to the north of the Lesser Himalaya and it is constituted of crystalline rocks. Lastly, the Tethys

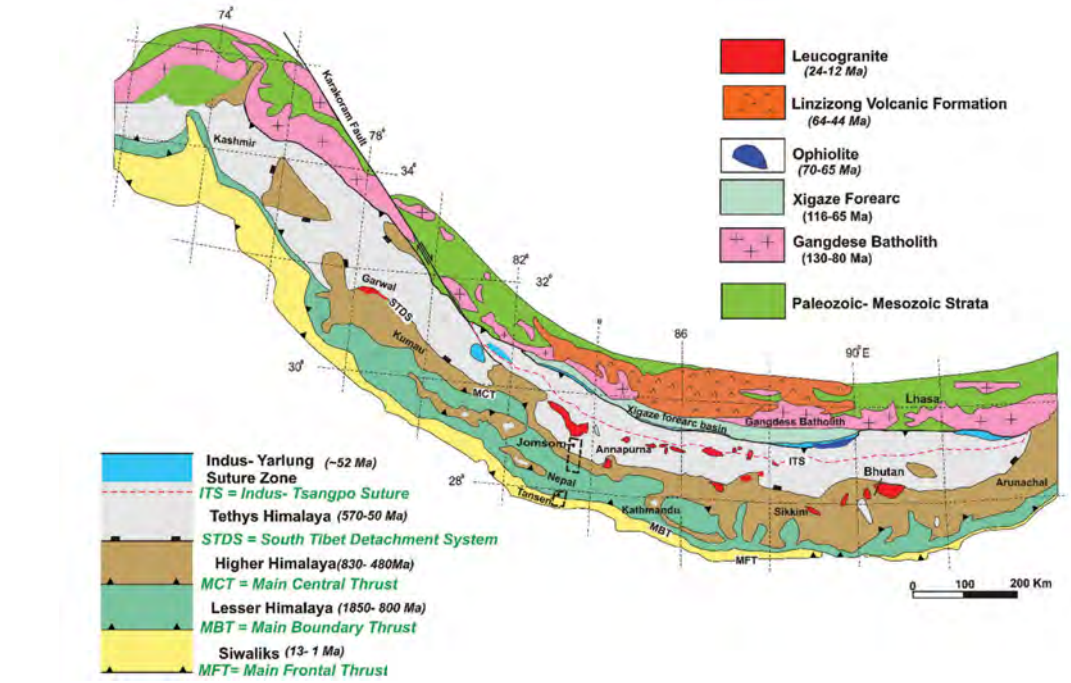

(a)

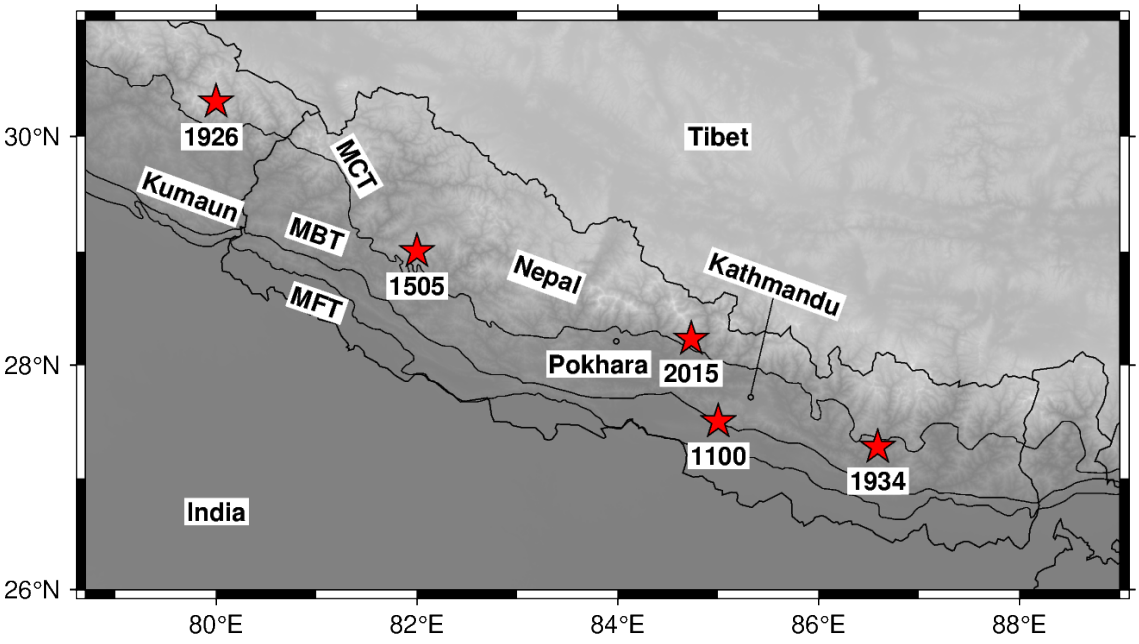

(b)

Figure 2.1: (a) Geological map of the Himalayan arc sourced from Neupane et al. (2018) [109]. (b) Locations of notable historical earthquakes and the recent 2015 Gorkha earthquake within the Kumaun and Nepal Himalaya region. Abbreviations are as: MFT, Main Frontal Thrust; MBT, Main Boundary Thrust; MCT, Main Central Thrust.

Himalaya, comprising sedimentary rocks, extends beyond the northern reaches of the Higher Himalaya within this geological framework. The Siwalik boundary is marked by the southernmost MFT, along with the traversal of the MBT over the Lesser Himalaya [44]. Metamorphic crystalline rocks from the Higher Himalaya, dating back to the Cambrian and Proterozoic eras, displace over the meta-sediments of the Lesser Himalaya along the MCT [44]. This movement along the MCT, defining the southern boundary of the Central Crystalline Zone, causes displacement of crystalline rocks over the sedimentary and low-grade metamorphic formations of the Lesser Himalaya [44, 52]. Furthermore, the geological sequence, spanning from the Late Precambrian to Cretaceous ages and positioned north of the Higher Himalaya, encompasses the rocks of the Tethys Himalaya [110]. The transition from the crystalline rocks of the MCT Zone to the sedimentary formations of the Tethys Himalaya involves alterations in lithology, metamorphic grade, as well as changes in features' mode and orientation.

According to recent GPS studies, the rate of convergence between India and Eurasia varies spatially, for example, from 37 mm/yr to 44 mm/yr from west to east [10, 91]. The GPS measurements over the Kumaun Himalaya revealed a 15 mm/yr to 18 mm/yr convergence rate [85, 90], whereas the convergence rate in the Nepal Himalaya region varies from 17 mm/yr to 21 mm/yr from eastern Nepal Himalaya to western Nepal Himalaya [11, 12]. It appears that the shallow section of the decollement (MHT) is locked beneath the Lesser Himalayas, accumulating elastic strain energy, whereas the deeper part creeps underneath the Higher Himalaya [16, 71, 111]. This stored strain will be subsequently unleashed by major to great earthquakes along the study region [73, 85, 108, 112].

2.2.1 Literature review

The Himalayan arc is on the brink of producing a sequence of major to great earthquakes, posing a catastrophic threat to densely populated countries in Southeast Asia situated along the orogenic belt. Various geological, historical, and space-based geodetic methods have been employed to evaluate seismic hazards, including earthquake potential, strain release

and accumulation, slip rate estimation, and convergence rate along different segments of the Himalayan arc. This section presents an in-depth literature review related to the study area. For this, first, a few important studies covering the entire Himalayan segment are highlighted, followed by specific studies pertaining to the Kumaun Himalaya and the Nepal Himalaya, respectively.

Bilham et al. (2001) [7] partitioned the entire Himalayan arc into 10 segments to estimate potential magnitudes and slip for future earthquakes. They observed that the potential magnitude in all segments is sufficiently high to produce events with M_w>8.0, except in the rupture zones of twentieth-century earthquakes (i.e., the earthquakes in 1905, 1934, and 1950) [7]. Following two recent significant earthquakes, namely the 2005 Kashmir earthquake and the 2015 Gorkha earthquake, Bilham (2019) [5] reevaluated the potential magnitude and slip for future earthquakes along 15 segments of the Himalayan arc, utilizing data from paleoseismic trenching, historical records of major earthquakes, and GPS measurements. He observed that the potential magnitude along the central seismic gap and eastern Bhutan has risen to M_w 8.5 for future events [5].

Bilham and Ambraseys (2005) [113] reported an average convergence rate of less than 5 mm/yr based on historical earthquakes and approximately 18 mm/yr from GPS observations along the Himalayan arc. The observed slip deficit, estimated at around 13 mm/yr, is sufficient to trigger earthquakes with a magnitude equal to or greater than 8.5 along the Himalayan arc [113].

Stevens and Avouac (2015) [73] determined the convergence rate of the MHT through geodetic observations. The slip rate along the decollement ranges from 13.3$\pm$1.7 mm/yr to 21.2$\pm$2.0 mm/yr across a fully locked MFT extending up to 100$\pm$20 km to the north [73]. Additionally, Stevens and Avouac (2016) [93] calculated the moment deficit rate and the magnitude of an anticipated large earthquake that corresponds to the cumulative moment deficit over the past 1000 years along the Himalaya. They utilized the interseismic coupling ratio to identify locked zones both across and along the MHT, indicating potential locations for future large earthquakes, or alternatively, an aseismic barrier capable of halting earthquake ruptures [93]. Their observations revealed that the locked barrier in

the frontal arc accumulates a moment deficit rate of $15.1 \pm 1.0 \times 10^{19}$ Nm/yr for the entire Himalaya, implying the potential occurrence of a magnitude 9.0 earthquake in the future [93].

Bungum et al. (2017) [114] determined the strain rate field along the northwest and central Himalaya, displaying variations of 50.09×10^{-9} strain/yr in Kashmir, $61.36 \pm 4.87 \times 10^{-9}$ strain/yr in Himachal, 61.84×10^{-9} strain/yr in Garhwal-Kumaun, 54.59×10^{-9} strain/yr in western and central Nepal, to 57.95×10^{-9} strain/yr in eastern Nepal. Furthermore, they converted these strain rates into geodetic moment rates and compared the findings with seismic moment rates obtained from 115 years of earthquake data, revealing an almost perfect match. When compared with seismic moment rates derived from 515 years of seismicity data, geodetic moment rates were observed to be higher by a factor of two. The study reported an elevated seismic hazard in the central seismic gap [114].

Li et al. (2018) [115] combined GPS data with publicly available data to visualize the coupling along the MHT and observed that high coupling extends from 100 km to beyond 140 km along the MFT moving further north. The observed slip rate of the MHT varies from 18.6 ± 1.6 mm/yr in the northwest, 20.2 ± 1.2 mm/yr in the central region, to 22.2 ± 1.7 mm/yr in the northeast Himalaya. This slip rate accumulates strain over the past 300 years, potentially leading to the occurrence of a significant $M_w \sim 8.6$ earthquake in the future [115].

Sharma et al. (2020) [10] divided the Himalayan arc into 24 segments and compared the geodetic and seismic moment rates for each segment, highlighting the stored and released strain energy, respectively. The results show that the geodetic and seismic moment rates vary significantly along the arc. They found that the segments with high earthquake potential ($M_w \geq 8.0$) belong to the central seismic gap and northeast part of Himalaya, whereas the segments with low earthquake potential ($M_w \leq 7.0$) lie in the rupture areas of recent large events.

2.2.1.1 Literature review for the Kumaun Himalaya

Jayangondaperumal et al. (2013) [116] investigated two trenching sites along the MFT in the Garhwal-Kumaun Himalaya. Their analysis revealed (i) an evidence of two significant earthquakes occurring before 1400 AD and (ii) a remaining seismic energy equivalent to an earthquake of $M_w \sim 8.5$ in the future.

Jade (2004) [117] and Jade et al. (2004) [118] calculated the convergence rate in the range of $14-20$ mm/yr between the Indian subcontinent and the Tibetan Plateau and $10-18$ mm/yr over the Garhwal Himalaya. Furthermore, Jade et al. (2014) [119] provided a comprehensive summary of horizontal velocities, convergence, and extension rates from 14 permanent and 42 campaign GPS stations along the northwest Himalaya. They noted that surface velocities range between $30-48$ mm/yr, and arc-normal shortening rates vary from $10-14$ mm/yr along different transects of the northwest Himalayan wedge [119]. Additionally, they reported the slip rate, dip angle, and locking width of the MHT as 18 ± 1.5 mm/yr, 8°, and 110 km, respectively in the Kumaun Himalaya [119].

Ponraj et al. (2010, 2011) [85, 120] conducted an analysis of the geodetic strain field and slip rate distribution beneath the northwest Himalaya using three years of measurements from 16 campaign sites. Specifically, Ponraj et al. (2010) [85] calculated a horizontal velocity of $41-50$ mm/yr for all GPS stations and observed that a convergence rate of approximately 15 mm/yr is accumulated within the Kumaun Himalaya [85]. They also noted higher dilatational and maximum shear strain rates along the MCT in this region [85]. Similarly, Ponraj et al. (2011) [120] estimated a slip rate of 10 mm/yr for the MHT beneath the northwest Himalaya. Their analysis using the Non-Uniform Creep (NUC) dislocation model suggested a locking depth of approximately 15 km in the northwest Himalaya [120]. They concluded that deformation is concentrated between the Lesser Himalaya and the Higher Himalaya, indicating the presence of a structural discontinuity on the fault between the Kumaun and Garhwal Himalaya [120]. In a subsequent study, Ponraj et al. (2019) [89] recalculated slip rate as 17.2 ± 1.0 mm/yr and they identified a locking depth of about 20 km along a dipping MHT with an inclination of approximately

7° in the Kumaun Himalaya using a NUC dislocation model. The calculated slip rate of the MHT, corresponding to a moment deficit rate of 8.4±1.0× 10^{18} Nm/yr, indicates the potential occurrence of a great earthquake ($M_w \geq 8.0$) with a return period of ∼600 years in the Kumaun region [89].

Dumka et al. (2014) [121] conducted a study on crustal deformation in the Kumaun Himalaya based on 25 GPS observations spanning the years 2003–2006 along two transects. Their analysis indicated that both MFT and MBT are presently locked, while the MCT exhibits maximum deformation rates [121]. They observed a horizontal shortening of 6.7±2.5 mm/yr between the Lesser Himalaya and the IGP [122]. In a subsequent study, Dumka et al. (2018) [123] recalculated slip rates for the MFT, MBT, and MCT. They found a slip rate of 1.5±1.0 mm/yr for the MFT, 5.2±1.2 mm/yr for the MBT, and 8.7±1.7 mm/yr for the MCT. High compression and shear strain rates were estimated along the MCT, leading the researchers to suggest that the shallow to the down-dip edge of the MHT is fully locked.

Based on observations from five continuous GPS stations in the Garhwal-Kumaun Himalaya, Gautam et al. (2017) [92] determined a slip rate of approximately 18 mm/yr for the MHT over a locked segment spanning around 100 km in the region. They remarked that the accumulated strain energy over the past 500−700 years is significant enough to generate a great earthquake in the Garhwal-Kumaun Himalaya [92].

Utilizing data from 28 GPS stations, Yadav et al. (2019) [90] determined a robust seismic coupling extending over 85 km along the MHT in the Garhwal-Kumaun Himalaya. They observed a slip rate of 18 mm/yr along the MHT at a depth of approximately 20 km. The accumulated strain along the fully locked MHT over the last 500 years lists the northwest Himalaya among the regions with high seismic hazard worldwide [90]. Furthermore, Yadav et al. (2021) [124] calculated a higher compression strain rate of approximately –0.15 μstrain/yr along the upper Kumaun Himalaya. They suggested that the Kumaun Himalaya has stored sufficient strain energy equivalent to a earthquake potential of magnitude M_w ∼8.2 [124].

Kannaujiya et al. (2022) [99] calculated a mean compression rate of –0.07 ± 0.01 μ

strain/yr in the Garhwal-Kumaun region by analyzing data from eighteen GNSS stations. Their examination, employing a dip-slip dislocation model, indicated a convergence rate of 16.7±2.0 mm/yr, a locking width of 17.4±3.5 km, and estimated earthquake potential of M_w ∼8.0 for the megathrust MHT in the region.

Sharma et al. (2023a) [125] utilized a comprehensive dataset comprising 144 GNSS surface velocities to calculate the geometry of MHT in the northwest Himalaya. Particularly in the Kumaun Himalaya, their findings revealed a locking depth, fault depth, and slip rate of 6±2 km, 18±1 km, and 19±2 mm/yr, respectively.

2.2.1.2 Literature review for the Nepal Himalaya

In the Nepal-Himalaya region, Bilham et al. (1997) initiated GPS-based research on India-Tibet convergence as early as 1991. Utilizing six years of GPS measurements, Bilham et al. (1997, 1998) [16, 126] calculated the slip rate of the MHT to be 20.5±2.0 mm/yr in western Nepal and 21.0±3.0 mm/yr in central and eastern Nepal. This estimation suggests a higher likelihood of experiencing a great earthquake in regions like western Nepal, where no significant event has occurred in the last 300 years [16, 126].

Larson et al. (1999) [111] determined a convergence rate of 18±2 mm/yr in western Nepal using a 2D dislocation model. The dip-slip rate of the MHT was obtained as 23±2 mm/yr and 21±1 mm/yr, with a dip angle of 8° and 3°, and a strike angle of 112° and 101° in western Nepal and eastern Nepal, respectively [111].

Bürgmann et al. (1999) [127] proposed a segmented fault model for the Nepal Himalaya, revealing an along-the-arc variation in the convergence process. Models with varying dip angles (3°−8°) indicated a locking depth of 15−25 km of the MHT. They concluded that a 500 km stretch of the fault system, with a width of about 140 km, is locked, resulting in 6−15 m of accumulated potential slip since the 1505 earthquake. This suggests that this part of the Himalayan orogeny is ready to trigger one or more future great earthquakes [127]. The short-term geodetic slip rate of 20±2 mm/yr was consistent with the long-term geological rate of 21.0±1.5 mm/yr deduced from folded terraces across the Siwalik Hills in central Nepal [127].

Chen et al. (2004) [128] used GPS data from 33 sites to study ongoing crustal deformation along Nepal and southern Tibet. They reported an elongation rate of 13±2 mm/yr along southern Tibet, comprising 9.7±3.0 mm/yr of permanent extension and ∼3 mm/yr of elastic deformation along the locked MHT. Additionally, they computed slip rates of the decollement (MHT) as 17±1 mm/yr, 12.4±0.4 mm/yr, and 19±1 mm/yr along northwest, central, and northeast Himalaya, respectively [128].

Jouanne et al. (2004) [71] characterized fault parameters using a two-dimensional dislocation model based on velocity field data from 35 GPS sites in Nepal. In western Nepal, a 117° striking MHT revealed 19 mm/yr of dip-slip and 0−1 mm/yr of strike-slip at 20−21 km depth. In central Nepal, a 108° striking MHT revealed slip rates of 19−20 mm/yr and 0−2 mm/yr of dextral motion at 17−21 km depth. The larger locking width in western Nepal than in central Nepal indicates a higher possibility of M_w>8.0 earthquake in this region [71].

Bettinelli et al. (2006) [42] used GPS and DORIS measurements to determine the deformation pattern along western Nepal, observing a slip rate of MHT as 13.4±5.0 mm/yr with a locking width of 150 km. Similarly, they calculated a slip rate of 19.0±2.5 mm/yr for MHT and 115 km of locking width at about 20 km depth in central and eastern Nepal [42].

Ader et al. (2012) [12] calculated the slip rate of the 10° dipping MHT as 17.8±0.5 mm/yr in the central and eastern Nepal and 20.5±1 mm/yr in western Nepal. They proposed that western Nepal has not experienced ruptures since the 1505 earthquake, accumulating a substantial moment deficit between the 1934 Bihar-Nepal earthquake and the western border of Nepal. Consequently, this region might generate an earthquake of up to M_w ∼8.9 [12]. The authors concluded that background seismicity does not contribute significantly to releasing interseismic stress build-up but reflects areas of the most rapid stress increase [12]. Finally, they observed that the estimated slip rate of MHT represents a moment deficit rate of 6.6±0.4 $\times 10^{19}$ Nm/yr beneath the central Himalaya [12]. This moment deficit rate is equivalent to a great earthquake of M_w ∼8.5 with a recurrence interval of ∼270 years [12].

Grandin et al. (2012) [129] utilized InSAR data to measure long-term growth and crustal deformation in central Nepal. They reported that the frontal part (MFT) of the Himalayan range is uplifting at a rate of 7 mm/yr. The flat portion of the decollement (MHT) is slipping at a rate of $18-21$ mm/yr, while the mid-crustal ramp of the decollement is fully locked in the Higher Himalayan part [129].

Li et al. (2016) [130] calculated the locking depth and slip deficit rate along the MHT as $12-17$ km and $0-5$ mm/yr in western Nepal, $16-21$ km and $6-10$ mm/yr in central Nepal, and $23-26$ km and $8-13$ mm/yr in eastern Nepal, respectively. They observed that the 2015 Gorkha event created a boundary between western and central Nepal, where the slip deficit rate changes significantly from 0–9 mm/yr, causing high strain accumulation in the central and eastern parts [130].

Jouanne et al. (2017) [131] examined approximately 15 years of GPS data along the Nepal Himalaya and proposed that the MHT is fully locked along the upper part of the flat, partially locked along the mid-crustal ramp, and is creeping along the lower edge of the flat. They found that the 2015 Gorkha earthquake occurred along the highly coupled upper flat of the MHT, whereas its postseismic rupture propagated towards the eastern side in the lower coupled zone of the MHT [131].

Lindsey et al. (2018) [11] estimated that the fault coupling width varies between 70–90 km in eastern Nepal, $100-110$ km in central Nepal, and narrows down again in western Nepal. Their findings along western Nepal suggest that either the shallow portion of the decollement contains an anomalous coupling transition zone or is partially locked. They inferred 15.2 ± 1.2 mm/yr of reverse faulting with -2.2 ± 2.5 mm/yr of strike-slip motion along the MHT at a depth of 20 km [11].

Sreejith et al. (2018) [108] determined that the mainshock and aftershocks of the 2015 Gorkha event have partially released the accumulated strain energy in the north of the epicenter. They suggested the possibility of similar earthquakes occurring in the west or south where the MHT is fully locked [108].

Diao et al. (2022) [132] utilized a viscoelastic model to study the slip rate and locking width of the MHT based on GPS data acquired in the past three decades along the central

Himalaya. They found that the slip rate and locking width of the MHT are 18.8±1.6 mm/yr and 85±2.1 km, respectively.

Sharma et al. (2023b) [125] utilized a comprehensive dataset comprising 145 GNSS surface velocities and employed a Bayesian inversion model to elucidate the complex geometry of the MHT. The study estimates the locking depth and fault depth along the central Himalaya, revealing ranges of 4.3±2.6 km to 9.7±2.2 km and 13.5±3.1 km to 15.8±1.9 km, respectively. The slip rate along the MHT exhibits variability from 12.8±1.6 mm/yr in the east to 19.4±2.5 mm/yr in the west. The calculated slip deficit rates in different regions are reported as approximately 15.1 mm/yr in western Nepal, 12.7 mm/yr in central Nepal, and 10.6 mm/yr in eastern Nepal.

From the above discussed studies in the Kumaun and Nepal Himalaya, it is evident that the slip rate along the MHT varies within the range of approximately 8 mm/yr to 20 mm/yr. The locking width varies between 70 km to 110 km in the study area. The accumulated strain energy in this area indicates the potential occurrence of a significant earthquake, with a magnitude exceeding 8.0.

2.3 Dataset

To accomplish the primary objective of the present thesis, a contemporary cutting-edge dataset is necessary. As a result, to obtain a high-resolution integrated velocity field over the study region, firstly, (i) GPS velocity field is derived; then, (ii) InSAR line of sight (LOS) velocity field is calculated, and finally, (iii) high-resolution integrated velocity field is calculated from the combination of GPS and InSAR based velocities. This estimated high-resolution velocity field is one of the main bases for further seismic hazard analysis (in estimating strain rate distribution, seismic moment budget calculation, and fault parameters estimation) in the thesis. Another important base is the earthquake dataset over the study region, which is utilized for estimating the seismic moment budget and for performing probabilistic earthquake recurrence modeling and the current progression of the earthquake cycle of large events. In the following subsections, extensive information regarding these aforementioned datasets is presented. However, prior to this, some preliminary discussion

about GPS and InSAR basics, data collection, and data processing is provided below.

2.3.1 Global Positioning System

During the 1960s, the United States (US) military pioneered the creation of a satellite-based initiative called the Navy Navigation Satellite System (NNSS) [133]. The primary purpose of NNSS was to accurately ascertain the coordinates of naval vessels at sea and monitor the trajectories of hostile missiles. Over time, some aspects of this program were made accessible for civilian applications, including navigation and land surveying. However, the NNSS had notable limitations, including significant gaps between satellite coverage and suboptimal navigation precision [133]. To overcome these limitations, the Global Positioning System (GPS) was developed by the US Department of Defense and also known as NAVSTAR (Navigation Satellite Timing and Ranging) [133]. The GPS technology has evolved into a crucial tool in various geophysical studies [133, 134]. It offers precise three-dimensional relative positioning, with an accuracy of the order of millimeters. The GPS based horizontal position has precision of up to 1 mm and vertical accuracy of several mm [24, 135]. Compared to alternative geodetic techniques like Very Long Baseline Interferometry (VLBI) and Satellite Laser Ranging (SLR), GPS is more cost-effective. The GPS plays a vital role in a wide range of applications, including monitoring the movement of Earth's tectonic plates, identifying active deformation zones and volcanic-related changes, measuring postglacial uplift, studying active landslides or subsidence, and monitoring atmospheric and ionospheric variations [133, 134].

The GPS consists of three primary components: the space segment, control segment, and user segment (Figure 2.2). The space segment encompasses 31 satellites distributed across six distinct orbital planes, each positioned at an inclination of 55 degrees and an altitude of approximately 20,200 km above the Earth's surface (Figure 2.2) [133]. These satellites transmit data on two separate L-band carrier frequencies: L1 at 1575.42 MHz and L2 at 1227.69 MHz. The L-band carries vital navigation information, including ephemeris data, predicted satellite orbits, clock corrections, ionospheric data, and the health status of the satellites [136, 137].

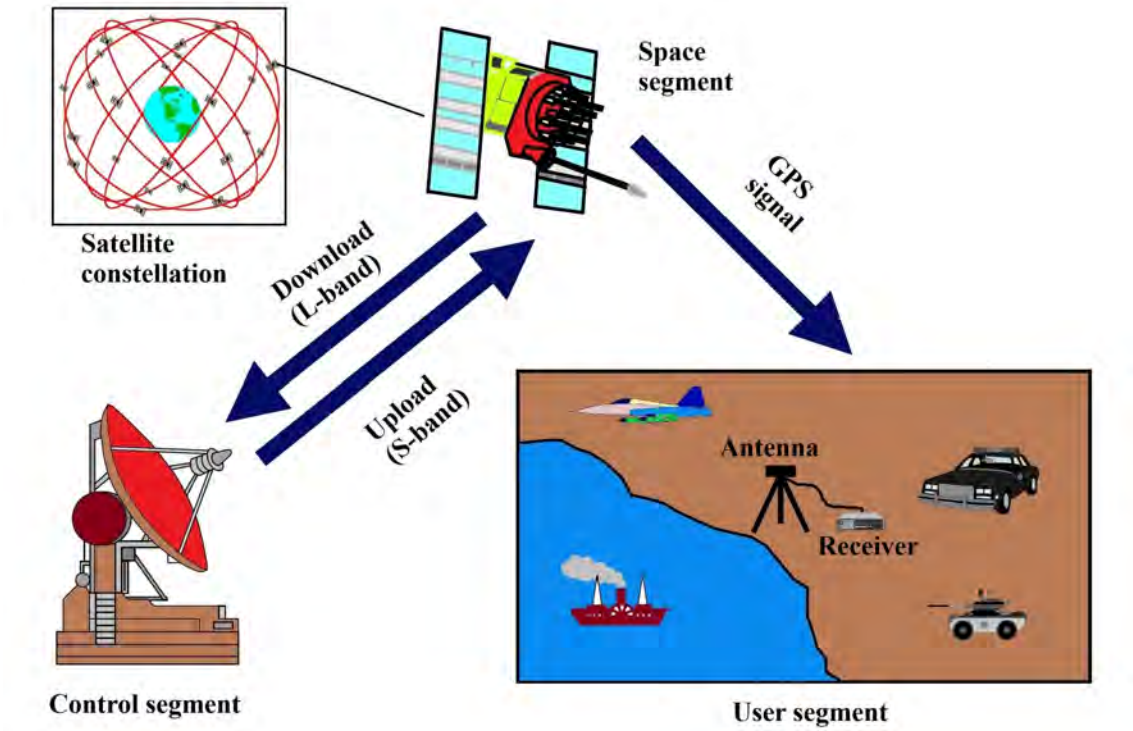

Figure 2.2: GPS satellite constellation and segments [133].

In the control segment, there is one Master Control Station (MCS), an alternative MCS, 16 monitoring stations, and 11 control and command antennas. This segment is primarily responsible for tracking satellite orbits, determining clock corrections, and generating navigation data. Subsequently, this information is modulated onto the S-band frequency and transmitted back to the GPS satellites for dissemination (Figure 2.2). The user segment encompasses GPS receivers that utilize the data received from the satellites to compute their own position and determine accurate time (Figure 2.2) [133].

The clock reading at the satellite antenna is cross-referenced with the clock reading at the receiver antenna, allowing for the determination of the pseudorange, which represents the distance between the receiver antenna and the tracked satellite, along with the time taken by the signal to travel between the satellite and the receiver (in the satellite-receiver pairing) [133, 137]. The pseudorange can be expressed as follows:

$$R = \mu_r^s + c\Delta\delta + d_{ion} + d_{tide} + d_{trop} + \varepsilon_p \tag{2.3.1}$$

and

$$\mu_r^s = \sqrt{(U^s(t) - U_r)^2 + (V^s(t) - V_r)^2 + (W^s(t) - W_r)^2} \tag{2.3.2}$$

Here, μ_r^s represents the geometric range between satellite and receiver antenna; U_r, V_r, W_r represent the three coordinates of the observing receiver; $U_s(t), V_s(t), W_s(t)$ represent the components of the geocentric position vector of the satellite at epoch t; c represents the speed of light; $\Delta\delta$ represents the offset between the satellite and receiver clock; d_{tide}, d_{trop}, and d_{ion} represent tidal loading, tropospheric delays, and ionospheric delays effects, respectively; and ε_p represents the effect of receiver and multipath noise [133, 134, 136, 137].

Conversely, the carrier phase indicates the phase discrepancy between the incoming carrier and the signal produced by the GPS receiver. The positional precision derived from the carrier phase (ϕ) surpasses code pseudoranges by approximately tenfold [133, 134, 136, 137]. The equation for the carrier phase can be expressed as follows:

$$\lambda\phi = \mu_r^s + c\Delta\delta + \lambda N + d_{ion} + d_{tide} + d_{trop} + \varepsilon_p \tag{2.3.3}$$

Here, N denotes the ambiguity related to both the receiver and satellite (representing the number of fractional phases), and λ denotes the carrier wavelength [133, 134, 136, 137]. The GPS observations are subject to various sources of error, encompassing ionospheric and tropospheric delays, satellite orbital inaccuracies, ocean tide loading effects, biases in receiver and satellite clocks, multipath interference, among others. To enhance the accuracy of GPS coordinate and relative velocity estimations, a common practice is the utilization of linear combination approaches [133, 134, 136, 137]. In particular, the double-difference method can be employed to significantly mitigate biases in receiver and satellite clocks [133]. To illustrate the double-difference method, let's consider two receivers denoted as a, b and two satellites represented by j, k. Two carrier phase observation equations, in accordance with Equation 2.3.3, can be formulated as follows:

$$\lambda\phi_a^j = \mu_a^j + c\Delta\delta_a + \lambda N_a^j + d_{a\ ion}^j + d_{a\ tide}^j + d_{a\ trop}^j + \varepsilon_{a\ p}^j \tag{2.3.4}$$

$$\lambda\phi_b^j = \mu_b^j + c\Delta\delta_b + \lambda N_b^j + d_{b\ ion}^j + d_{b\ tide}^j + d_{b\ trop}^j + \varepsilon_{b\ p}^j \tag{2.3.5}$$

The initial step involves calculating the single difference for satellite j and receivers a and b by subtracting Equation 2.3.4 from Equation 2.3.5.

$$\lambda\phi_{ab}^j = \mu_{ab}^j + c\Delta\delta_{ab} + \lambda N_{ab}^j + d_{ab\ ion}^j + d_{ab\ tide}^j + d_{ab\ trop}^j + \varepsilon_{ab\ p}^j \tag{2.3.6}$$

Similarly, the following is the single difference for receivers a and b and satellite k:

$$\lambda\phi_{ab}^k = \mu_{ab}^k + c\Delta\delta_{ab} + \lambda N_{ab}^k + d_{ab\ ion}^k + d_{ab\ tide}^k + d_{ab\ trop}^k + \varepsilon_{ab\ p}^k \tag{2.3.7}$$

Then, to create a double-difference equation, the single-difference equations are subtracted (Equation 2.3.7 from Equation 2.3.6).

$$\phi_{ab}^{jk} = \frac{1}{\lambda}\mu_{ab}^{jk} + N_{ab}^{jk} + \frac{1}{\lambda}(d_{ab\ ion}^{jk} + d_{ab\ tide}^{jk} + d_{ab\ trop}^{jk} + \varepsilon_{ab\ p}^{jk}) \tag{2.3.8}$$

The double-difference technique offers the advantage of eliminating receiver clock biases entirely and significantly reducing ionospheric and tropospheric effects [133, 134, 136, 137]. These corrected GPS observations can be used to compute the receiver's position and relative velocity.

2.3.1.1 GPS network and collection of data

To understand crustal deformation within the study region, a GPS network was established during the period of 2013–14 in the Kumaun Himalaya region (Figure 2.4). This regional network comprises two permanent GPS stations, THKD and DHLC, along with twenty campaign-surveyed GPS sites (details in Table 2.1). Each permanent station is set up on a concrete pillar, serving as the foundation for the GPS antenna (Figure 2.3). The site installation includes the GPS receiver, connecting cables, solar panels, an Uninterrupted

Table 2.1: Details of the regional GPS stations along the Kumaun Himalaya

Site code	Longitude ($^{\circ}E$)	Latitude ($^{\circ}N$)	Observation mode	Time interval
THKD	78.8569	29.1486	Continuous	2013 – 2018
NYGN	79.3143	29.2743	Campaign	2013 – 2021
GTGH	79.3768	29.3284	Campaign	2013 – 2021
MNGL	79.3874	29.3466	Campaign	2013 – 2021
NTAL	79.4425	29.3879	Campaign	2013 – 2022
CHRA	79.4966	29.5004	Campaign	2013 – 2022
JNVN	79.5488	29.5465	Campaign	2013 – 2019
ALMR	79.6708	29.6152	Campaign	2013 – 2022
DHLC	79.7870	29.6741	Continuous	2013 – 2018
I001	79.4110	29.3683	Campaign	2014 – 2019
I002	79.3183	29.4082	Campaign	2014 – 2022
I006	79.3187	29.3525	Campaign	2014 – 2021
I007	79.3192	29.3739	Campaign	2014 – 2022
I009	79.2684	29.3753	Campaign	2014 – 2022
I010	79.2319	29.3571	Campaign	2014 – 2021
I011	79.1871	29.3048	Campaign	2014 – 2021
I013	79.2429	29.2988	Campaign	2014 – 2017
I015	79.3368	29.2952	Campaign	2014 – 2021
I016	79.4464	29.3359	Campaign	2014 – 2022
I017	79.5231	29.2308	Campaign	2014 – 2021
I018	79.5539	29.3529	Campaign	2014 – 2022
I019	79.5519	29.4369	Campaign	2014 – 2022

Power Supply (UPS) for power backup, and internal batteries to ensure operation during emergencies (Figure 2.3). All the campaign sites are chosen on the Reinforced Cement Concrete (RCC) government or private building rooftops with a clear sky visibility. For each permanent GPS station, the Leica GR25 GNSS (Global Navigation Satellite System) receiver is utilized in conjunction with the high-performance Leica AS10 geodetic quality antenna. In the case of campaign-mode stations, the Leica Viva GS15 GNSS receiver and Leica Viva GS15 geodetic quality antenna are employed. The GS15 receiver and GS15 antenna are linked via Bluetooth. In addition, the location coordinates, measurement mode, and observation times for each station is provided in Table 2.1.

Two permanent stations are situated at the rear ends of the transect. Specifically, DHLC (79.7870º E, 29.6700º N) is located on private property in Dhaulachhina along the Lower

Figure 2.3: A typical setup of a continuous GPS site. (a) RCC pillar; (b) enclosure of GPS receiver, UPS power back up, internal batteries, and solar panels; and (c) GPS antenna on RCC pillar.

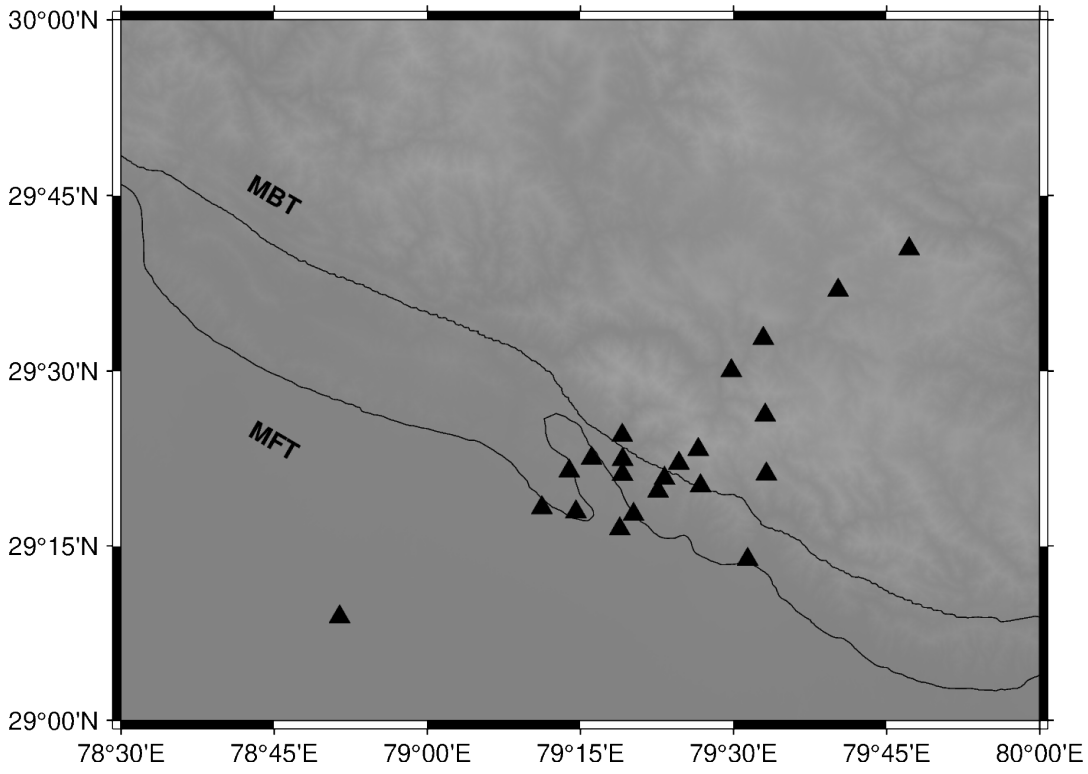

Figure 2.4: Location of regional GPS network along the Kumaun Himalaya. Abbreviations align with the Figure 2.1.

Himalaya and THKD (78.8569º E, 29.1486º N) lies in an open lawn of the premises of the Jawahar Navodaya Vidyalaya school in Thakurdwara, adjacent to the IGP (Figure 2.4).

2.3.1.2 GPS data processing

Since 2013, yearly raw data is continuously collected at sampling intervals of one second and thirty seconds. The 1s data serves the primary purpose of studying coseismic deformation during earthquakes. Additionally, the campaign stations are occupied two to three times annually, utilizing a 1s sampling interval for each campaign session. These sessions are configured for approximately 24-hour observations, maintaining a 15º elevation angle while tracking all available satellites. Following this, a comprehensive quality check of the raw GPS data is executed using the Translation, Editing, and Quality Check (TEQC) software. This process involves various tasks, including the identification of outliers and addressing data gaps [138].

When the raw GPS data is scrutinized and refined, it undergoes conversion into the Receiver Independent Exchange (RINEX) format via the TEQC software, which allows for subsequent analysis. The RINEX files become the basis for data processing. In geodesy, particularly for high-precision research, reliance is placed on standard scientific GPS post-processing software such as GAMIT-GLOBK, BERNESE, and GIPSY. For the present study, the GAMIT-GLOBK post-processing software is employed. This software is compatible with the LINUX environment and was developed by the Massachusetts Institute of Technology (MIT) for the purpose of estimating three-dimensional relative positions of ground stations. GAMIT utilizes GPS broadcast carrier phase and pseudorange observables (stored in RINEX files), satellite ephemeris data (found in navigation files), and satellite orbit information (located in orbit files). Through a least-squares estimation procedure, GAMIT generates values for various parameters, encompassing positions, orbits, Earth orientation, ambiguities, and atmospheric delays [139, 140]. This setup enables the calculation of the receiver antenna's position based on Equation 2.3.2. The linearized form of this equation facilitates the implementation of a least-squares algorithm. Below is the simplified and linearized representation of Equation 2.3.2 in terms of the

observation equation:

$$d = Ax + v \tag{2.3.9}$$

where, d $[n \times 1]$: vector of observations, A $[n \times u]$: design matrix, x $[u \times 1]$: vector of unknowns (parameter), v $[n \times 1]$: noise or residual vector.

For further computation, let us define some other parameters:

σ_0^2: a priori variance, Σ : covariance matrix, $Q_d = \frac{1}{\sigma_0^2}\Sigma$: the co-factor matrix of observations, and $P = Q_d^{-1}$: the weight matrix.

The least-squares adjustment provides a unique solution of Equation 2.3.9 subject to the condition $v^T Pv$ = minimum.

This adjustment principle provides the following normal equation:

$$A^T PAx = A^T Pd \tag{2.3.10}$$

The solution of Equation 2.3.10 is

$$x = (A^T PA)^{-1} A^T Pd \ , \tag{2.3.11}$$

which can be simplified to

$$x = G^{-1} g \ , \tag{2.3.12}$$

where, $G = A^T PA$ and $g = A^T Pd$.

The cofactor matrix Q_x follows from $x = G^{-1}A^T Pd$ by the covariance propagation law as:

$$Q_x = (G^{-1}A^T P) Q_d (G^{-1}A^T P)^T \tag{2.3.13}$$

By substituting $Q_d = P^{-1}$, the above equation further reduces to

$$Q_x = G^{-1} = (A^T PA)^{-1} \tag{2.3.14}$$

The daily solutions produced by GAMIT yield the location coordinates for each GPS

station, in addition to Earth orientation and satellite orbit corrections. These initially estimated, loosely constrained daily solutions serve as the basis for determining the station positions and plate motion through GLOBK [139].

The processing of GPS data within the GAMIT-GLOBK framework is generally carried out in three sequential stages. First, all data undergo processing using GAMIT to derive preliminary, loosely constrained coordinates for each station, alongside the inclusion of data from International GNSS Service (IGS) fiducial stations. Subsequently, the time series of position coordinates for each station is subjected to scrutiny for any outliers using the GG-MATLAB (GAMIT-GLOBK MATLAB) tool. Finally, the refined time-series data are harnessed for estimating station velocities within the GLOBK software [139].

A step-by-step procedure for data processing is as follows:

Step 1: Begin by installing the GAMIT-GLOBK software on a LINUX system. Additionally, verify the integrity of several key files:

process.defaults (edit to specify computation environment, source for internal and external data and orbit files, start time sampling interval, and instructions for archiving the results)

sestbl. (edit the *AUTCLN* postfit command to suit processing strategy)

sites.defaults (edit to specify sites to ftp from RINEX data archives, to search for RINEX files on the local system, and to exclude from automatic *station.info* updating)

station.info (edit to include all the continuous stations as well as all the IGS stations)

and ***lfile., leap.sec, luntab., nutabl.*** (these files need to be up to dated).

Step 2: Create four sub-directories within an experimental directory: 'brdc' (housing navigation files in the .n format), 'igs' (storing SP3 or satellite orbit files

for all the utilized IGS stations), 'rinex' (containing RINEX files for observations from both regional and IGS stations), and 'tables' (dedicated to the GAMIT tables folder).

To obtain the observation, navigation, and orbit SP3 files for the selected IGS stations, the following commands are employed:

(i) **RINEX files**: *sh_get_rinex -archive <archive> -yr <year> -doy <day of year> -ndays <number of days> -sites <IGS sites>*

<archive> here the observation files of the IGS stations are stored (e.g., SOPAC, CDDIS, MIT, and others)

<year> year of observation

<day of year> day of observation in the corresponding year

<number of days> number of consecutive days of data to retrieve

<IGS sites> List of IGS stations to be retrieved from archive (e.g., here 16 IGS stations are used: WUHN, URUM, TEHN, SOLA, PLO2, LHAZ, LCK2, KRTV, KIT3, IISC, HYDE, GUAO, DRAG, DGAR, COCO, and CHUM)

Example *sh_get_rinex -archive sopac -yr 2020 -doy 301 -ndays 5 -sites HYDE IISC*

(ii) **Navigation files**: *sh_get_nav -archive <archive> -yr <year> -doy <day of year> -ndays <number of days>*

Example *sh_get_nav -archive sopac -yr 2020 -doy 301 -ndays 5*

(iii) **Orbit/SP3 files** *sh_get_orbit -archive <archive> -yr <year> -doy <day of year> -ndays <number of years> -type <type of orbit file sp3/gfile> -center <IGS processing center igs/esa/sio>*

Example *sh_get_orbit -archive sopac -yr 2020 -doy 301 -ndays 5 -type gfile -center*

igs

Step 3: Following the acquisition of all necessary files, including observation, navigation, and orbit data, we incorporate a global tide model known as FES2004 (*otlFES2004.grid*) to address solid Earth tides and ocean loading effects. Subsequently, a sequence of GAMIT commands is employed:

sh_gamit -d yr days/-s yr d1 d2 -expt -orbit -aprfile -yrext

-d yr days (need to use if data are processed for each specified day (e.g., 2020 301 305 306))

-s yr d1 d2 (need to use if data are processed for continuously from starting day to *n* number of days (e.g., 2020 301 310))

-expt (four character experiment name (e.g., BITS))

-orbit (type of orbit to be used (e.g., IGSF, SIOF, and others))

-aprfile (name of reference frame (e.g., itrf2008.apr)

-yrext (to specify output directory by corresponding year and day (e.g., 2020_301))

Example *sh_gamit -d 2020 301 306 -expt BITS -orbit SIOF -aprfile itrf2008.apr -yrext*

Step 4: GAMIT generates a series of daily station coordinates represented in the form of *h*-files with loosely constrained solutions. Detecting existing outliers, such as unlevelled antenna errors, multipath effects, snow accumulation on the antenna, and others can be challenging solely on the GAMIT output files. To identify these outliers, time series plots of the station coordinates prove invaluable. In this context, the GLRED program is commonly employed, utilizing the following commands to

generate a time series of three-dimensional positions (North, East, and Up):

(i) In the primary experimental directory, establish two subordinate directories named **glbf** and **gsoln**.

(ii) Transform the ASCII *h*-files into binary format, which is compatible with GLRED and GLOBK, using the **htoglb** tool (*htoglb [glbf_directory] [ephemeris_file] <GAMIT h-file>*). Subsequently, transfer all the binary *h*-files into the **glbf** directory, alongside the SOPAC global binary *h*-files obtained from the IGS network using the (*sh_get_hflies*) command.

(iii) Generate an inventory of binary *h*-files in the **gsoln** directory by executing the command *ls ../glbf/h*.glx > expt.gdl*. Additionally, copy the files *globk_rep.cmd* and *globk_vel.cmd* from the **table** directory.

(iv) Run GLRED using *glred <crt> <prt> <log> <input_list> <globk cmd file>*

Example *glred 6 globk_rep.prt globk_rep.log expt.gdl globk_rep.cmd -mb*

The final component, represented as $-mb$, generates multibase (time series) files. These files can be subsequently processed using the *tsview* program within the **GG-MATLAB** (GAMIT-GLOBK MATLAB) tool. This program allows for the removal of outliers and seasonal modulations, as needed[139].

Step 5: After all data corrections and refinements have been completed, the data undergo a filtering process using GLOBK to derive station velocities. This is achieved through the execution of the following command:

globk <crt> <prt> <log> <input_list> <globk cmd file> VEL

Example *globk 6 globk_vel.prt globk_vel.log expt.gdl globk_vel.cmd VEL*

The above described procedure provides a file named *globk_vel.org* containing three-dimensional (north, east, and up) velocities for each station. The collective velocity

information from multiple stations facilitates the construction of a velocity field for the study area. These seasonal variations may result from a combination of factors, including surface loading related to water fluctuations, ionospheric-tropospheric pressure, and vapor loading during the winter season [141]. This seasonal effect can be deconstructed into annual and semi-annual components using a linear function involving sine and cosine terms:

$$y(t) = a + b \times t + c \times cos(2\pi t/T) + d \times sin(2\pi t/T) + e \times cos(4\pi t/T) + f \times sin(4\pi t/T) \tag{2.3.15}$$

Here, a represents the constant intercept, b represents to the secular rate; c and d represent the amplitudes of the annual (12 months) periodic perturbations described by sine and cosine terms, respectively; and e and f represent the amplitudes of semi-annual (six months) periodic disturbances also expressed using sine and cosine terms, respectively.

2.3.1.3 GPS time series and velocity field in the Kumaun Himalaya

The final estimated daily positions at each site of regional network are converted into the International Terrestrial Reference Frame 2008 (ITRF08) for further analysis [142]. Figure 2.5 to Figure 2.9 illustrate time series plots in the north, east, and upward directions for all the regional GPS stations over the Kumaun Himalaya. Discontinuities or jumps within the GPS position time series can likely be attributed to factors like receiver interruptions, antenna errors, multipath effects, or seasonal variations. The vertical component displays substantial seasonal variation, while minor variations are noticeable in the north and east components for all stations. In addition, some GPS sites (such as I001 and I013) have been interrupted due to reasons such as station breakdown or building construction. Moreover, data for the JNVN site is available only up to 2019, as data collection on this site was not possible due to the impact of the COVID-19 pandemic.

The semi-annual seasonal effect typically exhibits smaller amplitudes compared to the annual seasonal effects. Prolonged observations spanning more than 2.5 years have been observed to mitigate the impact of seasonal variations in the calculation of station velocity [143]. Visual inspection of time-series data for each station using the “tsview” program

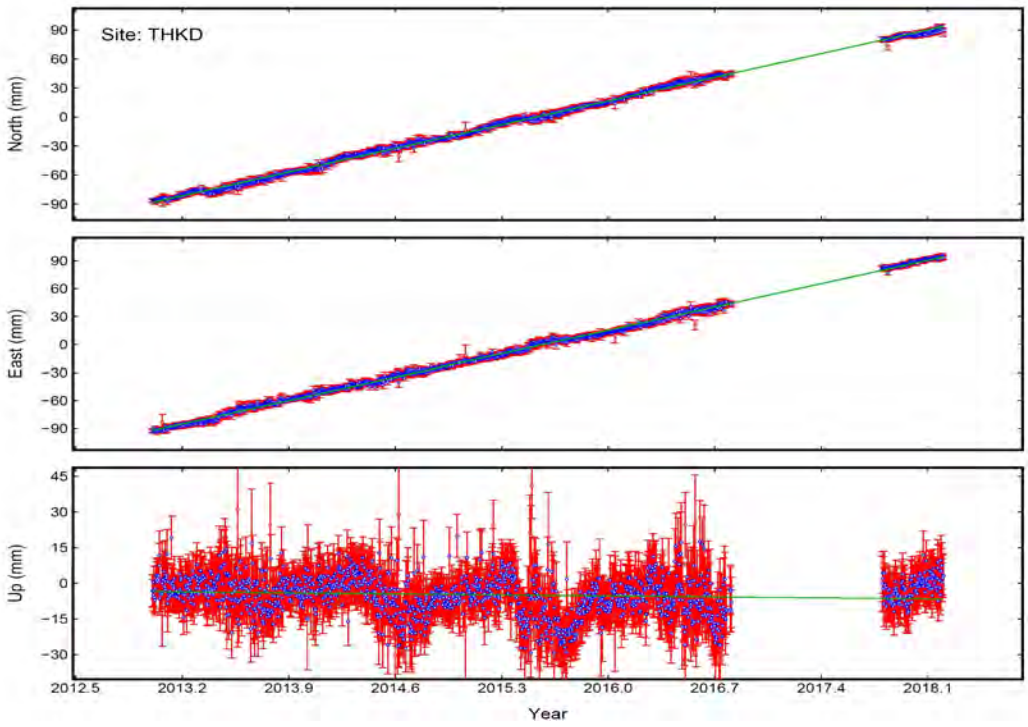

Figure 2.5: Time series for a regional GPS site located at Thakurdwara (THKD).

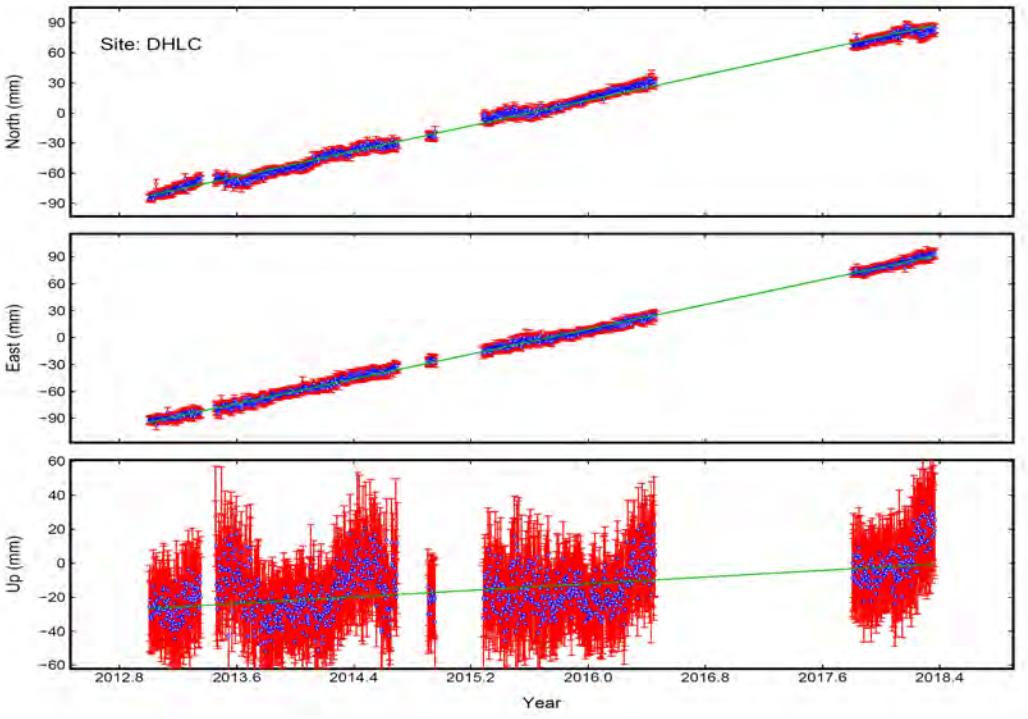

Figure 2.6: Time series for a regional GPS site located at Dhaulachhina (DHLC).

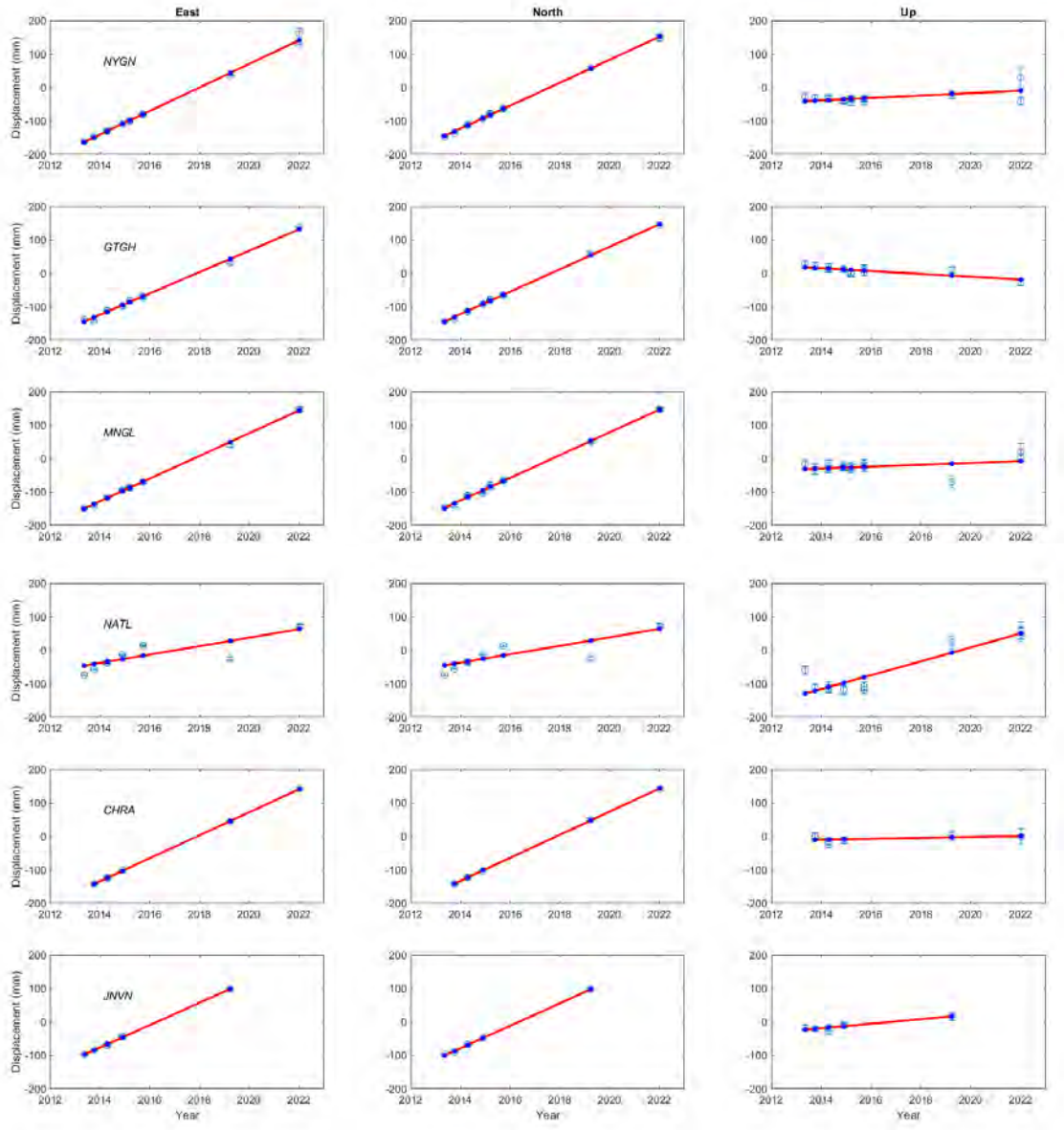

Figure 2.7: Time series for the GPS sites NYGN, GTGH, MNGL, NATL, CHRA, and JNVN.

in GG-MATLAB facilitates the identification and subsequent removal of outliers on a case-by-case basis. Additionally, the Kalman filter within GLOBK is utilized to compute the interseismic deformation velocity for each site, refined from a time-series analysis in the ITRF08 reference frame [139]. While the station velocities in the ITRF08 reference frame reveal a general northeast trend in Indian plate motion, regional deformation within

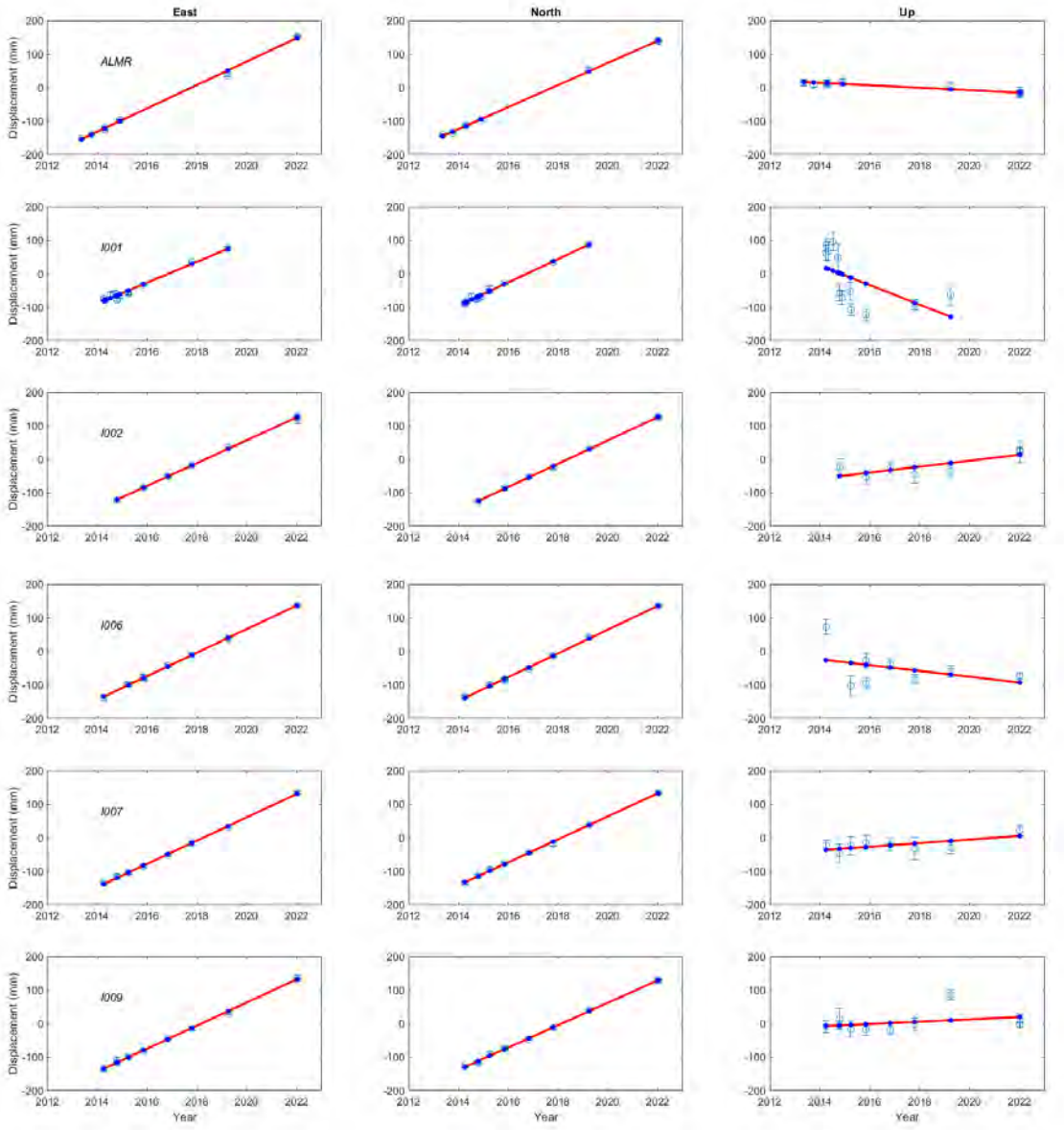

Figure 2.8: Time series for the GPS sites ALMR, I001, I002, I006, I007, and I009.

the study area remains challenging to discern. Consequently, the India- or Eurasia-fixed reference frames are often favored due to their ability to offer regional deformation within the study area. In the India-fixed frame, site velocities are presented relative to the fixed India plate, incorporating rotation pole information, such as a latitude of $51.698 \pm 0.271^{\circ}$N, longitude of $11.853 \pm 1.790^{\circ}$N, and a rotation rate of 0.553 ± 0.006 M/yr, as provided by Jade et al. (2017) [144]. The horizontal and vertical velocities of all regional GPS stations

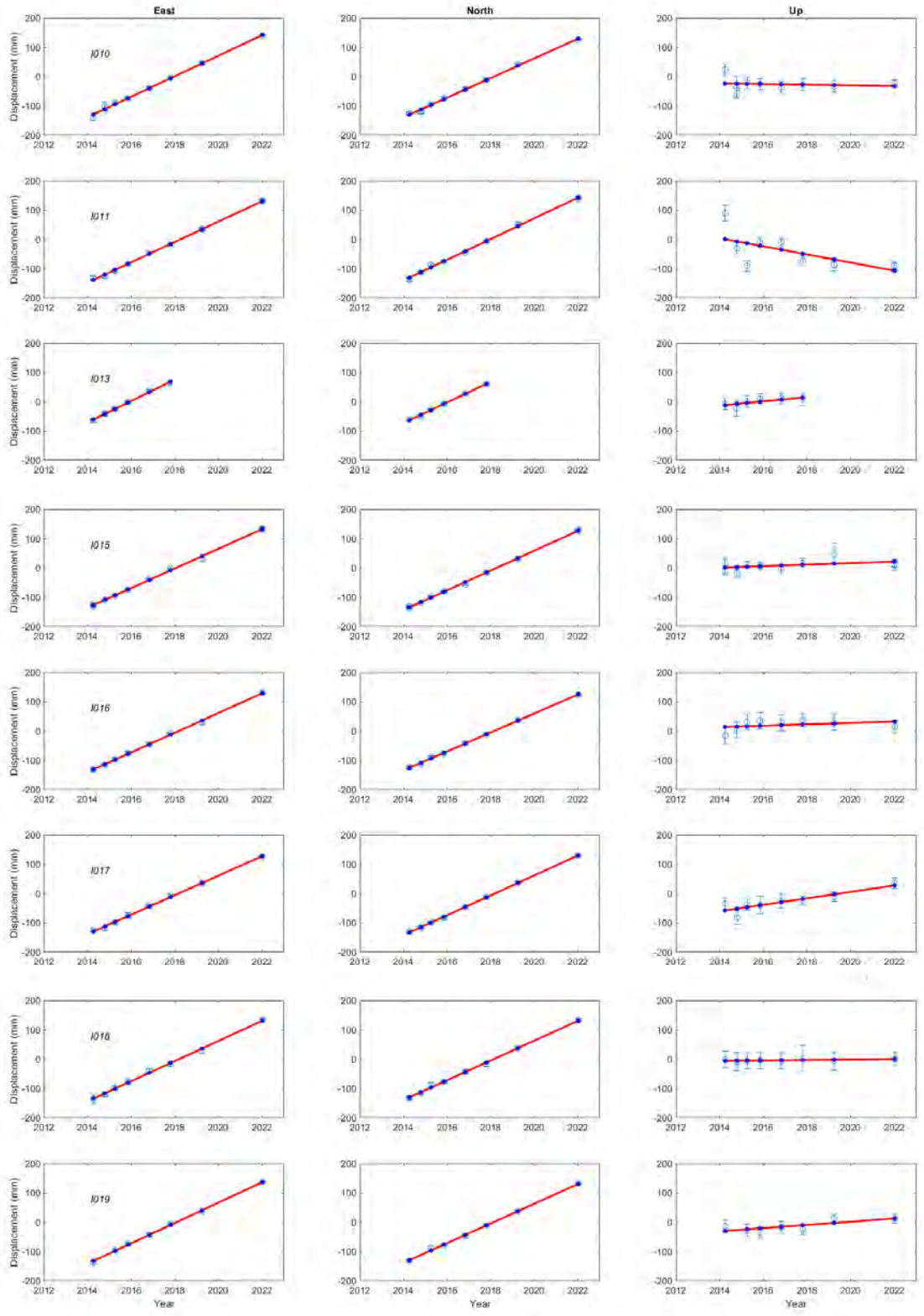

Figure 2.9: Time series for the GPS sites I010, I011, I013, I015, I016, I017, I018, and I019.

are described in Tables 2.3 and 2.4, and visually depicted in Figure 2.10.

The surface velocities in the ITRF08 reference frame for the regional GPS network over the Kumaun Himalaya exhibit a predominant northeast-directed motion of the Indian plate with velocities ranging from 42.32–50.68 mm/yr (Table 2.3). The regional GPS network covers only the southern Kumaun Himalaya. Therefore, to increase the spatial resolution over the Kumaun Himalaya, 26 published [89, 92, 99, 119, 144–146] GPS velocities over the Kumaun Himalaya are utilized. These published velocities are combined with the regional GPS network in the ITRF08 reference frame using a seven-parameter Helmert transformation (Equation 2.3.16). If the Euler rotation angles are quite small, the Helmert transformation can be interpreted through the Bursa–Wolf's equation [147]:

$$\begin{bmatrix} X_2 \\ Y_2 \\ Z_2 \end{bmatrix} = \begin{bmatrix} X_1 \\ Y_1 \\ Z_1 \end{bmatrix} + \begin{bmatrix} T_X \\ T_Y \\ T_Z \end{bmatrix} + \begin{bmatrix} 0 & -R_Z & R_Y \\ R_Z & 0 & -R_X \\ -R_Y & R_X & 0 \end{bmatrix} \begin{bmatrix} X_1 \\ Y_1 \\ Z_1 \end{bmatrix} + D \begin{bmatrix} X_1 \\ Y_1 \\ Z_1 \end{bmatrix} \tag{2.3.16}$$

In the Helmert transformation, two 3-dimensional coordinate systems that are different in their origins or axes can be suitably linked. The seven parameters therefore comprise three translations of the coordinate origin along the axes (T_X, T_Y, T_Z), three Euler rotation angles for three axes (R_X, R_Y, R_Z), and a scale factor $(1+D)$. The Helmert transformation allows transforming the coordinates of points $[X_1\ Y_1\ Z_1]'$ in the first coordinate system to $[X_2\ Y_2\ Z_2]'$ in the second coordinate system. To combine two datasets, a seven-parameter Helmert transformation is used to rotate one set of velocities to align with the other, ensuring that they share a common reference frame [11]. This process consists of three main steps for combining the published velocities with the regional velocities, outlined as follows:

Table 2.2: Translation, rotation, and scale factor parameters to convert ITRF05 and ITRF14 based velocities into ITRF08 based velocities

Transformation	T_X	T_Y	T_Z	R_X	R_Y	R_Z	D
ITRF05 to ITRF08	2.6	1	0	0.3	0.01	0	-1.05
ITRF14 to ITRF08	1.6	1.9	2.4	0	0.01	0.1	-0.93

Table 2.3: GPS-derived velocities of the regional GPS network in the ITRF08 frame; V_e: east direction velocity; V_n: north direction velocity; V_u: vertical direction velocity, σ_e: east direction uncertainty; σ_n: north direction uncertainty; σ_u: vertical direction uncertainty

Site code	V_e (mm/yr)	V_n (mm/yr)	V_u (mm/yr)	σ_e (mm/yr)	σ_n (mm/yr)	σ_u (mm/yr)
THKD	34.94	34.81	-3.15	0.40	0.40	0.16
NYGN	33.38	34.80	–9.15	0.10	0.26	3.53
GTGH	31.93	33.64	–12.26	0.67	0.37	2.27
MNGL	34.31	34.02	0.28	0.43	0.48	5.52
NTAL	34.41	35.33	6.23	0.56	0.62	5.48
CHRA	34.29	34.47	2.52	0.20	0.25	1.66
JNVN	33.26	33.57	6.41	0.40	0.41	1.03
ALMR	34.25	33.16	–3.19	0.60	0.38	1.05
DHLC	33.77	32.01	2.32	0.80	0.70	0.43
I001	31.28	34.84	14.75	1.78	1.27	21.35
I002	34.12	34.76	3.14	0.53	0.42	9.58
I006	35.21	35.26	–3.43	0.43	0.50	7.90
I007	34.68	34.30	0.13	0.55	0.54	6.00
I009	34.44	33.36	0.03	0.62	0.53	4.60
I010	34.96	33.52	–0.41	0.71	0.63	1.34
I011	34.69	35.19	–3.23	0.54	0.66	2.32
I013	36.60	35.05	7.22	1.40	1.23	7.89
I015	33.62	33.69	10.48	0.60	0.44	6.30
I016	33.57	32.36	–2.10	0.62	0.51	3.63
I017	33.21	33.93	6.93	0.70	0.32	2.38
I018	34.24	33.72	0.76	1.06	0.91	1.45
I019	34.68	33.59	–4.19	0.69	0.72	6.65

Step I: The data obtained from the regional network are analyzed using the GAMIT-GLOBK software in the ITRF05, ITRF08, and ITRF14 reference frames.

Step II: A seven-parameter Helmert transformation, as described in Equation 2.2, is employed to convert the observed data from one reference frame to another (e.g., from ITRF05 to ITRF08).

Step III: Subsequently, the least-squares approach is used to minimize the velocity residuals between co-located stations in both datasets. The transformation parame-

ters that provide the best fit are then applied to convert all other published velocities into the ITRF08 reference frame as provided in Table 2.2.

Table 2.4: GPS-derived velocities of the regional GPS network in the India fixed reference frame; V_e: east direction velocity; V_n: north direction velocity; V_u: vertical direction velocity, σ_e: east direction uncertainty; σ_n: north direction uncertainty; σ_u: vertical direction uncertainty

Site code	V_e (mm/yr)	V_n (mm/yr)	V_u (mm/yr)	σ_e (mm/yr)	σ_n (mm/yr)	σ_u (mm/yr)
THKD	1.56	0.01	–3.15	0.40	0.40	0.16
NYGN	0.03	0.02	–9.15	0.10	0.26	3.53
GTGH	–1.45	–1.16	–12.26	0.67	0.37	2.27
MNGL	0.93	–0.78	0.28	0.43	0.48	5.52
NTAL	1.03	0.53	6.23	0.56	0.62	5.48
CHRA	0.91	–0.33	2.52	0.20	0.25	1.66
JNVN	–0.12	–1.23	6.41	0.40	0.41	1.03
ALMR	0.87	–1.64	–3.19	0.60	0.38	1.05
DHLC	0.39	–2.79	2.32	0.80	0.70	0.43
I001	–2.10	0.04	14.75	1.78	1.27	21.35
I002	0.74	–0.04	3.14	0.53	0.42	9.58
I006	1.83	0.46	–3.43	0.43	0.50	7.90
I007	1.30	–0.50	0.13	0.55	0.54	6.00
I009	1.06	–1.44	0.03	0.62	0.53	4.60
I010	1.58	–1.28	–0.41	0.71	0.63	1.34
I011	1.31	0.39	–3.23	0.54	0.66	2.32
I013	3.22	0.25	7.22	1.40	1.23	7.89
I015	0.24	–1.11	10.48	0.60	0.44	6.30
I016	0.19	–2.44	–2.10	0.62	0.51	3.63
I017	–0.17	–0.87	6.93	0.70	0.32	2.38
I018	0.86	–1.08	0.76	1.06	0.91	1.45
I019	1.30	–1.21	–4.19	0.69	0.72	6.65

The surface velocity field of 48 combined GPS sites indicates motion towards the Eurasia plate at a rate of 38–51 mm/yr with uncertainties ranging from 0.2 mm/yr to 2.2 mm/yr (Figure 2.10a). From the velocity field (in India-fixed reference frame), it is observed that the northern portion of the study region shows southward movement as a result of the India-Eurasia convergence (Figure 2.10b). Conversely, in the southern region,

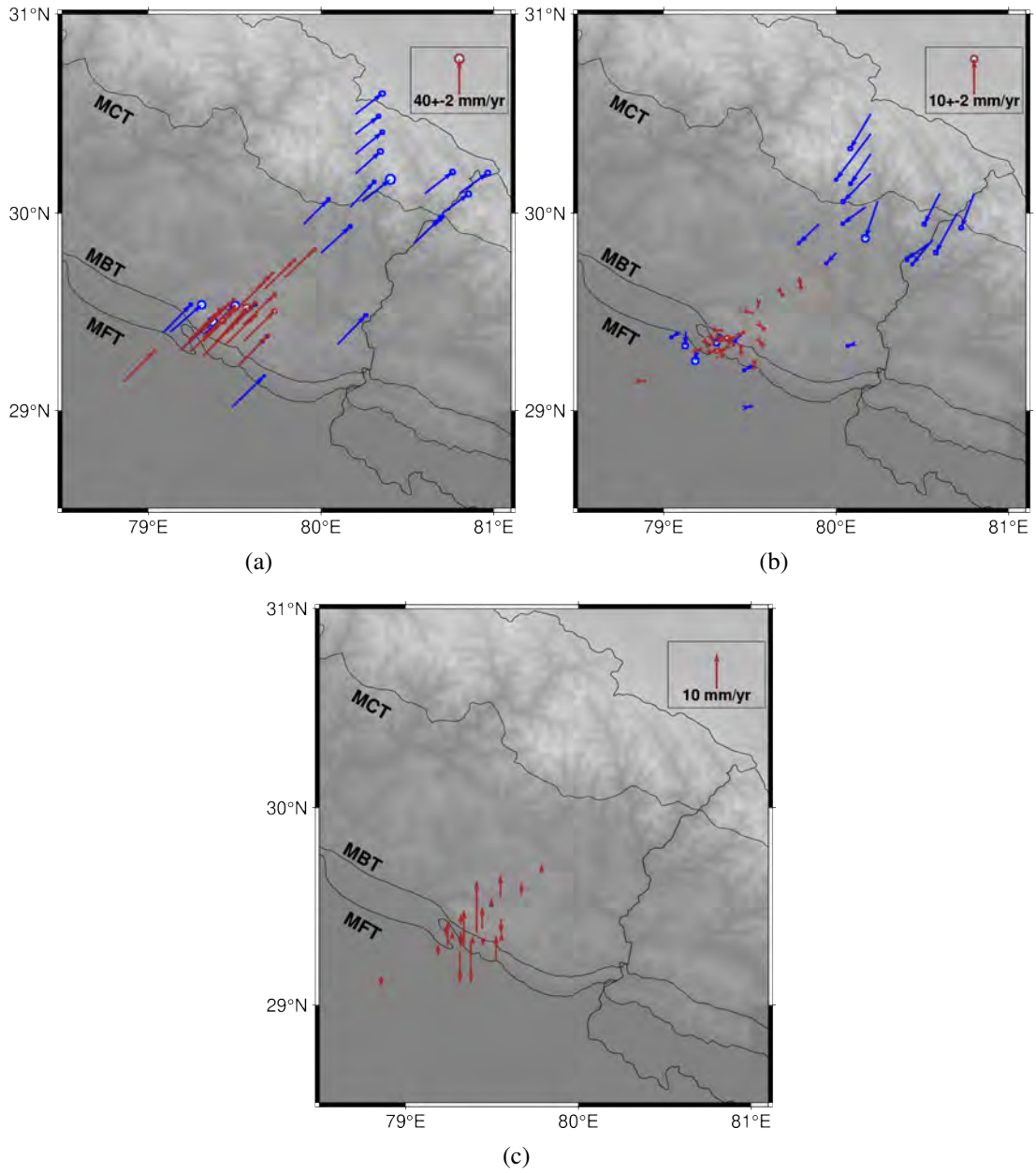

Figure 2.10: GPS based surface velocities in (a) the ITFR08 and (b) the India fixed reference frame along the Kumaun Himalaya. (c) GPS based verical velocities along the Kumaun Himalaya from regional GPS network. Brown and blue colored vectors represent GPS velocities from the regional setup and published works, respectively. Vertical velocities in the region are predominantly confined to the southern section due to the limited availability of vertical velocity data from the regional network. Abbreviations align with the Figure 2.1.

the velocity vectors exhibit reduced magnitudes and there is a lack of any discernible consistent pattern (Figure 2.10b). The decrease in velocity vector magnitudes in the southern part indicates that the MFT is locked along the study area. In addition, unlike the northern half, the magnitude of horizontal velocity vectors is nearly within the range of their associated errors, showing apparent random orientations. On the other hand, the vertical velocities derived from the regional GPS network range from –12.3 mm/yr to 14.8 mm/yr with uncertainties lying in the range of 0.2 mm/yr to 21.4 mm/yr (Figure 2.10c). Nevertheless, because of significant uncertainty in the vertical component of the site I001, the vertical velocity of this site is not incorporated into the subsequent analysis of the thesis.

2.3.1.4 GPS velocity field in the Nepal Himalaya

To understand the deformation pattern over the Nepal Himalaya, a set of 77 GPS-based velocities provided by the Nevada Geodetic Laboratory (NGL; geodesy.unr.edu/) and other published data [11, 12, 42, 73, 148–152] across the Nepal Himalaya are utilized.

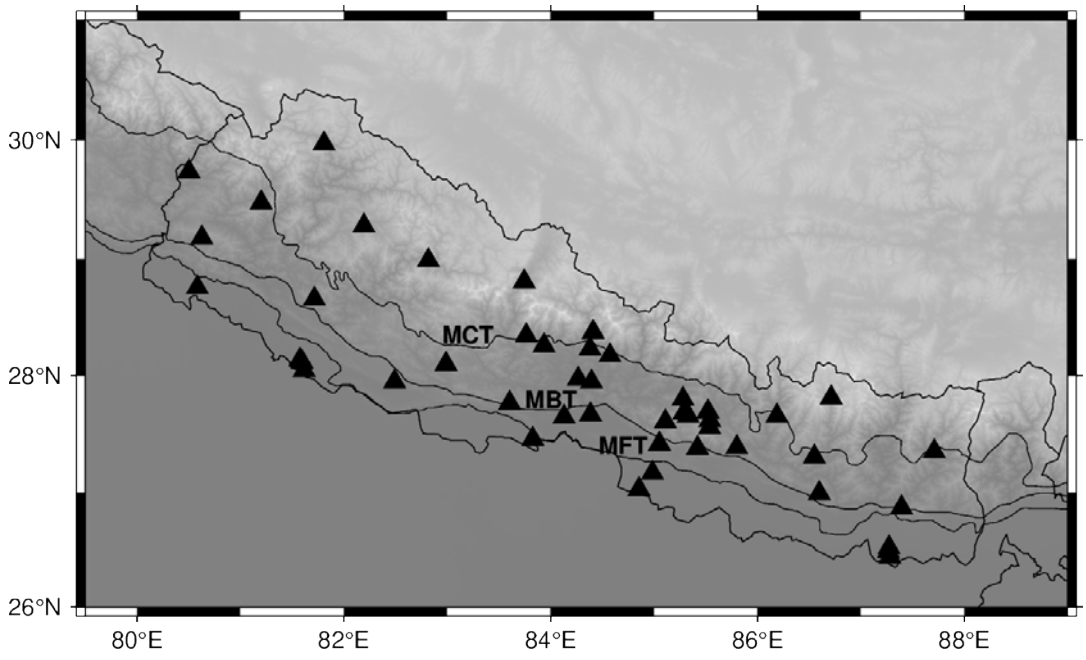

Figure 2.11: Location of NGL based GPS sites along the Nepal Himalaya. Abbreviations align with the Figure 2.1.

These large number of GPS sites in the Nepal Himalaya enhance the spatial resolution

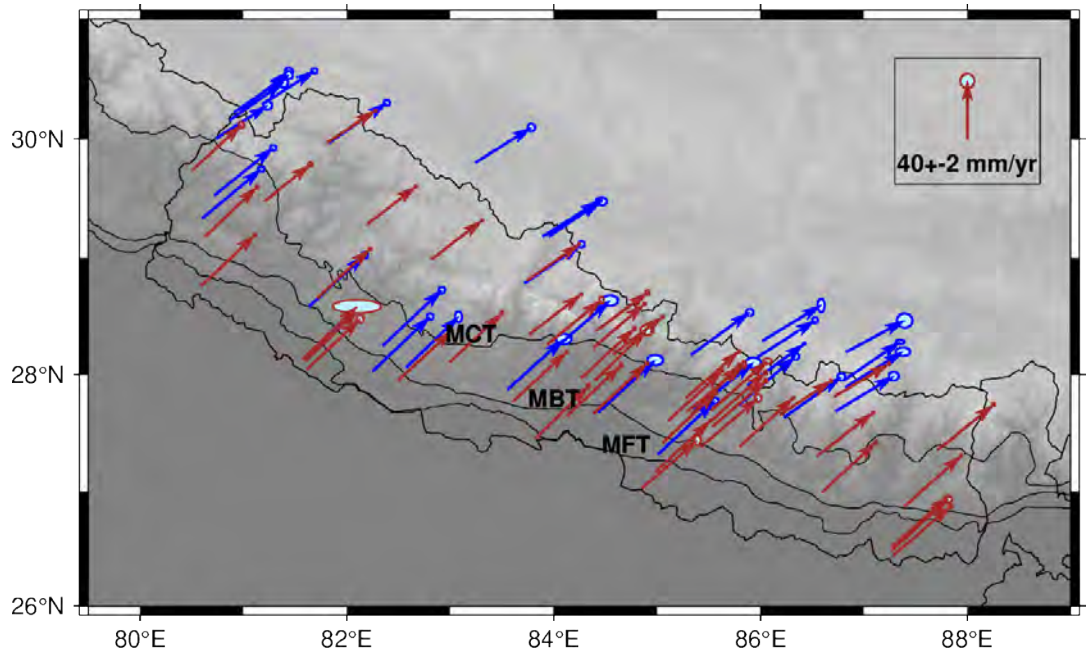

(a)

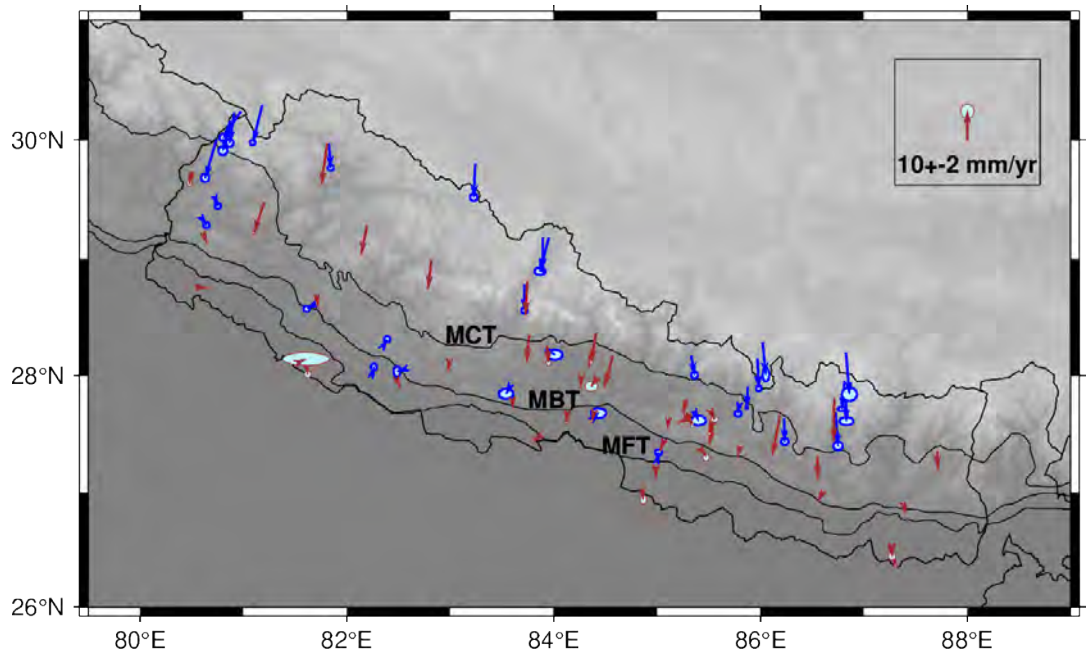

(b)

Figure 2.12: GPS based surface velocities in (a) the ITFR08 and (b) the India fixed reference frame along the Nepal Himalaya. Brown and blue colored vectors represent GPS velocities from the NGL and published works, respectively. Abbreviations align with the Figure 2.1.

of horizontal velocity field (Figure 2.12). The NGL adopted velocities of 46 GPS sites (Figure 2.11) are estimated using the Median Interannual Difference Adjusted for Skewness (MIDAS), a robust GPS time-series trend estimator. The GPS time series is processed (by NGL) using the GipsyX software, and MIDAS is applied to remove data outliers, steps (i.e., coseismic offsets), and seasonal signals [148]. Then, a seven-parameter Helmert transformation is used to combine these surface velocities in the ITRF08 reference frame (Equation 2.2). The surface velocity field of 77 combined GPS sites indicates motion towards the Eurasia plate at a rate of 40–50 mm/yr with the uncertainties ranging from 0.2–2.2 mm/yr (Figure 2.12). In addition, using the Euler pole of Jade et al. (2017), the velocity field in the India-fixed reference frame is derived to account for the regional deformation pattern (Figure 2.12). Similar to the Kumaun Himalaya region, it is observed that the northern portion of the study region shows southward movement as a result of the India-Eurasia convergence, whereas the south-western and the south-eastern portion show relatively smaller movement in the northward and southward directions, respectively, due to the north-south shortening across the Nepal Himalaya (Figure 2.12) [10, 11, 153].

Moreover, a distinct shift in the velocity pattern is evident, showing a transition from higher to lower velocity magnitudes as one moves from the northern to the southern part of the Nepal Himalaya near the MCT (Figure 2.12).

2.3.2 Interferometric Synthetic Aperture Radar

The Interferometric Synthetic Aperture Radar (InSAR) is a space-based technique that combines the phases of two different radar images obtained from satellites simultaneously or at different looking angles (Figure 2.13) [154–162]. Since 1978, InSAR is a feasible technology. However, because observation data required for InSAR were not enough and a computer for InSAR analysis required an enormous amount of memory and calculation, InSAR did not come into practical use before 1990. The synthetic aperture radar (SAR) had been successively installed on airplanes and satellites in the 1990s. The InSAR is used in many areas, such as crustal deformation analysis, ocean currents, landscape surveys, vegetation parameters, classifications of terrain, glacial techniques, and landslides [163].

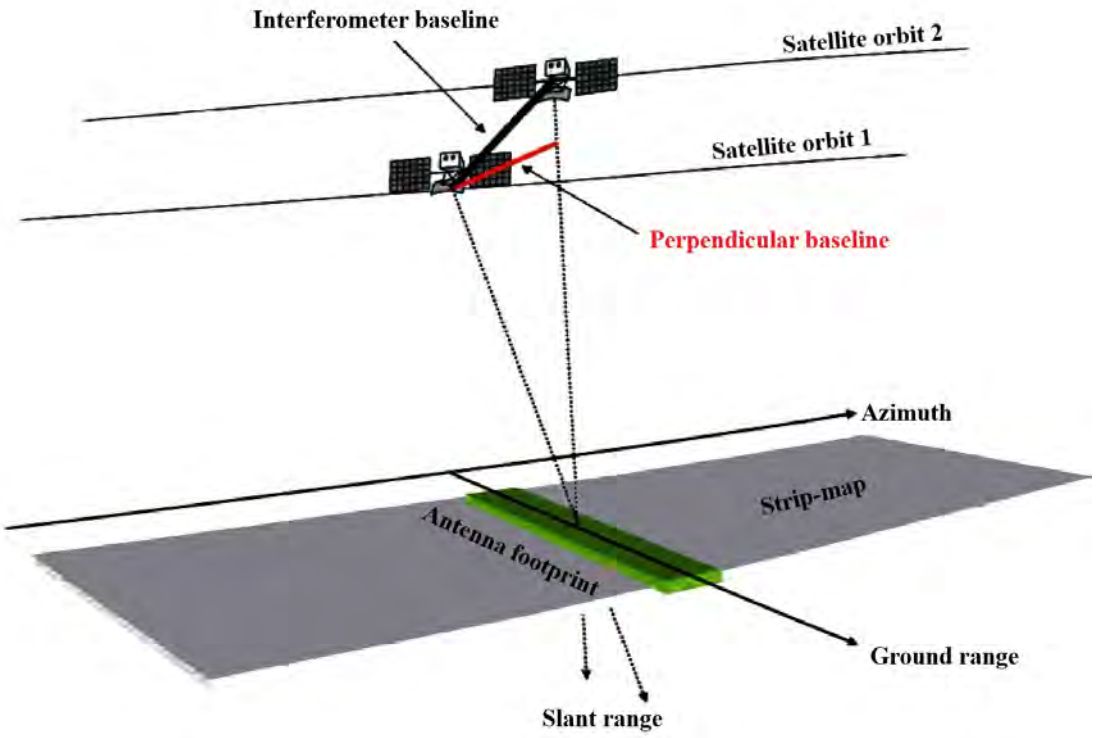

Figure 2.13: Geometry of interferometric SAR system [162].

A digital SAR image is a 2-D account of the phases in the imaging region of the returns from targets. To produce a radar interferogram, two or more SAR images can be combined. The interference pattern caused by the phase difference between these images can measure the topography or minute changes in the topography of the order of several mm between two image acquisitions along the satellite look path (Figure 2.13). To generate an interferogram, a phase of two digital SAR images, obtained simultaneously or at different viewing angles from space, can be combined. Relative phase observations from two images captured from slightly distinct viewing angles provide information on changes in the range of targets on the area and can thus recover the topography at the pixel of the SAR image with information of the geometry of the imagery (Figure 2.13). The phase change between two SAR images captured from the same point of view, but at different times, is capable of reliably calculating any changes in the return phase. Therefore, if the Earth's crust has changed between the two imaging passes towards or away from the radar, this would result in phase changes in line of sight (LOS) that can be calculated with an

accuracy equal to displacements at the millimeter level [164].

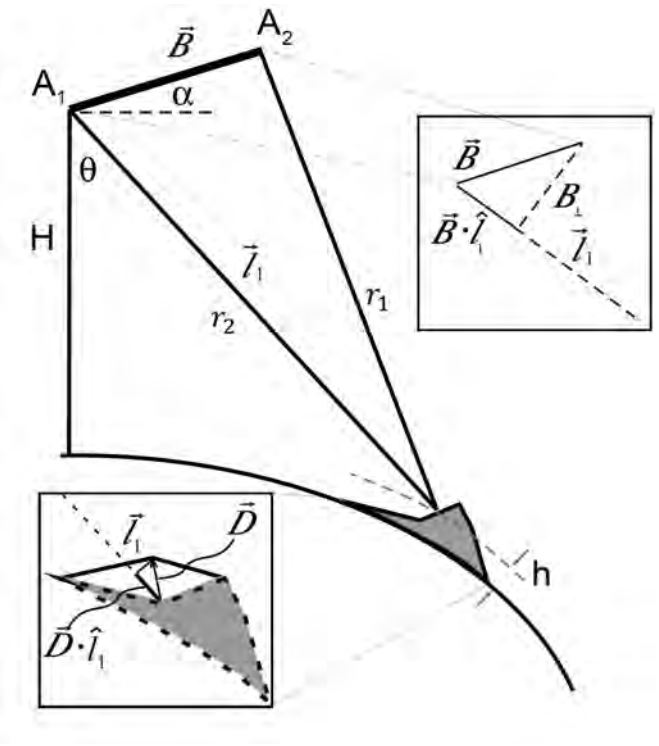

Figure 2.14: Side-looking InSAR acquisition geometry [164].

Figure 2.14 depicts the geometry utilized in repeat-track interferometry. The objective involves deriving the elevation h for every image point from the data of two SAR images. The radar carrier wavelength λ is a known value obtained from the radar system design. The satellite's flight height H and the orbit separation vector can be estimated based on accurate satellite orbits. The initial distance r_1 from the satellite to the image point along the look vector $\vec{l}_1$ is determined via radar signal delay, and the relative difference between the two phase measurements ϕ constitutes interferogram.

The interferometric phase in repeat-pass interferometry can measure any ground displacement in addition to topography. If the distance between the ground and satellite changes between the two acquisitions due to surface movement, a phase shift will occur (Figure 2.14). The elevation h of each pixel location can be determined from the pair of SAR images. From the radar control system, the radar transmitter wavelength λ is identified. From appropriate satellite orbits, the satellite flying height H and orbit

separation vector $\vec{B}$ can be calculated. To the radar signal delay, r_1 along the looking vector $\vec{l_1}$ is calculated and the interferogram is the relative change between the two-phase observations ϕ (i.e., the interferometric phase). The phase change calculated between the image pair is directly proportional to the path delay change provided by $\phi = \frac{4\pi}{\lambda}(r_1 - r_2)$, where $r_{1,2}$ is the $A_{1,2}$ antenna range. Therefore, if r_1 and $\vec{B}$ are known, the phase change can be determined. The interferometric phase difference can only be determined on modulo 2π. Then, the interferometric phase is given by [165]:

$$\phi = \frac{4\pi r_1}{\lambda}\left[1 - \frac{2(\vec{B}\cdot\hat{l}_1)}{r_1} + \left(\frac{B}{r_1}\right)^4 - 1\right] \tag{2.3.17}$$

where $\hat{l}_1$ is the unit vector in the direction of the range and $\vec{B}$ is the vector of length B's baseline separation. A parallel ray approximation can be applied if $B \leq\leq r_{1,2}$. Then,

$$\phi \approx -\frac{4\pi}{\lambda}(\vec{B}\cdot\hat{l}_1) = -\frac{4\pi}{\lambda}B\cdot\sin(\theta-\alpha) \tag{2.3.18}$$

where $\theta = \sin^{-1}\left(-\frac{\lambda\phi}{4\pi B}\right) + \alpha$ and $h = H - r_1\cos\theta$, with the known wavelength of radar as demonstrated in Figure 2.14. It is useful to describe the uncertainty height h_a, the change in height that corresponds to a complete 2π shift in phase, to explain the impact of satellite orbital separation on the interferometric phase [165], as

$$h_a = 2\pi\frac{\partial h}{\partial\phi} = \frac{\lambda r_1\sin\theta}{2}B\cdot\cos(\theta-\alpha) \tag{2.3.19}$$

where the term $B\cdot\cos(\theta-\alpha)$ denotes the component of the antenna baseline that lies perpendicular to the range direction, represented as $B_\perp$.

2.3.2.1 InSAR processing

For the InSAR-based velocity field, the ascending and descending SAR data is collected from the "COMET-LiCS Sentinel-1 InSAR" portal (comet.nerc.ac.uk/COMET-LiCS-portal/) [158] as LiCSBAS delivers InSAR time series and velocity estimations wherever enough LiCSAR products are available. While processing the SAR data, due to obvious

significant atmospheric fluctuation, the noise on every SAR image is mainly random and can easily be reduced by stacking the interferograms [166]. To reduce the atmospheric delay, we utilize the atmospheric data of each epoch in the SAR frame provided by the Generic Atmospheric Correction Online Service for InSAR (GACOS) [167–169]. Then, using the small baseline subset (SBAS) approach, progressive and cumulative deformations as well as mean displacement rates are calculated. The incremental displacements are combined to obtain the cumulative displacement field. Then, the least-squares approach is used to determine the mean displacement velocity from the cumulative displacements [158]. Although Sentinel-1 data provides small temporal and spatial baseline SAR images, discontinuities in the network might well exist because of strong decorrelation, prolonged periods without acquisitions, and unwrapping tests. The LiCSBAS resolves this issue by assuming that displacements across the gaps are linear in duration (i.e., consistent velocity) [170, 171]. Then, the percentile bootstrap approach computes the uncertainty in velocity estimation based on standard deviation [172]. The step-by-step method for InSAR data processing is as follows:

In order to commence LiCSBAS processing, a dedicated conda environment is required, equipped with specific dependencies. For this, one needs to create a conda environment that includes Python version 3.6 or higher and proceed to install essential libraries like Astropy, BeautifulSoup4, GDAL (version 2.4 or above), h5py, Matplotlib, NumPy, Psutil, Requests, Shapely, and Statsmodels. This environment should encompass all necessary packages for enabling LiCSBAS functionalities. Once the environment is established and the dependencies are installed, InSAR data processing is initiated with the following steps:

Step I (Download GeoTIFF files and convert them into a single-point format): The LiCSBAS starts with downloading the LiCSAR products covering the area of interest. The downloaded data is then converted into a single-precision floating-point format.

Example (for downloading GeoTIFF files) *LiCSBAS01_get_geotiff.py -f 092D_06191_141214 -s 20170306 -e 20210311*

-f (Frame ID in COMET-LiCS Sentinel-1 InSAR portal)

-s (Start date)

-e (End date)

Example (for downloading GeoTIFF files) *LiCSBAS02_ml_prep.py -i GEOC -n 1*

-i (Path to the input GEOC dir containing stack of geotiff data)

-n (Number of donwsampling factor (Default: 1, no donwsampling))

Step II (Tropospheric noise correction): To remove the tropospheric noise, Generic Atmospheric Correction Online Service (GACOS) data is utilized (http://www.gacos.net/) [169]. The GACOS data for each day of InSAR acquisition is downloaded and subsequently removed from the InSAR phases [169].

Example *LiCSBAS03op_GACOS.py -i GEOCml -o GEOCml0 -g GACOS*

-i (Path to the GEOCml directory containing stack of unwrapped data)

-o (Path to the output directory))

-g (Path to the directory containing GACOS data))

Step III (Mask interferograms): This step masks specified rectangular areas in the stack of unwrapped data. It is useful when some areas have unwrapping errors,

probably due to vegetation and topographic effect. For the present study, we set the coherence threshold value in the interferometric stack to 0.3 to reduce the vegetation effect [158].

Example *LiCSBAS04op_mask_unw.py -i GEOCml0 -o GEOCml1 -c 0.2*

-i (Path to the GEOCml* directory containing stack of unwrapped data)

-o (Path to the output directory))

-c (Threshold for average coherence))

Step IV (Quality check to remove low coverage data): As Sentinel-1 SLC data distributed by ESA do not always cover an entire LiCSAR frame (i.e., some bursts may be missing in a frame), it is essential to remove incomplete data with low coverage. Following this, the low-coverage interferograms from the InSAR dataset are removed [158].

Example *LiCSBAS11_check_unw.py -d GEOCml1*

-d (Path to the GEOCml* directory containing stack of unwrapped data)

Step V (Data refinement by loop closure): As unwrapped data may include unwrapping errors, it can cause significant impact to the derived velocity field. To identify poorly unwrapped interferograms and subsequently to remove them from the dataset, the loop closure technique is utilized [158]. The loop closure can be defined as below:

Suppose, there are three SAR images ϕ_1, ϕ_2, and ϕ_3 and three unwrapped interferograms ω_1, ω_2, and ω_3. Then, a loop phase can be calculated by [158]:

$$\omega_{123} = \omega_{12} + \omega_{23} - \omega_{13} \tag{2.3.20}$$

If there are no unwrapping errors in these three interferograms, the loop phase should be close to zero [173]. On the other hand, if one (or more) of the interferograms contains unwrapping errors, the loop phase will usually be close to an integer multiple of 2π. If all loops associated with an interferogram are problematic, it would be considered as a bad interferogram and consequently it should be removed.

Example *LiCSBAS12_loop_closure.py -d GEOCml1*

-d (Path to the GEOCml* directory containing stack of unwrapped data)

Step VI (Computation of velocity field through small baseline inversion): To derive the InSAR-based velocity field in the study region, we utilize the New Small Baseline Subset (NSBAS) method [158]. This method follows an incremental displacement strategy to derive the displacement rate. The method suitably takes care of the discontinuous data that may be present because of strong decorrelation, prolonged periods without acquisitions, and unwrapping tests. In such a situation, the LiCSBAS resolves this issue of discontinuity by assuming that displacements across the gaps are linear in duration (i.e., consistent velocity).

Example (To obtain the time series and velocity using NSBAS) *LiCSBAS13_sb_inv.py -d GEOCml1*

-d (Path to the GEOCml* directory containing stack of unwrapped data)

Example (To calculate the standard deviation of the velocity by the bootstrap method and STC (spatio-temporal consistency)) *LiCSBAS14_vel_std.py -t TS_GEOCml1*

-t (Path to the time-series and velocities files directory)

2.3.2.2 InSAR velocity field over the Kumaun Himalaya

For the calculation of InSAR-based LOS velocities in the Kumaun Himalaya, three frames of ascending and two frames of descending acquisitions are employed (Figure 2.15). A consolidated summary of the InSAR dataset is provided in Table 2.5. The time interval for each frame of SAR data is $\sim$ 9 years (2014–2022). For each Sentinel-1 InSAR frame, an interferometric stack using several chains of small-baseline interferograms is developed. After obtaining the LOS rate map from the LiCSAR process, every frame will have its unique point of reference within that frame for subsequent velocity calculation [158]. The regional GPS velocity field over the Kumaun Himalaya is utilized to translate the LOS rate map into the India fixed reference frame [27, 174]. For this, (i) the GPS velocities in the India fixed reference are projected into LOS [175], (ii) the best fit-plane between the GPS in LOS and average InSAR LOS velocities located 500 m from each GPS station is constructed, and (iii) the estimated plane is subtracted from the InSAR velocity map [174, 175]. The estimated India fixed ascending and descending velocities (Figure 2.16) provide the surface motions in the LOS direction (towards or away from the satellite) of the study area. Both the InSAR ascending and descending LOS rate maps (Figure 2.16) illustrate a noticeable change in upliftment between the Higher Himalaya and the Lower/Siwalik Himalaya, due to the convergence of the Indian and Eurasian plates. Specifically, the Higher Himalaya exhibits a relatively higher uplift in comparison to the Lower/Siwalik Himalaya. In the ascending LOS rate map (Figure 2.16a), the southern region of the study area demonstrates movement away from the satellite. Conversely, in the descending LOS rate map (Figure 2.16b), this southern area exhibits movement towards the satellite.

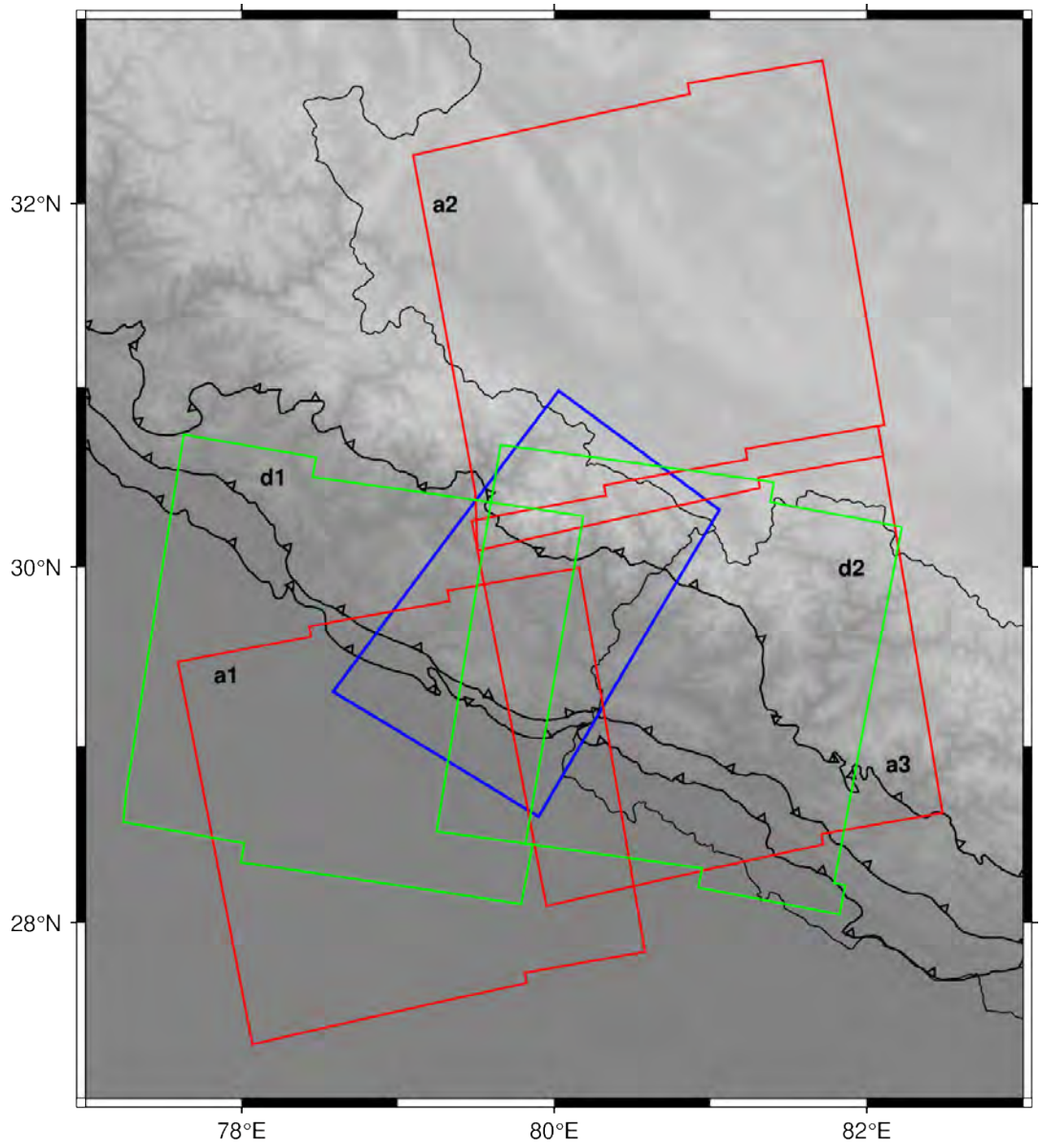

Figure 2.15: InSAR ascending and descending frame used for the Kumaun Himalaya. The red and green boxes represent the ascending and descending frame, respectively. The blue box represents the Kumaun region.

Notably, a change in the pattern within the ascending and descending LOS velocity fields along MBT/MFT is observed.

2.3.2.3 InSAR velocity field over the Nepal Himalaya

To estimate InSAR-based LOS velocities in the Nepal Himalaya, five frames of ascending and four frames of descending acquisitions are employed (Figure 2.17). A consolidated

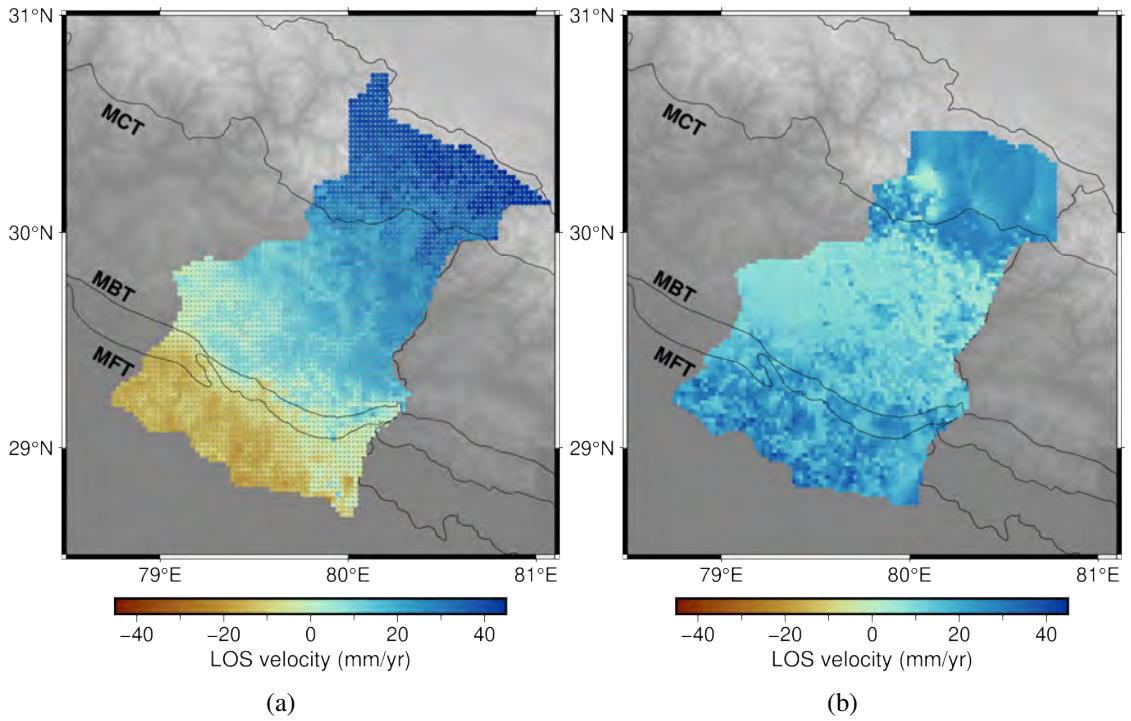

Figure 2.16: (a) Ascending and (b) descending LOS velocities are shown. Positive (blue) and negative (brown) values represent relative velocity away and towards from the satellite. Abbreviations align with the Figure 2.1.

Table 2.5: Summary of InSAR dataset for ascending and descending frames over the Kumaun Himalaya

Ascending frame	Number of images	Number of interferograms	Descending frame	Number of images	Number of interferograms
a1	118	255	d1	110	248
a2	176	538	d2	96	159
a3	131	301			

summary of the InSAR dataset for the Nepal Himalaya is provided Table 2.6. The time interval for each frame of SAR data is ∼5 years (2017–2021). In a similar manner of Kumaun Himalaya, the India fixed ascending and descending InSAR velocities are estimated for the Nepal Himalaya using the GPS velocities. The estimated India fixed ascending and descending velocities (Figure 2.18) provide the surface motions in the LOS direction (towards or away from the satellite) of the study area. Due to the subsidence of the Indian plate, the InSAR ascending (Figure 2.18a) and InSAR descending (Figure

2.18b) LOS rate maps represent the dominance of motion away from the satellite. The InSAR-based ascending LOS map reveals a notable increase in subsidence rates within the area spanning from 85°E to 86°E. Following the calculation of GPS and InSAR-derived velocity fields, the subsequent step involves integrating these velocities to derive a high-resolution velocity field along the study area.

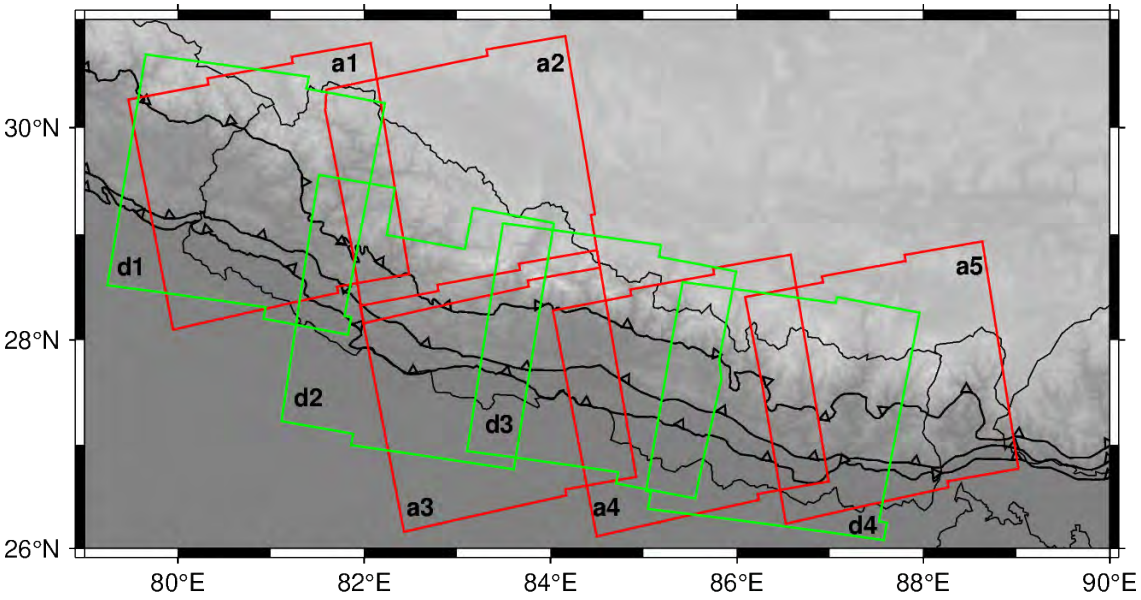

Figure 2.17: InSAR ascending and descending frame used for the Nepal Himalaya. The red and green boxes represent the ascending and descending frame, respectively.

Table 2.6: Summary of InSAR dataset for ascending and descending frames over the Nepal Himalaya

Ascending frame	Number of images	Number of interferograms	Descending frame	Number of images	Number of interferograms
a1	117	294	d1	75	134
a2	130	312	d2	102	180
a3	81	138	d3	103	200
a4	120	263	d4	125	291
a5	133	365			

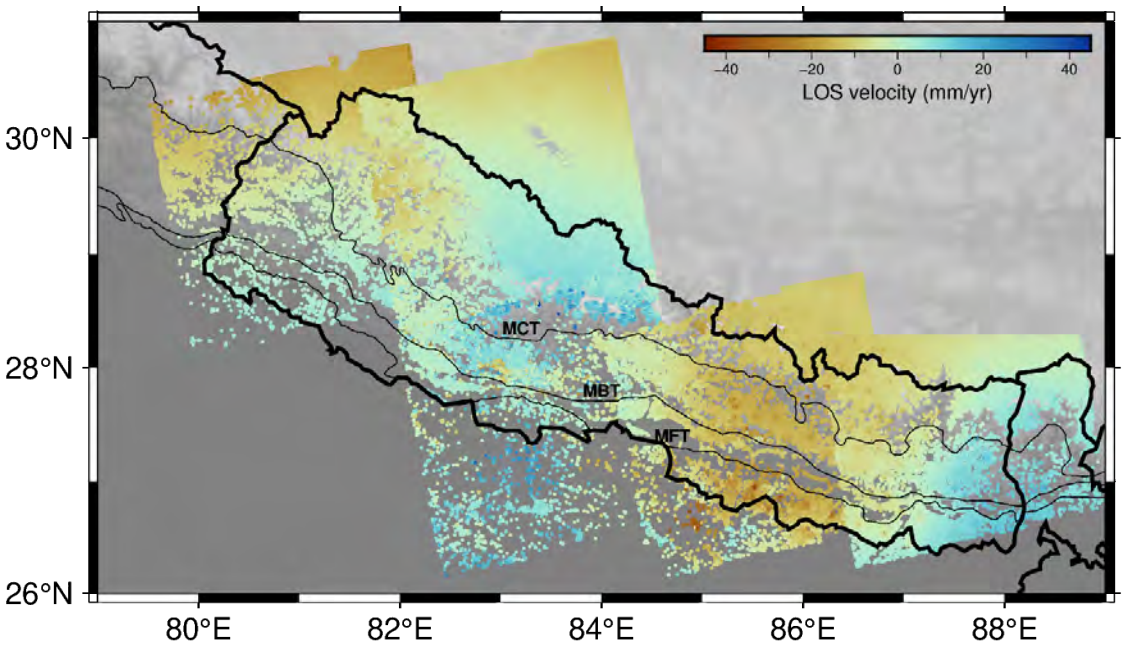

(a)

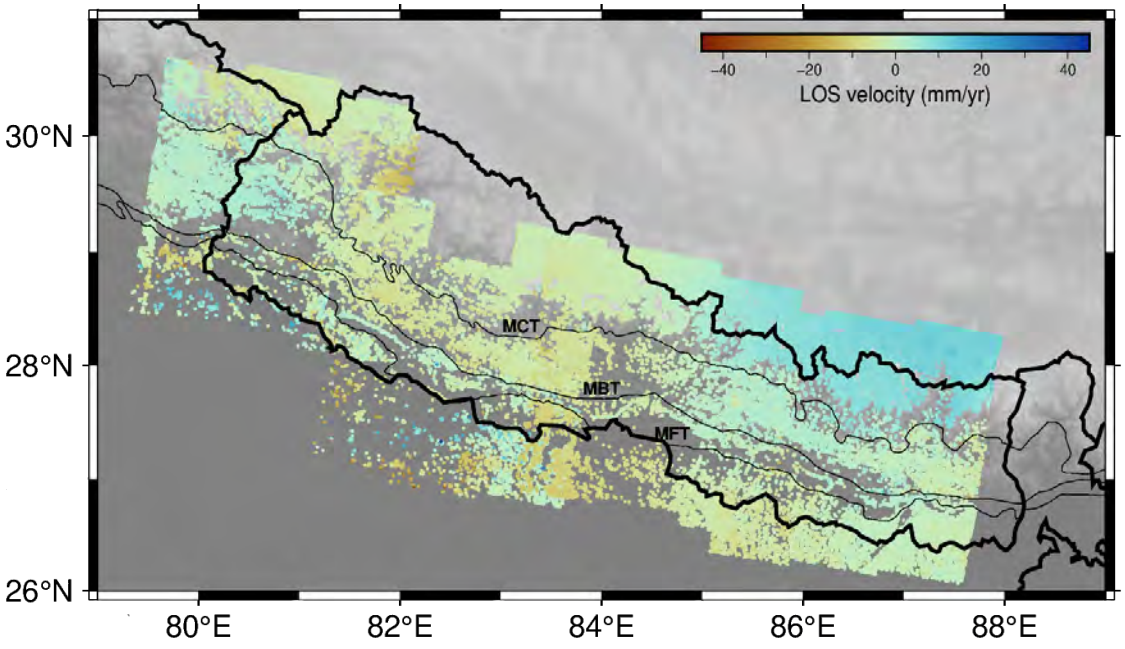

(b)

Figure 2.18: (a) Ascending and (b) descending LOS velocities are shown. Positive (blue) and negative (brown) values represent relative velocity away and towards from the satellite. Abbreviations align with the Figure 2.1.

2.3.3 Integrated velocity field

Satellite-based measures of surface deformation, such as GPS and InSAR products, have already demonstrated their effectiveness in quantifying tectonic deformation at several active regions [17–23]. While the ground-based GPS technique provides dense time series of accurate positions at a limited number of points, the remote sensing InSAR technique can provide dense spatial coverage at a limited number of epochs. The GPS technique is used to precisely measure three-dimensional positions with horizontal precision of mm level and vertical accuracy of two to five times of horizontal ones [24], whereas InSAR methods can quantify deformations in the line-of-sight (LOS) direction with high precision ranging from mm to cm [25, 26]. As a consequence, these two geodetic methods complement one another in crustal deformation monitoring and their integration enables a uniform spatio-temporal range for higher spatial and temporal resolution than any of them alone [27–31]. By integrating GPS and InSAR data, Wang and Wright (2012) [27] developed a procedure for measuring high-resolution velocity field. Such a method has been adopted to study several active regions of the world, including Afar [28], eastern Turkey [176], South-Central Tibet [177], and Antolia [175]. In this thesis, the similar approach is adopted to obtain a high resolution integrated velocity field from the combination of GPS and InSAR velocities.

2.3.3.1 Methodology for the integrated velocity field

To integrate the InSAR LOS velocities with the GPS-based velocity field for high-resolution integrated velocity field, the methodology outlined in Wang and Wright (2012) [27] is employed. This approach allows us to generate a velocity distribution in the India-fixed reference frame with significantly enhanced spatial resolution compared to using GPS data alone. For this, the study area is subdivided into small triangular meshes (approximately 400 points constituting the vertices of triangles across both the Kumaun and Nepal regions), and it is assumed that velocity changes linearly with longitude and latitude within each triangle. Then, an interpolation function is utilized to connect the GPS and InSAR velocities within each triangle to the velocities of its vertices. While the

velocity field exhibits lower resolution compared to the original InSAR data, this technique offers the advantage of eliminating short-wavelength noise that is irrelevant to tectonic processes, ultimately providing a final 3-D velocity field [27]. The system of equations to integrate InSAR and GPS velocities can be stated as follows [27]:

$$\begin{bmatrix} H_{sar} & H_{orb} & H_{atm} \\ H_{gps} & 0 & 0 \\ \kappa^2\nabla^2 & 0 & 0 \end{bmatrix} \begin{bmatrix} k_{vel} \\ k_{orb} \\ k_{atm} \end{bmatrix} = \begin{bmatrix} d_{sar} \\ d_{gps} \\ 0 \end{bmatrix} \tag{2.3.21}$$

Here, d_{gps} and d_{sar} denote GPS velocities and InSAR displacement rates, respectively; H_{sar} denotes the InSAR rate map design matrix operated by local LOS unit vectors and interpolation kernels; H_{atm} and H_{orb} are matrices for the atmospheric lag compensation and InSAR orbit models (k_{atm} and k_{orb}), respectively; H_{gps} denotes the design matrix of the GPS interpolation kernel, and k_{vel} denotes the unknown velocities of the triangle vertices. In Equation 2.3.21, ∇^2 denotes the Laplacian smoothing operator estimated by a scale-dependent umbrella operator [178], and the smoothing weight is determined by the component κ^2. To fit orbital and long-wavelength atmospheric lag issues, a quadratic model H_{orb} is utilized. Then, the integrated velocity field can be estimated using a full covariance matrix produced by the formal uncertainties of GPS data along with a full covariance matrix of InSAR calculated using an exponential function [179].

2.3.3.2 High-resolution integrated velocity field along the Kumaun Himalaya

Instead of using GPS velocities directly to estimate the seismic hazard over the region, a high-resolution velocity field that combines GPS and InSAR velocities is utilized. A high-resolution velocity field delivers more information at each position of the study area than a standalone GPS velocity field. The surface velocities derived from the integrated InSAR and GPS data are provided in Figure 2.19. It is observed that the northern part of Kumaun Himalaya has deformation towards the south at a rate of 10–15 mm/yr, whereas the deformation of the southern part is relatively small (Figure 2.19), due to the north-south convergence of Indian and Eurasian plates [153]. The change in motion from north to

south in the study area indicates high strain build-up near the MCT region. The estimated high-resolution integrated velocity field in the vertical direction indicates upliftment over the study region with an average of 3 mm/yr (Figure 2.19). The upliftment in the lower Himalaya is less as compared to the other regions. The residual plots for the integrated velocity field are provided in Figure 2.20 to Figure 2.22.

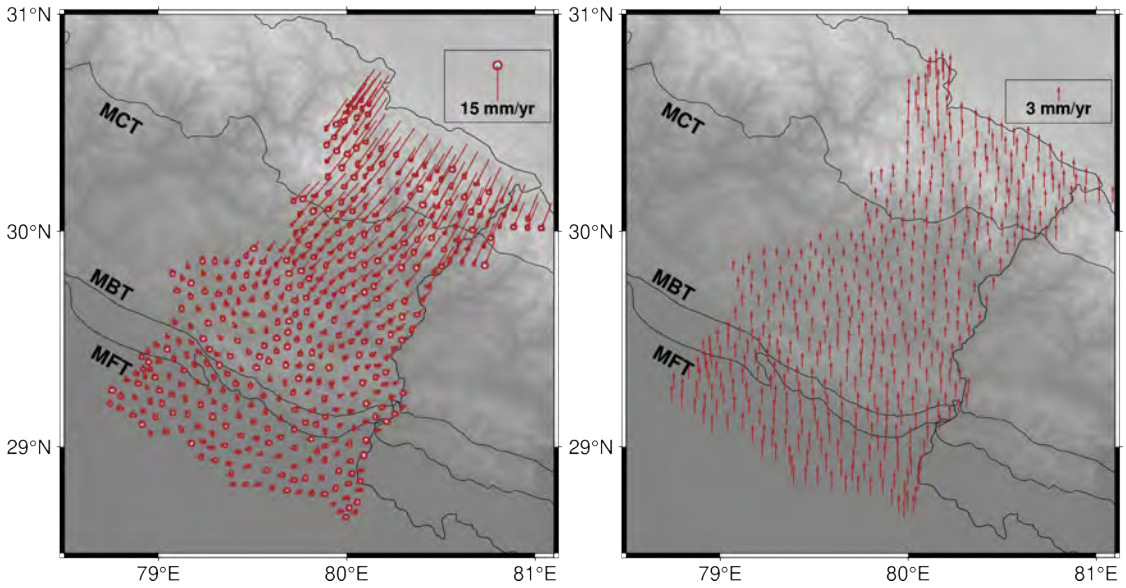

Figure 2.19: High resolution integrated (from combination of GPS and InSAR) (a) surface and (b) vertical velocities in the India fixed reference frame along the Kumaun Himalaya. Abbreviations align with the Figure 2.1.

The root mean square error (RMSE) value of 1.29 and 1.26 for the GPS calculated velocities in east and north direction respectively, indicates the level of deviation between calculated and observed values.

2.3.3.3 High-resolution integrated velocity field along the Nepal Himalaya

The surface velocities derived from the integrated InSAR and GPS data are provided in Figure 2.23. Similar to the observations in the Kumaun Himalaya, a discernible change in motion from north to south is evident in the Nepal Himalaya, signifying the accumulation of high strain near the MCT region. This minimal deformation within the Siwalik and Lesser Himalaya regions suggests a locking behavior of the MFT in this region.

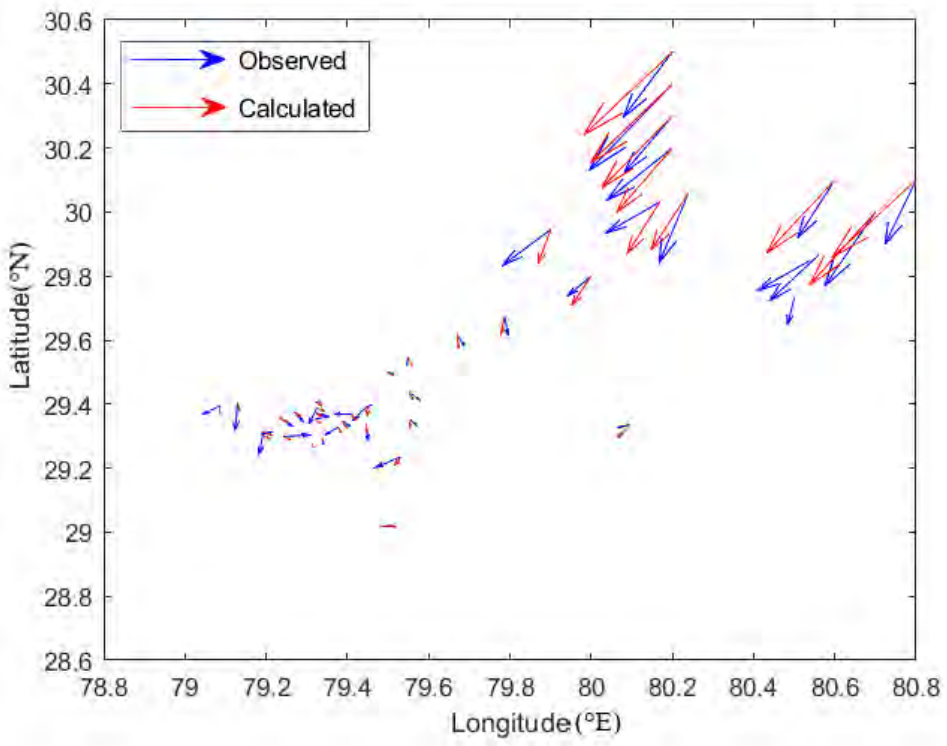

Figure 2.20: Observed and calculated (from the integration of InSAR and GPS) velocities at the GPS sites along the Kumaun Himalaya.

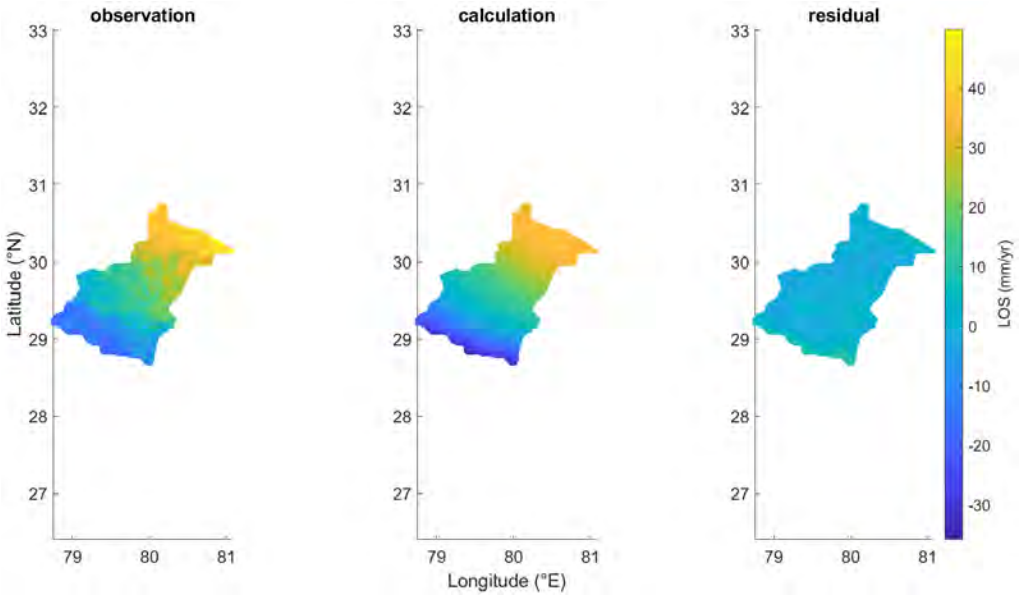

Figure 2.21: Observed, calculated (from the integration of InSAR and GPS), and residual velocities for InSAR ascending pixels along the Kumaun Himalaya.

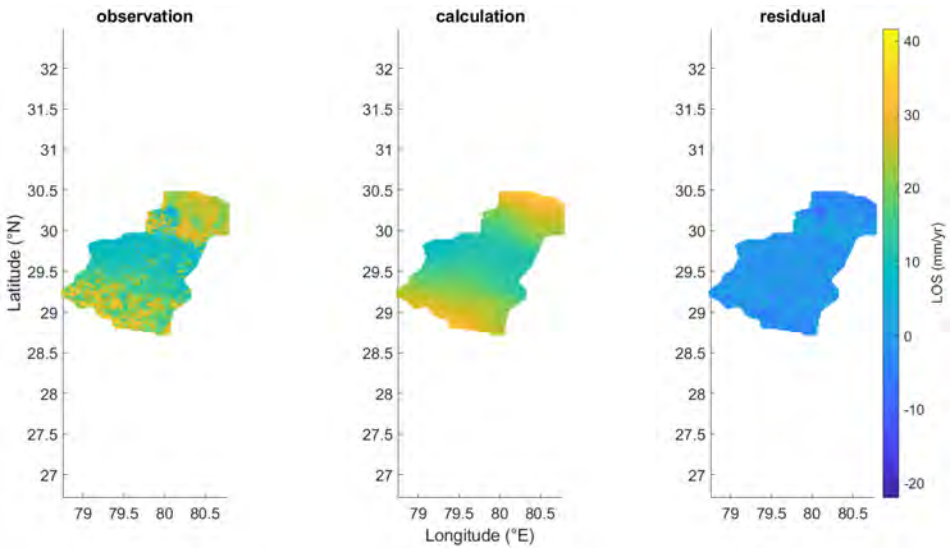

Figure 2.22: Observed, calculated (from the integration of InSAR and GPS), and residual velocities for InSAR descending pixels along the Kumaun Himalaya.

Specifically, the northern part of the Nepal Himalaya exhibits deformation towards the south at a rate ranging from 9 mm/yr to 15 mm/yr, while the deformation in the southern part is relatively smaller (Figure 2.23). This pattern of deformation is a consequence of the ongoing north-south convergence between the Indian and Eurasian tectonic plates [153].

Additionally, the integrated velocity field reveals upliftment across the study area, with an average rate of approximately 3 mm/yr, as illustrated in Figure 2.23. Notably, the extent of upliftment in the lower Himalaya is comparatively less than the other regions. The residual plots for the integrated velocity field along the Nepal Himalaya are provided in Figure 2.24 to Figure 2.26. The RMSE values of 1.10 and 1.53 for the calculated GPS velocities in the east and north directions, respectively, signify the extent of difference between the calculated and observed values.

In summary, analysis of the integrated velocities in both Kumaun and Nepal Himalaya indicate that beneath the Siwalik Himalaya and the southern portion of the Lesser Himalaya, a distinct locking behavior is observed as these regions exhibit minimal deformation. Conversely, the northern section of the Lesser Himalaya and the Higher Himalaya experiences the most significant deformation, notably concentrated in the vicinity of the MCT. This could be related to the buckling of the Higher Himalayan Crystalline sheets

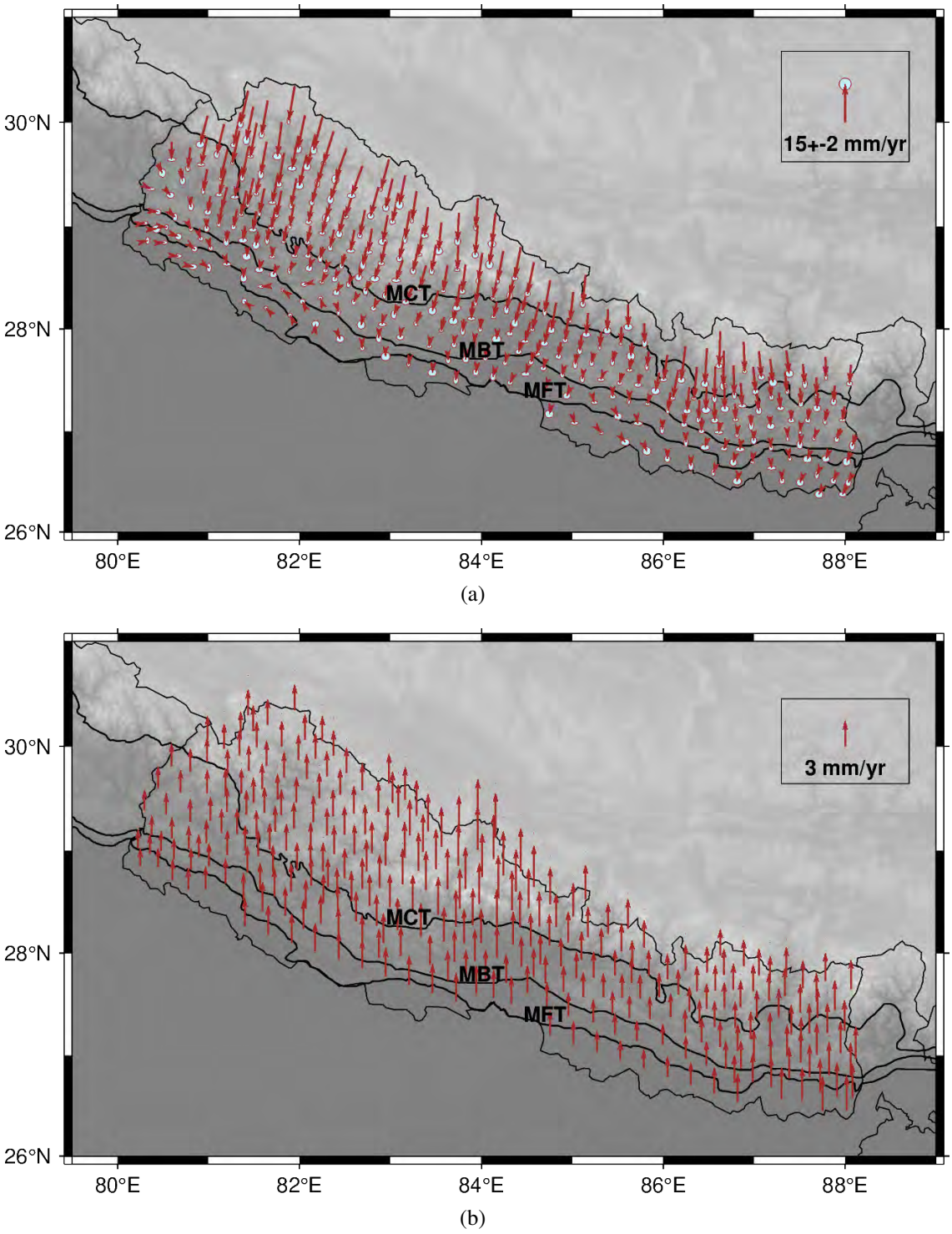

Figure 2.23: High resolution integrated (from combination of GPS and InSAR) (a) surface and (b) vertical velocities in the India fixed reference frame along the Nepal Himalaya. Abbreviations align with the Figure 2.1.

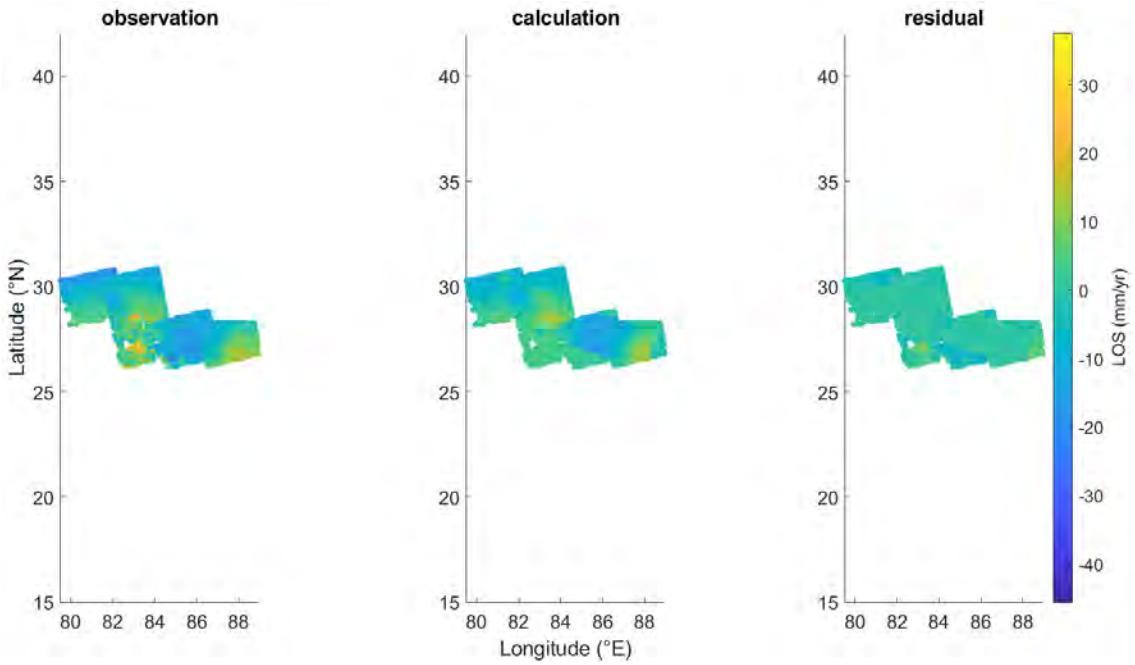

Figure 2.24: Observed, calculated (from the integration of InSAR and GPS), and residual velocities for InSAR ascending pixels along the Kumaun Himalaya.

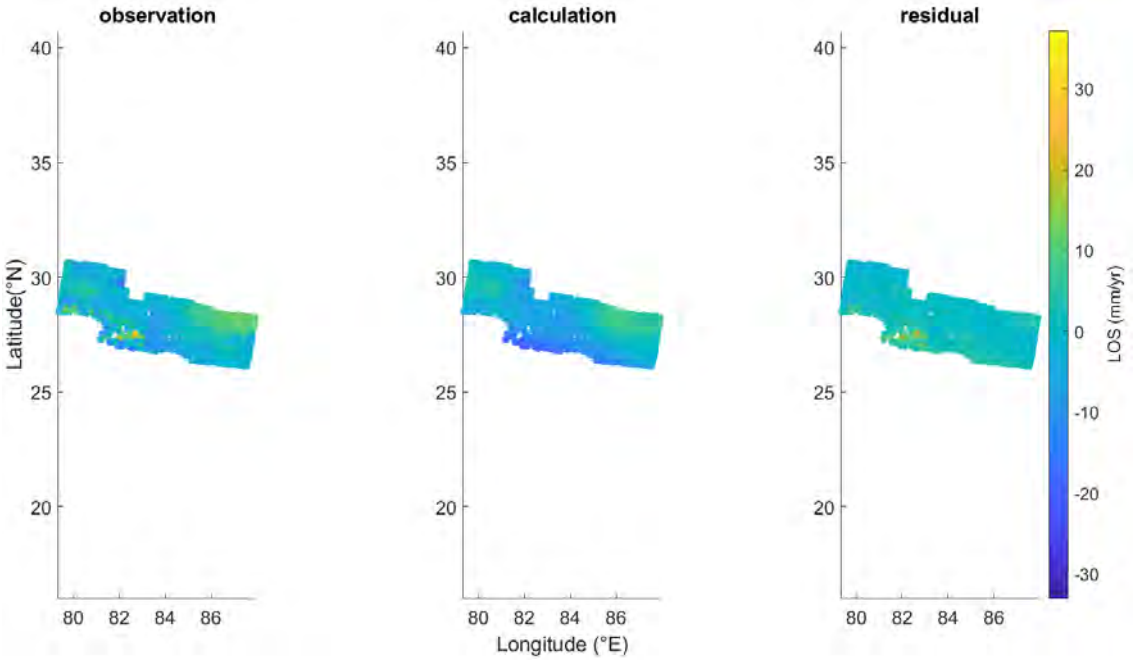

Figure 2.25: Observed, calculated (from the integration of InSAR and GPS), and residual velocities for InSAR descending pixels along the Kumaun Himalaya.

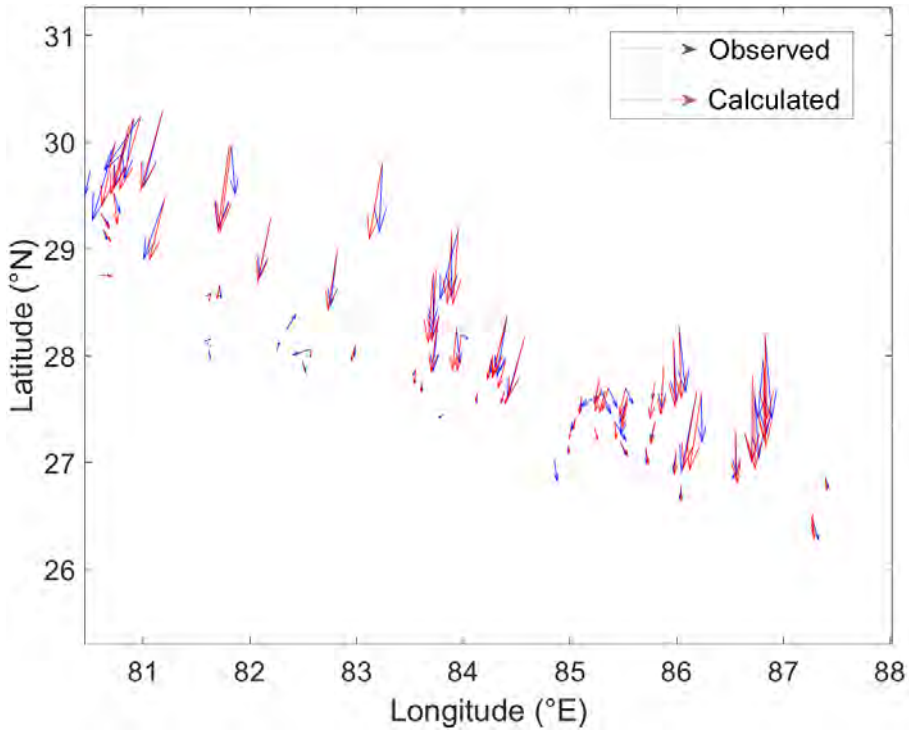

Figure 2.26: Observed and calculated (from the integration of InSAR and GPS) velocities at the GPS sites along the Kumaun Himalaya.

southward along the MCT. The southward motion of the Higher Himalaya is correlated with heightened seismic activity along the down-dip edge of the fault system [180, 181].

The derived integrated velocities along the Kumaun and Nepal Himalaya will be directly utilized in the upcoming chapters. For example, the integrated velocity field is a crucial input for computing strain rate distribution (Chapter 3), seismic moment budget (Chapter 3), and fault parameters (Chapter 4) in subsequent chapters.

Following the estimation of the integrated velocity field along the study region, the subsequent step involves assembling earthquake data within the area as narrated below.

2.3.4 Earthquake dataset

For assembling the earthquake dataset in this thesis, an expanded area is selected (as shown in Figure 2.27). This selection is made to facilitate earthquake nowcasting (Chapter 5) in various cities across the study area. The earthquake catalog is prepared using several open sources catalogs, such as International Seismological Centre (ISC), United States

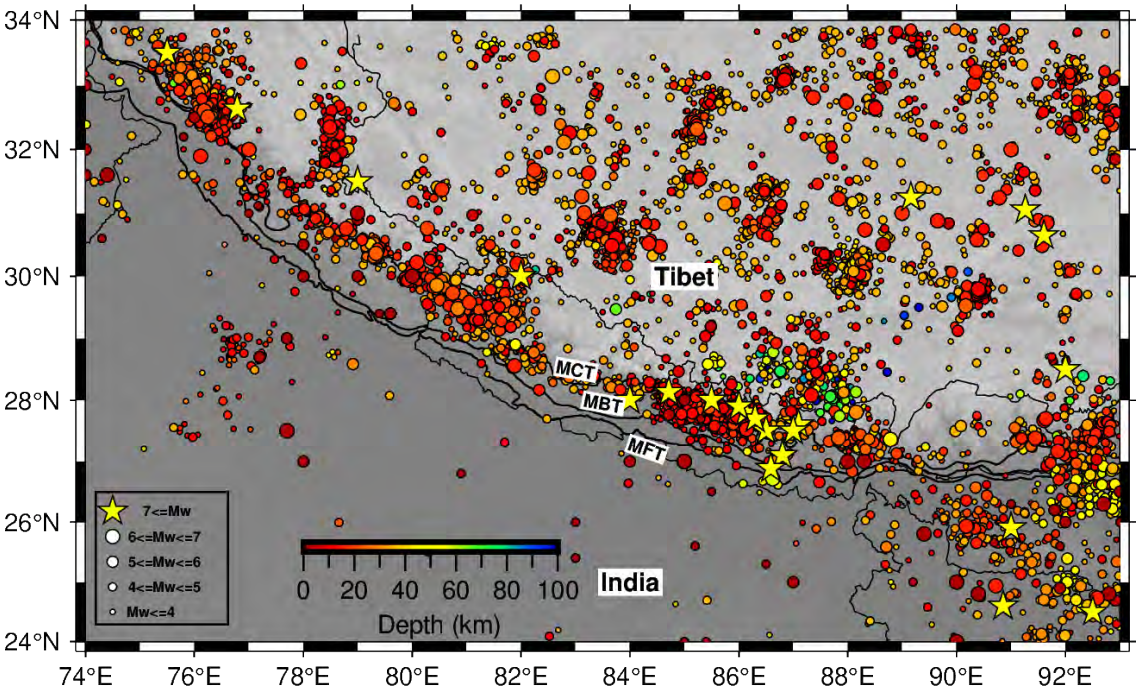

Figure 2.27: Seismotectonic setting of the study area. The earthquake database is compiled from the International Seismological Centre (ISC), United States Geological Survey (USGS), and several published works [4, 6, 8, 73–77, 182]; the color and size of the circle represent the depth and magnitude of earthquakes, respectively. Abbreviations align with the Figure 2.1.

Geological Survey (USGS), India Meteorological Department (IMD), and other published works [4, 6, 8, 73–77, 182] over the Kumaun Himalaya and Nepal Himalaya. This compiled catalog encompasses a comprehensive dataset consisting of 5790 seismic events with magnitudes exceeding or equal to 3.5 (Figure 2.27). The temporal coverage of the catalog spans from 1100 to 2022, consisting of three distinct phases: historical earthquakes (1100–1903, from IMD), early instrumental seismic events (1904–1963, from ISC and USGS), and modern instrumental earthquakes (1964–2022, from ISC and USGS).

It is observed that acquired earthquake events in the Himalaya are not homogeneous in magnitude scale [183, 184]. As a result, various magnitude scales (M_L, M_S, m_b) from the initial sources are standardized to the moment-magnitude scale (M_w). To convert the recent earthquakes' (from 1976–2022) magnitudes, the open source Global Centroid Moment Tensor Catalog (GCMT) is used. To convert earthquake of before 1976 (which are not in moment magnitude), empirical relations outlined in prior studies [183, 185] and published

data is used. The empirical relations can be expressed as:

$$M_w = 0.67(\pm 0.005)M_S + 2.07(\pm 0.03), \quad \text{for} \quad (3.0 \leq M_S \leq 6.1), \tag{2.3.22}$$

$$M_w = 0.99(\pm 0.020)M_S + 0.08(\pm 0.13), \quad \text{for} \quad (6.2 \leq M_S \leq 8.2), \tag{2.3.23}$$

$$M_w = 0.85(\pm 0.040)m_b + 1.03(\pm 0.23), \quad \text{for} \quad (3.5 \leq m_b \leq 6.2), \tag{2.3.24}$$

$$M_w = 0.934(\pm 0.135)M_L + 0.356(\pm 0.714), \quad \text{for} \quad (3.4 \leq M_L \leq 7.6). \tag{2.3.25}$$

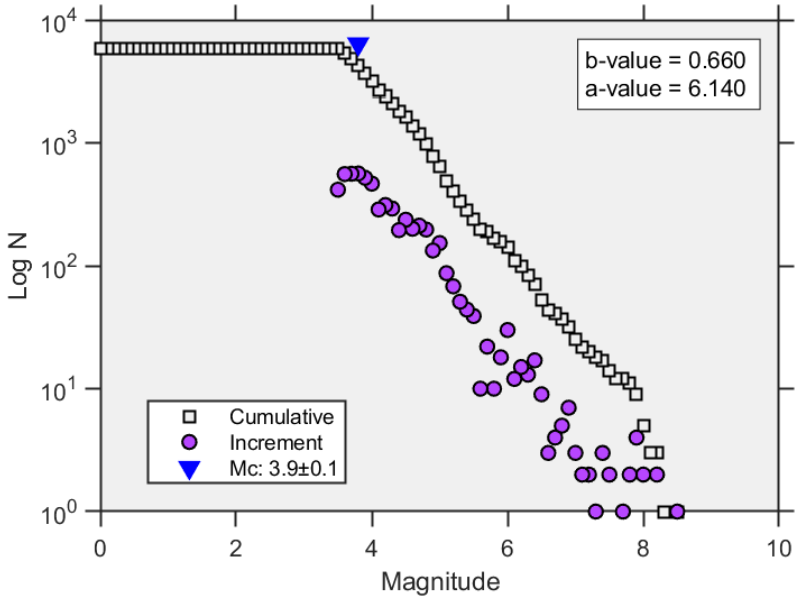

Figure 2.28: Magnitude-frequency plot of the compiled earthquake catalog.

After compiling the earthquake dataset in homogeneous manner, a magnitude of completeness threshold (serving as the lower limit beyond which earthquakes are consistently recorded and included in the catalog) of ∼4.0 has been established (Figure 2.28), to ensure the accuracy and reliability of earthquake dataset. However, it may be noted that this completeness threshold is somewhat dominated by the events during the modern instrumental era. Although the overall magnitude completeness threshold for earthquakes from 1100–2022 is 4.0, the thresholds for historical, early instrumental, and modern instrumental periods are 5.0, 5.5, and 3.6, respectively.

Moreover, to observe the spatial distribution of earthquake occurrences along longitude

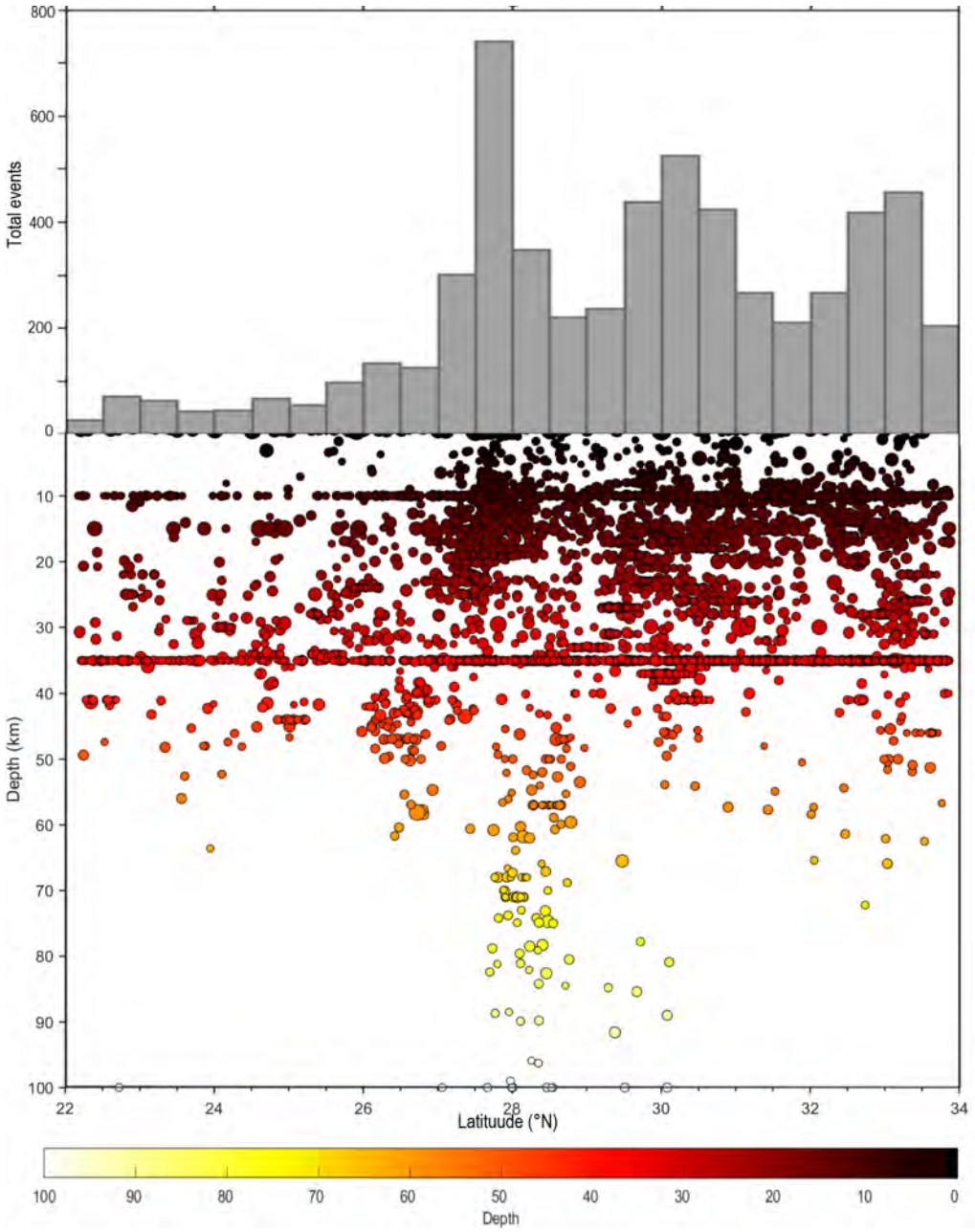

Figure 2.29: Cross-section view along latitude of the compiled earthquake catalog.

and latitude, the ZMAP software (open source) is employed. Figures 2.29 and 2.30 depict cross-sectional views along the longitude and latitude, respectively. The vertical sections' map in the latitude direction (Figure 2.29) displays a significant concentration of earthquakes around the latitude 28°N. Similarly, the vertical sections' map in the longitude direction (Figure 2.30) reveals multiple earthquakes occurring within the longitude range

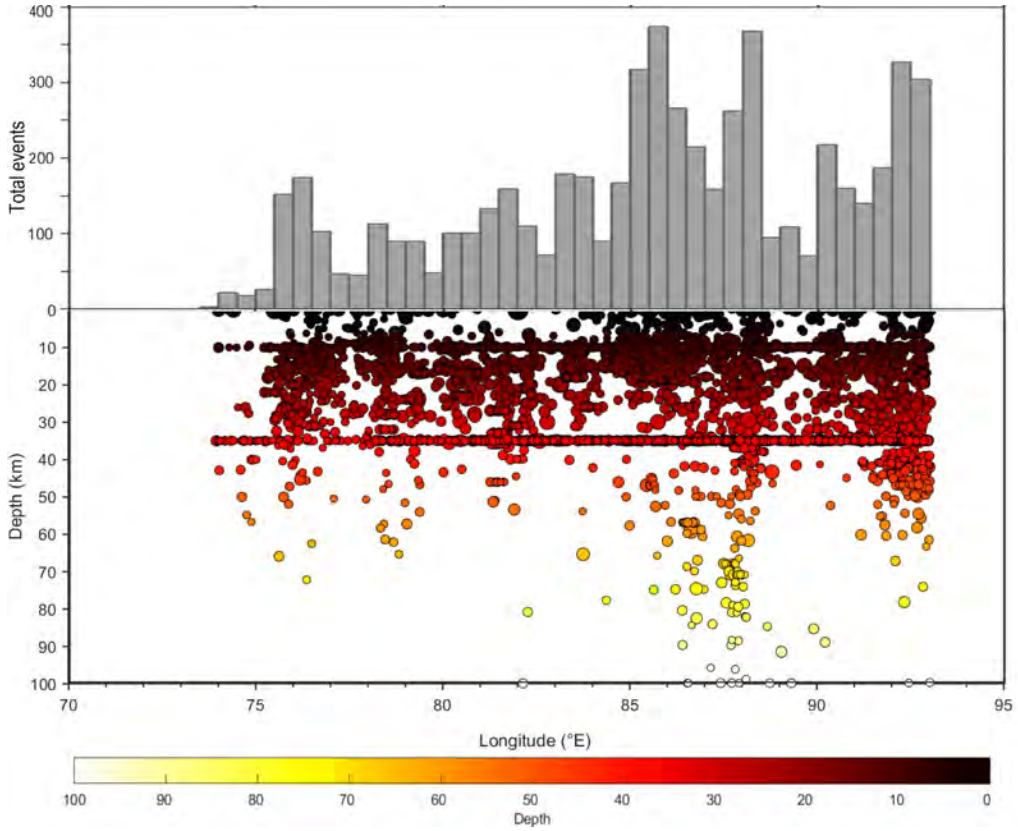

Figure 2.30: Cross-section view along longitude of the compiled earthquake catalog.

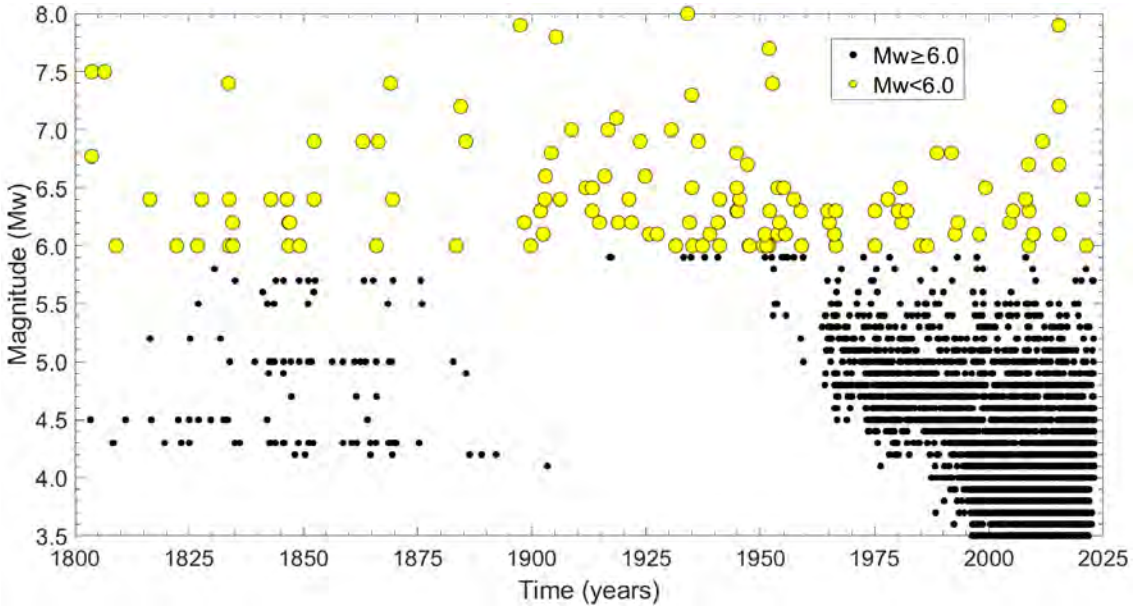

Figure 2.31: The magnitude-time graph of the compiled earthquake catalog.

of 85°E to 89°E. Notably, most of these events take place at depths ranging from 25 km to 35 km in the region. Additionally, a time-magnitude graph is provided for a visual representation of earthquake occurrences spanning from 1800 to 2022 (Figure 2.31). The graph illustrates a consistent reporting of earthquakes with magnitudes $M_w \geq 6.0$ throughout the entire period. On the other hand, earthquakes with magnitudes $M_w < 6.0$ are observed to be documented only during the early instrumental and modern instrumental periods.

The earthquake dataset assembled in this chapter will play a crucial role in computing seismic moment rate, a key parameter in the seismic moment budget estimation (Chapters 3 and 4). Additionally, it will aid in conducting probabilistic earthquake recurrence modeling and understanding the ongoing evolution of the earthquake cycle, particularly in relation to large events within the study region (Chapter 5).

2.4 Summary

In this chapter, a detailed overview of the study area and relevant dataset is provided. Particularly, (i) the seismotectonic setting of the study area encompassing Nepal and Kumaun Himalaya is discussed; then, (ii) a description of GPS and InSAR techniques and associated velocities is presented; subsequently, (iii) integration of GPS and InSAR velocities is performed to create a high-resolution integrated velocity field along the study region; and finally, (iv) a homogenized and complete earthquake dataset is prepared from several sources. The observed integrated velocities serve as a pivotal input in the following chapters (Chapters 3 and 4) for estimating strain rate distribution, seismic moment budget, and fault parameters. On the other hand, the compiled earthquake dataset will find direct application in carrying out seismic moment estimation, earthquake forecasting, and earthquake nowcasting in the study region (Chapters 3 to 5).

Chapter 3

Strain Distribution and Seismic Moment Budget along the Study Area

"Nature is relentless and unchangeable, and it is indifferent as to whether its hidden reasons and actions are understandable to man or not."

— Nate Silver

Understanding the characteristics of strain accumulation and its subsequent release through seismic events is of paramount importance due to its direct implication for seismic moment budget. In light of this, the present chapter provides the contemporary seismic moment budget in the Kumaun Himalaya and three spatial sections along the Nepal Himalaya using the state-of-the-art high-resolution integrated velocity field. For this, (i) the derived integrated velocity field and compiled earthquake data are re-considered from the previous chapter (Chapter 2); then, (ii) the three types of geodetic strains, namely dilatational, maximum shear, and rotational strains are calculated from a grid based method; subsequently, (iii) geodetic and seismic moment rates are computed using the estimated strain tensor and compiled earthquake data, respectively; finally, (iv) a section-wise seismic moment budget is estimated through a comparison between geodetic and seismic moment rates over the study region. By investigating the spatial variation in strain rates and associated seismic moment budgets, this chapter offers a contemporary seismic hazard scenario along the

study region.

Contents

Parts of this chapter have been published/submitted in the following refereed publications:

H. Verma, S. Pasari, Y. Sharma, K. E. Ching. "High-resolution velocity and strain rate fields in the Kumaun Himalaya: An implication for seismic moment budget". *Journal of Geodynamics* 160 (2024) 102023 (SCI).

H. Verma, Y. Sharma, K. E. Ching, S. Pasari. "Contemporary seismic moment budget along the Nepal Himalaya derived from high-resolution InSAR and GPS velocity field". *Acta Geophysica* (2024) (in print, SCIE).

3.1 Introduction

For ages, strain rate has found applications in measuring torque, developing strain gauge technology in aerospace engineering, structural health monitoring of railway and cable bridges, and power management in spinning devices, such as propellers, wheels, generators, and fans, as well as in analyzing Earth's deformation. Particularly, the strain in the upper crust of Earth is significant in geological processes, such as volcanic eruptions, earthquakes, and strain development in rocks [186].

Earth deformation is concerned with the changes in the shape of Earth. Therefore, the crustal deformation is strongly linked to geodetic measurements. Over the last few decades, the rising quantity and precision of geodetic observations like GPS and InSAR satellite data have provided measurable values of deformation and velocities [29, 175, 177]. Strain tensors can be used to mathematically represent geodynamic processes as a predictable consequence of geodetic networks. Tensors exist independently in any coordinate system and their characteristics are unaffected by the frame of reference [187]. As a result, tensor analysis reveals several desirable features of deformation, such as principal, dilatational, and maximum shear strain, with directions, which are crucial factors for analysis of seismic hazard [187]. These variables are best suited in describing the mechanism of a continuous deformation [188].

In active tectonic regions like Kumaun and Nepal Himalaya, understanding the dynamics of strain accumulation and its subsequent release through seismic events is crucial due to its direct relation with seismic activity. The vast amounts of energy that accumulate over centuries can be suddenly unleashed in the form of earthquakes, making it imperative to decipher the contemporary spatial distribution of seismic moment budgets across extensive geographic areas. Assessing the disparity between geodetic moment accumulation and seismic moment release is a key parameter in time-dependent seismic hazard analysis for identifying regions of heightened seismic potential. Such an approach has been extensively implemented in numerous active regions worldwide [10, 114, 186]. For example, Pancha et al. (2022) [186] computed the moment deficit in various sections of western America

by comparing geodetic and seismic moment rates in the area. Bungum et al. (2015) [114] conducted a seismic hazard analysis in the northwest and central Himalaya by comparing geodetic and seismic moment rates. Palano et al. (2018) [189] identified regions with high potential for future earthquakes using these rates for the Zagros Fold-and-Thrust collisional belt. Sharma et al. (2020) [10] assessed the spatial distribution of earthquake potential along the Himalayan arc, employing a similar comparable approach. Spara-cino et al. (2022) [190] utilized these rates to estimate the maximum magnitude in the Aegean-Anatolian region. To calculate the geodetic moment accumulation and seismic moment release rates in any region, strain tensors and earthquake data are primary inputs. Therefore, this chapter focuses on providing an in-depth analysis of the contemporary seismic moment budget by comparing geodetic and seismic moment rates along the Ku-maun Himalaya and three distinct sections over the Nepal Himalaya. The methodology involves calculating seismic moment rates and geodetic moment rates for each section and subsequently employing moment rate ratios and moment deficit rates to delineate the contemporary earthquake potential in these sections. The results have several end-user applications.

3.2 Strain rate distribution

Crustal deformation refers to the movement of the Earth's surface produced by tectonic forces that build up in the crust and generate earthquakes [191]. These processes are driven by the immense forces generated by the movement of tectonic plates at plate boundaries. The resulting strain accumulates over time until it exceeds the strength of the rocks, leading to sudden releases of energy in the form of earthquakes [191]. In several active regions of the world, seismicity rates are observed to be correlated to geodetic strain rates [192–194]. For example, Wesnousky and Scholz (1982) [195] observed a one order of magnitude variation between the calculated moment-release rate from Quaternary fault and seismicity data of 400 years in Japan. Therefore, analyzing strain distribution provides valuable insights into seismic hazard assessment and risk mitigation strategies from the devastating impacts of earthquakes.

3.2.1 Mathematical formulation

Strain tensors serve as mathematical descriptors, unraveling the complex movements within geodynamic systems, elucidating their intricate behaviors through geodetic frameworks. Their application allows the precise modeling of geological phenomena, revealing the anticipated outcomes of tectonic activities within established geodetic networks. Within these tensors lie the encoded patterns of deformation, enabling us to forecast and understand the consequential dynamics inherent in geodetic observations. Below a comprehensive expression delineating the essence of strain rate distribution calculations is provided.

The displacement vector $u_i(x)$ at any arbitrary point x with respect to the origin x_0 can be expanded using the Taylor series [196]:

$$u_i(x) = u_i(x_0) + \frac{1}{2}\left(\frac{\partial u_i}{\partial x_j} + \frac{\partial u_j}{\partial x_i}\right) dx_i + \frac{1}{2}\left(\frac{\partial u_i}{\partial x_j} - \frac{\partial u_j}{\partial x_i}\right) dx_j \quad i = 1,2,3 \tag{3.2.1}$$

Here, $u_i(x_0)$ represents a rigid body translation and the subsequent partial derivatives represent the relative displacement in terms of the gradient of displacement. The symmetric part of the displacement gradient tensor is defined as an infinitesimal small strain tensor in the following manner:

$$\varepsilon_{ij} = \frac{1}{2}\left(\frac{\partial u_i}{\partial x_j} + \frac{\partial u_j}{\partial x_i}\right) \tag{3.2.2}$$

The anti-symmetric component of the displacement gradient tensor can be described as equivalent to a rigid body rotation, denoted by:

$$\omega_{ij} = \frac{1}{2}\left(\frac{\partial u_i}{\partial x_j} - \frac{\partial u_j}{\partial x_i}\right) \tag{3.2.3}$$

Thus, the surface displacement has three major components: rigid body translation $(u_i(x_0))$, strain (ε_{ij}), and rigid body rotation (ω_{ij}). Further, a 2D strain rate field can be

formed from Equation 3.2.1 as

$$\dot{\varepsilon}_{1,2} = \frac{\dot{\varepsilon}_{ee} + \dot{\varepsilon}_{nn}}{2} \pm \sqrt{\frac{1}{4}(\dot{\varepsilon}_{ee} + \dot{\varepsilon}_{nn})^2 + \dot{\varepsilon}_{en}^2}\,, \tag{3.2.4}$$

$$\theta = \frac{1}{2} tan^{-1}\left(\frac{2\dot{\varepsilon}_{en}}{\dot{\varepsilon}_{ee} - \dot{\varepsilon}_{nn}}\right), \tag{3.2.5}$$

$$\dot{\varepsilon} = \sqrt{\dot{\varepsilon}_{ee}^2 + \dot{\varepsilon}_{nn}^2 + 2\dot{\varepsilon}_{en}^2} \tag{3.2.6}$$

where, $\dot{\varepsilon}_1$ and $\dot{\varepsilon}_2$ are the principal axes of strain; $\dot{\varepsilon}_{ee} = \frac{\partial v_e}{\partial x_e}$, $\dot{\varepsilon}_{nn} = \frac{\partial v_n}{\partial x_n}$, $\dot{\varepsilon}_{en} = \frac{1}{2}\left(\frac{\partial v_e}{\partial x_e} + \frac{\partial v_n}{\partial x_n}\right)$; and v_e and v_n are the east and north velocity components, respectively [197]. On the right-hand side of Equation 3.2.4, the initial term signifies the dilatation strain rate, while the subsequent term denotes the maximum shear strain rate. Equation 3.2.5 introduces the directional principal strain rate, denoted as θ, and Equation 3.2.6 quantifies the second invariant strain rate, expressed as $\dot{\varepsilon}$.

Various approaches are available to estimate strain rates by solving the velocity gradient tensor, including the grid method, subnetwork method, and the Delaunay triangulation technique, as documented in studies such as [196, 198–201]. To estimate the strain field in the Kumaun and Nepal Himalaya, both regions are divided into homogeneous grids ($0.15^\circ \times 0.15^\circ$ for Kumaun Himalaya and $0.25^\circ \times 0.25^\circ$ for Nepal Himalaya) and the associated integrated velocities are utilized to estimate the 2-D velocity gradient tensor, which essentially depicts strain rate [196].

$$W_j = exp\left(\frac{-d_j^2}{2D^2}\right). \tag{3.2.7}$$

In the above expression, W_j represents the weighting factor; d_j represents the distance between the node point and the j^{th} velocity point, and D represents the distance of the 4^{th} nearest velocity location to the estimated location. The parameter D regulates the smoothness of the geodetic strain rate calculation. In the current study, the smoothness radius D is assumed to be 30 km and 50 km for Kumaun and Nepal Himalaya, respectively

based on the resolution of integrated velocity field. This value of D also results in the maximum strain rate change in the Kumaun and Nepal Himalaya [196].

3.2.2 Strain rate field over the Kumaun Himalaya

In this section, the strain rate distribution such as, dilatational strain rate, maximum shear strain rate and rotational rate over the Kumaun Himalaya is derived using the high resolution integrated velocity field obtained in Section 2.3.3.2. A high-resolution velocity field delivers more information at each position of the study area than a standalone GPS velocity field.

3.2.2.1 Dilatational strain rate

The dilatation strain rate, a fundamental invariant of the strain rate tensor, is independent of coordinate reference frames. This parameter is characterized by the sum of the eigenvalues of the strain rate tensor. Notably, the dilatation strain rate plays a crucial role in distinguishing between deformations associated with reverse or thrust faults and corresponding to normal faults [201]. Figure 3.1 depicts dilatation strain rate pattern along the Kumaun Himalaya region, the negative values indicate compression and positive values represent extension. It is observed that the compressional strain rates are dominant than the extensional strain rates, probably due to the presence of the recognized thrust faults. A large region of tectonic compression with a mean of -0.08μstrain/yr is observed, implying that the entire Kumaun Himalaya is experiencing contraction as a result of convergence between Indian and Eurasian plates. The dilatational strain rate is higher along the MCT in the Kumaun Himalaya, which corresponds to the seismicity pattern along the region. Previously, Ponraj et al. (2010) [85], Jade et al. (2014) [119], and Dumka et al. (2014) [121] also observed a high strain rate along the MCT in Kumaun, confirming the consistency in strain estimation. The tectonic compression in Kumaun region is an indication of large strain accumulation in the region. Additionally, the dilatational strain rate observed in the Kumaun Himalaya around the MFT and MFT exhibits a relatively lower value, probably attributed to the locking behavior evident in these faults.

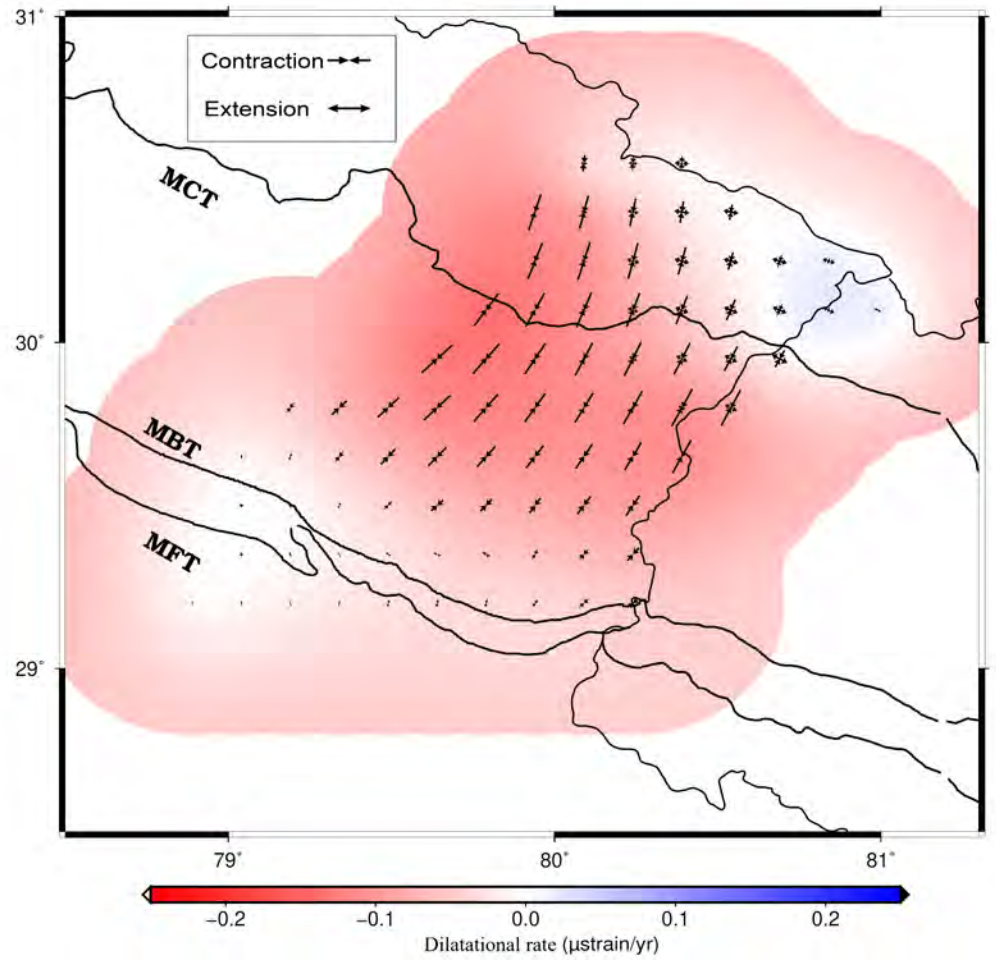

Figure 3.1: Dilatational strain rate (principal axes of the strain rates) estimated along the Kumaun Himalaya. Abbreviations are as: MFT, Main Frontal Thrust; MBT, Main Boundary Thrust; MCT, Main Central Thrust.

3.2.2.2 Maximum shear strain rate

The maximum shear strain rates provide insights into the deformation resulting from strike-slip faulting, with elevated values signifying localized shear deformation. These rates are derived by linearly combining the maximum and minimum eigenvalues [201].

The deformation pattern of maximum shear strain, as illustrated in Figure 3.2, exhibits relatively higher deformation along the MCT. In contrast, the regions along the MBT and MFT exhibit relatively lower maximum shear strain deformation, which is also observed in the dilatational rate map. The calculated maximum shear strain rate for the Kumaun Himalaya is approximately 250 nstrain/yr. To establish a relation between the maximum

shear strains with the seismological data, the earthquake dataset obtained in Figure 2.27 and the maximum shear strain rate in Figure 3.2 are compared, which shows high seismicity with higher maximum shear strain rates. The diminished strain rates and infrequent seismic activity observed in the vicinity of MFT and MBT suggest that internal deformation within this area is minimal. Additionally, it's important to note that seismic activity can trigger accumulated strain at the down-dip edge of the fault system [181], resulting in a seismic belt in the higher reaches of the frontal thrust [202].

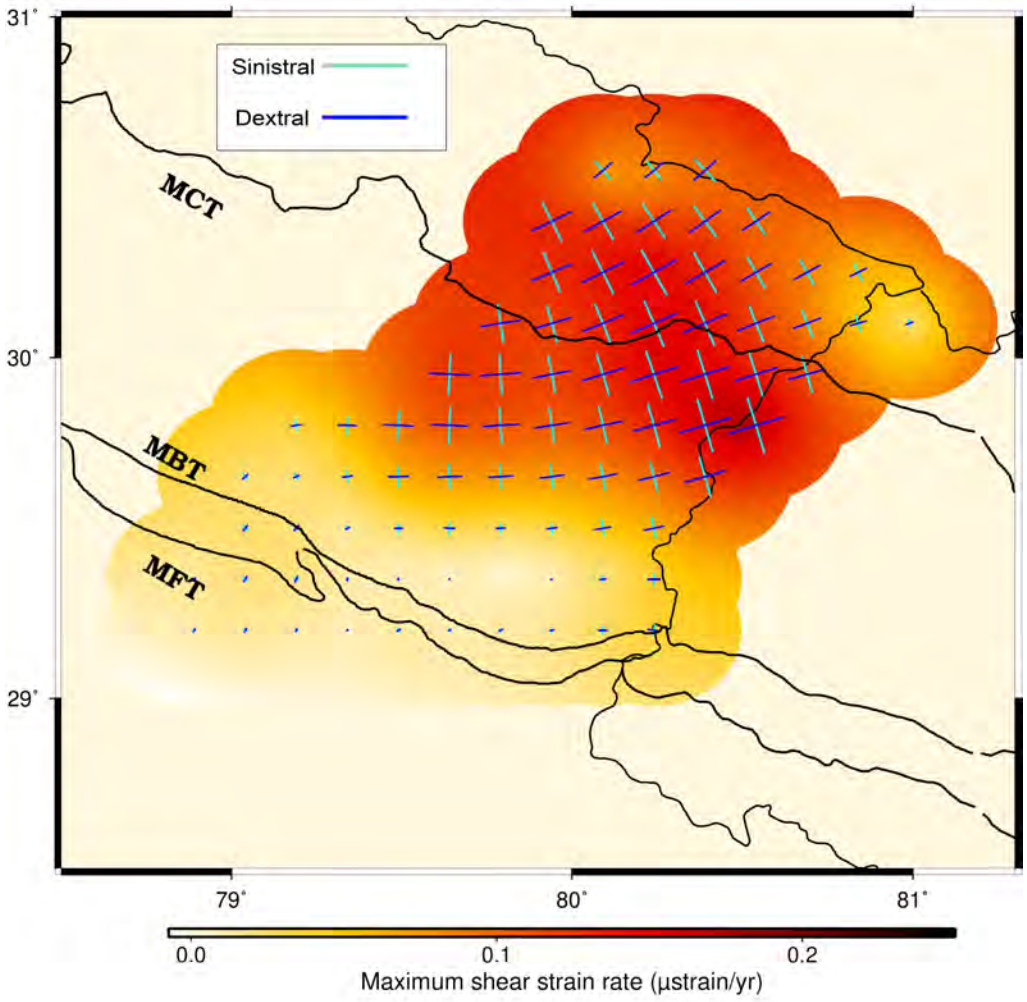

Figure 3.2: Maximum shear strain rate estimated along the Kumaun Himalaya. Abbreviations align with the Figure 3.1.

3.2.2.3 Rotational rate

The rotation rate is an expression of the antisymmetric component of the velocity gradient tensor (Equation 3.2.1). There are three proposed explanations for the cause of rotational strain: (i) the non-uniform distribution of gravitational potential energy, (ii) variations in heat flux within the lithosphere, and (iii) interactions at plate boundaries and their associated configurations [203–205]. Among these hypotheses, the third one, which pertains to plate boundary interactions, aligns with the tectonic setting of the Himalayan arc. In this context, the Arabian plate and the Hindu Kush Pamir range to the northwest induce counterclockwise rotation, while the Sunda block in the northeast leads to a clockwise rotation of the Himalayan arc [144, 206].

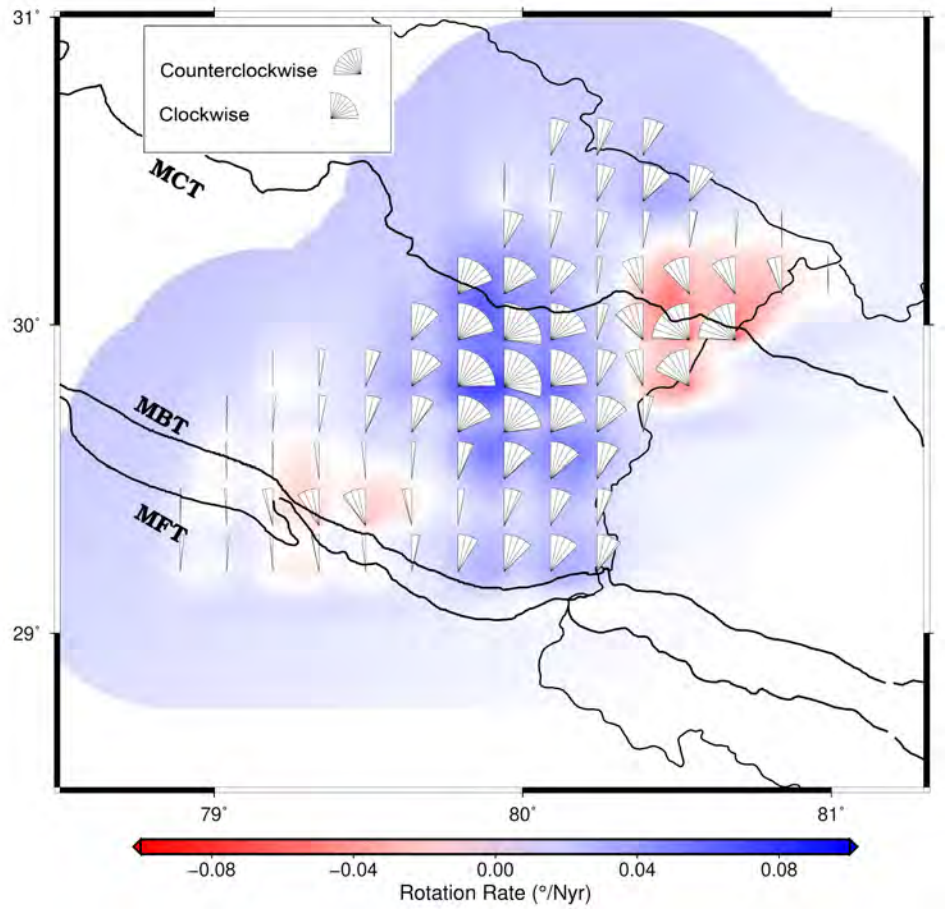

Figure 3.3: Rotational rate estimated along the Kumaun Himalaya. Abbreviations align with the Figure 3.1.

The rotational deformation pattern along the Kumaun Himalaya is shown in Figure 3.3. By inspecting the deformation pattern, it is noticed that the rotational rates are relatively high in the region between MCT and MBT. A large fraction of clockwise rotation is captured in this region. The rotation pattern changes from clockwise to anti-clockwise in northeast and southwest region of the Kumaun Himalaya.

3.2.3 Strain rate field over the Nepal Himalaya

In this section, the strain rate distribution, such as dilatational strain rate, maximum shear strain rate, and rotational rate over the Nepal Himalaya is derived using the high resolution integrated velocity field obtained in the Section 2.3.3.3.

3.2.3.1 Dilatational strain rate

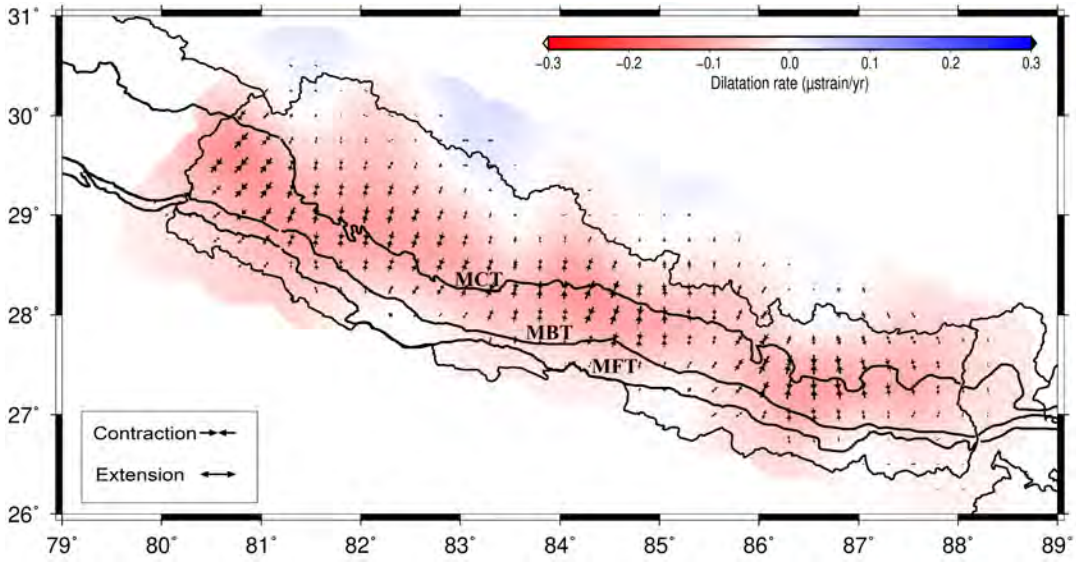

Figure 3.4: Dilatational strain rate (principal axes of the strain rates) estimated along the Nepal Himalaya. Abbreviations align with the Figure 3.1.

The principal strain rate along the Nepal Himalaya (Figure 3.4) demonstrates a large region of tectonic compression with a mean of -0.07μstrain/yr, implying that the entire Nepal Himalaya is experiencing contraction. Similar observation is also noted by Ansari (2018) [207] and Sharma et al. (2020) [10] using GPS data. From Figure 3.4, it is observed that the dilatational rates are relatively higher along the MCT, which is also observed

in Kumaun Himalaya region. The obtained higher strain rate along the MCT signifies substantial stress buildup in the vicinity of the fault. In the northern part of the area i.e., in the Tibet region, extensional deformation is observed. Moreover, the observed dilatational rate in the Nepal Himalaya surrounding the MFT and MBT displays a comparatively lower deformation, likely due to the locking behavior evident within these faults.

3.2.3.2 Maximum shear strain rate

The maximum shear strain rate over the Nepal Himalaya is represented in Figure 3.5. The maximum shear strain rate is relatively higher along the MCT. The calculated maximum shear strain rate for the study area is approximately 225 nstrain/yr, which indicates the presence of strike-slip deformation in the region. A clear patch of higher deformation in eastern part along the MCT is observed. Similar to the dilatational rate in the Nepal Himalaya, a relatively lower deformation is observed in the vicinity of MFT and MBT. Moreover, to establish a correlation between the maximum shear strain rate and seismological data along the Nepal Himalaya, a comparison is made between the seismic catalog obtained in Figure 2.27 and the maximum shear strain rate in Figure 3.5. This comparison reveals heightened seismic activity corresponding to higher maximum shear strain rates.

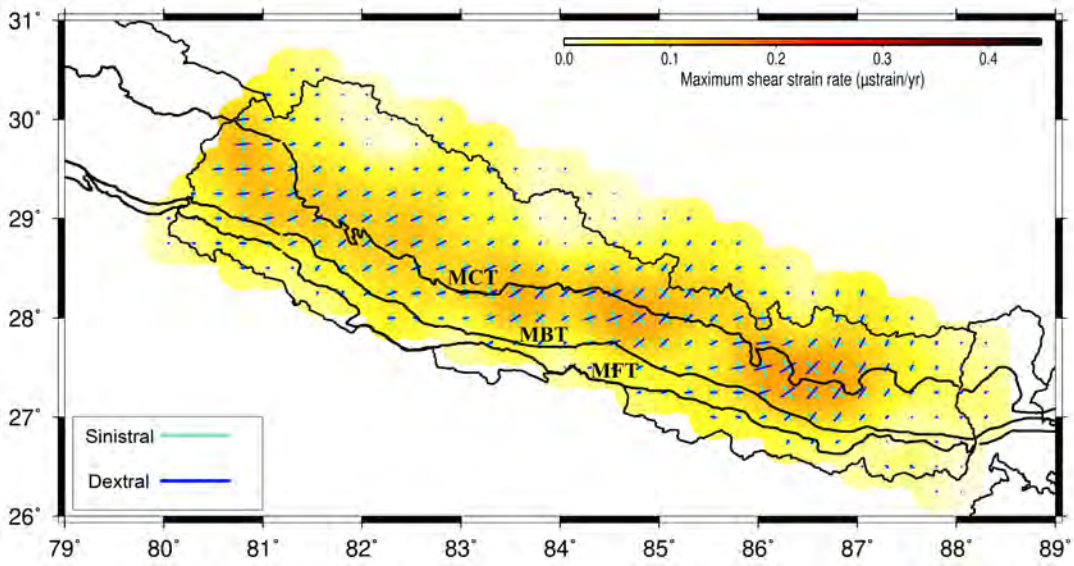

Figure 3.5: Maximum shear strain rate estimated along the Nepal Himalaya. Abbreviations align with the Figure 3.1.

3.2.3.3 Rotational rate

The rotational deformation pattern along the Nepal Himalaya is shown in Figure 3.6. By inspecting the deformation pattern, it is observed that the rotational rates in the southern section are dominant by clockwise direction, whereas in the northern section of the Nepal the dominance of anti-clockwise deformation is present. A clear patch of large fraction of clockwise rotation is observed in the northwest region of Nepal. The rotation pattern changes from clockwise to anti-clockwise from north to south along the MCT inthe Nepal Himalaya.

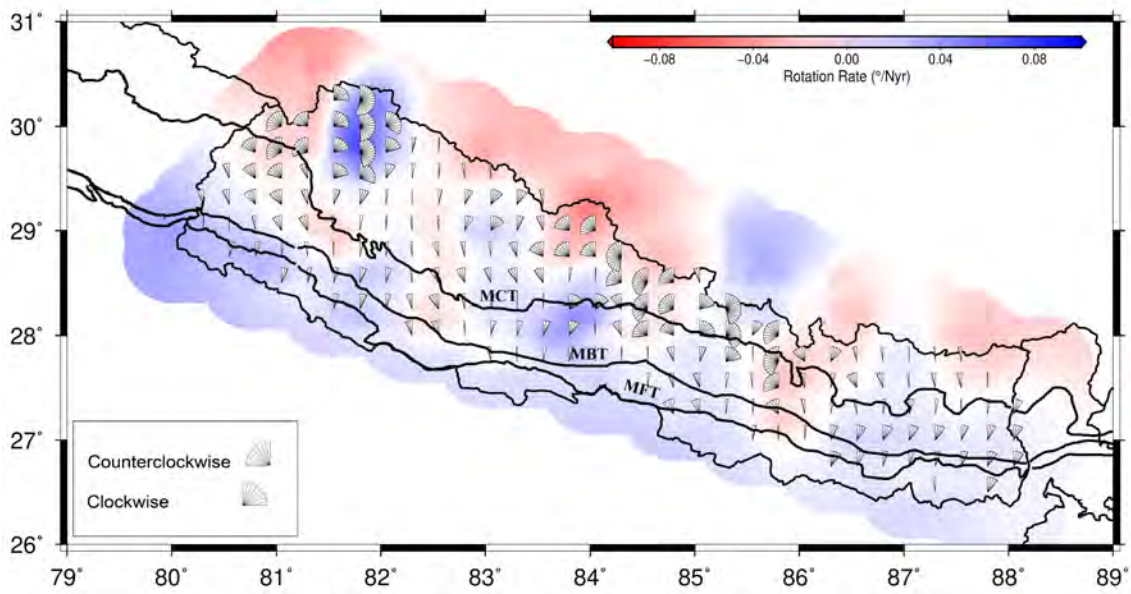

Figure 3.6: Rotational rate estimated along the Nepal Himalaya. Abbreviations align with the Figure 3.1.

The derived strain rate distribution across the Kumaun and Nepal Himalaya reveals the following notable observations:

1. Strain rate (dilatational rate and maximum shear strain rate) is not homogeneous over the Kumaun and Nepal Himalaya.

2. A relatively higher strain rate is observed along the MCT in the study region. In contrast, minimal strain rate is observed along the MBT and MFT.

3. The minimal deformation observed along the MBT and MFT signifies the locking behavior of these faults.

4. The obtained strain rate deformation in the Kumaun and Nepal Himalaya agrees with seismic pattern in these regions.

In the following sections of this chapter, the estimated strain rate along the Kumaun and Nepal Himalaya is utilized to derive geodetic moment rate. Subsequently, the obtained geodetic moment rate is compared with the seismic moment rate to obtain the seismic moment budget in the Kumaun and Nepal Himalaya.

3.3 Methodology for computing seismic moment budget

In order to determine the seismic moment budget along the study region, the geodetic moment rate (GeMR) and seismic moment rate (SeMR) are calculated and subsequently compared. The calculated strain rates serve as the foundation for determining GeMR, whereas the compiled earthquake data in Chapter 2 enables to calculate SeMR in the region. The computation steps of geodetic moment rate, seismic moment rate, and seismic moment budget potential are explained in the following subsections. Furthermore, a comparison of geodetic signals to seismic signals is also emphasized.

3.3.1 Comparison of geodetic deformation signals and seismic deformation signals

As the methodology involves comparing the geodetic moment rate with the seismic moment rate in a region, establishing a correlation between the geodetic and seismic deformation signals becomes essential. Therefore, initially, to establish a connection between geodesy-based signals (i.e., derived integrated velocity field in Figure 2.19 and Figure 2.23) and seismic signals (i.e., compiled earthquake data in Figure 3.7), an examination of crustal strain patterns and focal solutions is conducted. Focal solutions of earthquakes are recognized for their capacity to depict the prevailing tectonic stress configuration at the time of fault rupture, while GPS-derived strain signals offer insights

into the style of interseismic energy accumulation [208]. For this purpose, focal solutions since 1976 are sourced from the GCMT https://www.globalcmt.org/). Figure 3.7 presents the focal mechanism solutions of earthquakes along the Kumaun and Nepal Himalaya since 1976.

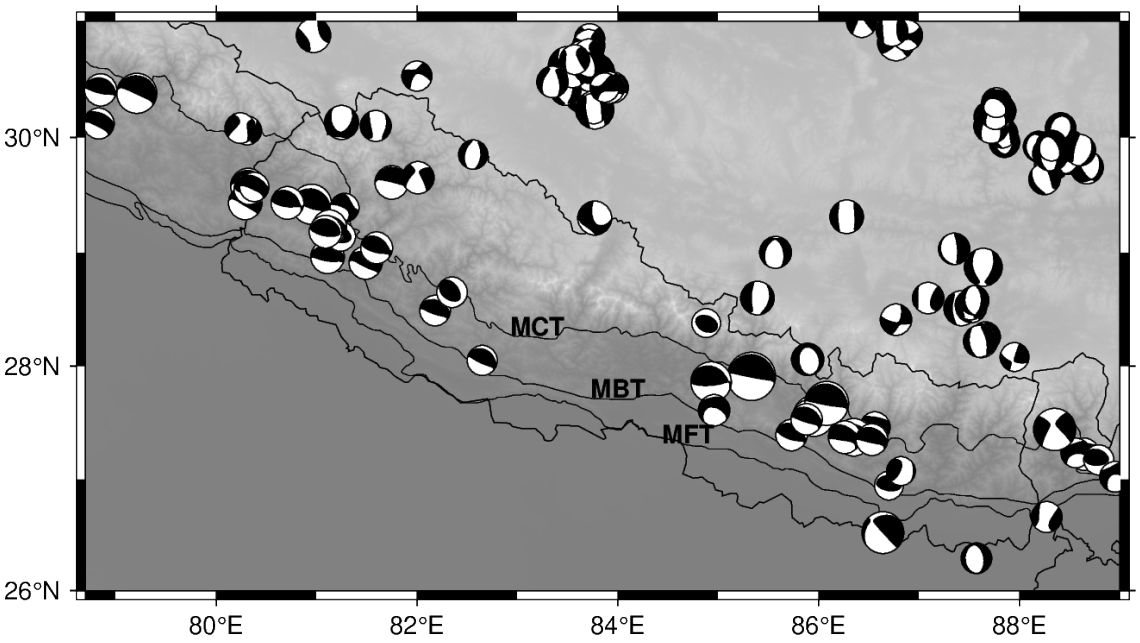

Figure 3.7: Focal mechanism solution of Kumaun and Nepal Himalaya's earthquakes since 1976. Abbreviations align with the Figure 3.1.

From Figure 3.1, Figure 3.4, and Figure 3.7, it is observed that along both the regions, Kumaun and Nepal Himalaya, a dominant compression mechanism (i.e., thrust faulting) is evident. This is due to the presence of major thrust fault such as, MFT, MBT, and MCT in the study area. In addition, the heightened seismic activity corresponds to higher maximum shear strain rates along the Kumaun and Nepal Himalaya. As a result, based on the above discussion, it is reasonable to conduct a comparison between geodetic moment rate and seismic moment rate to evaluate the seismic moment budget along the study area. Various studies in active tectonic regions have already employed the methodology of comparing geodetic and seismic moment rates for calculating the seismic moment budget, where a correlation exists between geodetic and seismic deformation signals [10–12, 73, 114, 201, 209].

3.3.2 Geodetic moment rate estimation

The derived strain rates form the fundamental framework for the computation of the geodetic moment rate. Using the strain rate tensors, the GeMR is determined through the expression provided by Savage and Simpson (1997) [210]:

$$\dot{M_0^g} = 2\mu H_t A_t Max(|\dot{\eta}_1|, |\dot{\eta}_2|, |\dot{\eta}_1 + \dot{\eta}_2|). \tag{3.3.1}$$

Here, $\dot{M_0^g}$ denotes the GeMR; $\mu = 3 \times 10^{10} N/m^2$ denotes the elastic layer's shear modulus; H_t denotes the seismogenic thickness; A_t denotes the area of the source section, and the maximum and minimum principal strain rates are denoted by $\dot{\eta}_1$ and $\dot{\eta}_2$, respectively. Particularly, for the seismogenic depth, previous studies [5, 12, 73, 114, 211, 212] have suggested that the Himalaya's seismic depth ranges from 20 km to 35 km. However, as the depth-wise distribution of events indicates that around 85% of all seismic events, including all major to great earthquakes, occur up to a depth of 25 km as shown in Figures 2.27, 2.30 and 3.8, the current study assumes 25 km as the base seismogenic depth. Nevertheless, a later part of this chapter has focused on the sensitivity testing of the input parameters.

3.3.3 Seismic moment rate estimation

To calculate the seismic moment release associated with each event, the following relationship is used [213]:

$$M_0 = 10^{(1.5M_w + 9.1)}. \tag{3.3.2}$$

Here, M_0 denotes the seismic moment and M_w denotes the moment magnitude of each earthquake. The calculated total seismic moments are then transformed into SeMR ($\dot{M_0^s}$) by dividing the catalog length. To estimate the seismic moment rate along the Kumaun and Nepal Himalaya, the earthquake dataset obtained in Chapter 2 is utilized.

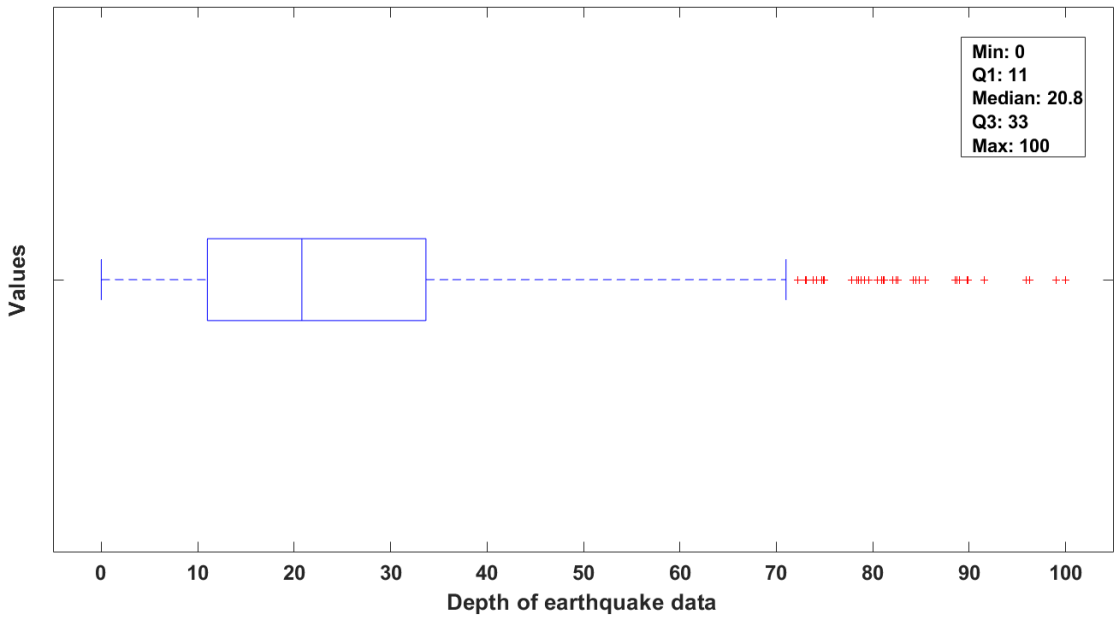

Figure 3.8: Boxplot illustrating the five number summary for earthquake depths.

3.3.4 Seismic moment budget estimation

After obtaining GeMR and SeMR, seismic moment budget, $\dot{M}_0 = \dot{M}_0^g - \dot{M}_0^s$, is calculated based on the assumption that the whole moment deficit rate within the section will be released by one or more earthquakes [10, 114, 186, 201, 214, 215]. The ratio of GeMR to SeMR enables an overview of the seismic moment budget estimation, whereas the difference between GeMR and SeMR provides the moment deficit rate and its equivalent earthquake potential. The moment rate ratio is calculated using the expression:

$$\text{Moment rate ratio} = \frac{\dot{M}_0^g}{\dot{M}_0^s} = R \ \ \text{(say)}. \tag{3.3.3}$$

Here, the value of R (i.e., moment rate ratio) offers an insight into the seismic moment budget across three distinct scenarios:

1. If $R > 1$, it signifies that the geodetic moment rate (energy accumulation) surpasses the seismic moment rate (energy release). This implies that the total moment deficit rate can be linked to future earthquakes, and it helps to determine the seismic activity needed to eliminate the disparity between the geodetic and seismic moment rates,

thereby achieving a moment rate ratio of unity.

2. If $R = 1$, it suggests that the geodetic moment rate matches the seismic moment rate, signifying that the accumulated energy is balanced by the background seismicity.

3. If $R < 1$, in this scenario, the seismic moment rate surpasses the geodetic moment rate, indicating that the accumulated strain energy has been entirely released, and the region is accumulating seismic energy during the interseismic period.

The moment deficit rate ($\dot{M}_0$) is determined by the difference between the SeMR and GeMR, calculated as:

$$\dot{M}_0 = \dot{M}_0^g - \dot{M}_0^s \tag{3.3.4}$$

3.4 Contemporary seismic moment budget along the Kumaun Himalaya

In order to calculate the contemporary seismic moment budget along the Kumaun Himalaya, the following settings are considered: (1) the seismogenic depth is assumed to be 25 km (as described in Section 3.3.2); (2) the length of the recalculated earthquake database is taken to be around 200 years (i.e.,1800–2022) as the time span of obtained catalog in Section 2.3.4 is only 200 years particularly in the Kumaun Himalaya region, and (3) no contribution from aseismic deformation is considered due to the lack of sufficient evidence of aseismic activity in the Himalayan region (e.g., Lindsey et al. 2018 [11]; Bilham et al. 1997 [16]; Bird and Kagan 2004 [216]; Li et al. 2018 [115]; Sreejith et al. 2018 [108]). Nevertheless, a later part of this section has focused on the sensitivity testing of these input parameters.

The estimated GeMR over the Kumaun Himalaya is $7.94 \pm 0.1 \times 10^{18}$ Nm/yr, whereas the SeMR is 0.35×10^{18} Nm/yr. The ratio of GeMR to SeMR in the Kumaun Himalaya is 22.87, indicating that GeMR is significantly higher than the SeMR in the region. The difference of GeMR and SeMR in the region corresponds to a moment deficit rate as high

as $7.59 \pm 0.1 \times 10^{18}$ Nm/yr in the study region. The observed moment deficit rate suggests an earthquake potential of M_w 8.1 in the Kumaun Himalaya region.

As the present study re-estimates the strain-rate field and associated earthquake potential along the Kumaun Himalaya, a comparison of the outcomes to previous studies is essential to validate the results. Similar to the present findings, Bilham (1997) [16] also suggested that bothe the western part of Nepal and the Kumaun Himalaya have the potential to cause a great earthquake ($M_w > 8$) as neither the Kumaun Himalaya nor the western Nepal has ruptured in the previous 350 years. Ponraj et al. (2010, 2019) [85, 89] utilized 16 GPS velocities and found that the moment deficit rate $8.4 \pm 1.0 \times 10^{18}$ Nm/yr of the MHT beneath the Kumaun Himalaya is high. Using 56 GPS sites over the northwest Himalaya, Jade et al. (2014) [119] suggested that just south of the MCT, the Garhwal-Kumaun Himalaya region has a high accumulation of strain. Similarly, Dumka et al. (2014) [122] estimated the higher strain rate along the MCT and the Higher Himalaya. Kannaujiya et al. (2022) [99] used 18 GPS velocities to estimate crustal strain buildup over the Kumaun-Garhwal. They observed that the northwest Himalaya could produce at least one $M_w \sim 8.0$ earthquake. Therefore, as a whole, the present analysis based on the integrated velocity information not only overcomes the limitation of low spatial coverage but also enables the most-updated earthquake potential estimation in the Kumaun Himalaya. The findings strongly suggest that the Kumaun Himalaya can produce large to great earthquake(s) and can be catastrophic for the human population.

3.4.1 Sensitivity analysis

As the above estimates of seismic moment budget and associated earthquake potential depend on several input parameters, a sensitivity analysis is essential to understand the variation of estimates. For this, seismogenic depth as 20 km, 25 km, 30 km, and 35 km, lower and upper limit of GeMR (due to uncertainty in velocity estimation), and earthquake database of 50 years, 100 years, and 200 years are considered. It is found that the seismic moment budget ranges from M_w 8.0 to M_w 8.2 as the seismogenic depth ranges from 20 km to 35 km (Table 3.1). The seismic moment budget remains unchanged for the lower

and upper limits of GeMR (Table 3.2). Furthermore, the seismic moment budget varies from M_w 7.7 to M_w 8.1 as the catalog length varies from 50 to 200 years (Table 3.3).

Table 3.1: Comparison of SeMR and GeMR over the Kumaun Himalaya at various seismogenic depths and 200 years of earthquake database length

Depth (km)	$\dot{M}_0^g$ (10^{18} Nm/yr)	$\dot{M}_0^s$ (10^{18} Nm/yr)	$\frac{\dot{M}_0^g}{\dot{M}_0^s}$	$\dot{M}_0$ (10^{18} Nm)	Earthquake potential (M_w)
20	6.34±0.09	0.33	19.16	6.01	8.0
25	7.94±0.10	0.35	22.87	7.59	8.1
30	9.51±0.12	0.36	26.64	9.16	8.1
35	11.10±0.15	0.36	30.84	10.74	8.2

Table 3.2: Comparison of SeMR and GeMR using the lower and upper limit of geodetic moment rates corresponding to 25 km seismic depth and 200 years of earthquake database length

Limit	$\dot{M}_0^g$ (10^{18} Nm/yr)	$\dot{M}_0^s$ (10^{18} Nm/yr)	$\frac{\dot{M}_0^g}{\dot{M}_0^s}$	$\dot{M}_0$ (10^{18} Nm)	Earthquake potential (M_w)
Lower	7.93	0.35	22.85	7.58	8.1
Upper	7.95	0.35	22.90	7.60	8.1

Table 3.3: Comparison of SeMR and GeMR corresponding to 25 km seismic depth and varying seismic catalog length

Catalog Length	$\dot{M}_0^g$ (10^{18} Nm/yr)	$\dot{M}_0^s$ (10^{18} Nm/yr)	$\frac{\dot{M}_0^g}{\dot{M}_0^s}$	$\dot{M}_0$ (10^{18} Nm)	Earthquake potential (M_w)
50	7.94±0.10	0.08	89.70	7.85	7.7
100	7.94±0.10	0.52	15.15	7.41	7.9
200	7.94±0.10	0.35	22.87	7.59	8.1

3.5 Contemporary seismic moment budget along the Nepal Himalaya

It is a well-known fact that earthquakes periodically release elastic strain energy accumulated throughout the interseismic interval, though this released amount may not be homogeneous over the entire area. Particularly in Nepal, the seismicity pattern exhibits spatial variation, indicating more frequent seismic activity in eastern Nepal compared to the western and central regions (Figures 2.27 and 2.30). In fact, the western Nepal belongs to the "central seismic gap", bounded by the epicentral locations of the 1905 Kangra earthquake and the 1934 Bihar-Nepal earthquake [96, 97]. In addition, the majority of earthquakes in the study region occur along a decollement MHT beneath the Himalaya. Similarly, the convergence rate inferred from geodetic measurements varies spatially, with more convergence rate in the western Nepal than that of central and eastern Nepal [11, 12]. Due to the heterogeneity in moment accumulation and moment release in the Nepal Himalaya, there have been spatial variations in the estimated moment deficit rate and associated magnitude potential across this region [5, 7, 10, 12, 73, 108, 114]. As a result, spatial distribution of earthquake potential is essential to better characterize the contemporary seismic hazard along the Nepal Himalaya. Therefore, a segmentation-based strategy (e.g., Pancha et al. 2006 [186]; Sharma et al. 2020 [10]) is considered to determine the spatial variation of seismic hazard throughout the Nepal Himalaya. For this, the Nepal Himalaya is divided into three continuous sections (from west to east) based on the following criteria (Figure 3.9): (i) each section should contain at least 15 earthquakes of $M_w \geq 4.0$; (ii) any large earthquake's rupture region should be contained inside a single section, and (iii) each section should contain homogeneous velocity/strain rate [5, 7, 114, 201, 217–219]. For brevity, these three sections may termed as: western Nepal Himalaya (section 1 in Figure 3.9), central Nepal Himalaya (section 2 in Figure 3.9), and eastern Nepal Himalaya (section 3 in Figure 3.9).

After dividing the Nepal Himalaya into various sections, the contemporary seismic

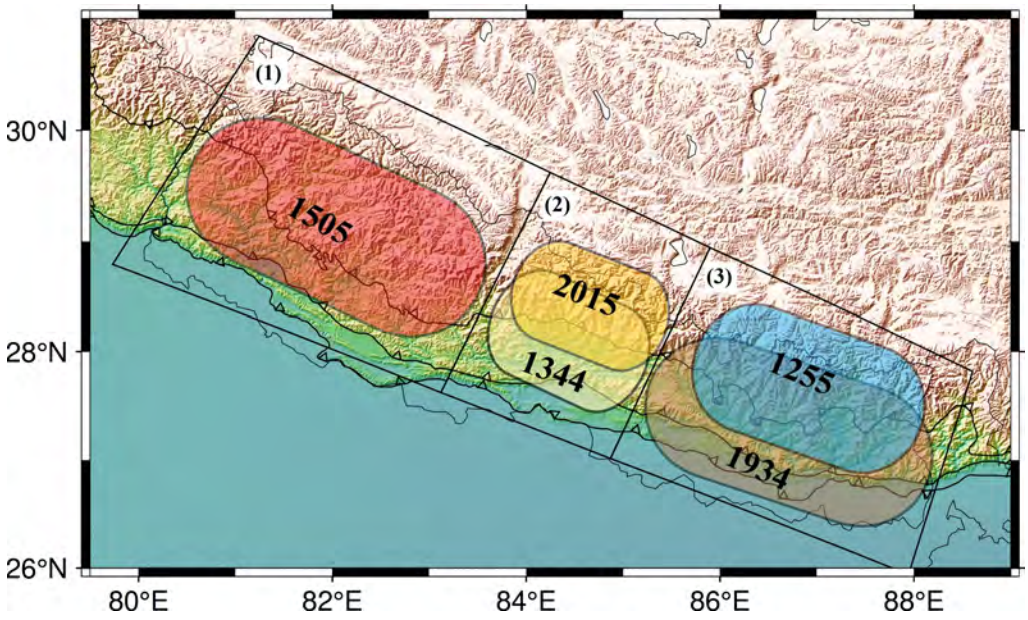

Figure 3.9: Distribution of various sections along the Nepal Himalaya with historical earthquake rupture zones (Zhang et al. 2016 [152]; Dal Zilio et al. 2019 [220]; Bilham and Szeliga 2008 [221]).

moment budget along the Nepal Himalaya is calculated, by considering the following settings: (i) the seismogenic depth is assumed to be 25 km (as described in Section 3.3.2); (ii) the length of the recalculated earthquake database is taken to be around 500 years (1500–2021), and (iii) similar to Kumaun Himalaya, there is no contribution from aseismic deformation. Similar to the analysis in the Kumaun Himalaya, a later part of this section has focused on the sensitivity testing of these input parameters including the upper and lower limits of the seismic moment budget for each section. This variation is achieved by varying the seismogenic depth (from 20 km to 35 km) and the duration of the considered catalog (e.g., 200 years, 500 years and 900 years). Afterward, GeMR and SeMR calculations are performed for each of the three sections (Table 3.4).

The geodetic moment rate from west to east across three sections ranges from 17.16×10^{18} Nm/yr to 16.74×10^{18} Nm/yr, with the minimum of 8.43×10^{18} Nm/yr in central Nepal Himalaya, whereas the seismic moment rate varies between 5.02×10^{18} Nm/yr to 11.41×10^{18} Nm/yr, with the minimum of 3.69×10^{18} Nm/yr in central Nepal Himalaya. The ratio of GeMR to SeMR in the Nepal Himalaya varies from 1.47 to 3.42, indicating a

Table 3.4: Comparison of SeMR and GeMR for various sections corresponding to 25 km seismic depth and 500 years of earthquake database length

Section	$\dot{M}_0^g$ (10^{18} Nm/yr)	$\dot{M}_0^s$ (10^{18} Nm/yr)	$\frac{\dot{M}_0^g}{\dot{M}_0^s}$	M_0 (10^{18} Nm)	Earthquake potential (M_w)
1	17.16±0.13	5.02	3.42	12.13	8.5
2	8.43±0.10	3.69	2.29	4.74	7.9
3	16.74±0.22	11.41	1.47	5.33	8.1

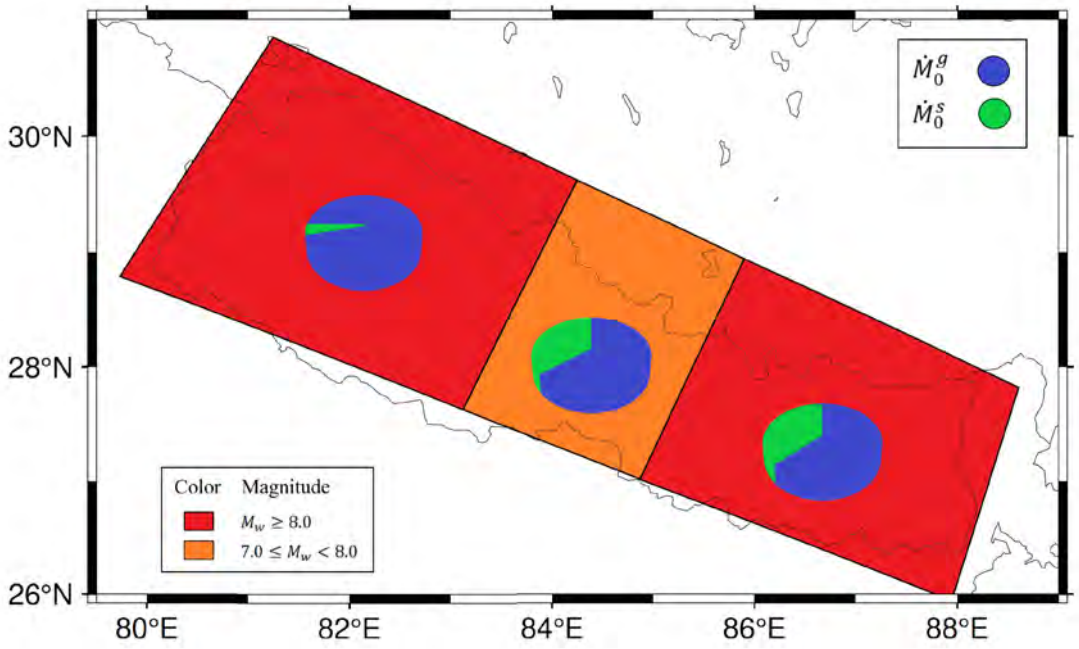

Figure 3.10: Seismic moment budget throughout the Nepal Himalaya. Pie chart represents the ratio of geodetic and seismic moment rate.

reasonable correlation between the moment accumulation and moment release along each section of Nepal Himalaya. Consequently, the moment deficit rate ($\dot{M}_0$) is estimated by deducting SeMR from GeMR along three sections of the Nepal Himalaya (Table 3.4). The moment deficit rates in central Nepal Himalaya and eastern Nepal Himalaya are equivalent to 4.74×10^{18} Nm/yr and 5.33×10^{18} Nm/yr, respectively, whereas the moment deficit rate in western Nepal Himalaya is relatively higher than other sections and is equivalent to 12.13×10^{18} Nm/yr (Table 3.4). The moment deficit rate suggests an earthquake potential of M_w 8.5 in the western Nepal Himalaya, M_w 7.9 in the central Nepal Himalaya, and M_w

8.1 in the eastern Nepal Himalaya (Table 2.1 and Figure 3.10). This variation is potentially due to several factors: the central seismic gap in western Nepal, the occurrence of the 2015 Gorkha earthquake in central Nepal, and a higher accumulation of geodetic moment in eastern Nepal. As a convention (e.g., Ader et al., 2012 [12]; Lindsey et al., 2018 [11]), the moment deficit rate and equivalent earthquake potential are also estimated by considering the entire Nepal Himalaya as a single segment. This results in a moment deficit rate of 4.08×10^{19} Nm/yr and an earthquake potential of M_w 8.8. In summary, there is a potential for major to great earthquakes in each of the three sections of the Nepal Himalaya. The following paragraph presents a comparison between present findings and the results from previous studies.

Bilham et al. (1997) [16], using 24 GPS sites, suggested that the both western part of Nepal and Kumaun Himalaya (along with the boundary of Western Nepal) have the potential to cause a great earthquake ($M_w > 8$) as neither the Kumaun Himalaya nor the western Nepal has ruptured in the previous 350 years. Ambraseys and Douglas (2004) [6] re-evaluated the size and location of Himalayan earthquakes and found that the western Nepal Himalaya has not ruptured since the 1505 earthquake. By utilizing 30 GPS stations from Nepal and south Tibet, Ader et al. (2012) [12] observed that the moment deficit rate on the MHT throughout Nepal is large, which could produce a great earthquake in the region. Lindsey et al. (2018) [11] used data of 275 GPS sites derived from 16 different published studies and found that the seismic hazard across the Nepal Himalaya is high. Sreejith et al. (2018) [161] utilized two decades of GPS, InSAR, and leveling data to estimate stored energy along the Nepal Himalaya. They found that the western part of Nepal with unreleased strain energy reveals asperity similar to the 2015 Gorkha event. In this study, the Nepal Himalaya is divided into three spatial sections and estimated the seismic moment budget for each section from the high resolution integrated velocity field. A similar work has been carried out earlier by Sharma et al. (2020) [10]. Using 487 GPS sites scattered over the entire Himalayan arc, they observed that the western and central sections of the Nepal Himalaya have high seismic potential, equivalent to a $M_w \sim 8.0$ earthquake in each section. Therefore, as a whole, the present analysis based

on the integrated velocity information not only overcomes the limitation of low spatial coverage, but also enables the most-updated earthquake potential estimation over three continuous sections of the Nepal Himalaya. The findings strongly suggest that each of the sections of the Nepal Himalaya can produce large earthquake(s) and can be catastrophic for the human population.

3.5.1 Sensitivity analysis

As the above estimates of seismic moment budget and associated earthquake potential depend on several input parameters, a sensitivity analysis is essential to understand the variation of estimates. For this, the seismogenic depth is varied between 20 km, 25 km, 30 km, and 35 km. The sensitivity analysis also includes the lower and upper limits of GeMR (accounting for uncertainty in velocity estimation) and earthquake databases spanning 200 years, 500 years, and 900 years. The results of the sensitivity analysis are summarized in Table 3.5 to Table 3.12. From these tables, the following observations are made:

Table 3.5: Comparison of SeMR and GeMR for various sections corresponding to 20 km seismic depth and 500 years of earthquake database length

Section	$\dot{M}_0^g$ (10^{18} Nm/yr)	$\dot{M}_0^s$ (10^{18} Nm/yr)	$\frac{\dot{M}_0^g}{\dot{M}_0^s}$	M_0 (10^{18} Nm)	Earthquake potential (M_w)
1	13.72±0.11	5.01	2.73	8.71	8.4
2	6.74±0.08	3.66	1.84	3.08	7.8
3	13.99±0.17	11.40	1.23	2.59	7.9

Table 3.6: Comparison of SeMR and GeMR for various sections corresponding to 25 km seismic depth and 500 years of earthquake database length

Section	$\dot{M}_0^g$ (10^{18} Nm/yr)	$\dot{M}_0^s$ (10^{18} Nm/yr)	$\frac{\dot{M}_0^g}{\dot{M}_0^s}$	M_0 (10^{18} Nm)	Earthquake potential (M_w)
1	17.16±0.13	5.02	3.42	12.13	8.5
2	8.43±0.10	3.69	2.29	4.74	7.9
3	16.74±0.22	11.41	1.47	5.33	8.1

Table 3.7: Comparison of SeMR and GeMR for various sections corresponding to 30 km seismic depth and 500 years of earthquake database length

Section	$\dot{M}_0^g$ (10^{18} Nm/yr)	$\dot{M}_0^s$ (10^{18} Nm/yr)	$\frac{\dot{M}_0^g}{\dot{M}_0^s}$	M_0 (10^{18} Nm)	Earthquake potential (M_w)
1	20.59±0.16	5.03	4.10	15.56	8.5
2	10.11±0.12	3.70	2.74	6.42	8.0
3	18.49±0.25	11.43	1.62	7.05	8.2

Table 3.8: Comparison of SeMR and GeMR for various sections corresponding to 35 km seismic depth and 500 years of earthquake database length

Section	$\dot{M}_0^g$ (10^{18} Nm/yr)	$\dot{M}_0^s$ (10^{18} Nm/yr)	$\frac{\dot{M}_0^g}{\dot{M}_0^s}$	M_0 (10^{18} Nm)	Earthquake potential (M_w)
1	24.02±0.19	5.03	4.78	18.99	8.6
2	11.80±0.13	3.69	3.20	8.11	8.1
3	21.23±0.30	11.43	1.86	9.80	8.3

Table 3.9: Comparison of SeMR and GeMR for various sections using the lower limit of geodetic moment rates corresponding to 25 km seismic depth and 500 years of earthquake database length

Section	$\left(\dot{M}_0^g\right)_{min}$ (10^{18} Nm/yr)	$\dot{M}_0^s$ (10^{18} Nm/yr)	$\frac{\dot{M}_0^g}{\dot{M}_0^s}$	M_0 (10^{18} Nm)	Earthquake potential (M_w)
1	17.03	5.02	3.39	12.00	8.5
2	8.33	3.69	2.26	4.64	7.9
3	16.52	11.41	1.45	5.11	8.1

Table 3.10: Comparison of SeMR and GeMR for various sections using the upper limit of geodetic moment rates corresponding to 25 km seismic depth and 500 years of earthquake database length

Section	$\left(\dot{M}_0^g\right)_{max}$ (10^{18} Nm/yr)	$\dot{M}_0^s$ (10^{18} Nm/yr)	$\frac{\dot{M}_0^g}{\dot{M}_0^s}$	M_0 (10^{18} Nm)	Earthquake potential (M_w)
1	17.29	5.02	3.44	12.26	8.5
2	8.53	3.69	2.31	4.84	7.9
3	16.96	11.41	1.49	5.54	8.1

Table 3.11: Comparison of SeMR and GeMR for various sections using the lower limit of geodetic moment rates corresponding to 25 km seismic depth and 900 years of earthquake database length (dash in the last column denotes no seismic potential)

Section	$\dot{M}_0^g$ (10^{18} Nm/yr)	$\dot{M}_0^s$ (10^{18} Nm/yr)	$\frac{\dot{M}_0^g}{\dot{M}_0^s}$	M_0 (10^{18} Nm)	Earthquake potential (M_w)
1	17.16±0.13	5.02	3.42	12.13	8.5
2	8.43±0.10	9.37	0.89	-9.44	–
3	16.74±0.22	9.24	1.81	7.94	8.4

Table 3.12: Comparison of SeMR and GeMR for various sections using the lower limit of geodetic moment rates corresponding to 25 km seismic depth and 200 years of earthquake database length

Section	$\dot{M}_0^g$ (10^{18} Nm/yr)	$\dot{M}_0^s$ (10^{18} Nm/yr)	$\frac{\dot{M}_0^g}{\dot{M}_0^s}$	M_0 (10^{18} Nm)	Earthquake potential (M_w)
1	17.16±0.13	0.82	20.95	16.34	8.1
2	8.43±0.10	3.69	2.29	4.74	7.9
3	16.74±0.22	8.88	1.88	7.86	8.1

- In western Nepal Himalaya, the results are broadly stable against the changes in input parameters. The earthquake potential varies slightly from M_w 8.4 to M_w 8.6 when the seismogenic depth is changed from 20 km to 35 km (Tables 3.5–3.8).

- In central Nepal Himalaya, the estimates are mostly consistent, except when the catalog length is considered to be 900 years (Tables 3.5–3.12). In case of 900-year catalog length, this section has no earthquake potential, as released energy is higher than the accumulated energy due to the inclusion of two large earthquakes, namely the 1344 event and the 1100 event.

- In eastern Nepal Himalaya, the seismic moment budget estimates are generally consistent. Particularly, the earthquake potential varies from M_w 7.9 to M_w 8.3, when the seismogenic depth is changed from 20 km to 35 km (Table 3.5–3.8); as the strain rate is relatively high in this section, GeMR increases rapidly with an increase in seismogenic depth.

- The seismic moment budget is not at all sensitive to the lower and upper limits of GeMR (Table 3.9– Table 3.10).

3.6 General uncertainties in the seismic moment budget estimation

Apart from the points discussed above, there are several general types of uncertainties related to the length and magnitude completeness threshold of the compiled catalog, aseismic deformation, and the formulation used for calculating the seismic moment rate. Although the overall magnitude completeness threshold for earthquakes from 1100–2022 is 4.0, the thresholds for historical, early instrumental, and modern instrumental periods are 5.0, 5.5, and 4.0, respectively. As a consequence, there may be few missing small-sized earthquakes during historical to early instrumental period. Nevertheless, the energy release due to these missing events is comparatively small, resulting in almost similar moment budget calculation. Similarly, in this analysis, aseismic deformation in the overall strain accumulation is not accounted due to insufficient evidence of aseismic activity in and around the Himalayan belt. This consideration aligns partially with several previous research [10, 11, 16, 108, 216, 222] that reported a lack of substantial evidence for aseismic activity in the Himalaya. However, it contradicts to the assumption of Stevens and Avouac (2015) [73] who assumed that one-third portion of the moment buildup rate is aseismically released.

Table 3.13: Comparison of SeMR and GeMR for various parameters in equation $M_0 = 10^{cM_w+d}$ along the Kumaun Himalaya

Changed Parameter	$\dot{M}_0^g$ (10^{18} Nm/yr)	$\dot{M}_0^s$ (10^{18} Nm/yr)	$\frac{\dot{M}_0^g}{\dot{M}_0^s}$	M_0 (10^{18} Nm)	Earthquake potential (M_w)
$c = 1.48$	7.94	0.26	30.54	7.68	8.2
$c = 1.52$	7.94	0.47	16.89	7.47	8.0
$d = 9.0$	7.94	0.28	28.35	7.66	8.1
$d = 9.2$	7.94	0.44	18.05	7.50	8.0

Table 3.14: Comparison of SeMR and GeMR for various parameters in equation $M_0 = 10^{cM_w+d}$ along the western Nepal Himalaya

Changed Parameter	$\dot{M}_0^g$ (10^{18} Nm/yr)	$\dot{M}_0^s$ (10^{18} Nm/yr)	$\frac{\dot{M}_0^g}{\dot{M}_0^s}$	M_0 (10^{18} Nm)	Earthquake potential (M_w)
$c = 1.48$	17.16	3.45	4.97	13.71	8.6
$c = 1.52$	17.16	7.31	2.35	9.85	8.3
$d = 9.0$	17.16	3.99	4.30	13.17	8.6
$d = 9.2$	17.16	6.32	2.72	10.84	8.4

Table 3.15: Comparison of SeMR and GeMR for various parameters in equation $M_0 = 10^{cM_w+d}$ along the central Nepal Himalaya

Changed Parameter	$\dot{M}_0^g$ (10^{18} Nm/yr)	$\dot{M}_0^s$ (10^{18} Nm/yr)	$\frac{\dot{M}_0^g}{\dot{M}_0^s}$	M_0 (10^{18} Nm)	Earthquake potential (M_w)
$c = 1.48$	8.43	2.40	3.51	6.03	8.1
$c = 1.52$	8.43	4.88	1.73	3.55	7.7
$d = 9.0$	8.43	2.72	3.10	5.71	8.0
$d = 9.2$	8.43	4.31	1.96	4.12	7.8

Table 3.16: Comparison of SeMR and GeMR for various parameters in equation $M_0 = 10^{cM_w+d}$ along the eastern Nepal Himalaya

Changed Parameter	$\dot{M}_0^g$ (10^{18} Nm/yr)	$\dot{M}_0^s$ (10^{18} Nm/yr)	$\frac{\dot{M}_0^g}{\dot{M}_0^s}$	M_0 (10^{18} Nm)	Earthquake potential (M_w)
$c = 1.48$	16.74	7.94	2.11	8.80	8.2
$c = 1.52$	16.74	16.40	1.02	0.34	7.1
$d = 9.0$	16.74	9.06	1.85	7.68	8.1
$d = 9.2$	16.74	14.37	1.16	2.37	7.6

Moreover, to estimate the seismic moment rate along the Kumaun and Nepal Himalaya, empirical relationship defined in Equation 3.3.2 is utilized. Though this empirical relation, linking moment magnitude (M_w) and seismic moment (M_0), was initially derived for the western USA, it has been widely accepted across different regions globally, including Greece [201] and the Himalayas [10, 89, 223–225]. Additionally, Bilham and Ambraseys (2005) [113] formulated an empirical relationship between surface-wave magnitude (M_S)

and seismic moment (M_0) as $M_0 = 10^{(1.5M_S+9.1)}$ for earthquakes in northern India, while Hazarika and Kumar (2012) [225] established an empirical relation between local magnitude (M_L) and seismic moment (M_0) as $M_0 = 10^{(1.56M_L+8.55)}$. Considering these relations, we estimated the uncertainties in the earthquake potential within the study area by varying the parameters c from 1.48 to 1.52 and d from 9.0 to 9.2 in the equation $M_0 = 10^{(cM_w+d)}$. This variation yielded a range of earthquake potentials from magnitude 8.0 to 8.2 in the Kumaun Himalaya, 8.3 to 8.6 in the western Nepal Himalaya, 7.7 to 8.1 in the central Nepal Himalaya, and 7.1 to 8.2 in the eastern Nepal Himalaya when c is varied between 1.52 to 1.48 (Table 1). Similarly, varying d from 9.2 to 9.0 has resulted in earthquake potentials varying from magnitude 8.0 to 8.1 in the Kumaun Himalaya, 8.4 to 8.6 in the western Nepal Himalaya, 7.8 to 8.0 in the central Nepal Himalaya, and 7.6 to 8.1 in the eastern Nepal Himalaya (Table 1).

In this chapter, the seismic moment budget and associated earthquake potential in the Kumaun region and three distinct sections of the Nepal Himalaya are computed through an area-based approach [10, 114]. This method aims to estimate seismic hazards, such as the seismic moment budget and associated earthquake potential, across a geographical region. It considers factors like historical seismicity and strain accumulation, evaluating seismic moment budgets by assessing overall seismic activity and strain accumulation within a defined area [10, 114].

In contrast to area-based approach, the fault-based earthquake potential focuses on a singular fault, analyzing the likelihood of earthquakes along the identified fault line [11, 12, 125]. This approach delves into fault characteristics like slip rates, geometry, and accumulated stress to estimate the possibility of seismic events occurring on that particular fault [11, 12, 125]. Since the MHT is recognized as the primary source of major to great Himalayan earthquakes [11, 125, 226], the next chapter (Chapter 4) is dedicated to evaluating the fault geometry and slip rate distribution of the MHT across the Kumaun and Nepal Himalaya.

Furthermore, Chapter 4 computes the slip deficit rate and associated earthquake potential of the megathrust MHT in the study region. As a whole, utilizing both area-based

and fault-based approaches, Chapter 3 and Chapter 4 aim to provide a comprehensive understanding of seismic hazards in terms of moment deficit rate and associated earthquake potential along the Kumaun and Nepal Himalaya.

3.7 Summary

In this chapter, strain rate distribution and associated seismic moment budget along the Kumaun and Nepal Himalaya are estimated. The estimated strain rate distribution from the high-resolution integrated velocity field (Figures 2.19 and 2.23) is utilized to estimate the geodetic moment accumulation and the earthquake dataset (Figure 2.27) is used to calculate the seismic moment release along the Kumaun Himalaya and three various sections of the Nepal Himalaya. In addition, calculated geodetic and seismic moment rates are compared to re-assess the seismic moment budget and associated earthquake potential. Specifically, the use of high-resolution integrated velocity field enables additional information for the entire region to better comprehend in estimating strain rate field and associated earthquake potential. The major findings of the chapter are listed below:

- The strain rate is not homogeneous over the Kumaun and Nepal Himalaya. Particularly, along the MCT, higher strain rates are observed and minimal strain rate is observed along the MBT and MFT, indicating the locking behavior of these faults in the study region.
- The moment deficit rate in the Kumaun area is as high as 7.64×10^{18} Nm/yr.
- The estimated moment deficit rate suggests an earthquake potential of M_w 8.1 in the Kumaun Himalaya.
- In the Nepal Himalaya, the moment deficit rates vary spatially within the regions. The central Nepal Himalaya and eastern Nepal Himalaya exhibit moment deficit rates equivalent to 4.74×10^{18} Nm/yr and 5.33×10^{18} Nm/yr, respectively. In contrast, the western Nepal Himalaya stands out with a relatively higher moment deficit rate, amounting to 12.13×10^{18} Nm/yr, compared to the other sections.

- The estimated moment deficit rate suggests an earthquake potential of M_w 8.5 in western Nepal, M_w 7.9 in central Nepal, and M_w 8.1 in eastern Nepal.

In this chapter, the seismic moment budget and earthquake potential in the Kumaun and Nepal Himalaya are computed through an area-based approach [10, 114]. However, the next chapter (Chapter 4) is dedicated to evaluating the fault geometry, slip rate distribution, and associated earthquake potential of the MHT along the Kumaun and Nepal Himalaya based on a fault-based approach to provide a comprehensive scenario of the seismic hazard in the study region.

Chapter 4

Analysis of Fault Kinematics along the Study Area

"Earthquakes are the most unpredictable and highly complicated natural phenomena. If you can prepare for earthquakes, you can prepare for anything."

— Neil deGrasse Tyson

Spatial distribution of fault kinematics has a long-term scientific and societal importance. To this end, the chapter aims to characterize fault parameters and associated earthquake potential of the Main Himalayan Thrust (MHT) along the arc covering Kumaun-Nepal region. For this, (i) the derived integrated velocity field and compiled earthquake data are re-considered from Chapter 2; then, (ii) twenty arc-normal profiles to the MHT are selected across the study region based on the velocity pattern; subsequently, (iii) the spatial distribution of slip rates and fault geometry for the MHT is determined from a two-dimensional Bayesian inversion model; then, (iv) a section-wise slip deficit rate, moment deficit rate, and associated earthquake potential are computed based on the estimated slip rate and seismic energy release; finally, (v) these fault-based moment deficit rates and associated earthquake potential are compared with their corresponding area-based values as mentioned in Chapter 3. Overall, the findings in this chapter inevitably contribute to the improvement of seismic hazard evaluation along the study region.

Contents

Parts of this chapter have been published/under preparation in the following refereed publications:

Y. Sharma, S. Pasari, K. E. Ching, **H. Verma**, T. Kato, and O. Dikshit. Interseismic slip rate and fault geometry along the northwest Himalaya. *Geophysical Journal International* 235.3 (2023) 2694–2706 (SCI).

Y. Sharma, S. Pasari, K. E. Ching, **H. Verma**, and N. Choudhary. Kinematics of crustal deformation along the central Himalaya. *Acta Geophysica* 72 (2024), pp. 553–564 (SCIE).

H. Verma, S. Pasari, Y. Sharma, K. E. Ching. "Spatial Distribution of Fault Dynamics in the Nepal Himalaya: Seismic Hazard Insights" (Under preparation).

H. Verma, S. Pasari, Y. Sharma, K. E. Ching. "Kinematics of crustal deformation along the Kumaun Himalaya derived from high-resolution InSAR and GPS velocity field" (Under preparation).

4.1 Introduction

Due to the convergence between Indian and Eurasian plates, several significant earthquakes have occurred in the Himalaya along the locked part of the MHT, releasing accumulated strain energy in its upper brittle segment [131, 227, 228]. Particularly, many historical great Himalayan earthquakes, including the 1934 Nepal-Bihar, 1505 western Nepal, and the 1100 A.D. central Nepal earthquake, are believed to have initiated in the transition zone between locked and creeping parts, propagating through the mid-crustal ramp and reaching to the surface at the MFT [8, 131, 229, 230]. In contrary, for the major Himalayan earthquakes, such as the recent 2015 Gorkha earthquake that occurred in the highly coupled brittle segment of the MHT, the surface ruptures do not reach up to the MFT [131, 231]. This phenomenon indicates that such incomplete rupture will eventually contribute to future great earthquakes in the study region [131, 231]. In addition, for several decades, the Kumaun and western Nepal Himalaya have been identified to be areas with a heightened potential for future devastating earthquakes, as these regions are in a seismic quiescence phase for the last few centuries [16, 99]. In fact, the seismic moment budget based on an area-based approach outlined in Chapter 3 also highlights the importance of these regions for seismic activities. As a result, modeling interseismic slip rate distribution and fault kinematics is inevitable to understand the geometry of the MHT and associated seismic potential along the study region.

In recent decades, geodetic methods for measuring ground deformation, notably GPS and InSAR, have made significant strides in both temporal and spatial resolutions [232–234]. Each of these techniques possesses distinct levels of precision. Using a multiple of geodetic observations proves beneficial in defining fault parameters such as dip-angle, fault depth, locking depth, and slip rate distributions beneath the Earth's surface [235–241]. These parameters are pivotal in evaluating potential earthquake hazards related to a fault [242]. Previous studies over the last few decades [12, 16, 108, 111, 126, 127, 243, 244] have notably contributed to understanding the locking behavior of the MHT and the creeping patterns observed along the lower edge of the Himalaya. However, delineating

the spatial distribution of fault geometry and slip rates necessitates a high-resolution velocity field, providing detailed insights at each location within the study area compared to a standalone GPS velocity field. Therefore, using high-resolution integrated velocities (obtained in Chapter 2), this chapter examines the spatial distribution of fault geometry and associated slip rates along the downward extent of the MHT in the study region.

Using the velocity field, the spatial distribution of slip rates and fault geometry (i.e., dip-angle, fault depth, locking depth, rake angle and locked to creeping transition zone) for the MHT is determined from a two-dimensional Bayesian inversion model. This comprehensive analysis is conducted across 20 arc-normal profiles, as depicted in Figure 4.1. The resulting slip distribution pattern effectively emphasizes two key aspects: (i) the identification of locked segments, as these locations are prone to future earthquakes, and (ii) the recognition of interseismic creeping behavior that can impede the propagation of seismic ruptures [73, 245–247]. Overall, the proposed approach enables a profound understanding of the dynamic fault behavior and its implications for seismic hazard assessment.

4.2 Spatial distribution of arc normal profiles

The megathrust MHT is often regarded as the primary source for large earthquakes along the Himalayan seismic belt [5, 248]. However, the released elastic strain energy is not uniform across the MHT. Particularly, in the study area, both seismic activity and convergence rates exhibit spatial variations [5, 11, 12, 248]. For example, the convergence rate inferred from geodetic measurements varies spatially, with higher convergence rates in Kumaun and western Nepal in comparison to that of central and eastern Nepal [12, 73]. Similarly, the seismicity pattern exhibits spatial variation, with higher seismic activity in central and eastern Nepal than in the Kumaun and western Nepal regions. Due to the heterogeneity in energy accumulation and energy release in the study area, there have been spatial variations in the estimated fault parameters and slip-rate for the MHT across the study region [10, 12, 73, 108, 249]. Therefore, re-evaluating the spatial distribution of fault kinematics and slip rates becomes essential in order to identify areas with a high

potential of future earthquakes within the study region.

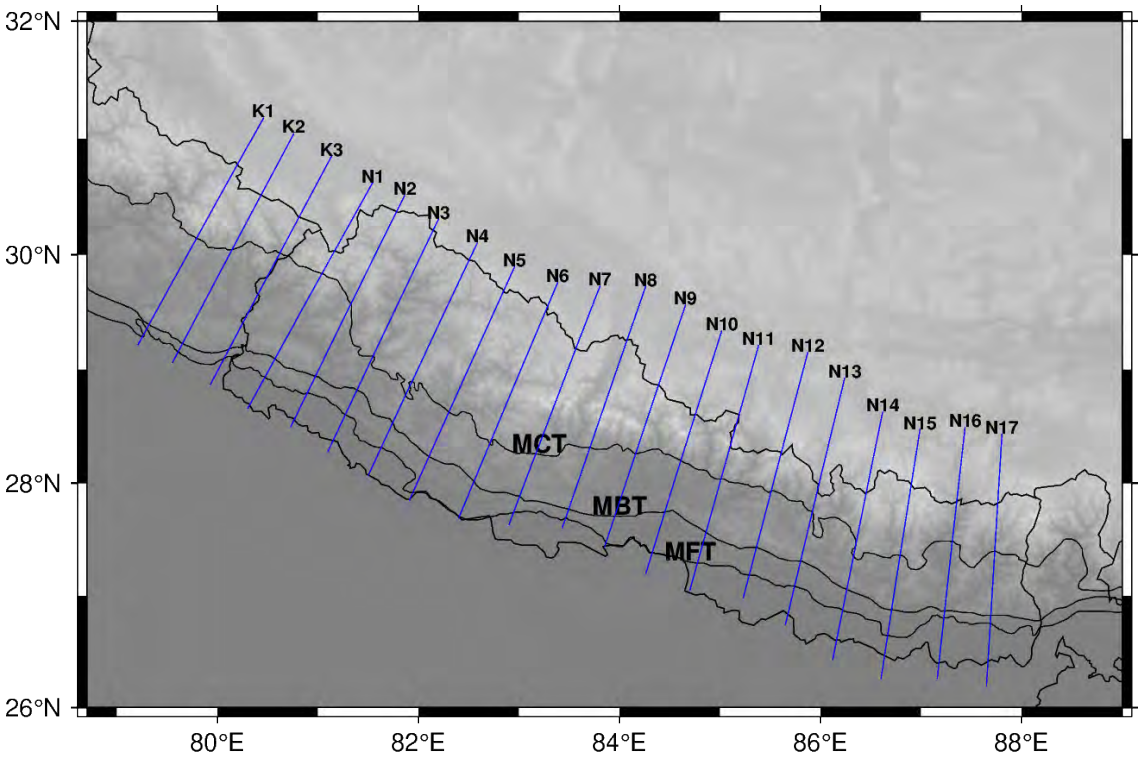

Figure 4.1: Location of all arc normal profiles along the Kumaun and Nepal Himalaya. Abbreviations are as: MFT, Main Frontal Thrust; MBT, Main Boundary Thrust; MCT, Main Central Thrust.

Several studies [e.g., 11, 12, 73, 90–92, 120] have estimated the fault characteristics and slip rate over the Kumaun and Nepal Himalaya based on the GPS velocity field (as discussed in Section 2.2.1). For example, Sharma et al. (2023a, 2023b) [125, 249] calculated fault parameters over 12 arc-normal profiles in the northwest and central Himalaya. Due to the sparse GPS resolution, the authors had to choose a non-uniformly distributed profiles (varying spatial gap between two consecutive profiles) over the study region. Therefore, a high-resolution integrated velocity field is preferable in choosing uniformly distributed profiles over a defined region. This not only helps to determine spatial distribution of fault kinematics in a comprehensive way but also allows to detect anomalous regional deformation over a region. Therefore, using a high-resolution integrated velocity field, the present analysis considers 20 uniformly arc-normal profiles over the study region.

There are three arc-normal profiles across the Kumaun Himalaya (K1 to K3) and 17 profiles across the Nepal Himalaya (N1 to N17), as depicted in Figure 4.1. Table 4.1 provides a summary of the configuration for each profile.

Table 4.1: The projection parameter (coordinates, azimuth, strike, width, and length in each arc-normal profile

Profile	Longitude (°E)	Latitude (°N)	Azimuth (°)	Strike (°)	Width (km)	Length (km)
K1	79.2087	29.2135	29.08	299.08	10	200
K2	79.5528	29.0586	28.03	298.03	10	200
K3	79.9297	28.8660	28.06	298.06	10	200
N1	80.3000	28.6552	27.91	297.91	10	250
N2	80.7300	28.4968	26.31	296.31	10	250
N3	81.1000	28.2792	25.55	295.55	10	250
N4	81.5000	28.0675	25.24	295.24	10	250
N5	81.9100	27.8489	24.34	294.34	10	250
N6	82.4000	27.6891	22.87	292.87	10	250
N7	82.9000	27.6300	20.95	290.95	10	250
N8	83.4300	27.6004	19.12	289.12	10	250
N9	83.8500	27.4341	18.61	288.61	10	250
N10	84.2600	27.1946	17.43	287.43	10	250
N11	84.7000	27.0496	15.75	285.75	10	250
N12	85.2300	26.9776	14.79	284.79	10	250
N13	85.6500	26.7421	13.58	283.58	10	250
N14	86.1200	26.4273	11.44	281.44	10	250
N15	86.6000	26.2552	8.94	278.94	10	250
N16	87.1600	26.2615	6.35	276.35	10	250
N17	87.6500	26.1905	3.55	273.55	10	250

4.3 Methodology

While it is important to note that stress accumulation along the Himalaya can be influenced by both elastic and inelastic processes, this chapter primarily focuses on characterizing fault parameters, including slip rate, rake, dip angle, depth, surface fault location, and locking depth, using a purely elastic Bayesian inversion model [5, 250]. The inversion is conducted on integrated velocities extracted from 20 arc-normal velocity profiles to derive fault slip rates and other fault parameters.

Within each profile, the relative surface velocity field is calculated, with the southernmost integrated velocity point serving as the reference. This relative velocity is then decomposed into two primary components: the fault-normal and fault-parallel components. The fault-normal component characterizes the surface velocity perpendicular to the arc, addressing regional extension or compression effects. On the other hand, the fault-parallel component reflects the horizontal velocity parallel to the arc, offering insights into strike-slip displacements [251].

In the chosen inversion approach, a fault geometry is assumed to consist of a basal detachment along with a fully locked zone, a locked-to-creeping transition zone, and a creeping zone. This geometry extends from the surface trace of the MFT to the down-dip end of the MHT (Figure 4.2) [11]. To ensure the stability of the inversion, a-priori upper and lower bounds for each fault parameter are provided based on the previous geological studies [2, 66, 84, 252–255]. If a parameter falls outside of these bounds, the prior probability is set to zero. Within this framework, the locking depth is defined as the portion of the fault plane with no slip (with lower and upper bounds of 0 km and 12 km, respectively). The locked-to-creeping transition zone encompasses the area where the fault transitions occur from fully locked to creeping zone (with bounds ranging from 12 km to 22 km) (Figure 4.2). The creeping zone represents the deeper part of the fault plane, where relatively significant slip rates occur. The boundary between the transition zone and the creeping zone is delineated by a locking line, which ranges between 70 km and 170 km from the surface trace of the MFT to the front of the Higher Himalaya along the study region. Additionally, following the work of Lindsey et al. (2018) [11], the dip angle for the MFT is estimated with prior bounds from 15° to 45°. Moreover, surface locations, rake angles, and slip rates are inferred as part of the study. The slip rate of the MHT is estimated with bounds ranging 0 to ∞ based on the input geodetic observations. To minimize edge effects in the dislocation model, a fault length of 5000 km is assumed [256]. Slip rates are derived from observed geodetic data using the observation equation below:

$$d = G(m) \times s + \varepsilon. \tag{4.3.1}$$

In the above equation, the Green function matrix is represented as G, while m corresponds to a vector comprising various fault parameters, including dip, slip, length, width, depth, rake, and fault surface location. Additionally, s is a vector specifically containing strike-slip and dip-slip components of slip rate, and d corresponds to a vector encompassing surface velocities. The symbol ε denotes normally (Gaussian) distributed errors characterized by a mean of zero and a covariance of $\sum_0$ (i.e., $\in \sim N(0, \sum_0)$).

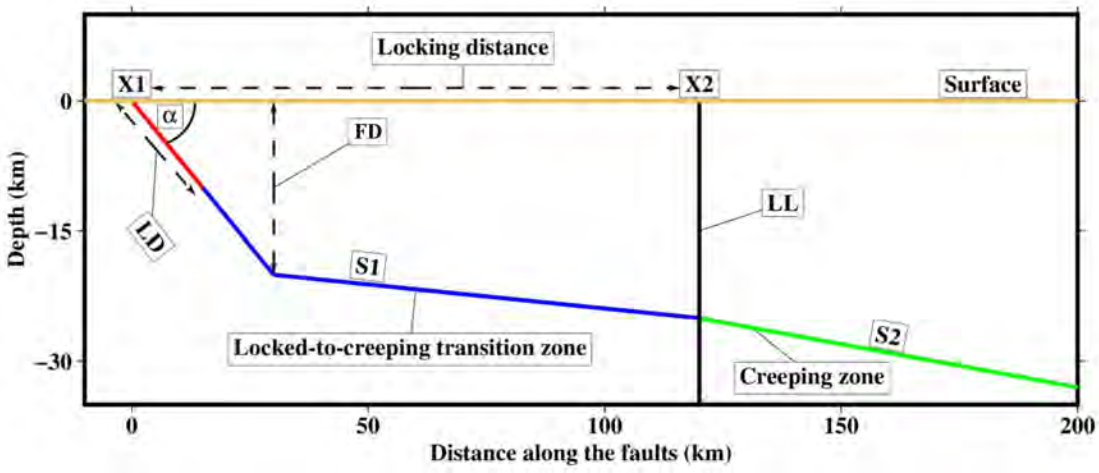

Figure 4.2: Illustration of the single-fault model used in the study. The map includes key fault parameters determined in this study. Abbreviations are as follows: X1, the surface location of MFT; LD, the locking depth, FD, the fault depth, S1, the slip rate along the transition zone; S2, the slip rate along the creeping zone, α, dip-angle of the MFT, and LL, the locking line.

Moreover, a Bayesian inversion framework, as outlined by Fukuda and Johnson (2008) [257], is applied to deduce the distribution of fault slip and various other fault parameters. In a Bayesian approach, the posterior distribution, denoted as $P(s, \sigma^2, m|d)$, is established through numerous iterations of prior information, represented by $P(s, m, \sigma^2)$, taking into account how effectively the known parameters align with the observed data (likelihood function). Mathematically, the posterior distribution can be expressed as follows:

$$P(s, \sigma^2, m|d) = \frac{p(d|s, m, \sigma^2) \times p(s, m, \sigma^2)}{\int_{-\infty}^{\infty} p(d|s, m, \sigma^2) \times p(s, m, \sigma^2)\, dm\, ds\, d\sigma^2}. \tag{4.3.2}$$

Since the integral part in the denominator of Equation 4.3.2 remains unaffected by the

unknown parameters, the posterior distribution is directly proportional to the product of the likelihood function and the prior information.

$$P(s,\sigma^2,m|d) \propto p(d|s,m,\sigma^2) \times p(s,m,\sigma^2) \tag{4.3.3}$$

The likelihood function, $p(d|s,m,\sigma^2)$, based on observed geodetic data for a given fault-slip, is formulated as a normal distribution with mean $G(m) \times s$ and covariance matrix $\sigma^2 \sum_0$. In this analysis, a-priori knowledge of the fault parameters is confined for the regularization of Bayesian inversion based on the existing geological studies [2, 66, 84, 253–255]. To estimate the joint posterior distribution of fault parameters and fault slip, a Markov Chain Monte Carlo (MCMC) method that incorporates the Metropolis algorithm is employed [257]. A MATLAB code is developed to simulate the MCMC chain of samples from prior and likelihood. A total of 10^6 iterations are performed for each parameter in the posterior distribution. Among these iterations, the initial "n" samples (20% of the total number of iterations) are removed as burn-in samples from the final estimation [252, 258, 259]. These burn-in samples are considered initial values and can be influenced by the initial coarse parameter estimates [252, 258, 259]. After discarding the burn-in samples, the mean and standard deviation of the model parameters are calculated [257]. The parameter estimates are represented using statistical descriptors derived from their posterior distributions.

The posterior probability distribution (PPD) is a fundamental concept in Bayesian statistics, representing the updated probability distribution of model parameters after incorporating observed data and prior knowledge [260, 261]. Through iterative sampling, MCMC algorithms aim to approximate this distribution by generating a series of parameter values according to their likelihood [261, 262]. These samples from the posterior distribution allow us to estimate the most likely values of parameters and their uncertainty ranges. Understanding this distribution is crucial as it provides insights into the likelihood of different parameter configurations, allowing for comprehensive uncertainty quantification. The importance lies in its ability to encapsulate the most probable values for parameters

and their variability, guiding model calibration and aiding in decision-making processes by offering a comprehensive view of the possible model parameter space [261, 262]. Additionally, by providing an estimate of parameter uncertainty, it enables the interpretation of the reliability of model predictions and the sensitivity of outcomes to the changes in parameter values. The posterior probability distribution acquired through MCMC stands as a pivotal element guiding informed inferences and decision-making within complex models. In the subsequent sections, modeling results for the each profile in Kumaun and Nepal Himalaya are presented.

4.4 Modeling results for fault kinematics and slip distribution along Kumaun Himalaya

To estimate the fault kinematics of the MHT along the Kumaun Himalaya, the high-resolution integrated velocity field obtained in Section 2.3.3.2 is utilized over three arc-normal profiles K1, K2, and K3 (Figure 4.1). The used model, which encompasses these three profiles, reveals a good agreement between the outcomes of the current inversion and the observed integrated velocity field along the Kumaun Himalaya (Figures 4.3 to 4.5). In the Kumaun Himalaya region, the fault parameters for the MFT as follows: dip angle consistently ranges from 29.0° to 32.7°; locking depth falls within the range of 9.5±2.5 km to 10.2±1.3 km, and fault depth is approximately 12.2±0.2 km. Additionally, the PPDs corresponding to these fault parameters exhibit an asymmetric distributional shapes (Figures 4.3 to 4.5). The locking depth and fault depth estimates for MFT strongly suggest that the position of the upper ramp of the MHT remains consistent within the Kumaun Himalaya (Figures 4.3 to 4.5 and Table 4.2). However, it is important to note that the PPDs of locking depth or fault depth may occasionally deviate from a Gaussian or unimodal distribution in some profiles due to the inclusion of upper and lower bounds for these parameters [125, 249]. Specifically, an upper bound of 12 km has been imposed on the locking depth to ensure its physical feasibility. Without this constraint, the model may generate PPDs with larger estimated locking depths compared to the fault depths. For

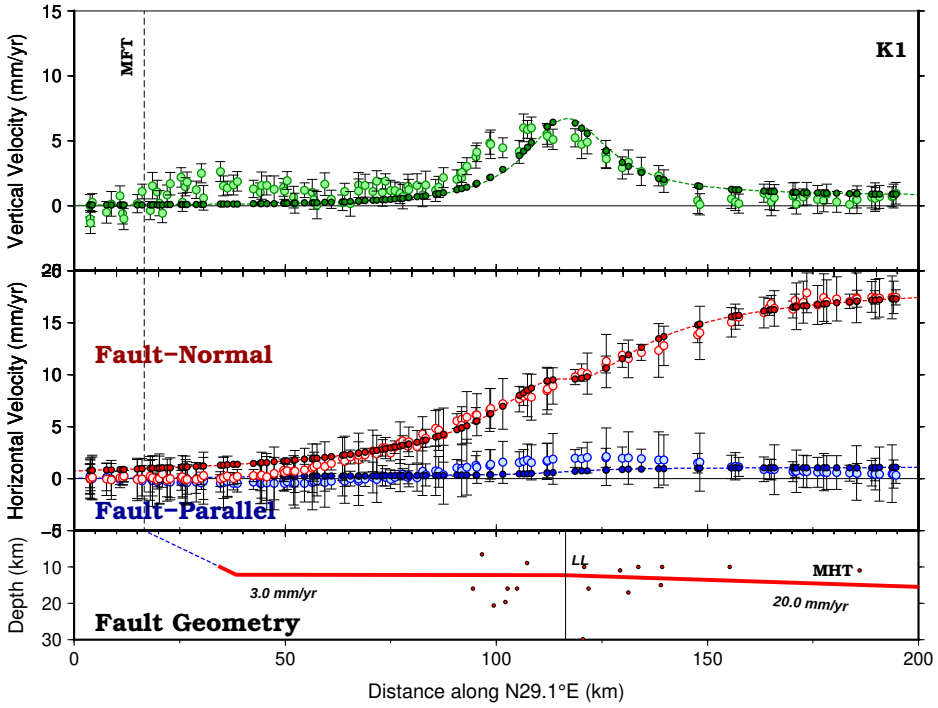

Figure 4.3: Fault-normal, fault-parallel, and vertical velocities along the profile K1.

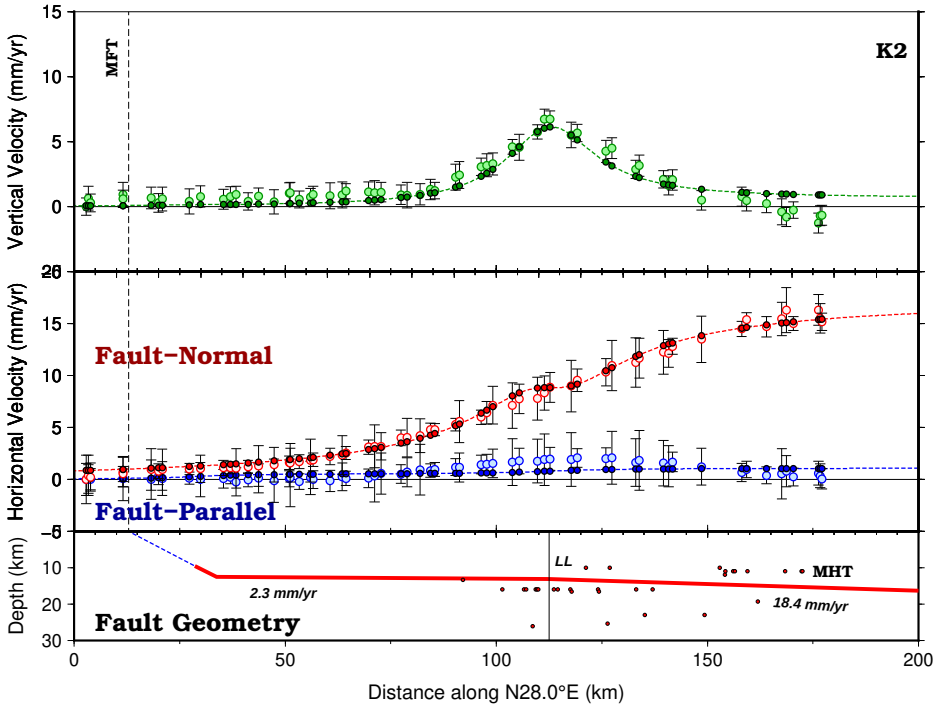

Figure 4.4: Fault-normal, fault-parallel, and vertical velocities along the profile K2.

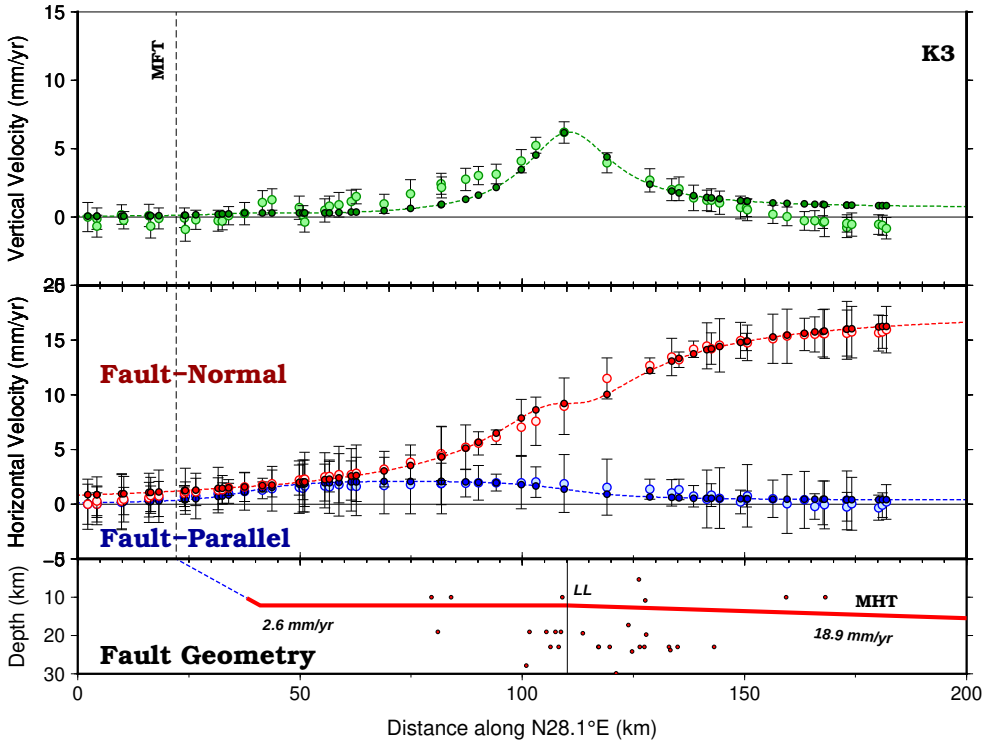

Figure 4.5: Fault-normal, fault-parallel, and vertical velocities along the profile K3.

example, the model may suggest a locking depth of 17 km with a fault depth of 15 km.

Table 4.2: Modeled fault parameters along the Kumaun Himalaya

Profile	Dip-angle of MFT (°)	Fault depth (km)	Locking depth (km)	Surface location (km)	Locking line (km)
K1	29.03±5.16	12.11±0.1	9.77±2.19	16.59±2.56	116.41±1.17
K2	31.13±4.35	12.54±0.38	9.48±2.46	12.96±2.79	112.56±1.17
K3	32.72±2.53	12.09±0.09	10.21±1.35	22.17±1.63	110.12±0.77
Profile	Slip-rate at transition zone (mm/yr)	Slip-rate of MHT (mm/yr)	Rake angle of MFT (°)	Rake angle of MHT (°)	
K1	2.96±0.23	20.00±0.22	87.39±0.53	86.75±0.33	
K2	2.27±0.27	18.37±0.24	88.15±0.81	86.48±0.55	
K3	2.62±0.22	18.88±0.16	96.72±0.66	88.89±0.26	

Another noteworthy finding in this analysis concerns the locking line, which has been defined to lie within a range of 70–170 km (based on prior bounds) from the surface trace of the MFT (Figures 4.3 to 4.5 and Table 4.2). In the Kumaun Himalaya, the modeled

locking line ranges from 110.1±0.8 km to 116.4±1.2 km from the surface trace of the MFT. Additionally, the concentration of seismic events in the Kumaun Himalaya strongly corresponds to the presumed locations of locking lines (Figure 4.11). The PPDs of the locking line parameter, evaluated across all profiles, consistently display a Gaussian shape, indicating its high degree of constraint (Figures 4.6 to 4.8).

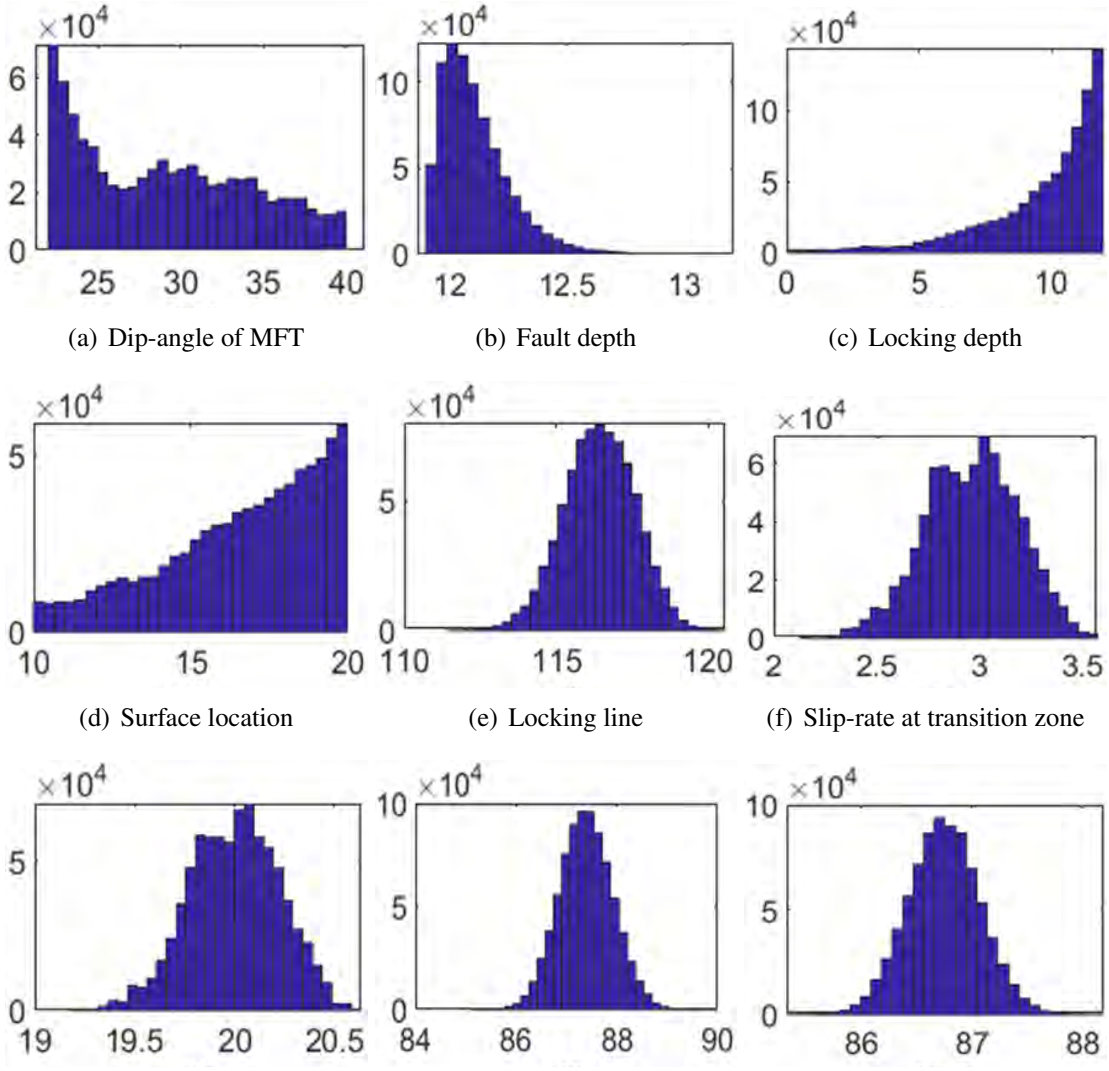

(a) Dip-angle of MFT (b) Fault depth (c) Locking depth

(d) Surface location (e) Locking line (f) Slip-rate at transition zone

(g) Slip-rate of MHT (h) Rake angle of MFT (i) Rake angle of MHT

Figure 4.6: Posterior probability distributions for the inversion fault model in the K1 profile.

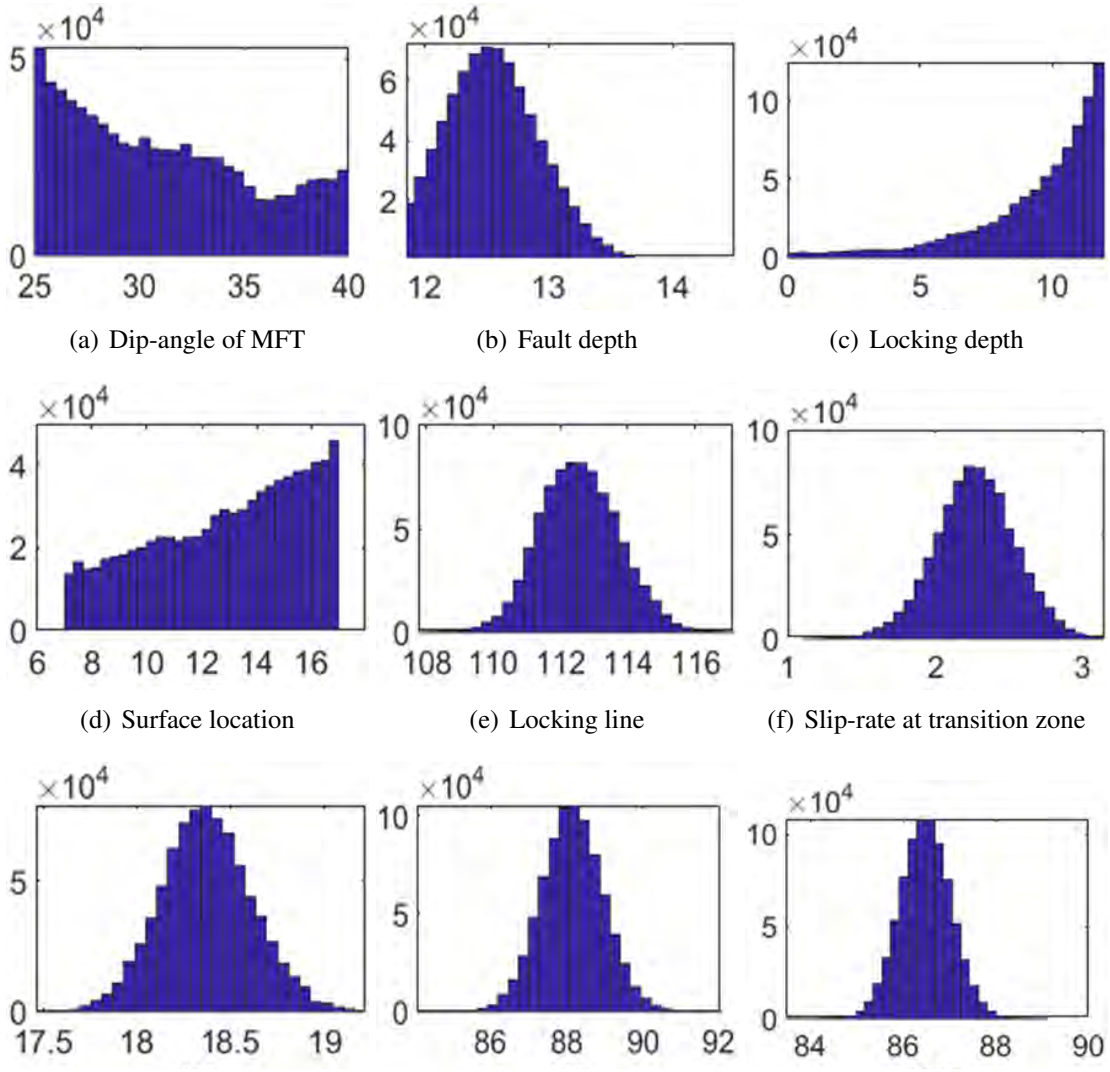

(a) Dip-angle of MFT (b) Fault depth (c) Locking depth

(d) Surface location (e) Locking line (f) Slip-rate at transition zone

(g) Slip-rate of MHT (h) Rake angle of MFT (i) Rake angle of MHT

Figure 4.7: Posterior probability distributions for the inversion fault model in the K2 profile.

In this study, the estimation of the slip rate of the MHT is performed both along its strike and in the down-dip direction. The results revealed that the slip rate along the transition zone, spanning from the locked to creeping segments, falls within the range of 2.3±0.3 mm/yr to 2.9±0.2 mm/yr in the Kumaun region (Figures 4.3 to 4.5 and Table 4.2). Importantly, it is observed that the strike-slip component is almost negligible in the region (Figures 4.3 to 4.5). This is probably due to the predominance of pure arc-normal convergence, where the Indian plate converges directly toward the Tibetan Plateau in

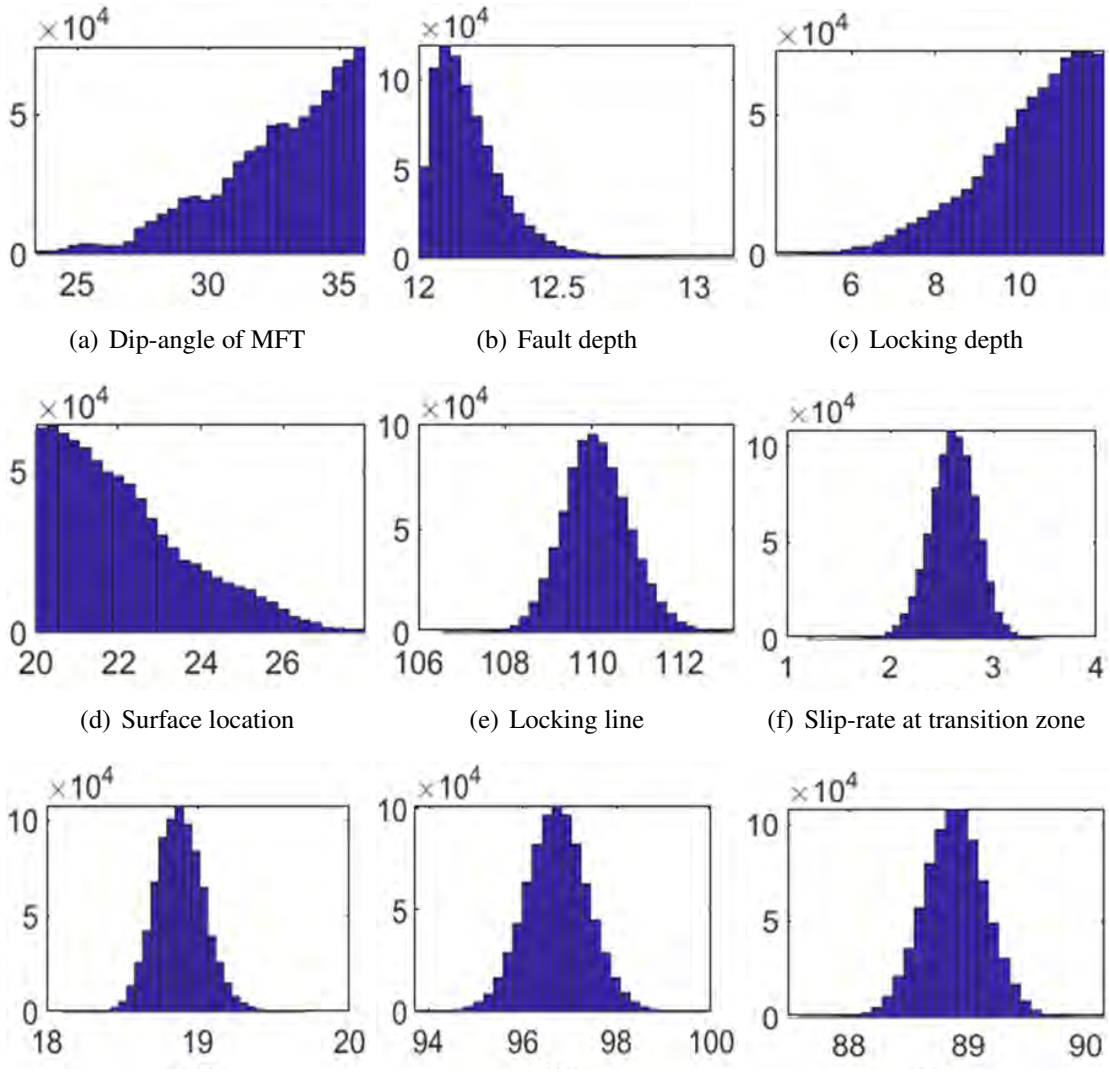

(a) Dip-angle of MFT (b) Fault depth (c) Locking depth

(d) Surface location (e) Locking line (f) Slip-rate at transition zone

(g) Slip-rate of MHT (h) Rake angle of MFT (i) Rake angle of MHT

Figure 4.8: Posterior probability distributions for the inversion fault model in the K3 profile.

this region [11, 12, 111, 265]. The absence of significant strike-slip motion may also be attributed to a high rake angle of approximately 87°, indicative of a predominantly thrust fault environment along the Kumaun Himalaya (Table 4.2). The slip rate of MHT across the Kumaun Himalaya ranges from 20.0±0.2 mm/yr to 18.4±0.2 mm/yr (Figure 4.10). The PPDs for the rake angle of MFT and MHT consistently exhibit a Gaussian shape, highlighting the well-constrained nature of this parameter (Figure 4.3 to Figure 4.5). The estimated slip rate of the MHT in the Kumaun Himalaya closely matches the findings of

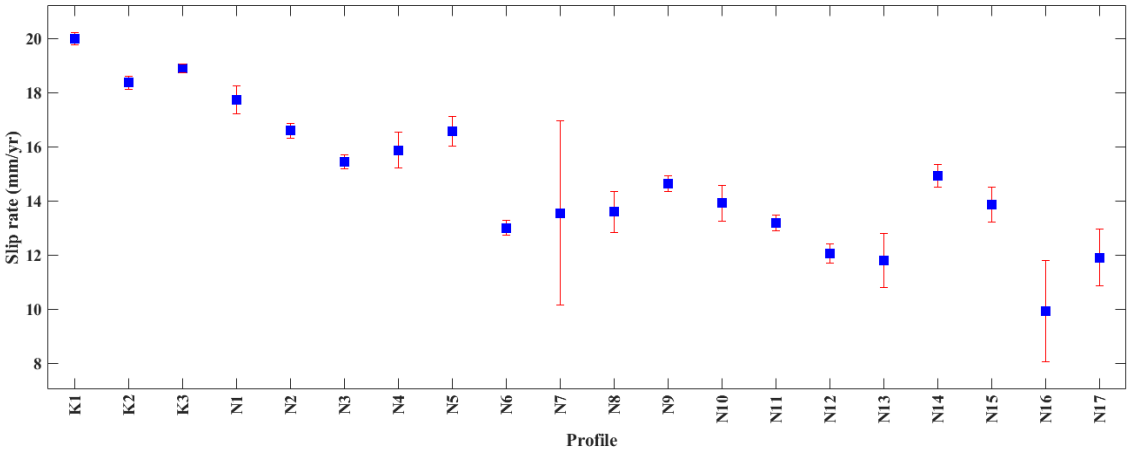

Figure 4.9: Bar chart illustrating a comparison of slip rates estimated in the current study with those from previous studies [12, 89, 117, 125, 129, 130, 249, 263, 264] across various sections of the study region.

Jade et al. (2014) [119] with a slip rate of 18.0±1.5 mm/yr, Ponraj et al. (2019) [89] with a slip rate of 17.2±1.0 mm/yr, and Sharma et al. (2023a) [249] with a slip rate of 19.0±2.0 mm/yr (Figure 4.9).

4.5 Modeling results for fault kinematics and slip distribution along Nepal Himalaya

To estimate fault kinematics along the Nepal Himalaya, the high-resolution integrated velocity field obtained in Section 2.3.3.3 is utilized over 17 arc-normal profiles, specifically N1 to N17 (Figure 4.1). The comprehensive model, which encompasses all profiles, demonstrates a reasonable alignment between the results of the inversion and the observed integrated velocity field (Figure 4.12 to Figure 4.28).

Within the Nepal Himalaya region, the fault parameters for the MFT are as follows: dip angle ranges from 25.0° to 32.3°, with an average value of 29.5°; locking depth varies from 6.2±3.4 km to 9.4±2.2 km, with an average value of 7.6 km and fault depth ranges from 13.1±1.1 km to 14.3±18 km, with an average value of 13.6 km. Additionally, based on the three sections of Nepal Himalaya as defined in Figure 3.9, the fault parameters in each section are also provided. The dip angle of the MFT is estimated as 28.0° in

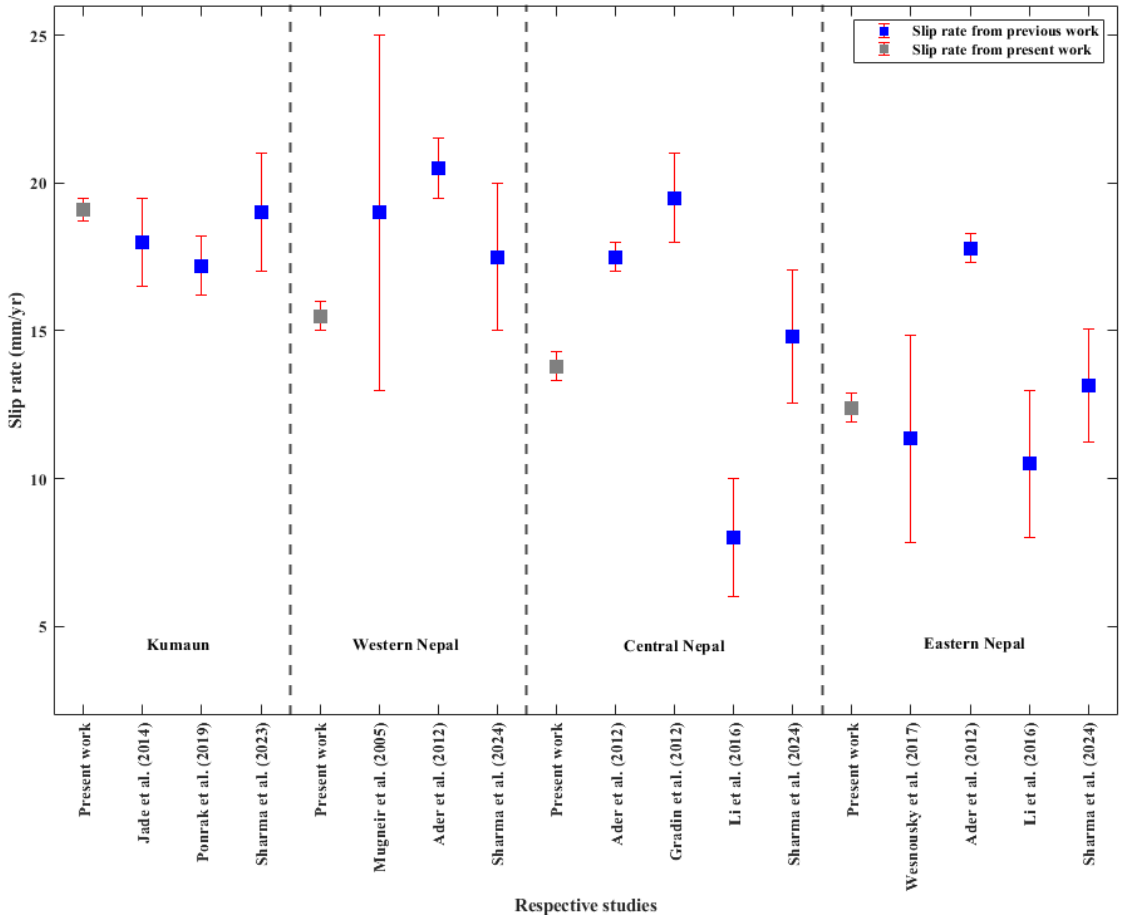

Figure 4.10: Bar chart depicting the distribution of slip along the Main Himalayan Thrust (MHT) across various geographical profiles along the Kumaun and Nepal Himalaya.

the western Nepal Himalaya, 30.5° in the central Nepal Himalaya, and 30.5° in the eastern Nepal Himalaya, indicating a uniformity in the dip angle parameter across the Nepal Himalaya. Similarly, the locking depth of the MFT is 7.8 km in the western Nepal Himalaya and 7.5 km both in the central and eastern Nepal Himalaya, indicating a uniformity in the estimation. On the other hand, the estimation of fault depth is consistent throughout the Nepal Himalaya, with 13.7 km in the western Nepal Himalaya, 13.4 km in the central Nepal Himalaya, and 13.5 km in the eastern Nepal Himalaya. Additionally, the PPDs corresponding to these fault parameters exhibit an asymmetric distributional shapes (Figures 4.12 to 4.28).

In addition to the parameters discussed above, another significant parameter in this

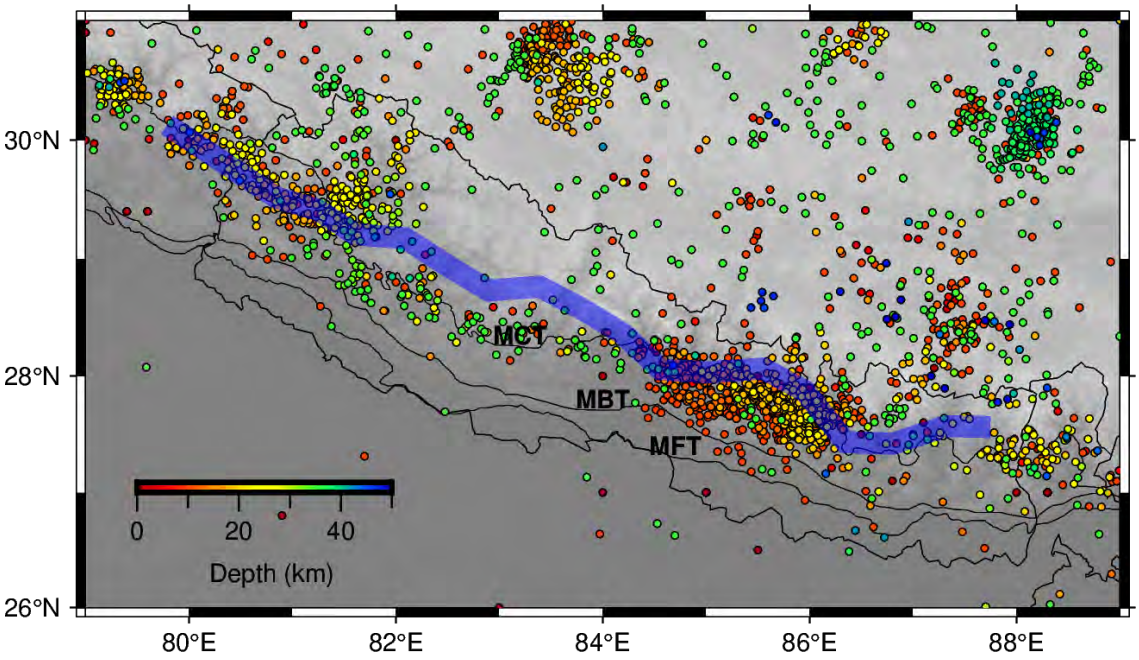

Figure 4.11: Simulated locking line and background seismic activity along the study region. The shaded blue band denotes the locking line.

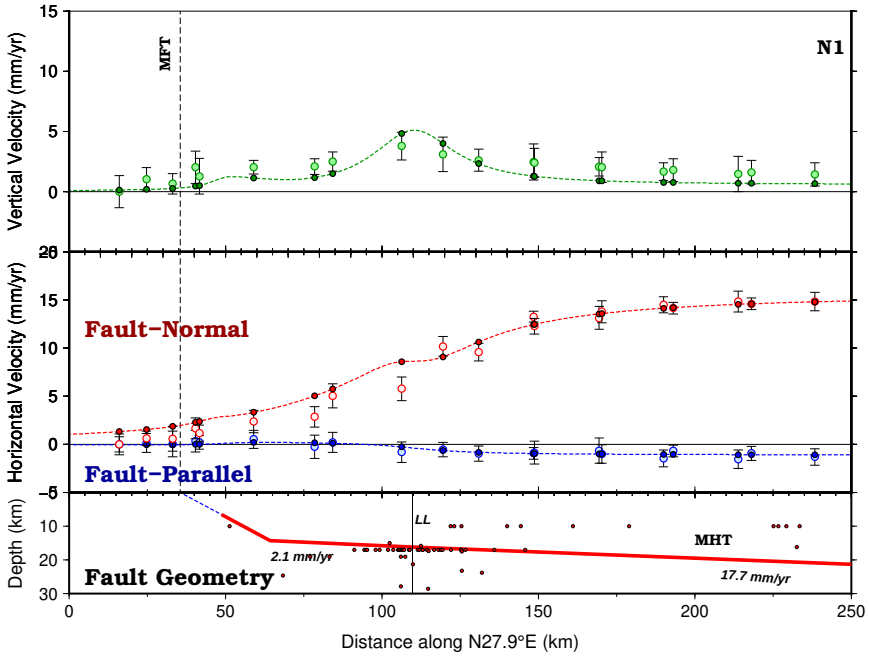

Figure 4.12: Fault-normal, fault-parallel, and vertical velocities along the profile N1.

analysis involves the locking line, defined to lie within a range of 70 km to 170 km (based on prior bounds) from the surface trace of the MFT. The modeled locking line positions in

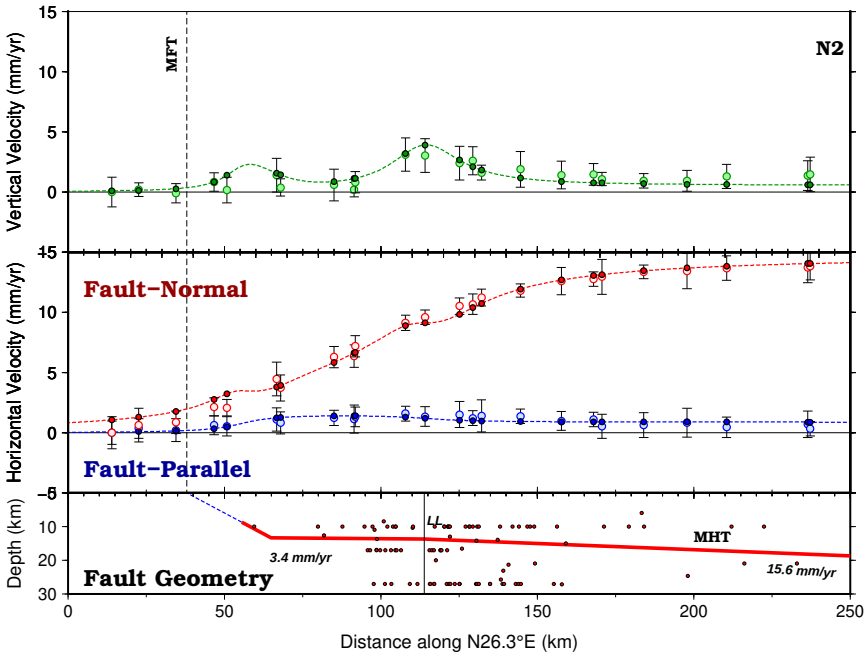

Figure 4.13: Fault-normal, fault-parallel, and vertical velocities along the profile N2.

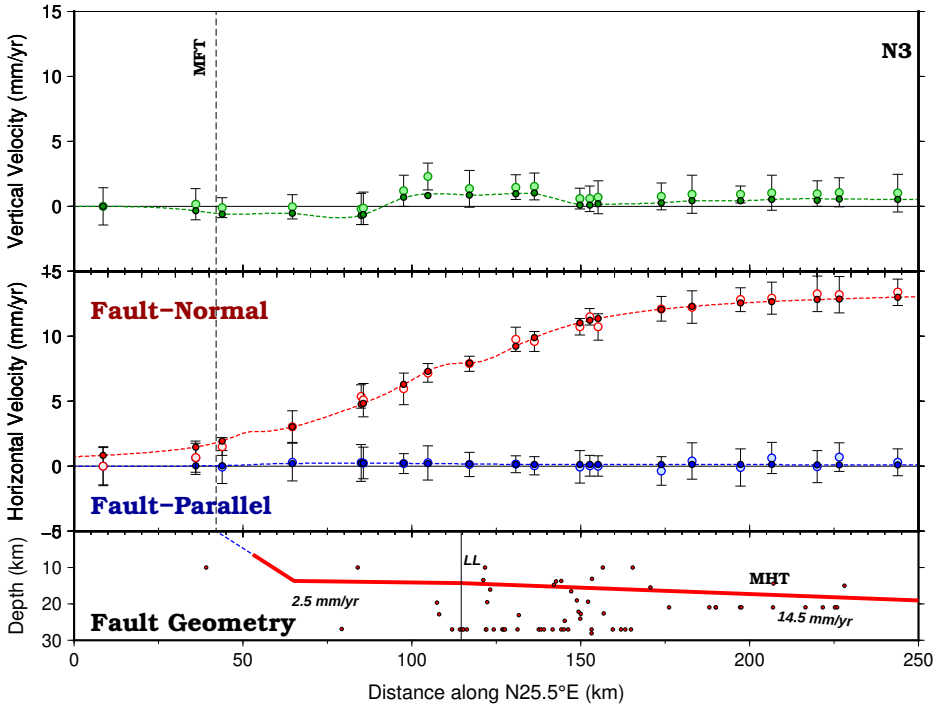

Figure 4.14: Fault-normal, fault-parallel, and vertical velocities along the profile N3.

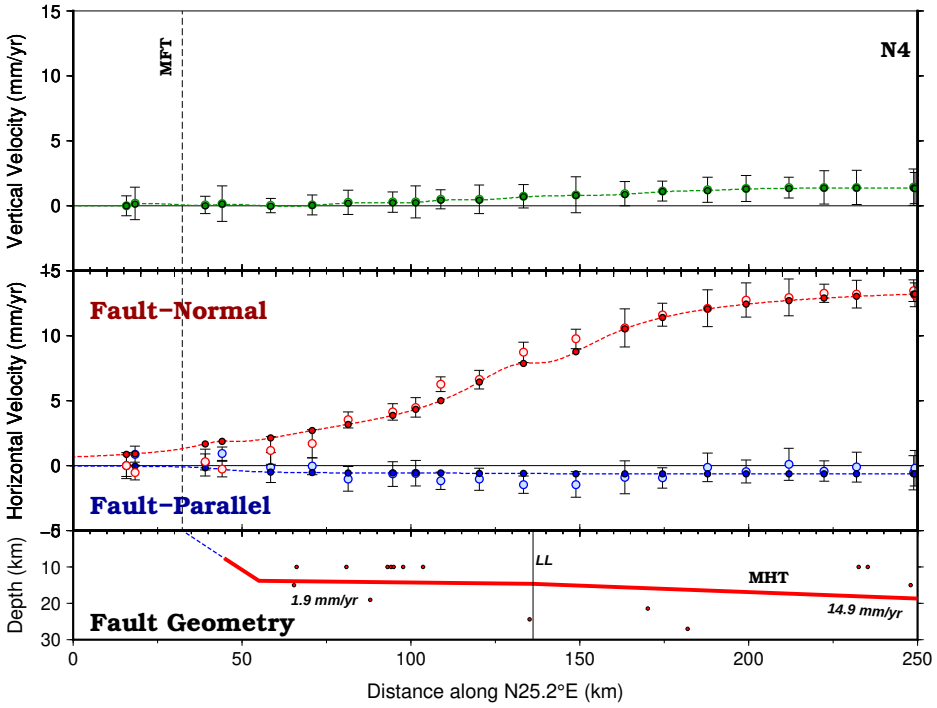

Figure 4.15: Fault-normal, fault-parallel, and vertical velocities along the profile N4.

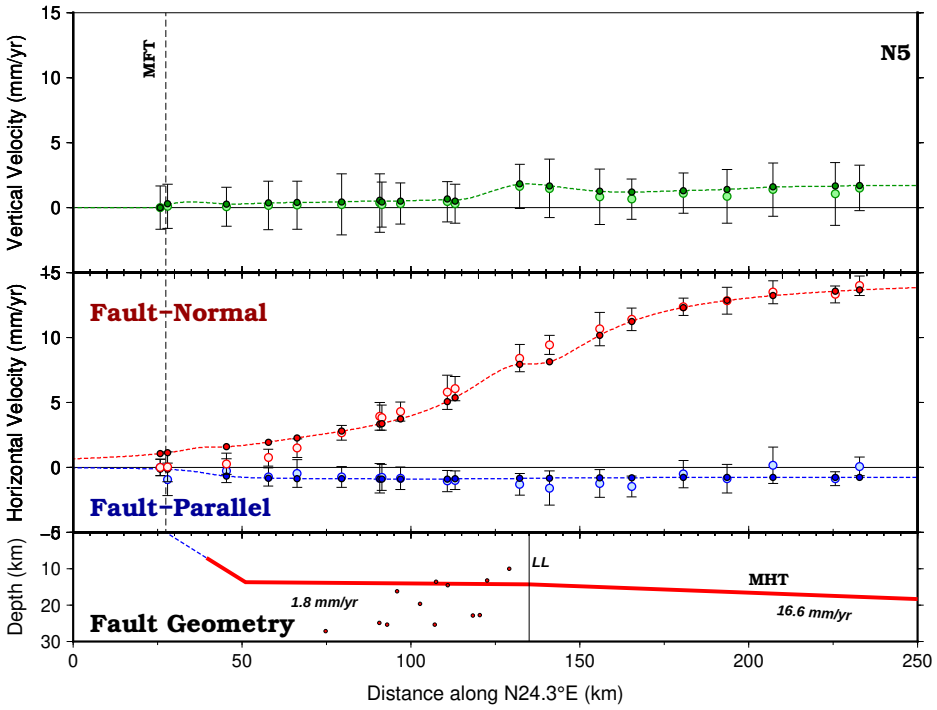

Figure 4.16: Fault-normal, fault-parallel, and vertical velocities along the profile N5.

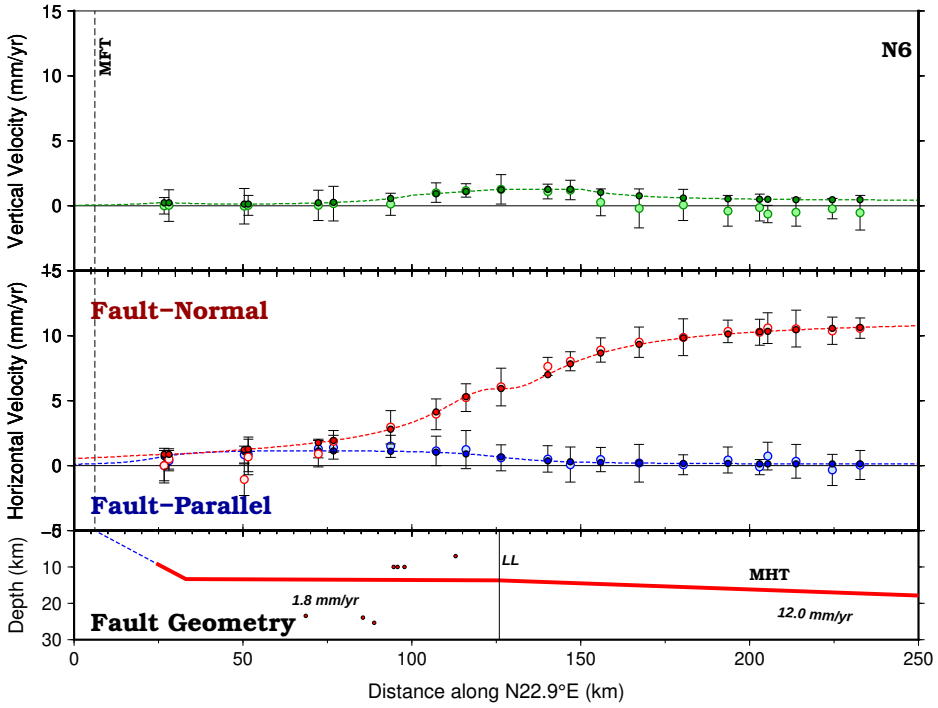

Figure 4.17: Fault-normal, fault-parallel, and vertical velocities along the profile N6.

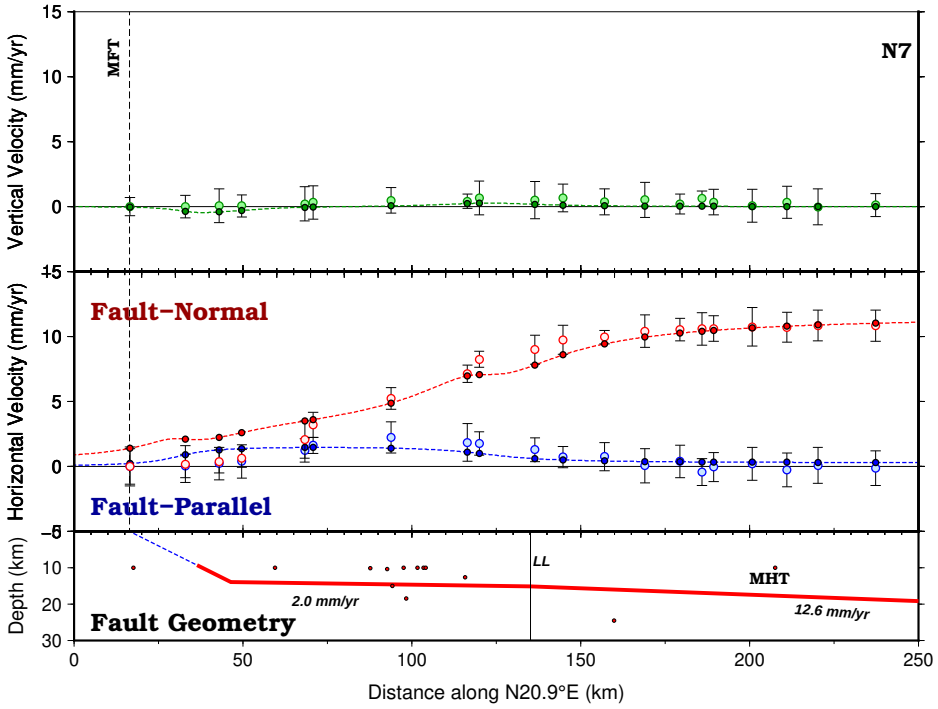

Figure 4.18: Fault-normal, fault-parallel, and vertical velocities along the profile N7.

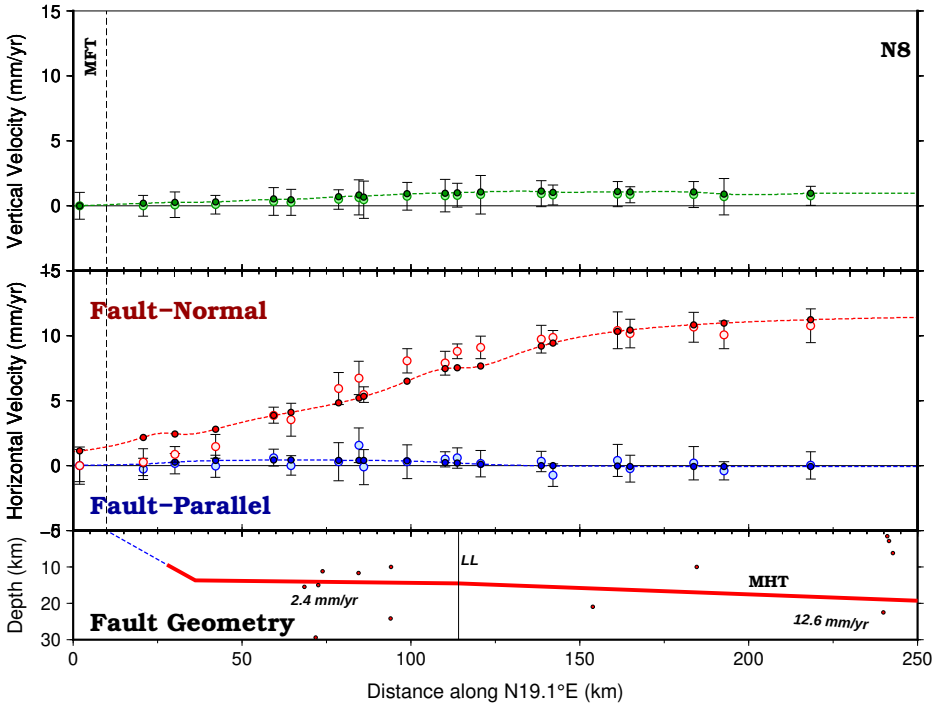

Figure 4.19: Fault-normal, fault-parallel, and vertical velocities along the profile N8.

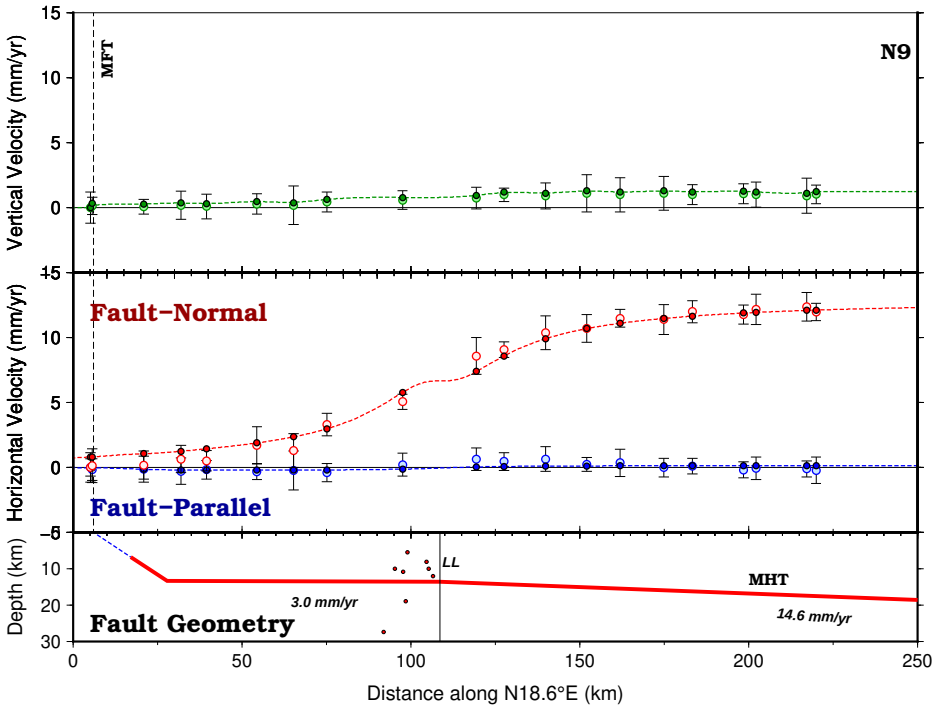

Figure 4.20: Fault-normal, fault-parallel, and vertical velocities along the profile N9.

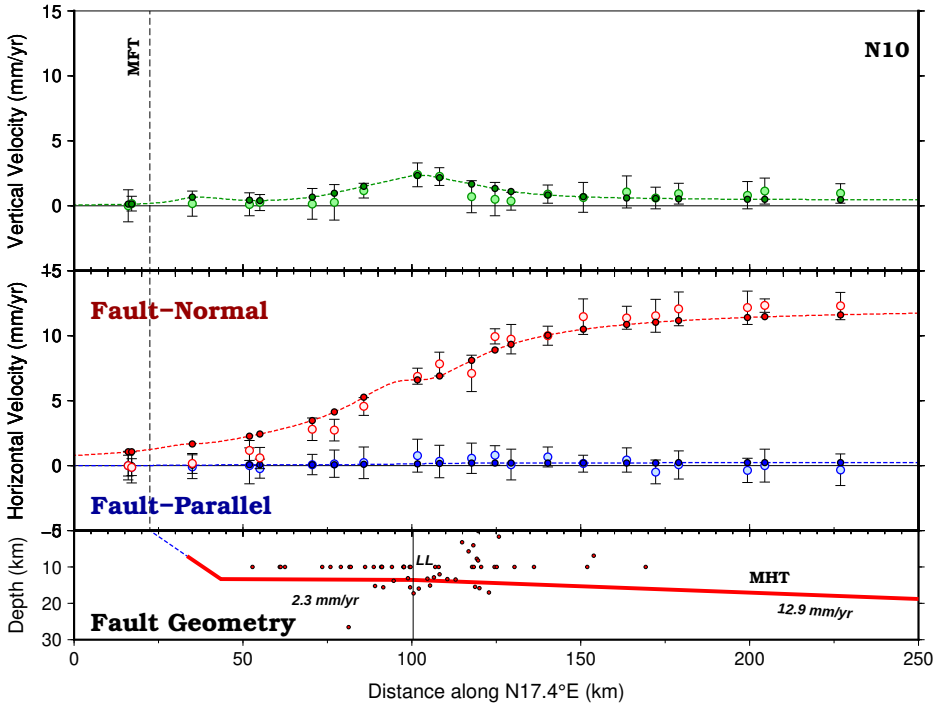

Figure 4.21: Fault-normal, fault-parallel, and vertical velocities along the profile N10.

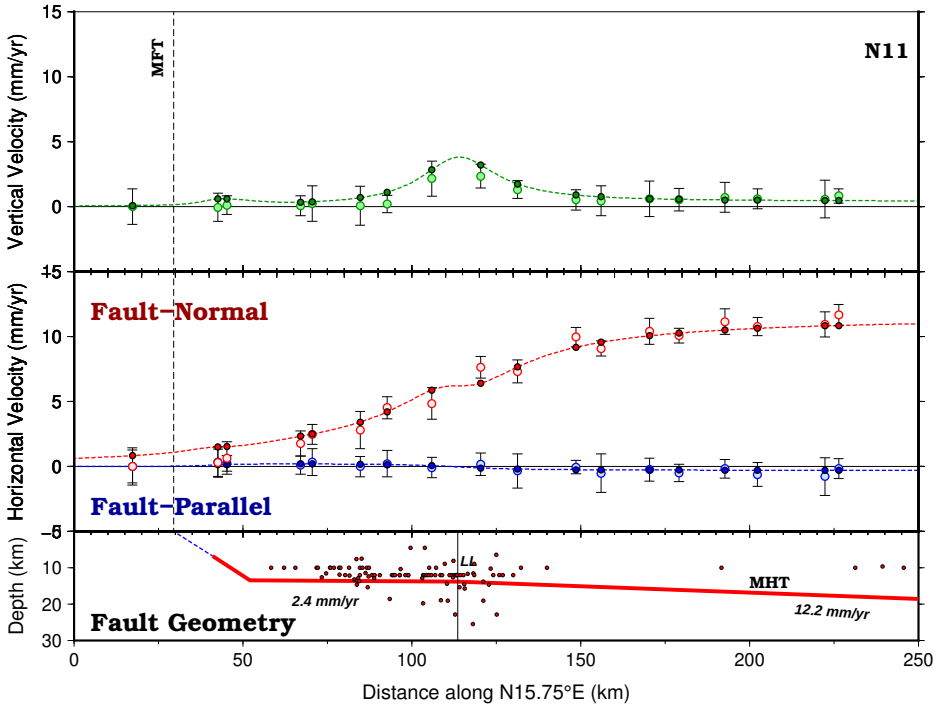

Figure 4.22: Fault-normal, fault-parallel, and vertical velocities along the profile N11.

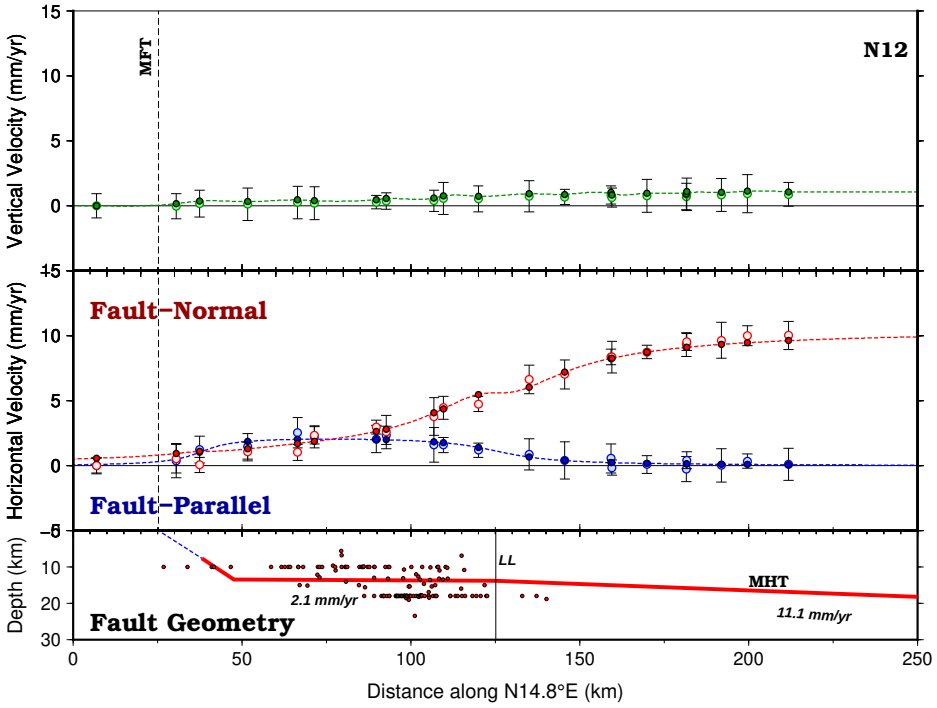

Figure 4.23: Fault-normal, fault-parallel, and vertical velocities along the profile N12.

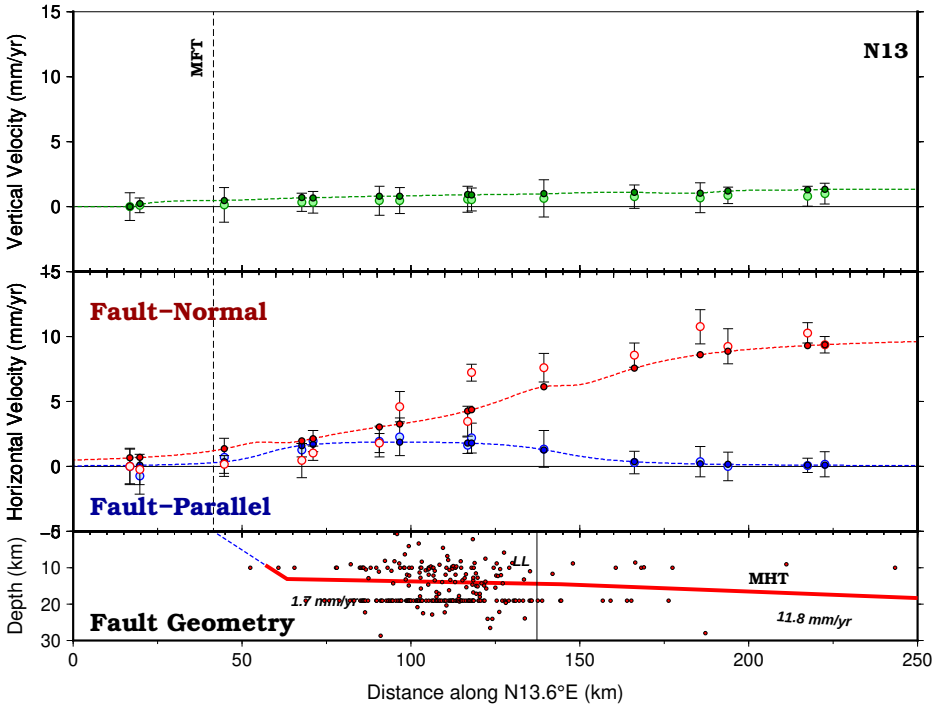

Figure 4.24: Fault-normal, fault-parallel, and vertical velocities along the profile N13.

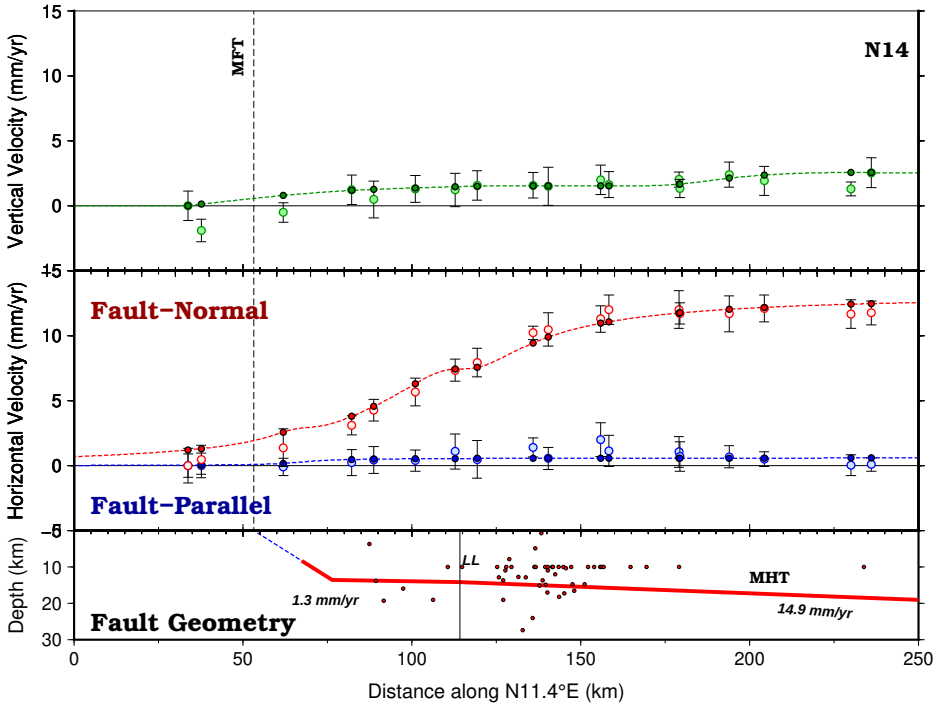

Figure 4.25: Fault-normal, fault-parallel, and vertical velocities along the profile N14.

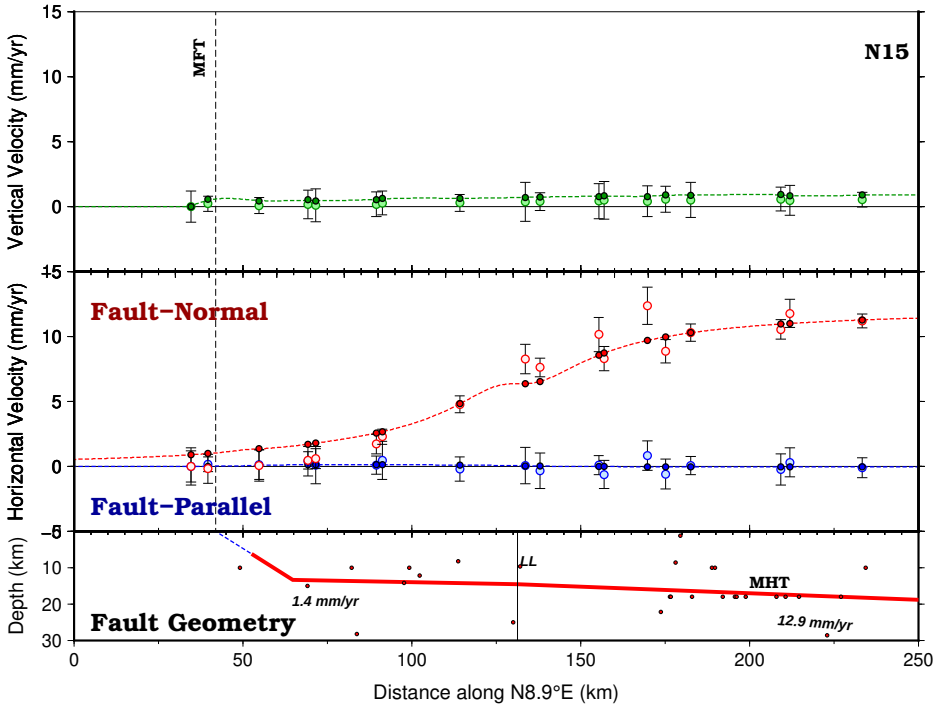

Figure 4.26: Fault-normal, fault-parallel, and vertical velocities along the profile N15.

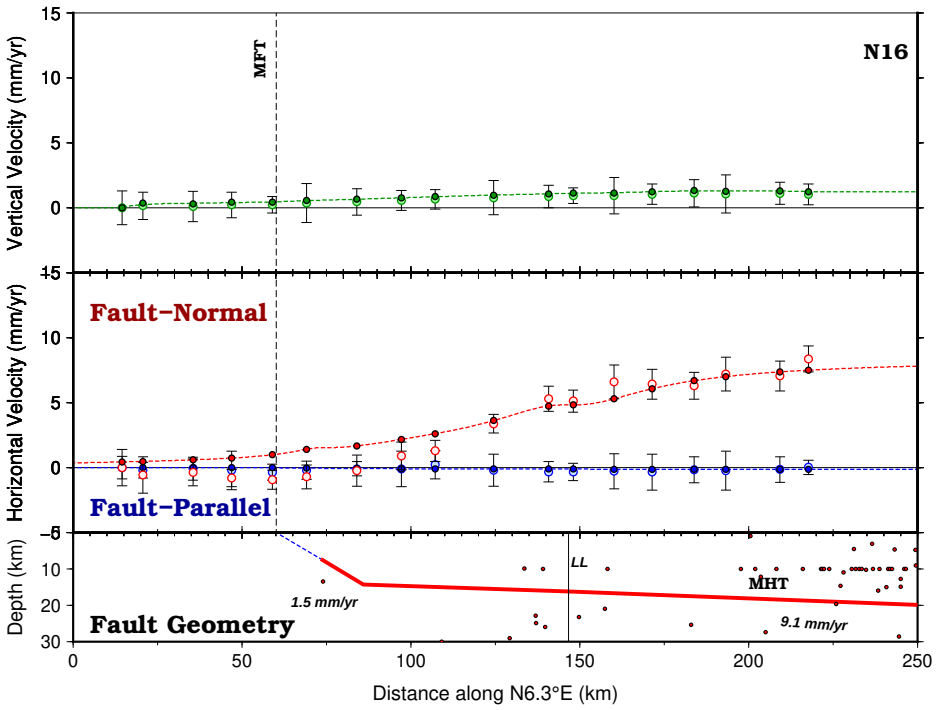

Figure 4.27: Fault-normal, fault-parallel, and vertical velocities along the profile N16.

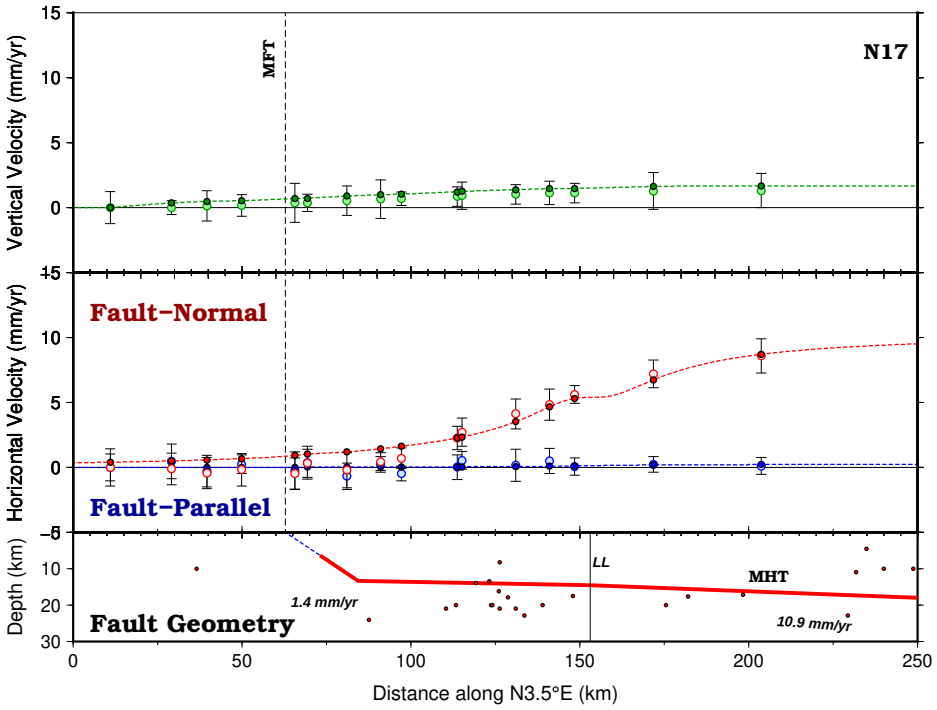

Figure 4.28: Fault-normal, fault-parallel, and vertical velocities along the profile N17.

Table 4.3: Modeled fault parameters along the Nepal Himalaya

Profile	Dip-angle of MFT (°)	Fault depth (km)	Locking depth (km)	Surface location (km)	Locking line (km)
N1	26.45±5.51	14.29±1.75	6.58±3.44	35.47±2.86	109.73±6.45
N2	26.25±2.78	13.32±0.31	8.65±1.03	37.92±1.76	113.9±2.28
N3	30.56±5.70	13.63±0.58	6.43±2.33	42.01±1.35	114.61±2.42
N4	31.37±5.20	13.83±0.79	7.57±1.87	32.29±1.99	136.1±8.85
N5	30.14±4.90	13.66±0.67	7.00±2.59	27.45±1.70	135.04±8.15
N6	26.28±3.38	13.32±0.32	8.99±1.06	6.14±1.49	125.88±1.87
N7	24.95±2.00	13.96±1.01	9.25±0.81	16.46±1.35	135.16±5.46
N8	27.62±4.04	13.69±0.69	9.36±1.59	9.93±2.29	114.12±12.21
N9	31.31±4.80	13.28±0.30	6.74±3.47	5.99±2.32	108.61±1.88
N10	32.30±4.97	13.29±0.29	6.99±3.45	22.47±2.22	100.44±2.80
N11	30.83±5.29	13.42±0.42	6.83±3.25	29.54±2.92	113.57±2.32
N12	31.05±4.86	13.44±0.43	7.68±2.45	25.30±2.20	125.19±3.09
N13	31.09±4.65	13.13±1.10	9.32±2.19	41.51±1.98	129.29±6.29
N14	30.36±4.59	13.60±0.72	8.28±2.81	53.24±6.19	114.21±10.04
N15	30.33±5.59	13.31±1.25	6.23±3.38	41.93±1.76	131.25±6.25
N16	28.88±4.79	14.23±1.73	7.32±3.47	60.07±2.35	146.63±23.72
N17	31.73±4.96	13.31±1.20	6.32±3.38	62.86±2.34	153.10±4.67

Profile	Slip-rate at transition zone (mm/yr)	Slip-rate of MHT (mm/yr)	Rake angle of MFT (°)	Rake angle of MHT (°)
N1	2.07±0.89	17.73±0.52	95.93±1.40	93.97±0.36
N2	3.38±0.92	16.59±0.27	93.91±1.34	86.70±0.42
N3	2.53±1.11	15.43±0.26	90.73±1.13	89.54±0.36
N4	1.90±0.98	15.87±0.67	90.31±2.47	92.58±1.28
N5	1.76±0.75	16.58±0.55	89.36±1.26	92.92±0.72
N6	1.78±0.64	13.00±0.28	95.95±1.04	89.53±0.55
N7	2.04±1.13	13.55±3.40	101.34±8.31	89.72±1.77
N8	2.38±0.50	13.59±0.77	93.91±2.40	90.45±0.96
N9	2.95±0.38	14.62±0.29	88.30±0.82	89.37±0.39
N10	2.32±0.32	13.92±0.66	89.14±1.40	88.97±0.60
N11	2.43±0.64	13.18±0.29	92.94±0.81	91.51±0.37
N12	1.71±0.78	12.06±0.35	103.13±1.50	90.09±0.59
N13	1.70±0.62	11.80±0.99	105.18±3.08	90.00±0.83
N14	1.30±0.59	14.93±0.43	89.82±3.14	87.51±0.73
N15	1.39±0.77	13.85±0.65	90.92±1.24	90.19±0.60
N16	1.54±1.47	9.93±1.88	90.39±8.02	90.91±0.92
N17	1.39±1.89	11.90±1.01	88.85±1.96	88.73±1.34

the Nepal Himalaya range from 100.4±2.8 km to 153.1±4.7 km across all profiles, and the PPDs consistently exhibit Gaussian shapes, confirming a high level of constraint for this parameter within the scope of this study (Figures 4.29 to 4.45). Notably, the estimated

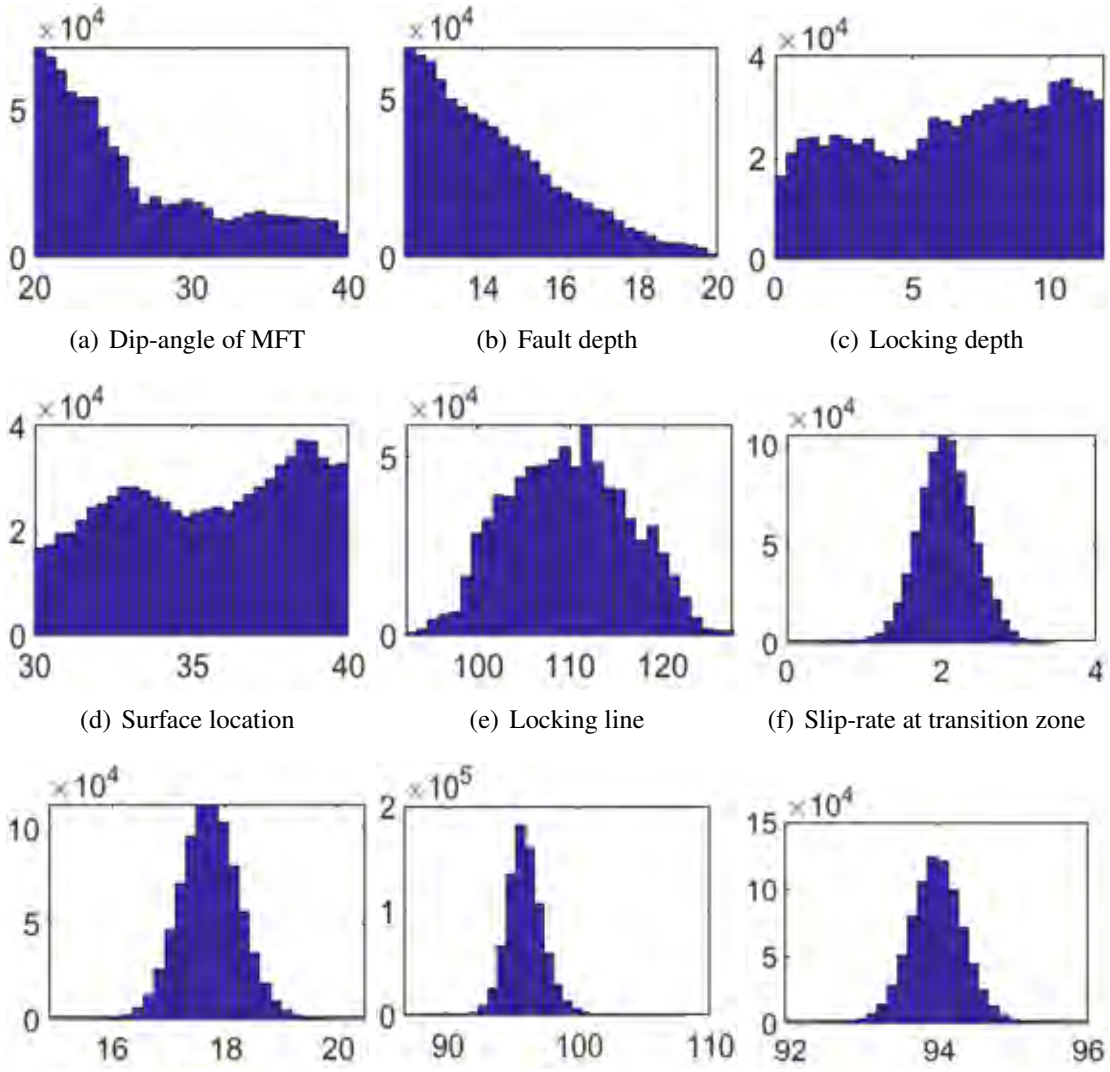

(a) Dip-angle of MFT (b) Fault depth (c) Locking depth

(d) Surface location (e) Locking line (f) Slip-rate at transition zone

(g) Slip-rate of MHT (h) Rake angle of MFT (i) Rake angle of MHT

Figure 4.29: Posterior probability distributions for the inversion fault model in the N1 profile.

locking line in the Nepal Himalaya closely corresponds to the assessments by Diao et al. (2022) [132] and Lindsey et al. (2018) [11]. Moreover, the clustering of seismic activity along the Nepal Himalaya, particularly at the Higher Himalaya's front, closely aligns with the inferred locking line locations (Figure 4.11) [12, 181, 230]. This correlation implies a potential relationship between interseismic strain accumulation at the creeping zone's tip and seismicity in the Nepal Himalaya [181, 230].

The estimation of the MHT's slip rate is a crucial parameter over the Nepal Himalaya,

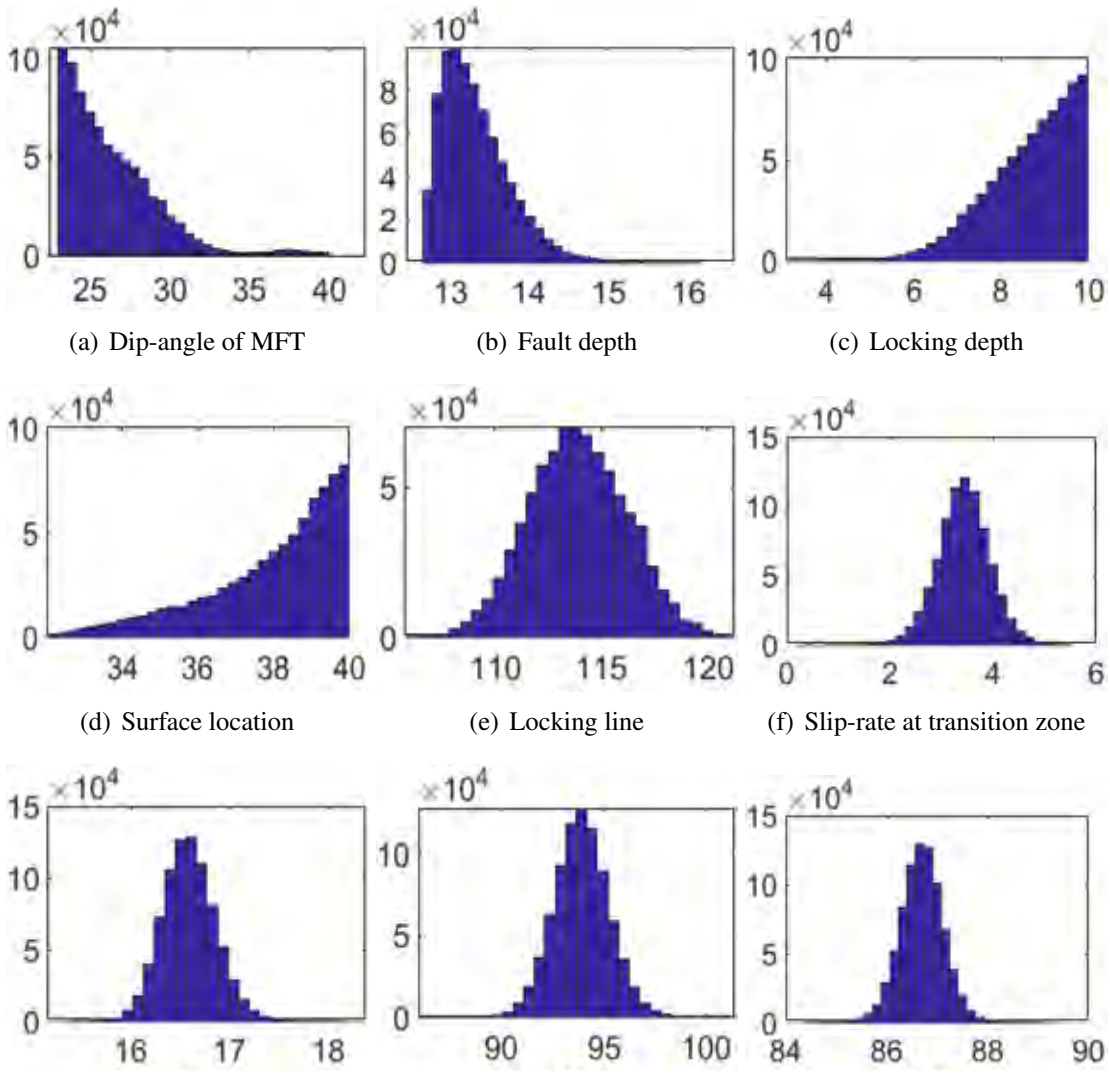

(a) Dip-angle of MFT (b) Fault depth (c) Locking depth

(d) Surface location (e) Locking line (f) Slip-rate at transition zone

(g) Slip-rate of MHT (h) Rake angle of MFT (i) Rake angle of MHT

Figure 4.30: Posterior probability distributions for the inversion fault model in the N2 profile.

serving as a primary input in seismic hazard analysis. The findings indicate a consistent slip rate within the transition zone, ranging from 1.3±0.6 mm/yr to 3.4±0.9 mm/yr across the Nepal Himalaya (Figures 4.12 to 4.28 and Table 4.3). Strike-slip motion along the Nepal Himalaya is negligible, attributed to the dominant arc-normal convergence of the Indian plate towards the Tibetan Plateau. The high rake angle of approximately 90° supports the predominantly thrust fault environment in the Nepal Himalaya (Figure 4.10 and Table 4.3). The average long-term slip rate of the MHT over the Nepal Himalaya

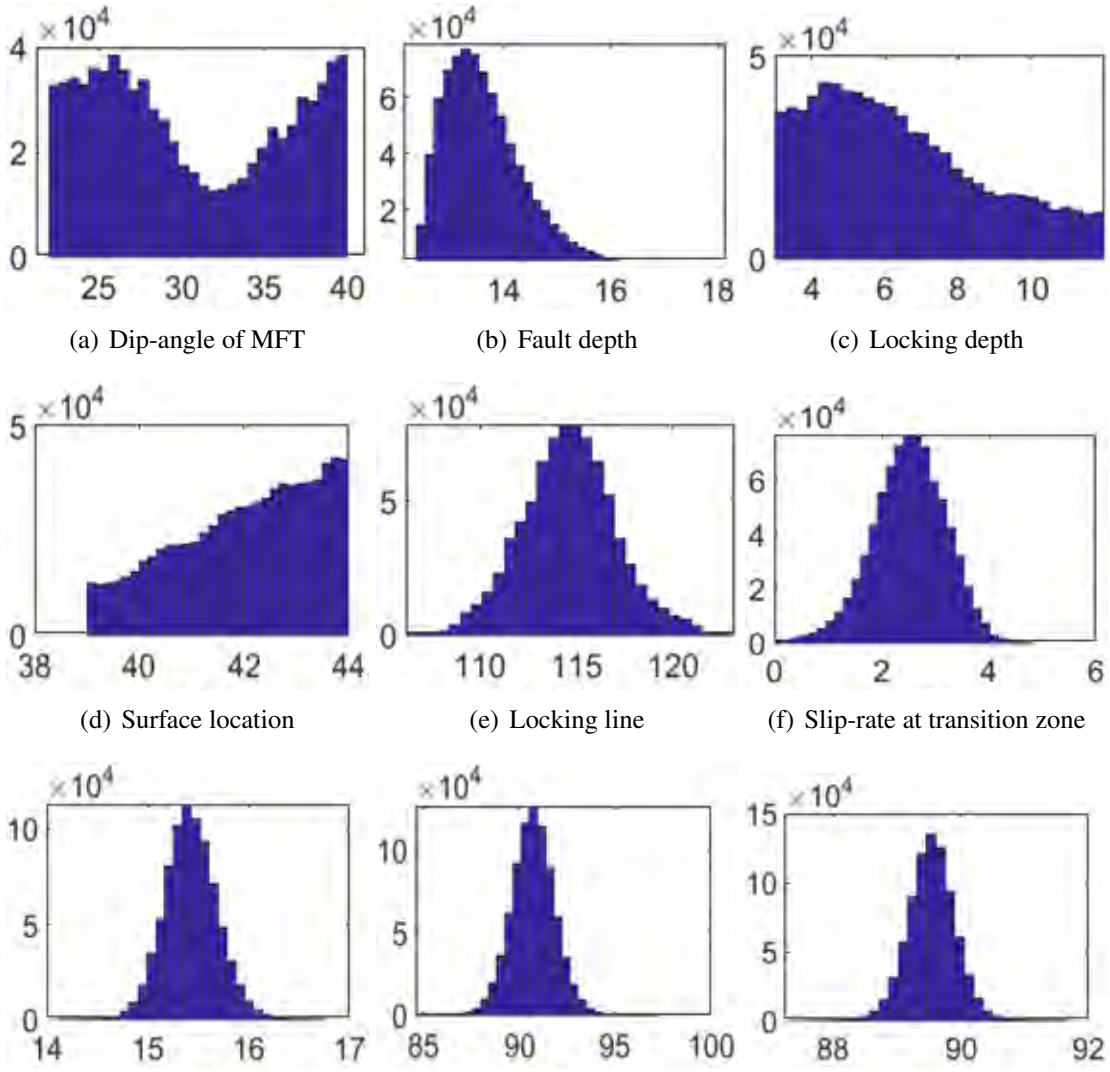

(a) Dip-angle of MFT (b) Fault depth (c) Locking depth

(d) Surface location (e) Locking line (f) Slip-rate at transition zone

(g) Slip-rate of MHT (h) Rake angle of MFT (i) Rake angle of MHT

Figure 4.31: Posterior probability distributions for the inversion fault model in the N3 profile.

is 14.2±0.8 mm/yr, decreasing from the western Nepal Himalaya to the eastern Nepal Himalaya (Table 4.3). This estimation of slip rate over the Nepal Himalaya is close to the estimated values of 15.0±2.4 mm/yr suggested by Lindsey et al. (2018) [11] and 15.2±2.3 mm/yr suggested by Sharma et al. (2023b) [125], but lower than the estimated values of 17.8±0.5 mm/yr in Ader et al. (2012) [12], 18.8±1.6 mm/yr in Diao et al. (2022) [132], and 19.4±1.4 mm/yr in Stevens and Avouac(2015) [73]. As a section-wise slip rate estimation, the values are estimated at 15.5 mm/yr in the western Nepal Himalaya,

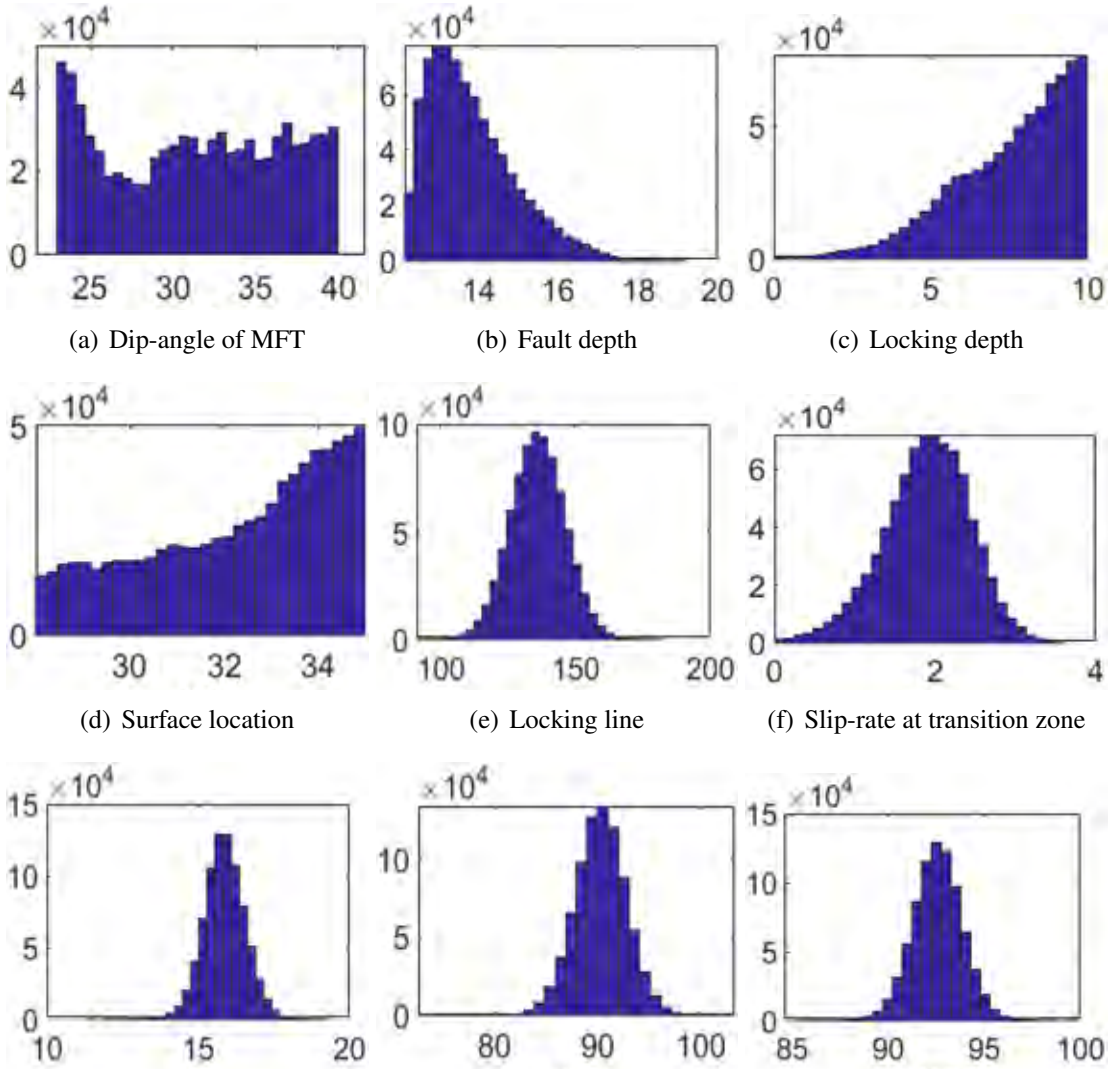

(a) Dip-angle of MFT (b) Fault depth (c) Locking depth

(d) Surface location (e) Locking line (f) Slip-rate at transition zone

(g) Slip-rate of MHT (h) Rake angle of MFT (i) Rake angle of MHT

Figure 4.32: Posterior probability distributions for the inversion fault model in the N4 profile.

13.8 mm/yr in the central Nepal Himalaya, and 12.4 mm/yr in the eastern Nepal Himalaya (Figure 4.10). Figure 4.9 presents a segment-wise comparison of slip rates estimated in this analysis with the corresponding values from previous studies. To note, the PPDs for rake angle and slip rate of MFT and MHT consistently exhibit Gaussian shapes, reaffirming a well-constrained nature of these parameters (Figures 4.29 to 4.45).

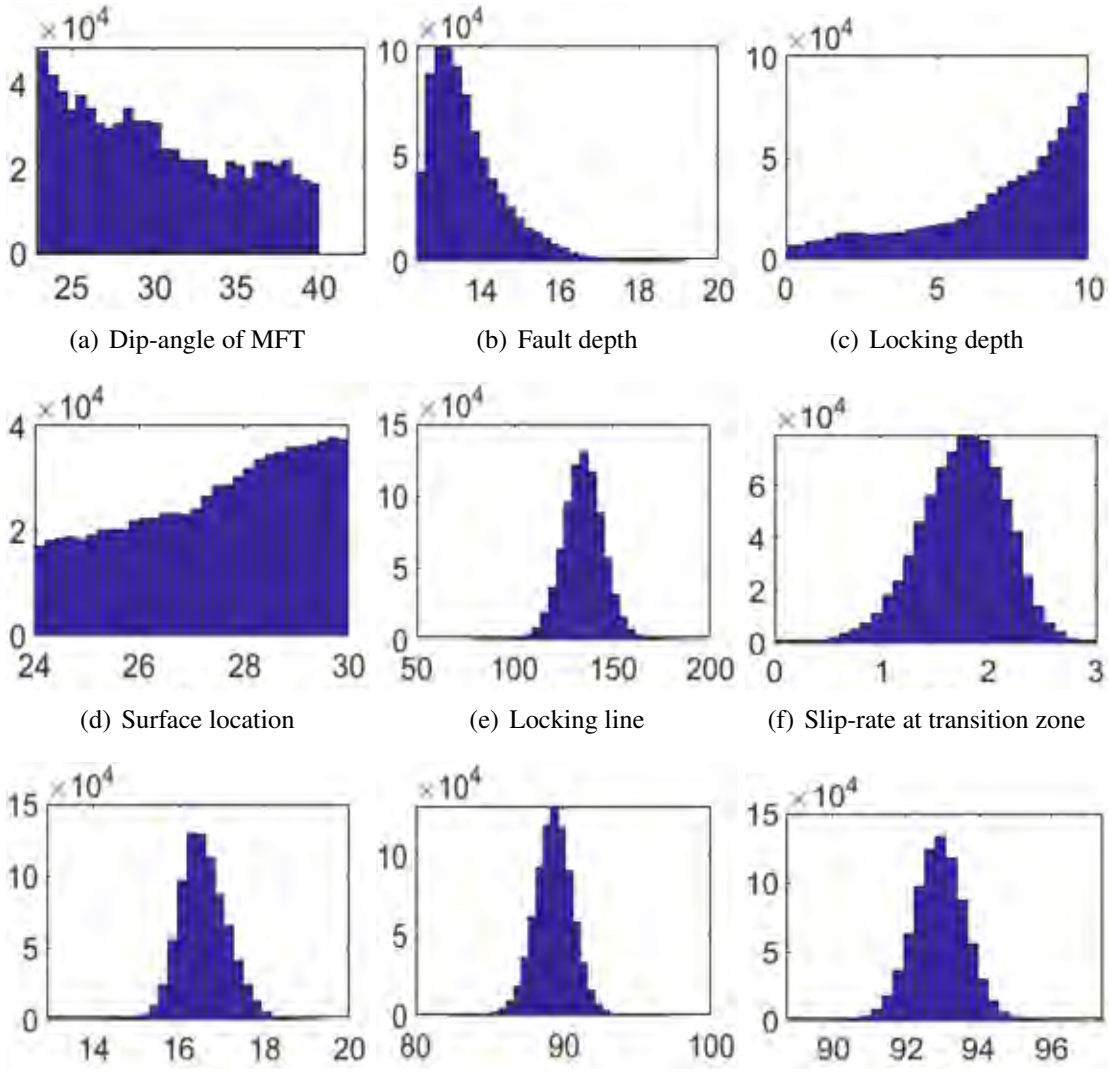

(a) Dip-angle of MFT (b) Fault depth (c) Locking depth

(d) Surface location (e) Locking line (f) Slip-rate at transition zone

(g) Slip-rate of MHT (h) Rake angle of MFT (i) Rake angle of MHT

Figure 4.33: Posterior probability distributions for the inversion fault model in the N5 profile.

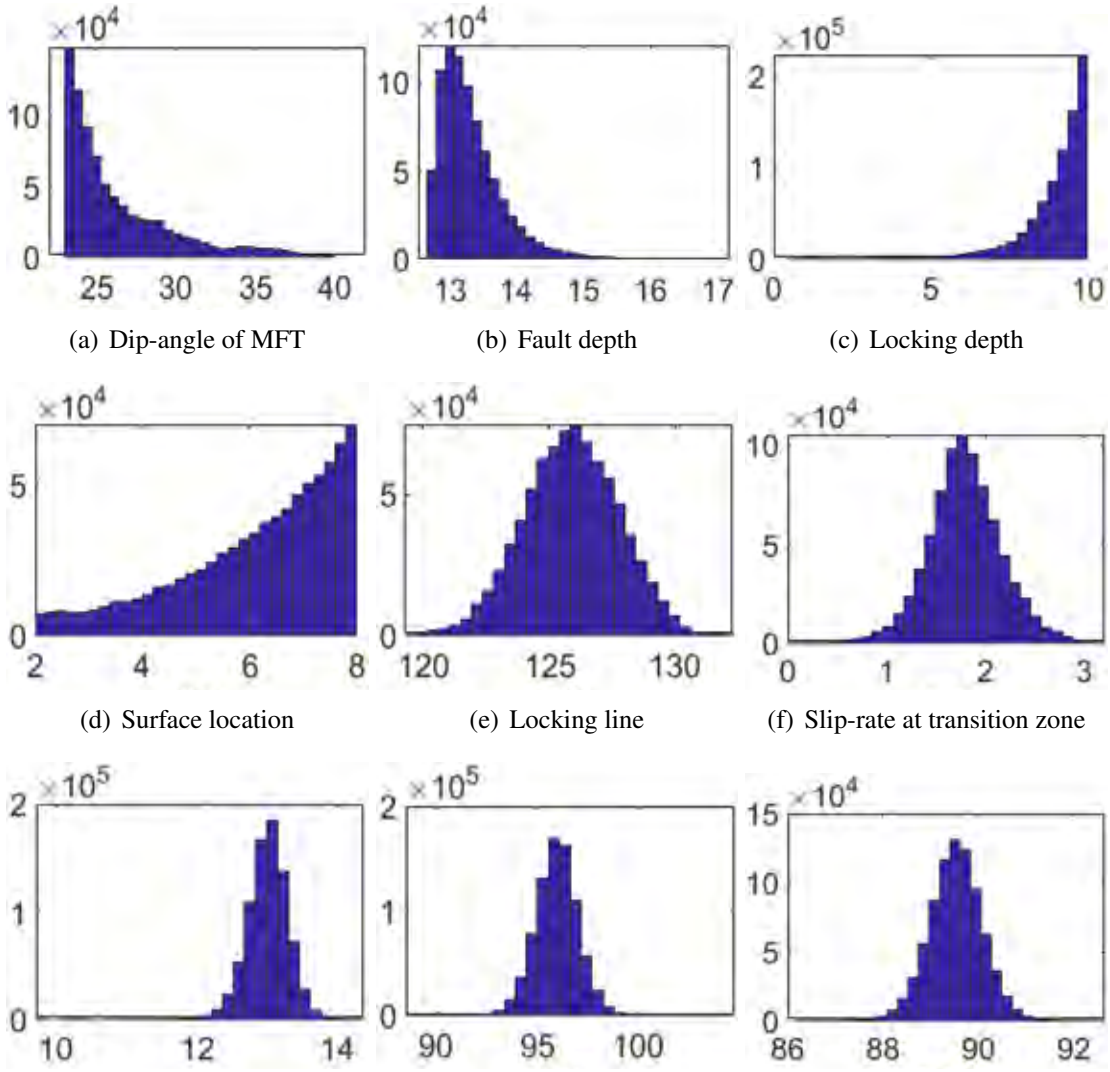

(a) Dip-angle of MFT (b) Fault depth (c) Locking depth

(d) Surface location (e) Locking line (f) Slip-rate at transition zone

(g) Slip-rate of MHT (h) Rake angle of MFT (i) Rake angle of MHT

Figure 4.34: Posterior probability distributions for the inversion fault model in the N6 profile.

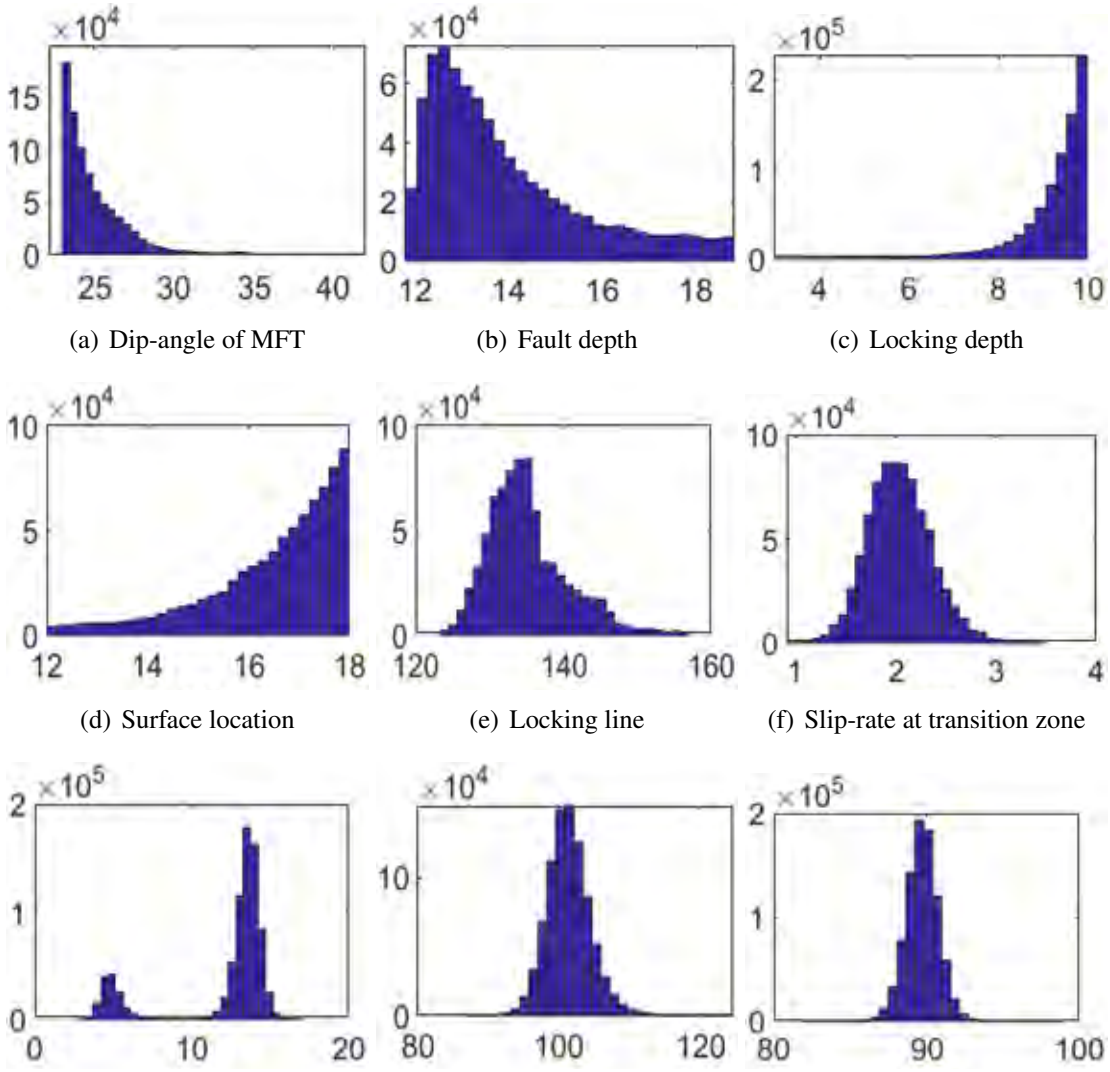

(a) Dip-angle of MFT (b) Fault depth (c) Locking depth

(d) Surface location (e) Locking line (f) Slip-rate at transition zone

(g) Slip-rate of MHT (h) Rake angle of MFT (i) Rake angle of MHT

Figure 4.35: Posterior probability distributions for the inversion fault model in the N7 profile.

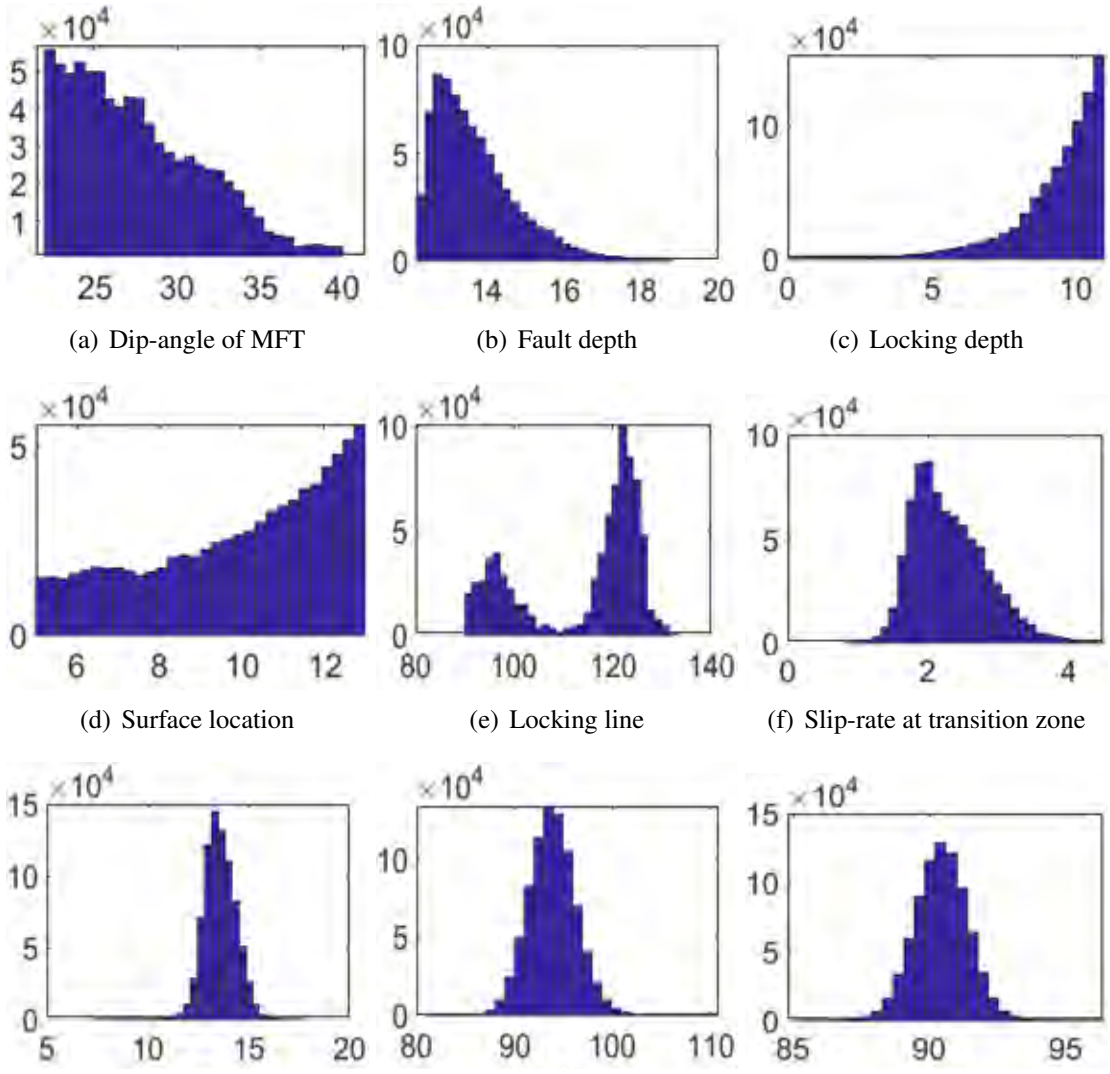

(a) Dip-angle of MFT (b) Fault depth (c) Locking depth

(d) Surface location (e) Locking line (f) Slip-rate at transition zone

(g) Slip-rate of MHT (h) Rake angle of MFT (i) Rake angle of MHT

Figure 4.36: Posterior probability distributions for the inversion fault model in the N8 profile.

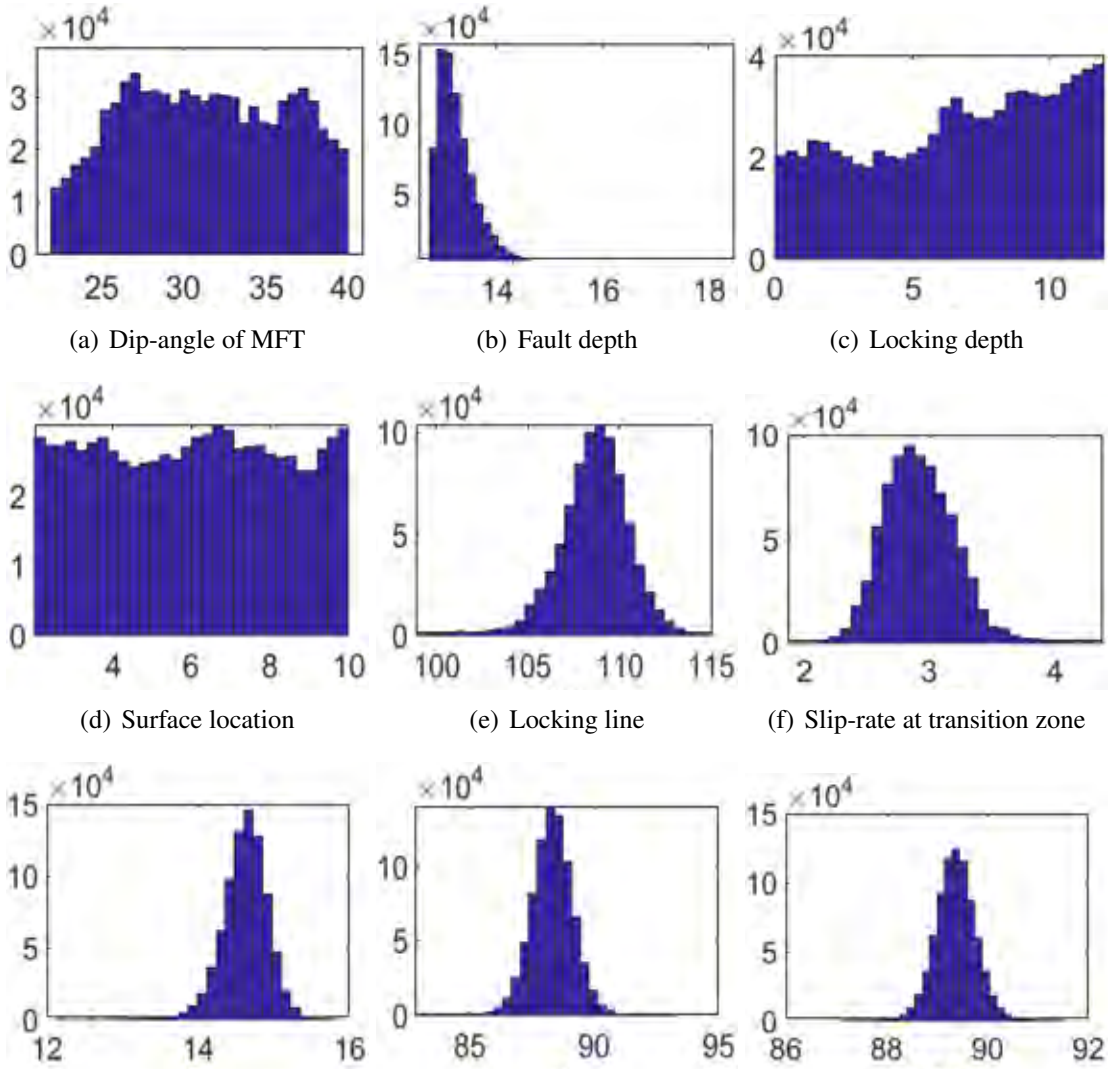

(a) Dip-angle of MFT (b) Fault depth (c) Locking depth

(d) Surface location (e) Locking line (f) Slip-rate at transition zone

(g) Slip-rate of MHT (h) Rake angle of MFT (i) Rake angle of MHT

Figure 4.37: Posterior probability distributions for the inversion fault model in the N9 profile.

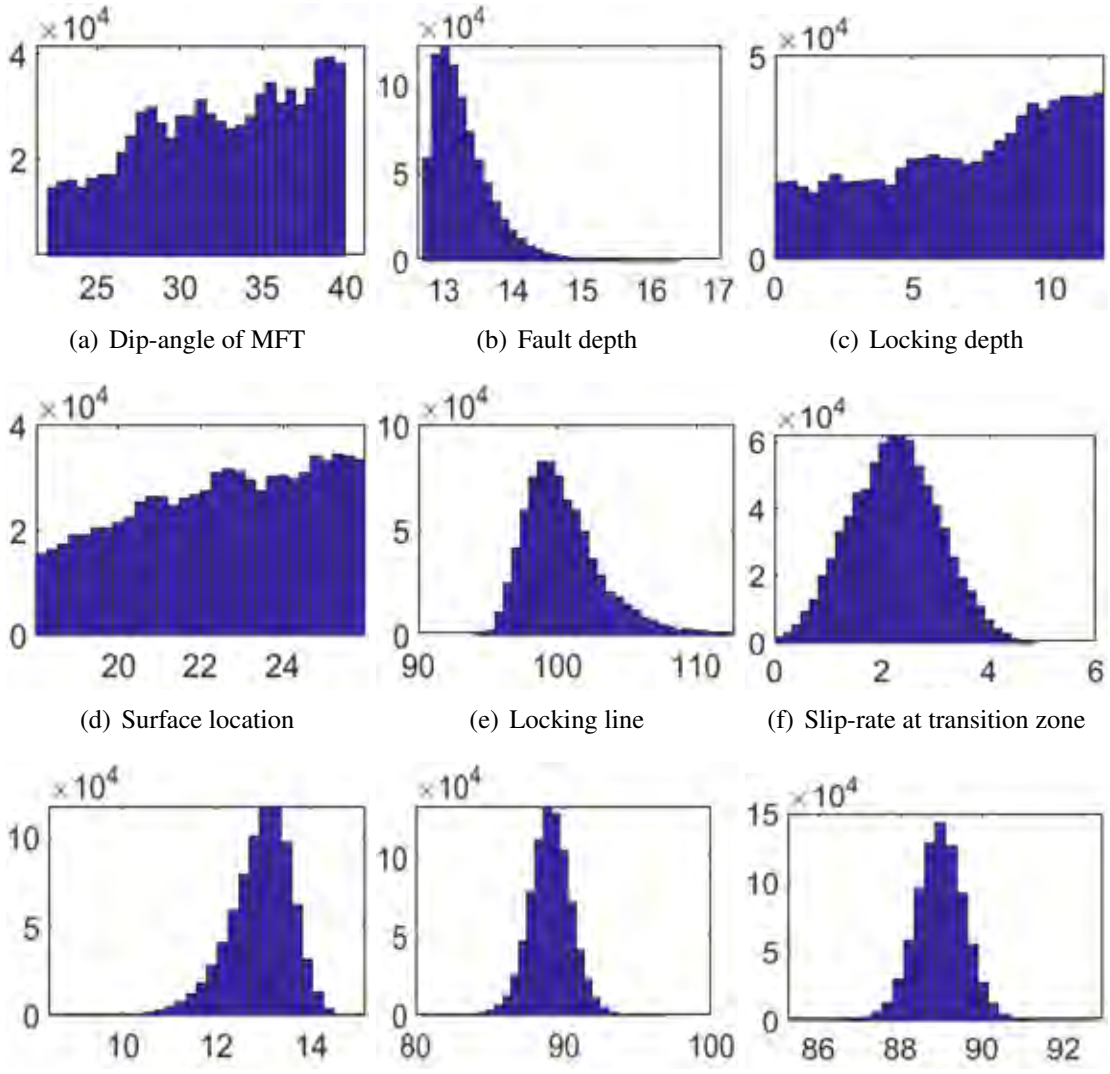

(a) Dip-angle of MFT (b) Fault depth (c) Locking depth

(d) Surface location (e) Locking line (f) Slip-rate at transition zone

(g) Slip-rate of MHT (h) Rake angle of MFT (i) Rake angle of MHT

Figure 4.38: Posterior probability distributions for the inversion fault model in the N10 profile.

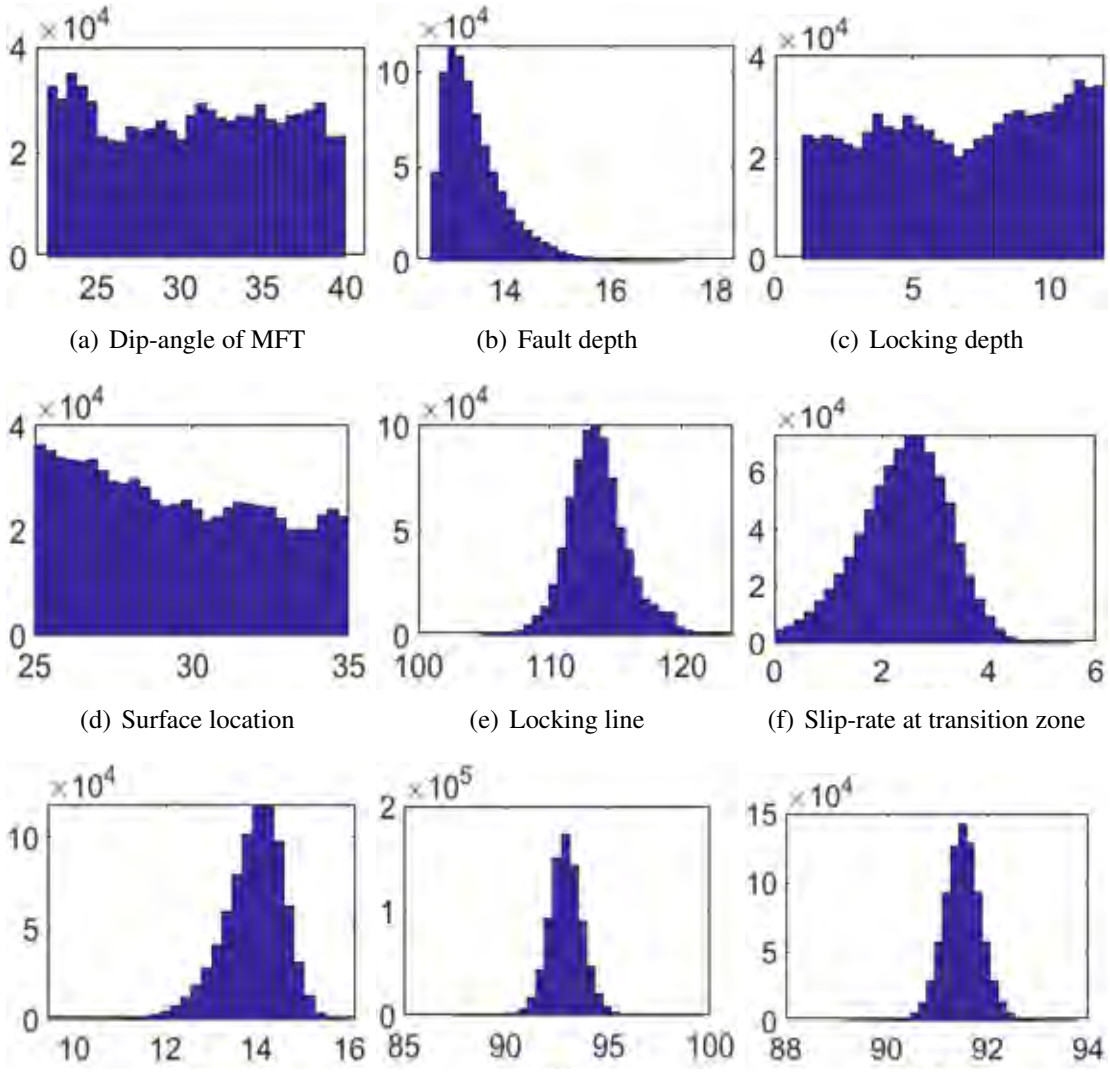

(a) Dip-angle of MFT (b) Fault depth (c) Locking depth

(d) Surface location (e) Locking line (f) Slip-rate at transition zone

(g) Slip-rate of MHT (h) Rake angle of MFT (i) Rake angle of MHT

Figure 4.39: Posterior probability distributions for the inversion fault model in the N11 profile.

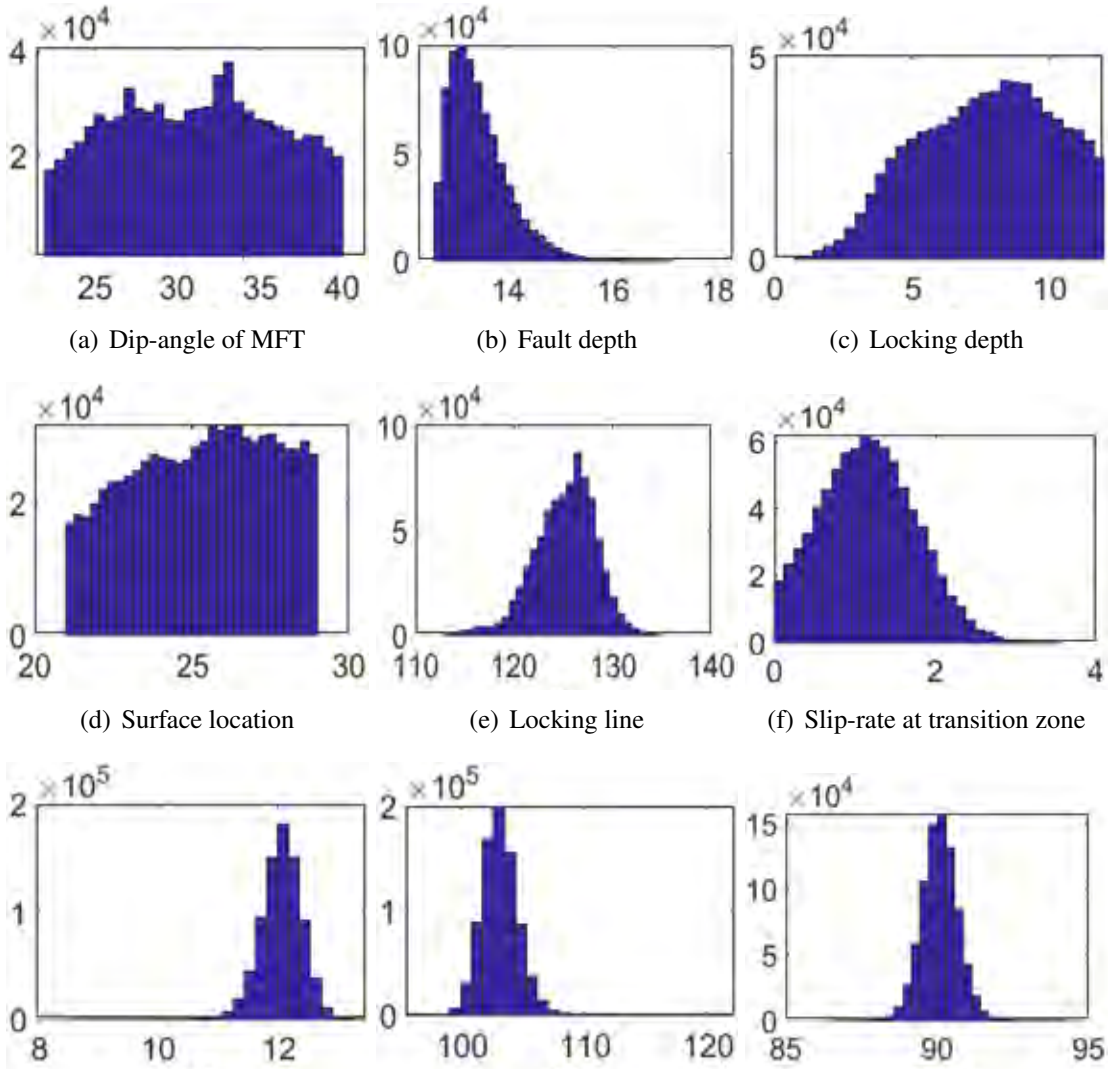

(a) Dip-angle of MFT (b) Fault depth (c) Locking depth

(d) Surface location (e) Locking line (f) Slip-rate at transition zone

(g) Slip-rate of MHT (h) Rake angle of MFT (i) Rake angle of MHT

Figure 4.40: Posterior probability distributions for the inversion fault model in the N12 profile.

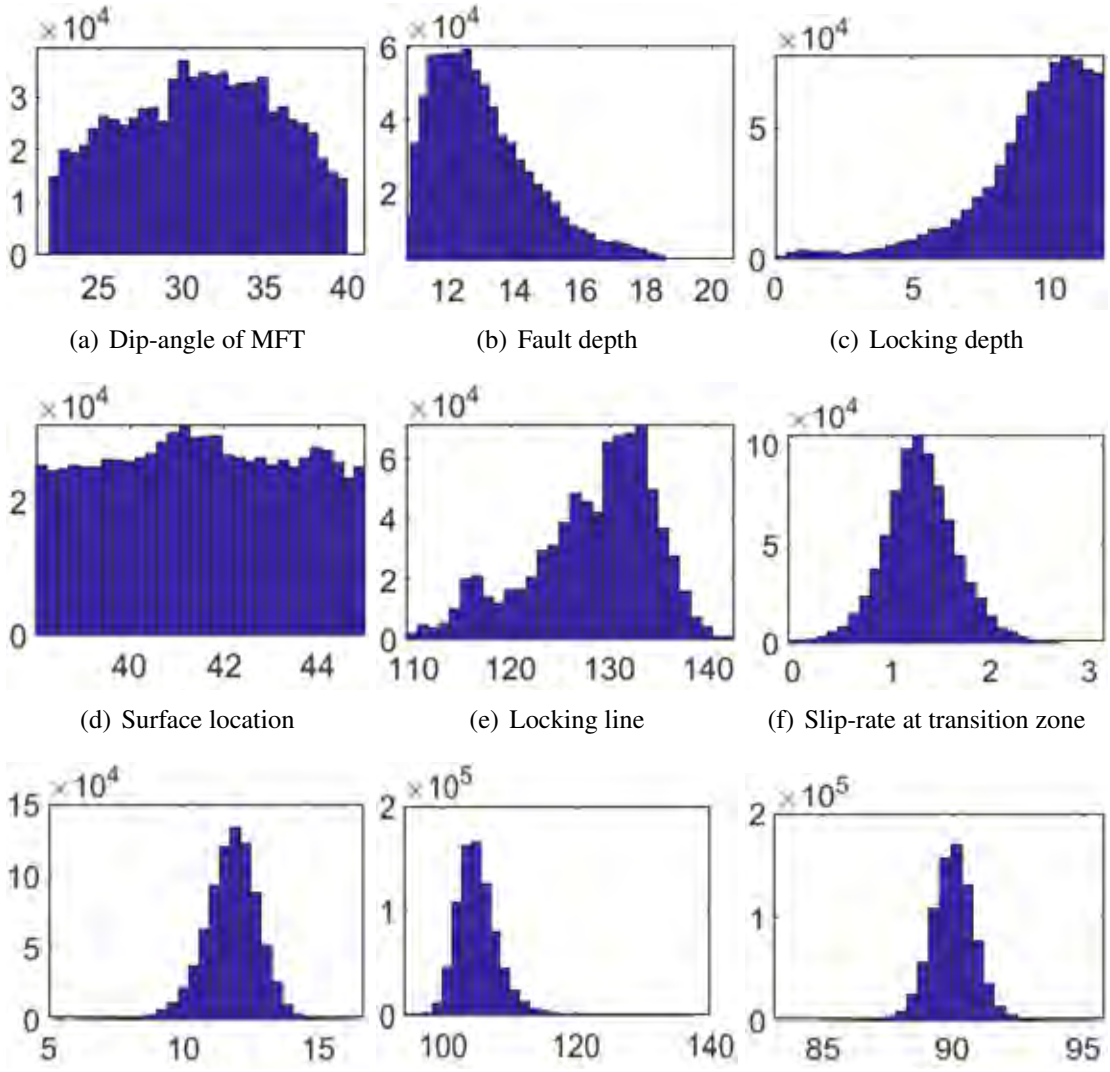

(a) Dip-angle of MFT (b) Fault depth (c) Locking depth

(d) Surface location (e) Locking line (f) Slip-rate at transition zone

(g) Slip-rate of MHT (h) Rake angle of MFT (i) Rake angle of MHT

Figure 4.41: Posterior probability distributions for the inversion fault model in the N13 profile.

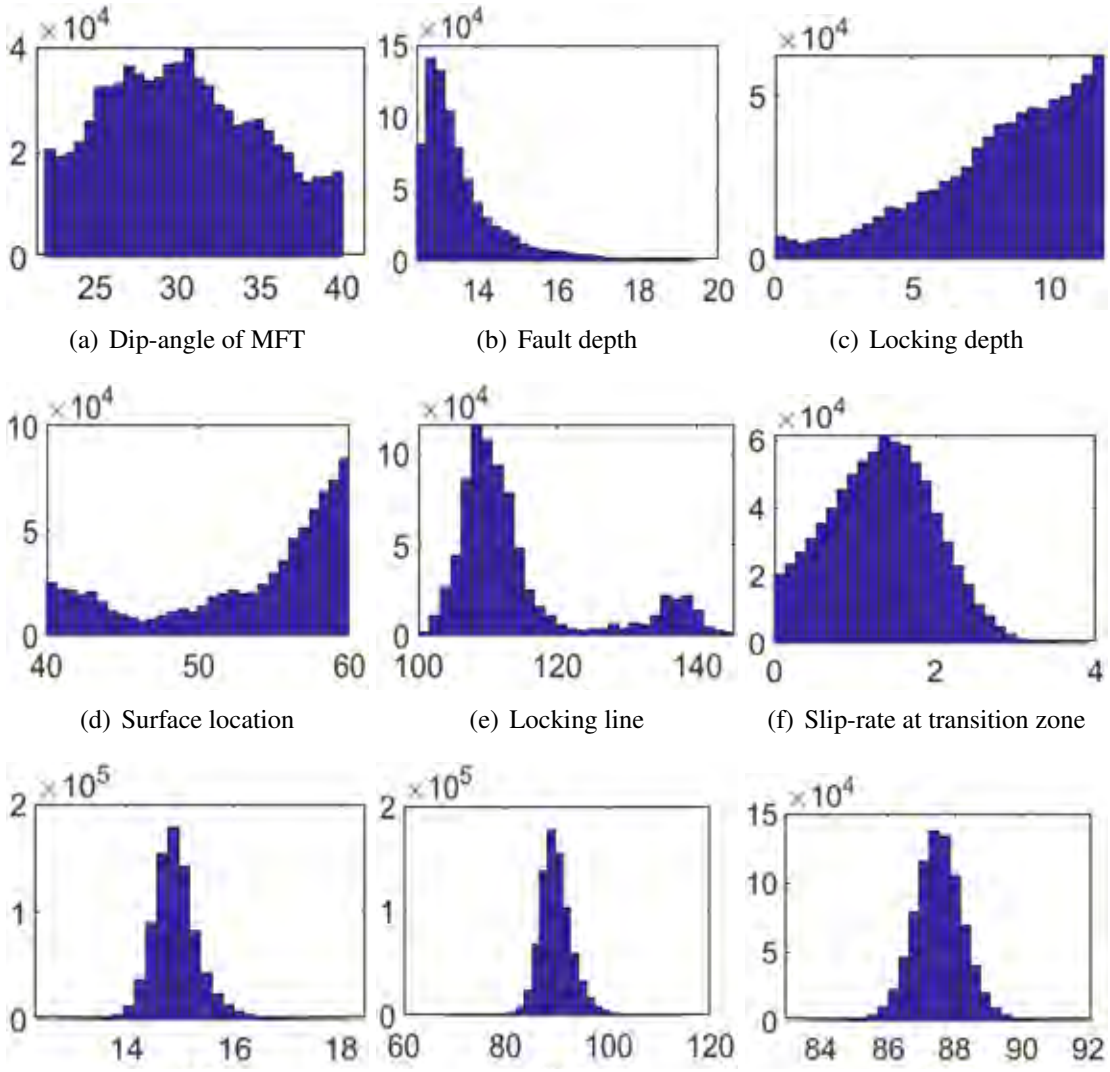

(a) Dip-angle of MFT (b) Fault depth (c) Locking depth

(d) Surface location (e) Locking line (f) Slip-rate at transition zone

(g) Slip-rate of MHT (h) Rake angle of MFT (i) Rake angle of MHT

Figure 4.42: Posterior probability distributions for the inversion fault model in the N14 profile.

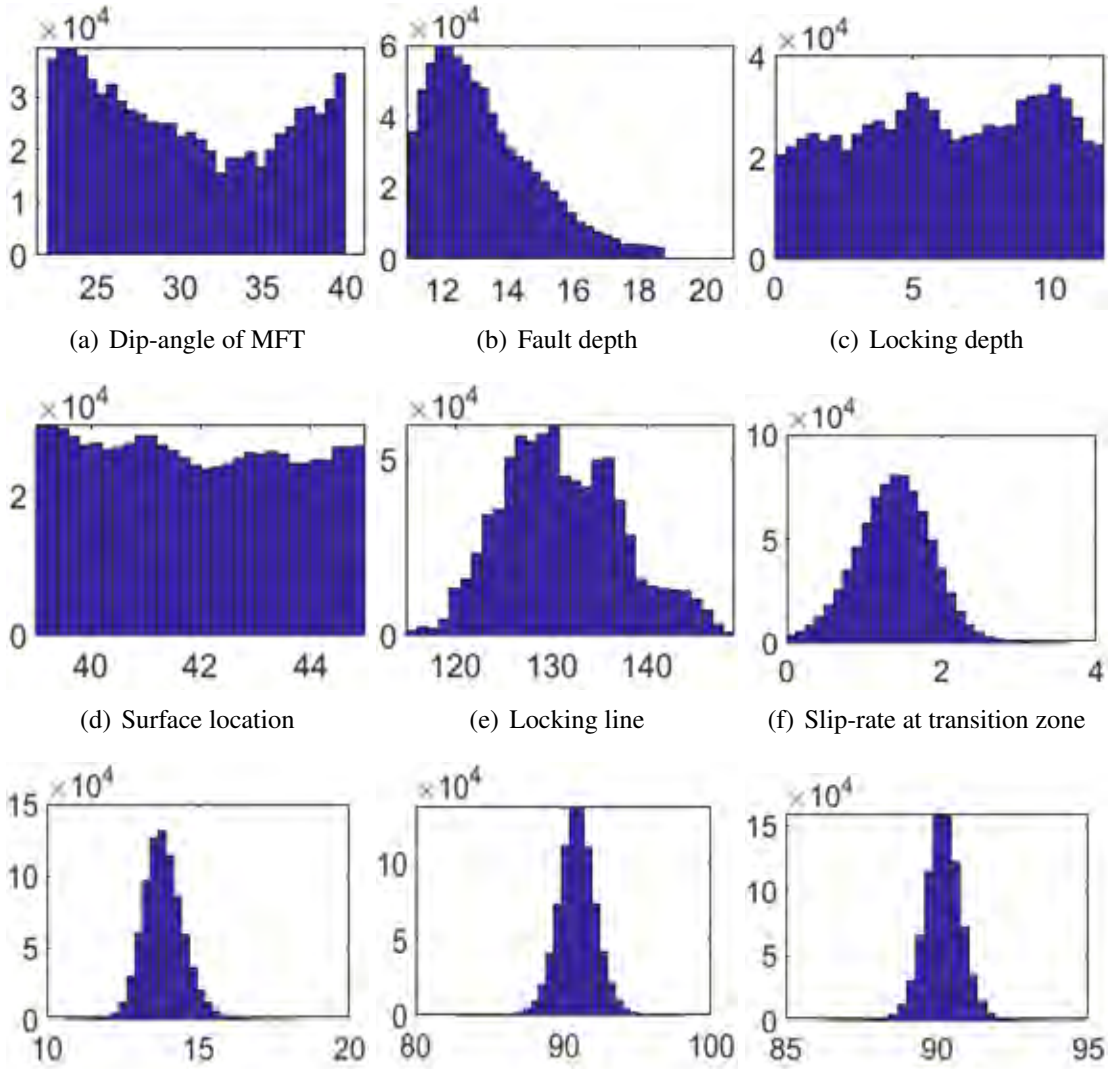

(a) Dip-angle of MFT (b) Fault depth (c) Locking depth

(d) Surface location (e) Locking line (f) Slip-rate at transition zone

(g) Slip-rate of MHT (h) Rake angle of MFT (i) Rake angle of MHT

Figure 4.43: Posterior probability distributions for the inversion fault model in the N15 profile.

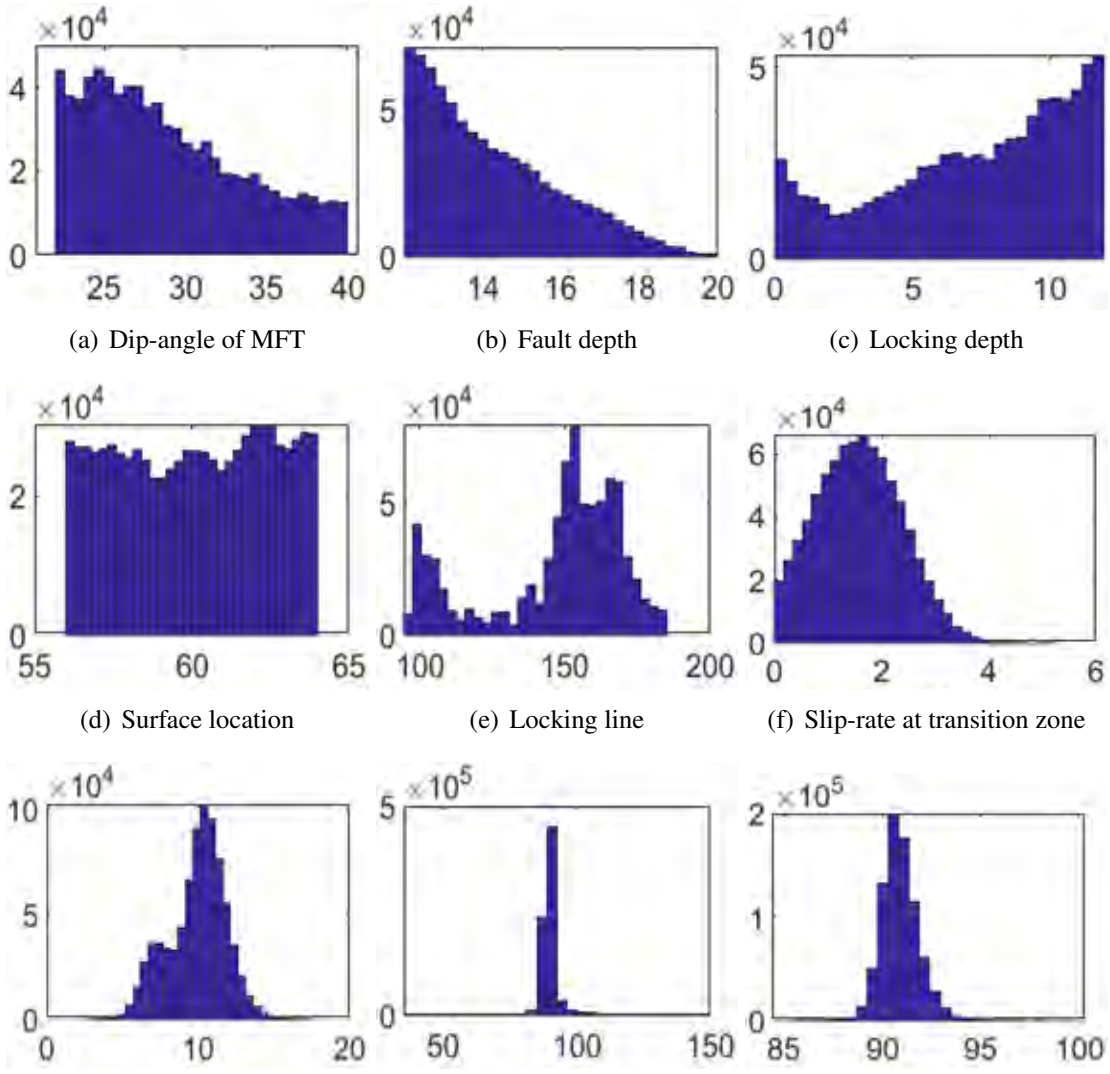

(a) Dip-angle of MFT (b) Fault depth (c) Locking depth

(d) Surface location (e) Locking line (f) Slip-rate at transition zone

(g) Slip-rate of MHT (h) Rake angle of MFT (i) Rake angle of MHT

Figure 4.44: Posterior probability distributions for the inversion fault model in the N16 profile.

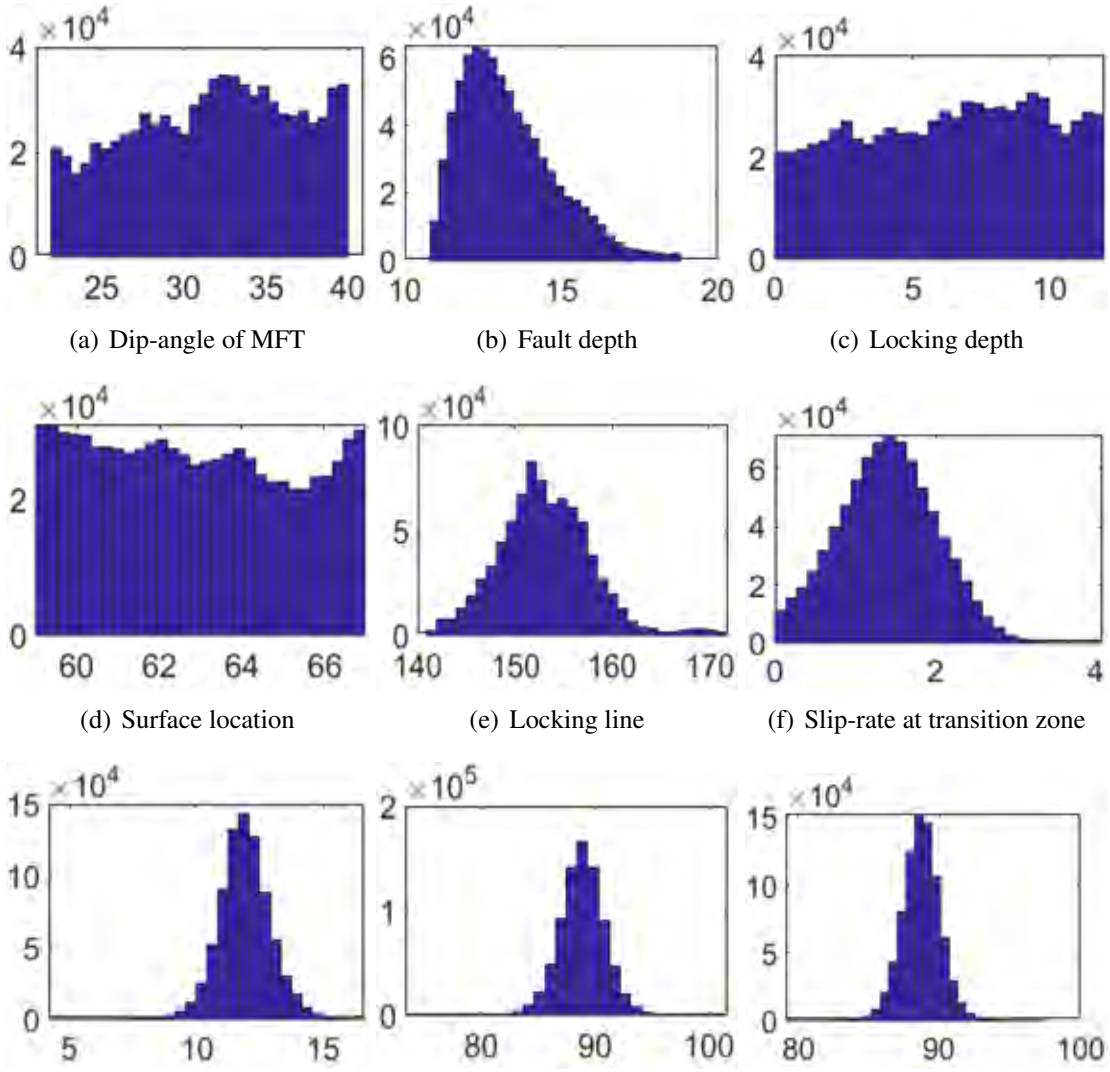

(a) Dip-angle of MFT (b) Fault depth (c) Locking depth

(d) Surface location (e) Locking line (f) Slip-rate at transition zone

(g) Slip-rate of MHT (h) Rake angle of MFT (i) Rake angle of MHT

Figure 4.45: Posterior probability distributions for the inversion fault model in the N17 profile.

In summary, the Kumaun Himalaya exhibits consistent fault parameters, with dip angles ranging from 29.0° to 32.7°, locking depths between 9.5±2.5 km and 10.2±1.3 km, and fault depths approximately 12.2±0.2 km. Notably, the modeled locking line positions fall within 110.1±0.8 km to 116.4±1.2 km from the surface trace of the MFT. The slip rate of the MHT across the Kumaun Himalaya ranges from 20.0±0.2 mm/yr to 18.4±0.2 mm/yr. Similarly, in the Nepal Himalaya, fault parameters are estimated across

distinct sections. In the western Nepal Himalaya, the MFT dip angle is estimated as 28.0°, with locking depth and fault depth of 7.8 km and 13.7 km, respectively. In the central Nepal Himalaya, the dip angle is 30.5°, with locking depth and fault depth of 7.5 km and 13.4 km, respectively. Modeled locking line positions span between 100.4±2.8 km to 153.1±4.7 km from the surface trace of the MFT. Slip rates of the MHT vary within each section, namely 15.5 mm/yr in the western Nepal Himalaya, 13.8 mm/yr in the central Nepal Himalaya, and 12.4 mm/yr in the eastern Nepal Himalaya. Overall, these findings offer valuable insights into fault kinematics and slip distribution as sought in the seismic hazard analysis and understanding tectonic dynamics in the Kumaun-Nepal Himalaya.

Table 4.4: Misfit test for the implemented inversion model

Profile	Rmisfit	Rnorm
K1	0.9355	0.3282
K2	0.6135	0.2144
K3	0.6834	0.2194
N1	0.8924	0.2781
N2	0.4839	0.1375
N3	0.5404	0.1712
N4	0.8321	0.3320
N5	0.7852	0.3548
N6	0.6567	0.2888
N7	1.1049	0.4172
N8	0.8456	0.3419
N9	0.5786	0.2349
N10	0.7029	0.2689
N11	0.4919	0.2118
N12	0.5301	0.2372
N13	0.8618	0.4065
N14	0.9164	0.2790
N15	1.0104	0.4709
N16	0.7210	0.6181
N17	0.5426	0.5513

In addition, to assess the robustness and accuracy of the Bayesian inversion model, the root-mean-square misfit (Rmisfit) and normalized misfit (Rnorm) are calculated for each profile. The Rmisfit values, ranging from 0.48 to 1.10 (Table 4.4), indicate the overall

discrepancy between observed and predicted velocities. Meanwhile, the Rnorm values, lying between 0.14 and 0.62 (Table 4.4), represent the normalized misfit, highlighting the relative agreement between observed and predicted velocities normalized by the observation errors. The calculated Rnorm and Rmisfit values across multiple profiles show an insignificantly small difference between observed and predicted velocities. Overall, these findings highlight the model's accuracy in depicting the observed velocity field, validating its suitability for understanding fault behaviors in the region.

4.6 Implication of seismic hazard in the Kumaun-Nepal Himalaya

In the previous sections of this chapter, the distribution of slip rates along the MHT is provided, offering valuable insights into the region's long-term deformation and seismic activity potential. In this section, earthquake potential across the study area is calculated by deriving moment rates from the slip deficit rate of the MHT in both Kumaun Himalaya and various sections (as described in Figure 3.9) of the Nepal Himalaya.

The estimated slip rates along the locked-to-creeping transition zone of the MHT in Kumaun Himalaya, western Nepal Himalaya, central Nepal Himalaya, and eastern Nepal Himalaya are as follows: 2.6 ± 0.4 mm/yr, 2.2 ± 0.9 mm/yr, 2.5 ± 0.5 mm/yr, and 1.5 ± 1.0 mm/yr, respectively (Tables 4.2 and 4.3). The differences between the slip rates observed along the transition zone and the creeping zone enable us to calculate the slip deficit rate along the MHT. The analysis reveals a slip deficit rate of approximately 16.5 mm/yr in Kumaun Himalaya, 13.3 mm/yr in western Nepal, 11.3 mm/yr in central Nepal, and 10.9 mm/yr in eastern Nepal. These values signify that the accumulated slip is yet to be released along the MHT in each respective region. Estimating the slip deficit rates provides valuable insights into the potential for future seismic activity and the associated seismic hazard in the locked segments of the MHT.

The estimation of moment deficit rate of the MHT is determined by the following

Table 4.5: Slip-deficit rate and earthquake potential along the Kumaun and Nepal Himalaya

Sections of Himalaya	Slip-deficit rate (mm/yr)	Moment deficit rate $(10^{18} Nm/yr)$	Earthquake Potential M_w
Kumaun	16.5	4.96	8.3
Western Nepal	13.3	11.74	8.5
Central Nepal	11.3	5.31	8.2
Eastern Nepal	10.9	8.07	8.0

equation:

$$\dot{M}_0 = \mu \dot{D} A. \tag{4.6.1}$$

In the above equation, μ represents the assumed shear modulus with a value of $3 \times 10^{10} N/m^2$, $\dot{D}$ is the slip deficit rate, and A denotes the specified area. By multiplying the fault length, estimated depth of MHT in each segment, and estimated slip deficit rate, the moment build-up rate for each section is computed (Table 4.5). The length of the MHT in each section approximately corresponds to the geographical extent of that particular section and the depth of the MHT in each section is determined by averaging the modeled depth from each transect within the respective section (Tables 4.2 and 4.3).

The accumulated moment deficit rates along the Kumaun Himalaya, western Nepal Himalaya, central Nepal Himalaya, and eastern Nepal Himalaya are 4.96×10^{18} Nm/yr, 11.74×10^{18} Nm/yr, 5.31×10^{18} Nm/yr, and 8.07×10^{18} Nm/yr, respectively. Considering an estimated seismic cycle duration of approximately 500 years for a great Himalayan earthquake [73, 89], the earthquake potential is evaluated for each section of the study region. The moment deficit rate observations indicate an earthquake potential of M_w 8.2 in the Kumaun Himalaya, M_w 8.4 in western Nepal, M_w 8.2 in central Nepal, and M_w 8.3 in eastern Nepal (Table 4.5). In summary, the earthquake potential estimates ranging from M_w 8.2 to M_w 8.4 in this study align with the earthquake magnitude range outlined by Bilham (2019) [5].

4.7 Comparison of area-based and fault-based moment deficit and earthquake potential in the study region

Comparing the moment deficit rates and earthquake potentials derived from different methodologies is crucial due to the multifaceted nature of seismic hazard assessment. Such a comparison helps to validate the robustness and reliability of each approach by examining the consistency or inconsistency in their outcomes. In the Chapter 3, an area-based approach was introduced, which evaluates the seismic budget by considering the overall seismic activity and strain accumulation within a specific section/area. Conversely, the fault-based approach focuses on fault characteristics, such as slip rates, geometry, and the stress build-up along a specific fault segment to calculate the likelihood of seismic occurrences exclusive to that fault.

The comparison between moment deficit rates from the area-based and fault-based approaches reveals different perspectives on seismic strain accumulation. The area-based approach in Kumaun Himalaya approximates a moment deficit rate of $7.59 \times 10^{18} Nm/yr$, while the fault-based analysis suggests a relatively lower rate, approximately $4.96 \times 10^{18} Nm/yr$. However, both methodology suggest significant amount of stress accumulation in the western Nepal Himalaya. In the western Nepal Himalaya, the area-based analysis suggests a moment deficit rate of $12.13 \times 10^{18} Nm/yr$, slightly lower than the fault-based estimation of approximately $11.74 \times 10^{18} Nm/yr$. With the minor variance, both methodologies suggest a consistent trend in stress accumulation within the western Nepal Himalaya. In case of central Nepal Himalaya, both approaches provide closely aligned estimates, with the area-based assessment suggesting a moment deficit rate of approximately $4.74 \times 10^{18} Nm/yr$ and the fault-based analysis yielding a value of approximately $5.31 \times 10^{18} Nm/yr$. Along the eastern Nepal Himalaya, the area-based assessment predicts a moment deficit rate of approximately $5.33 \times 10^{18} Nm/yr$, while the fault-based approach estimates a relatively higher value at around $8.07 \times 10^{18} Nm/yr$.

The above variation in the moment deficit rates results into different order of earthquake

potential across distinct sections of the study area. For instance, there is an earthquake potential of M_w 8.1 and M_w 8.2 in the Kumaun Himalaya corresponding to the area-based and fault-based approaches, respectively. Similar figures for the western Nepal are M_w 8.5 and M_w 8.4, respectively; for the central Nepal, these values are M_w 7.9 and M_w 8.2, respectively; for the eastern Nepal, there is a potential of M_w 8.1 and M_w 8.3, respectively. Overall, each section of the study area reveals the potential of a future great earthquake. To note, there have been some discrepancies in the area-based and fault-based earthquake potential estimation. This is mainly due to two factors: (i) inconsistency between area-based and fault-based moment deficits (as discussed above) and (ii) the consideration of time-span for moment accumulation in area-based and fault-based approaches. For example, in the Kumaun Himalaya, a catalog length of 200 years was considered in the area-based computation, whereas it was 500 years in the fault-based calculation.

4.8 Summary

Using a high-resolution integrated velocity field and a Bayesian inversion fault model, this chapter has presented the fault geometry and slip partitioning of the MHT over 20 arc-normal profiles across the Kumaun-Nepal Himalaya. In the chosen inversion approach, a fault geometry is assumed to consist of a basal detachment along with a fully locked zone, a locked-to-creeping transition zone, and a creeping zone. The analyses yield to the following findings:

1. In the Kumaun Himalaya, the dip angle, locking depth, and fault depth for the MFT are 31°, 9.8 km, and 12.3 km, respectively. In western Nepal, these values are 28°, 7.8 km, and 13.7 km, while in central Nepal, they are 30.5°, 7.5 km, and 13.4 km. Similarly, in eastern Nepal, the corresponding values are 30.5°, 7.5 km, and 13.5 km.

2. The long-term slip rate of the MHT is 19.1 mm/yr in the Kumaun Himalaya, 15.5 mm/yr in the western Nepal Himalaya, 13.8 mm/yr in the central Nepal Himalaya, and 12.4 mm/yr in the eastern Nepal Himalaya.

3. The determined slip rate of the MHT corresponds to a slip deficit of 16.5 mm/yr in the Kumaun Himalaya, 13.3 mm/yr in the western Nepal Himalaya, 11.3 mm/yr in the central Nepal Himalaya, and 10.9 mm/yr in the eastern Nepal Himalaya.

4. The observed slip-deficit rate across the study region implies an earthquake potential of M_w 8.2 in the Kumaun Himalaya, M_w 8.4 in the western Nepal Himalaya, M_w 8.2 in the central Nepal, and M_w 8.3 in the eastern Nepal Himalaya.

5. Overall, the findings regarding earthquake potentials from Chapter 3 and Chapter 4 suggest that each section of the study area has the potential to produce large earthquake(s), which could have catastrophic impacts on the human population.

In summary, the utilized Bayesian inversion model for fault analysis in this study offers a comprehensive analysis of the fault kinematics and slip distribution pertaining to the MHT across the study region. Consequently, this makes a substantial contribution towards enhancing the time-dependent seismic hazard analysis.

Chapter 5

Seismicity Statistics in the Kumaun-Nepal Himalaya

"Earthquake forecasting may never be perfect, but it has the potential to significantly reduce the impact of seismic events on communities."

—Thomas Jordan

Unlike the previous chapters (Chapters 3 and 4) that analyze the seismic hazards along the Kumaun-Nepal using geodetic methods, the present chapter has carried out statistics based empirical earthquake hazard estimation. Essentially, this chapter performs earthquake forecasting based on interevent times and earthquake nowcasting based on interevent counts (natural times) in the study region. To employ earthquake forecasting, (i) the compiled earthquake data is re-considered from Chapter 2; then, (ii) the interevent time of successive large events ($M_w \geq 6.5$) is modeled from several reference probability distributions and finally, (iii) the conditional probability of large events and associated hazard function curves are derived for a set of elapsed and residual times. On the other hand, to perform seismic nowcasting, (i) "natural time" counts, counts of $4.0 \leq M_w < 6.0$ earthquakes between two successive large events ($M_w \geq 6.0$), are tabulated; then, (ii) natural time seismicity statistics is derived through several reference probability distributions and finally, (iii) the current progression of regional earthquake cycle is

calculated at several city regions in terms of earthquake potential score (EPS). Overall, the findings from Chapters 3 to 5 provide a comprehensive seismic hazard analysis in the study area using both geodetic and statistical models.

Contents

Part of this chapter has been published in the following refereed publications:

S. Pasari, **H. Verma.** "Recurrence Statistics of M≥6 Earthquakes in the Nepal Himalaya: Formulation and Relevance to Future Earthquake Hazards". *Natural Hazards* 120 (2024), pp. 7725–7748 (SCIE).

5.1 Introduction

With the increasing population, urbanization and economic development, the occurrence of large earthquakes has a long lasting impression. The knowledge of temporal properties of these damaging earthquakes in a geographic region is a crucial factor in earthquake hazard quantification and associated disaster mitigation [191]. Statistical methods are often preferred for a quantitative assessment of the temporal properties. These methods inherently account for all possible random variations present in earthquake data. As the earthquake modeling often entails significant uncertainty and variability regarding magnitude, epicentral location, focal depth, and other factors [266–268], probabilistic approaches tend to offer a more realistic representation compared to deterministic ones [269]. Additionally, earthquake catalogs can differ depending on the seismic database source (e.g., ISC, IMD, USGS, and GCMT). Thus, applying a multitude of probability models to the same catalog may help mitigate the impact of inherent data variations.

Statistical properties of earthquake interevent times have long been the topic of interest to seismologists and earthquake professionals mainly for hazard related concerns. Traditionally, it has been assumed that the number of earthquakes in a fixed time interval follows a Poisson distribution, suggesting that the interevent times must follow the time-independent exponential distribution [270, 271]. However, due to the "memoryless" nature of the exponential model, recent studies have considered a variety of time-dependent models to examine the recurrence statistics of large earthquakes [183, 184, 271]. In fact, as earthquake occurrence is influenced by dynamic factors, such as aftershocks, foreshocks, and seismicity clusters that evolve over time, employing time-dependent models would be crucial to accurately capture and predict seismic activity patterns [272, 273]. Additionally, previous studies [183, 184, 271] assume that the occurrence of large events (mainshocks) in a spatial region is consistent with a random process. As a consequence, the dependent events, such as foreshocks and aftershocks, are commonly removed from the earthquake records to produce a sequence of random sample [274]. Then, the interevent time statistics and associated long-term (10–30 years) large earthquakes' occurrence probability values

can be derived through the observed sample data. Thus, the present analysis focuses on the interoccurrence time between successive $M_w \geq 6.5$ events in the seismically active Kumaun-Nepal Himalaya and its adjacent regions that host a population of more than 50 million people. Using time-independent, time-dependent, heavy-tailed, and exponentiated models, the study not only estimates the cumulative probability of $M_w \geq 6.5$ events, but also generates a series of hazard function curves for various combination of elapsed times (time elapsed since the last large earthquake) and residual times (time to a future large earthquake).

On the other hand, earthquake nowcasting based on discrete time series utilizes the cumulative counts of small events between large earthquakes to mark the evolution of the system, rather than the passage of clock time [275–277]. Initially emerging from economics and climate science domains, the nowcasting methodology has recently gained traction in seismology and disaster science, particularly where the dataset of interest exhibits a typical frequency-size power-law distribution [15, 184, 278–282]. This approach is developed through two fundamental concepts: the stochastic nature of large earthquakes (earthquake cycle) and the seismicity statistics of interspersed small event counts (natural times) within a defined fault system [276]. Natural time analysis encompasses all seismic events, including foreshocks, aftershocks, and triggered events, to derive ensemble seismicity statistics in the study area. Assuming that the entire study region adheres to a unified driven threshold system, natural time analysis demonstrates space-time invariance [282–285]. Since its inception in 2016, the seismic nowcasting approach has been applied in various countries, such as the United States, India, Indonesia, Iran, Bangladesh, and Pakistan, to assess the current state of regional earthquake hazard [184, 278, 279, 282, 286, 287], to analyze induced seismicity [283], to explore spatiotemporal clustering in global seismicity [285], and to evaluate risk exposure from significant global earthquakes or megatsunamis [15]. Several recent studies have shed light on the possible connection of nowcasting with earthquake forecasting and plate tectonics using, for example, natural time Weibull projection, slider-block toy model, space–time clustering behavior of bursts of small earthquakes and time-dependent earthquake cycle analysis through machine

learning [15, 277, 280].

In light of the above, the present chapter has carried out probabilistic earthquake recurrence modeling and natural time analysis to estimate the conditional probability of large-sized earthquakes and the current state of developing earthquake cycle at several city regions, respectively. A step-by-step procedure of earthquake interevent and nowcasting techniques is provided in the following sections.

5.2 Earthquake interevent time-modeling along Kumaun-Nepal Himalaya

This section offers a comprehensive account of earthquake interevent time modeling in the study region, encompassing detailed descriptions of the earthquake dataset, methodology, and associated results.

5.2.1 Earthquake data

Kumaun-Nepal and its adjacenent regions have a long history of large earthquakes. For the present analysis, the earthquake data of $M_w \geq 6.5$ events are considered from 1800 through 2023 from the earthquake dataset compiled in Chapter 2. The catalog, both homogenized and complete, comprises 28 events with magnitude $M_w \geq 6.5$. The geographical location of epicentre, earthquake depth, event size (magnitude), and time of occurrences of these large earthquakes are mentioned in Table 5.1. The catalog, however, contains dependent events, such as foreshocks and aftershocks, which must be identified and subsequently removed to adhere to the assumption of independent sequence of earthquake point processes in the study region [271]. For this, the dependent events are classified using a space-time window approach which states that any event in the proximity of another larger event in both space and time should be treated as a dependent event [288]. Moreover, realizing the earthquake-size dependency in aftershocks, a dynamic space-time window method is considered with a more conservative choice [184, 289]. After examining several distance and time windows in producing robust and consistent conclusions to remove dependent

events, 60 days are added/subtracted to the time window, and 15 km to the distance window of Uhrhammer (1986) [289] relations. Therefore, the search radius for earthquake declustering is considered as

$$r = exp(-1.024 + 0.804M_w) \pm 15 \tag{5.2.1}$$

and the time window as

$$t = exp(-2.870 + 1.235M_w) \pm 60. \tag{5.2.2}$$

Based on the above space-time window, four events ($\sim$14%) are marked as dependent events, including one aftershock of the October 1944 event (M_w 6.8) and three aftershocks of the 2015 Gorkha (M_w 7.8) earthquake. Without dependent events, the catalog finally contains 24 large events (Table 5.1 and Figure 5.1), producing 23 interevent times for further analysis.

After declustering, a magnitude-frequency-based visual cumulative test is employed to analyze time-completeness of the present catalog [274, 290]. For this, first the cumulative number of earthquakes versus occurrence times plot is obtained, followed by a linear fit to the data through least-squares regression [184]. It is observed that a near-perfect linear trend is present with $R^2 = 0.94$ (Figure 5.2). Therefore, the present catalog (Table 5.1) is deemed to be time-complete, indicating that earthquake rates and moment releases in the Kumaun-Nepal Himalaya are consistent over sufficiently longer time period. In the subsequent section, a step-by-step methodology and corresponding results of earthquake interevent time analysis are presented.

5.2.2 Methods and results

The principal task in earthquake forecasting is to investigate the best-fit probability distribution for seismic recurrence time between successive large earthquakes in the study region. Such inter-occurrence time analysis is commonly used to characterize long-term earthquake hazard in terms of occurrence probability. It is assumed that the observed

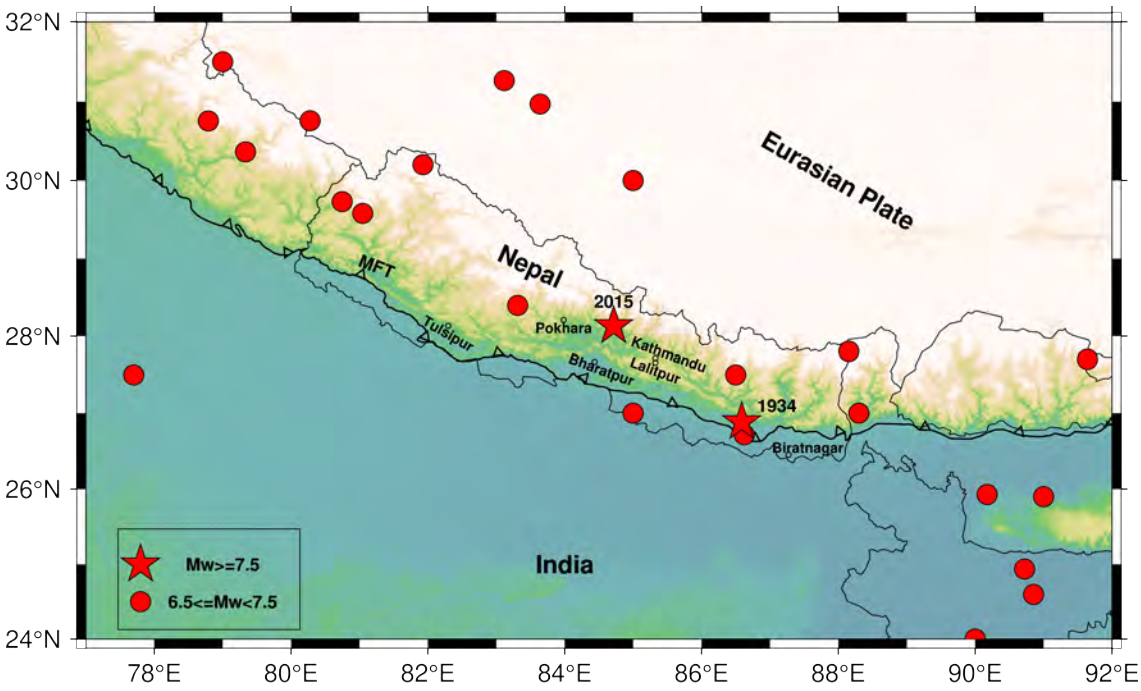

Figure 5.1: Spatial distribution of large earthquakes ($M_w \geq 6.5$) in the Kumaun-Nepal Himalaya and its adjacent regions (Table 5.1). Red stars indicate the location of the 1934 Bihar-Nepal event (M_w 8.0) and the most recent 2015 Gorkha event (M_w 7.8); MFT – Main Frontal Thrust.

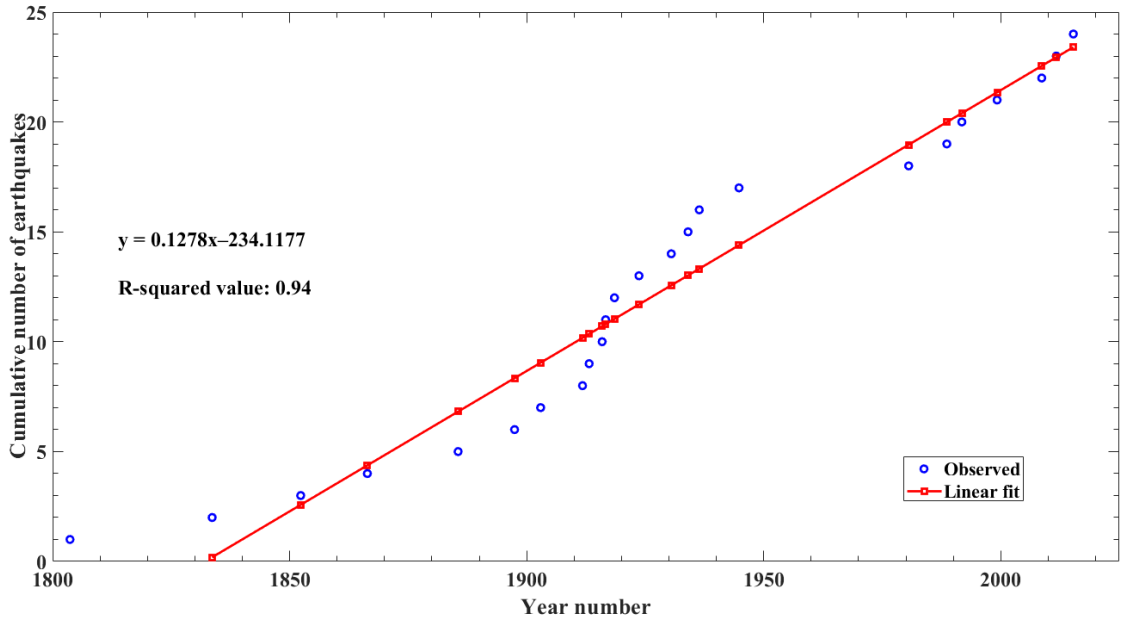

Figure 5.2: The cumulative number of earthquakes of magnitude $M_w \geq 6.5$ (as listed in Table 5.1) versus occurrence times plot in the study region during 1800–2023.

Table 5.1: Focal parameters of $M_w \geq 6.5$ events in Kumaun-Nepal Himalaya and its neighboring areas during 1800–2023

S. No.	Date	Latitude (°N)	Longitude (°E)	Focal Depth (km)	Magnitude (in M_w)	Data Source
1	01-09-1803	31.5000	79.0000	–	7.5^a	A&J[1]
2	26-08-1833	27.5000	86.5000	–	7.4	IMD[2]
3	01-05-1852	27.0000	88.3000	–	6.9	IMD
4	23-05-1866	27.0000	85.0000	–	6.9	IMD
5	14-07-1885	24.0000	90.0000	–	6.9	IMD
6	12-06-1897	25.9000	91.0000	–	7.9	IMD
7	13-12-1902	30.0000	85.0000	–	6.6	IMD
8	14-10-1911	30.7593	80.2794	20.0	6.5^b	ISC[3]
9	06-03-1913	30.2010	81.9290	15.0	6.5^c	USGS[4]
10	03-12-1915	27.6997	91.6401	15.0	6.6^c	ISC
11	28-08-1916	29.7300	80.7454	20.0	7.0^b	ISC
12	08-07-1918	24.5990	90.8528	15.0	7.1^c	ISC
13	09-09-1923	24.9372	90.7207	15.0	6.9^c	ISC
14	02-07-1930	25.9288	90.1765	15.0	7.0^c	ISC
15	15-01-1934	26.8847	86.5885	15.0	8.0^c	ISC
16	27-05-1936	28.3969	83.3110	15.0	6.9^c	ISC
17	17-10-1944	31.2656	83.1143	20.0	6.8^c	ISC
	29-10-1944	31.0080	83.1600	20.0	6.5^c	USGS
18	29-07-1980	29.5800	81.0481	17.5	6.5^d	ISC
19	20-08-1988	26.7162	86.6247	58.1	6.8^d	ISC
20	19-10-1991	30.7560	78.7907	16.1	6.8^d	ISC
21	28-03-1999	30.3635	79.3354	23.8	6.5^d	ISC
22	25-08-2008	30.9704	83.6411	23.9	6.7^d	ISC
23	18-09-2011	27.8039	88.1536	29.6	6.9^d	ISC
24	25-04-2015	28.1302	84.7168	13.4	7.9^d	ISC
	25-04-2015	28.1603	84.8433	14.7	6.7^d	ISC
	26-04-2015	27.7365	85.9788	13.4	6.7^d	ISC
	12-05-2015	27.8014	86.1260	12.3	7.2^d	ISC

[1]A&J: Ambraseys and Jackson (2003) [3],[2]IMD: Indian Meteorological Department, [3]ISC: International Seismological Centre, [4]USGS: United States Geological Survey. Conversion to moment magnitude by: [a]Ambraseys and Douglas (2004) [6], [b]Pasari (2018) [184], moment magnitude values directly obtained from [c]USGS and [d]GCMT (Global Centroid Moment Tensor) catalog.

interevent times exhibit no correlations among them, and they constitute a random sample corresponding to a positive continuous random variable [271]. Under this set up,

the adopted methodology has three primary steps: choice of reference probability distributions, statistical inference involving estimation and model testing, and estimating conditional probability for a future earthquake. In the first step, a set of 13 reference probability distributions are chosen based on previous studies and highlight their important characteristics in data analysis. In the second step, the maximum likelihood estimation (MLE) method is used to infer model parameters based on the available sample data. The estimated parameters' confidence bounds through Fisher information and Cramer-Rao lower bound are examined, whereas the performance of the applied distributions are tested using three model selection approaches, namely the Akaike Information Criterion (AIC), Kolmogorov-Smirnov (K-S) goodness of fit test, and the chi-square test. Finally, the best-fit probability distribution is used to derive a number of occurrence probability curves (hazard function curves) for different elapsed times and residual times.

5.2.2.1 Reference probability distributions

Let T denote the random variable of inter-occurrence times of $M_w \geq 6.5$ events (mainshocks) in the study region with its probablity density function $f(t)$, cumulative distribution function $F(t)$, and hazard function $h(t)$. Based on previous studies [e.g., 13, 183, 184, 271, 274, 280, 291–297], 13 candidate reference probability distributions are considered to model the observed sample $(t_1, t_2, t_3, \ldots, t_{23})$ of size 23. These distributions include the time-independent exponential model and time-dependent gamma, lognormal, Weibull, Levy, Maxwell, Pareto, Rayleigh, inverse Gaussian (Brownian passage-time, BPT), inverse Weibull (Frechet), exponentiated exponential, exponentiated Weibull and exponentiated Rayleigh models (Table 5.2).

In literature, following the reliability theory, recurrence statistics of earthquakes has been discussed by several Japanese researchers (e.g., Utsu (1972, 1984) [271, 298]; Hagiwara (1974) [299]; Rikitake (1976) [300]) in the early stages of implementation. Among these, Utsu (1984) [271] has formally discussed the recurrence of earthquakes in Japan through four renewal models, namely exponential, gamma, lognormal, and Weibull. Later on, a series of studies [e.g., 13, 183, 184, 271, 274, 280, 291–297] have concentrated

on these four probability distributions for earthquake inter-occurrence time analysis. To this end, Weibull distribution appears to be the most popular and versatile probability model in statistical seismology [274]. Abaimov et al. (2008) [301] also suggested that the Weibull distribution is the favored model for describing recurrence times on the San Andreas fault. Corral (2003, 2004) [302, 303] employed global catalogs and observed that the gamma distribution provides a good fit for intermediate and large values of recurrence time. To note, Kagan and Knopoff (1987) [304] introduced the inverse Gaussian distribution, which Matthews et al. (2002) [305] adopted as the Brownian passage-time (BPT) distribution for their specific regions.

Table 5.2: Probability distribution models

Distribution	Domain	Density function	Parameter domain
Exponential	$t>0$	$\frac{1}{\alpha}e^{-\frac{t}{\alpha}}$	$\alpha>0$
Gamma	$t>0$	$\frac{1}{\Gamma(\beta)}\frac{t\beta-1}{\alpha^{\beta}}e^{-\frac{t}{\alpha}}$	$\alpha,\beta>0$
Lognormal	$t>0$	$\frac{1}{t\beta\sqrt{2\pi}}\exp\left[-\frac{1}{2}\left(\frac{\ln t-\alpha}{\beta}\right)^2\right]$	$-\infty<\alpha<\infty,\beta>0$
Weibull	$t>0$	$\frac{\beta}{\alpha}t^{\beta-1}e^{-\left(\frac{t}{\alpha}\right)^{\beta}}$	$\alpha,\beta>0$
Levy	$t>0$	$\sqrt{\frac{\alpha}{2\pi}}\frac{e^{-\alpha/2t}}{t^{3/2}}$	$\alpha>0$
Maxwell	$t>0$	$\sqrt{\frac{2}{\pi}}\frac{t^2}{\alpha^3}\exp\left[-\frac{1}{2}\left(\frac{t}{\alpha}\right)^2\right]$	$\alpha>0$
Pareto	$t>\alpha$	$\beta\frac{\alpha^{\beta}}{t^{\beta+1}}$	$t>\alpha>0,\beta>0$
Rayleigh	$t>0$	$\frac{t}{\alpha^2}\exp\left(-\frac{t^2}{2\alpha^2}\right)$	$\alpha>0$
Inverse Gaussian	$t>0$	$\sqrt{\frac{\beta}{2\pi t^3}}\exp\left[-\frac{\beta(t-\alpha)^2}{2\alpha^2 t}\right]$	$\alpha,\beta>0$
Inverse Weibull	$t>0$	$\beta\alpha^{\beta}t^{-\beta-1}e^{-\left(\frac{t}{\alpha}\right)^{-\beta}}$	$\alpha,\beta>0$
Exponentiated Exponential	$t>0$	$\alpha\beta\left(1-e^{-\alpha t}\right)^{\beta-1}e^{-\alpha t}$	$\alpha,\beta>0$
Exponentiated Weibull	$t>0$	$\frac{\beta\gamma}{\alpha}\left(\frac{t}{\alpha}\right)^{\beta-1}e^{\left(\frac{t}{\alpha}\right)^{\beta}}\left(1-e^{\left(\frac{t}{\alpha}\right)^{\beta}}\right)^{\gamma-1}$	$\alpha,\beta,\gamma>0$
Exponentiated Rayleigh	$t>0$	$\frac{2\beta t}{\alpha^2}e^{-\left(\frac{t}{\alpha}\right)^2}\left(1-e^{-\left(\frac{t}{\alpha}\right)^2}\right)^{\beta-1}$	$\alpha,\beta>0$

Table 5.3: Fisher information matrices (FIM) of probability distribution models; the FIM of the exponentiated Weibull and exponentiated Rayleigh distributions are not calculated, as the FIM contains nonlinear implicit terms [306]

Distribution	FIM ($I(\theta)$)
Exponential	$\frac{1}{\alpha^2}$
Gamma	$\begin{bmatrix} \frac{\beta}{\alpha^2} & \frac{1}{\alpha} \\ \frac{1}{\alpha} & \psi'(\beta) \end{bmatrix}$
Lognormal	$\begin{bmatrix} \frac{2}{\beta^2} & 0 \\ 0 & \frac{1}{\beta^2} \end{bmatrix}$
Weibull	$\begin{bmatrix} \frac{\beta^2}{\alpha^2} & -\frac{1}{\alpha}(1+\psi(1)) \\ -\frac{1}{\alpha}(1+\psi(1)) & \frac{1}{\beta^2}\left(\psi'(1)+\psi^2(2)\right) \end{bmatrix}$
Levy	$\frac{1}{2\alpha^2}$
Maxwell	$\frac{6}{\alpha^2}$
Pareto	$\begin{bmatrix} \frac{\beta}{\alpha^2(\beta+2)} & -\frac{1}{\alpha(\beta+1)} \\ -\frac{1}{\alpha(\beta+1)} & \frac{1}{\beta^2} \end{bmatrix}$
Rayleigh	$\frac{4}{\alpha^2}$
Inverse Gaussian	$\begin{bmatrix} \frac{1}{2\beta^2} & 0 \\ 0 & \frac{\beta}{\alpha^3} \end{bmatrix}$

Inverse Weibull	$\begin{bmatrix} \frac{\beta^2}{\alpha^2} & \frac{1}{\alpha}(1+\psi(1)) \\ \frac{1}{\alpha}(1+\psi(1)) & \frac{1}{\beta^2}\left(\psi'(1)+\psi^2(2)\right) \end{bmatrix}$
Exponentiated Exponential	$\begin{bmatrix} a_{11} & a_{12} \\ a_{21} & a_{22} \end{bmatrix}$ $a_{11} = \frac{1}{\alpha^2}\left[1+\frac{\beta(\beta-1)}{\beta-2}\left(\psi'(1)-\psi'(\beta-1)\right)+\left(\psi(\beta-1)-\psi(1)\right)^2\right]$ $-\frac{\beta}{\alpha^2}\left[\psi'(1)-\psi(\beta)+\left(\psi(\beta)-\psi(1)\right)^2\right];\ \beta>1,\ \beta\neq 2$ $a_{12}=a_{21}=\frac{1}{\alpha}\left[\frac{\beta}{\beta-1}\left(\psi(\beta)-\psi(1)\right)-\left(\psi(\beta+1)-\psi(1)\right)\right];\ \beta\neq 1$ $a_{22}=\frac{1}{\beta^2}$
Exponentiated Weibull	–
Exponentiated Rayleigh	–

For the studied probability distributions, density functions, their supports, and a basic explanantion of model parameters are mentioned in Table 5.2. It is noted that except Pareto, all distributions consider positive real line as their support. Out of these 13 distributions, four distributions (exponential, Levy, Maxwell, and Rayleigh) have one parameter and exponentiated Weibull has three parameters, whereas the rest of them have two parameters. The exponential distribution appears in seismology to describe earthquake interevent times under a homogeneous Poisson process, though it produces a constant hazard function over time. The gamma and Weibull distributions have two parameters, one scale parameter (responsible to control the spread of distribution) and one shape parameter (responsible to produce various appearances). The shape parameter particularly brings out a large variety of flexibility. When the shape parameter takes unit value, both distributions become identical to an exponential distribution. Moreover, as these distributions are popular in survival analysis to model residual times (also known as

waiting time or time to failure), they are commonly used in seismic inter-occurrence time analysis [274]. Under different conditions, these two distributions enable monotonically increasing, decreasing, and constant failure rate. The lognormal distribution, like Levy, Pareto or inverse Weibull (Frechet), is a commonly used heavy-tailed distribution that puts higher probability to large events. While the lognormal distribution has distinctive applications in modeling maintenance time of a system, the heavy-tailed models are generally used in modeling huge insurance losses, income data, wildfire, and earthquake sizes [307]. The hazard functions of lognormal and Frechet distributions are non-monotone unimodal upside-down (concave-down $\cap$ shape) bathtub shape, whereas the hazard rate pattern of Pareto is decreasing [308]. The Maxwell and Rayleigh distributions belong to one-parameter family of distributions, with Maxwell having extensive applications in particle speed analysis in statistical physics, while Rayleigh with increasing hazard rate has found applications in medical statistics and oceanographic studies among others. Both distributions have been used in statistical seismology. The inverse Gaussian distribution, also known as BPT distribution, is a popular temporal model [e.g., 295, 305] for inter-arrival times and consequent long-term seismic forecasting. Unlike many probability models, this distribution with a non-monotone hazard pattern asymptotically attaining a non-zero value enables noteworthy connection to the earthquake mechanics of stress and strain accumulation [305]. In addition, three distributions from the exponentiated group are considered, namely the exponentiated exponential, exponentiated Weibull, and the exponentiated Rayleigh [309]. With an additional shape parameter, these distributions generalize the exponential, Weibull, and Rayleigh distributions, respectively. These distributions have many characteristics with commonly used renewal-time distributions, such as exponential, gamma, and Weibull distributions [274, 306, 310, 311].

5.2.2.2 Statistical inference

In order to carry out statistical inference based on available earthquake inter-arrival times, the maximum likelihood estimation (MLE) method is used for parameter estimation of the studied distributions, the Fisher information matrix to compute the variance-covariance

matrix associated with the MLE estimates, and three model selection approaches to arrange the distributions' performance. The MLE method works on the principle that the estimated model parameters must maximize the joint likelihood for a given set of sample data points [308]. The method often requires to solve a set of linear or non-linear likelihood equations. On the other hand, the Fisher information matrix (FIM), coupled with the Cramer-Rao lower bound, provides a measure of uncertainty in terms of asymptotic standard deviations and confidence limits of the estimated model parameters [274, 312].

Let $\theta = (\theta_1, \theta_2, ..., \theta_p)$ denote the parameters for a reference distribution. Then, the symmetric and positive semi-definite FIM $I_{p\times p}(\theta)$ can be defined [312] as below:

$$\begin{aligned} I_{p\times p}(\theta) &= (I_{ij}(\theta))_{i,j=1,2,...,p} \\ &= E\left(-\frac{\partial^2 \ln f(T;\theta)}{\partial\theta_i \partial\theta_j}\right)_{i,j=1,2,...,p} \\ &= E\left[\left(\frac{\partial \ln f(T;\theta)}{\partial\theta_i}\right)\left(\frac{\partial \ln f(T;\theta)}{\partial\theta_j}\right)\right]_{i,j=1,2,...,p} \\ &= \frac{1}{n}E\left(-\frac{\partial^2 L(T;\theta)}{\partial\theta_i \partial\theta_j}\right)_{i,j=1,2,...,p} \end{aligned} \tag{5.2.3}$$

Here, E denotes the expectation, $f(t;\theta)$ is the density function, and $L(T;\theta)$ is the log-likelihood function. After obtaining Fisher information matrix (Table 5.3), the asymptotic variance-covariance matrix $\sum_{\hat{\theta}}$ is computed for each distribution through the Cramer-Rao bound defined as $\sum_{\hat{\theta}} \geq \left[nI(\hat{\theta})\right]^{-1}$; $\hat{\theta}$ is the maximum likelihood estimate of θ [312]. Finally, a 95% two-sided confidence limit of the estimated model parameters is provided as $\hat{\theta} - 1.96\sqrt{\left[\sum_{ij}(\hat{\theta})\right]_{i,j=1,2,...,p}} < \theta < \hat{\theta} + 1.96\sqrt{\left[\sum_{ij}(\hat{\theta})\right]_{i,j=1,2,...,p}}$. To note, the exact (not asymptotic) standard deviations are available for the Pareto distribution [274, 313], whereas the uncertainty analysis for the exponentiated Rayleigh and exponentiated Weibull distributions cannot be performed as the explicit formulation of the FIM is unavailable [306]. In Table 5.4, the estimated parameter values along with their associated uncertainties are listed.

Table 5.4: Estimated parameter values with their asymptotic standard deviations and confidence bounds

Model	Parameter Values	Asymptotic Standard Deviation	Confidence Bound (95%)
Exponential	$\hat{\alpha}$= 9.2082	$\sigma_{\hat{\alpha}}$= 1.9201	5.4449–12.9715
Gamma	$\hat{\alpha}$= 7.8698	$\sigma_{\hat{\alpha}}$= 1.6933	4.5509–11.1886
	$\hat{\beta}$= 1.1701	$\sigma_{\hat{\beta}}$= 0.1118	0.9508–1.3892
Lognormal	$\hat{\alpha}$= 1.7928	$\sigma_{\hat{\alpha}}$= 0.1410	1.5164–2.0691
	$\hat{\beta}$= 0.9564	$\sigma_{\hat{\beta}}$= 0.1994	0.5655–1.3473
Weibull	$\hat{\alpha}$= 9.6459	$\sigma_{\hat{\alpha}}$= 1.8860	5.9494–13.3424
	$\hat{\beta}$= 1.1229	$\sigma_{\hat{\beta}}$= 0.1826	0.7651–1.4807
Levy	$\hat{\alpha}$= 3.8073	$\sigma_{\hat{\alpha}}$= 1.1227	1.6068–6.0079
Maxwell	$\hat{\alpha}$= 7.3860	$\sigma_{\hat{\alpha}}$= 0.6287	6.1537–8.6184
Pareto	$\hat{\alpha}$= 0.7370	$\sigma_{\hat{\alpha}}$=0.0067	0.5766–0.7370
	$\hat{\beta}$= 0.4767	$\sigma_{\hat{\beta}}$= 0.0136	0.2478–0.7055
Rayleigh	$\hat{\alpha}$= 9.0460	$\sigma_{\hat{\alpha}}$= 0.9431	7.1975–10.8945
Inverse Gaussian	$\hat{\alpha}$= 9.2082	$\sigma_{\hat{\alpha}}$= 2.7071	3.9024–14.5141
	$\hat{\beta}$= 6.4913	$\sigma_{\hat{\beta}}$= 2.2868	0.0000–10.9735
Inverse Weibull	$\hat{\alpha}$= 3.7081	$\sigma_{\hat{\alpha}}$=0.7677	2.2036–5.2126
	$\hat{\beta}$= 1.0605	$\sigma_{\hat{\beta}}$= 0.1724	0.7226–1.3984
Exponentiated exponential[a]	$\hat{\alpha}$= 7.5446	–	–
	$\hat{\beta}$= 1.3722		
Exponentiated Weibull[b]	$\hat{\alpha}$= 0.8292	–	–
	$\hat{\beta}$= 0.4620		
	$\hat{\gamma}$= 8.2338		
Exponentiated Rayleigh[b]	$\hat{\alpha}$= 17.7231	–	–
	$\hat{\beta}$= 0.4206		

[a]Parametric model uncertainties are not calculated as the values are not real. [b]For the exponentiated Rayleigh and exponentiated Weibull distributions, parametric model uncertainties are not calculated, as the FIM is not explicitly available [306].

The estimated parameter values given in Table 5.4 suggest the following noteworthy characteristics of the underlying earthquake system: (i) as the shape parameter ($\hat{\beta}$) in each of gamma, Weibull, and exponentiated exponential is greater than 1.0, the associated hazard function turns out to be monotonically increasing, indicating that the expected time to the next earthquake will decrease with an increasing elapsed time [274, 314]; (ii) inverse Gaussian and lognormal distributions exhibit non-monotone hazard shapes that gradually

reach to a constant asymptotic value $\frac{\beta}{2\alpha^2} \approx 0.038$ and zero, respectively [184]; (iii) as the estimated shape parameter of the Pareto distribution is less than 1, it does not allow us to compute mean interevent time or standard deviation [308]; (iv) the hazard function associated with the exponentiated Rayleigh and exponentiated Weibull distributions assume a "bathtub-type" shape as $\hat{\beta} < 0.5$ [184, 306], and (v) for exponentiated exponential distribution with $\hat{\beta} > 1$, the hazard shape decreases over time [310].

After parameter estimation and uncertainty analysis, the best-performed reference distributions are chosen according to their performance against the observed interevent times. For this, three popular model selection approaches, namely the AIC, K-S, and the chi-square criterion are used. The AIC in general penalizes a model with more parameters and it is defined as $AIC = 2k - 2L$, where k denotes the number of parameters and L is the log-likelihood value. Therefore, a model with the least AIC value is deemed to be the most preferable model for a given dataset. In contrary, the K-S non-parametric goodness-of-fit test compares the distance between the cumulative distribution function (CDF) of the tested distribution and the empirical distribution function (EDF), under the null hypothesis that the data are distributed according to the distribution. In addition to the K-S point measures, a number of K-S plots are also presented in Figures 5.3 and 5.4 to examine the overall fit of the reference CDFs with the EDF. After AIC and K-S tests, the minimum chi-square criterion that uses observed and expected frequencies is employed to prioritize a group of distributions. For computation of chi-square value, here four classes are used ($<$3, 3–6, 6–12, $>$12). The detailed results of model selection tests are summarized in Table 5.5.

From Table 5.5, it is noted that the lognormal, exponentiated Weibull, and exponential distributions are the best performed models as they have lowest AIC value, least K-S distance, and the minimum chi-square value, whereas inverse Gaussian, gamma, inverse Weibull, Weibull, exponentiated exponential distributions also reveal a satisfactory fit to the observed inter-arrival times in the study region. On the other hand, remaining distributions have poor suitability to the observed inter-arrival times of large events in the study region. From Figure 5.4, it is observed that lognormal is almost inseparable from the

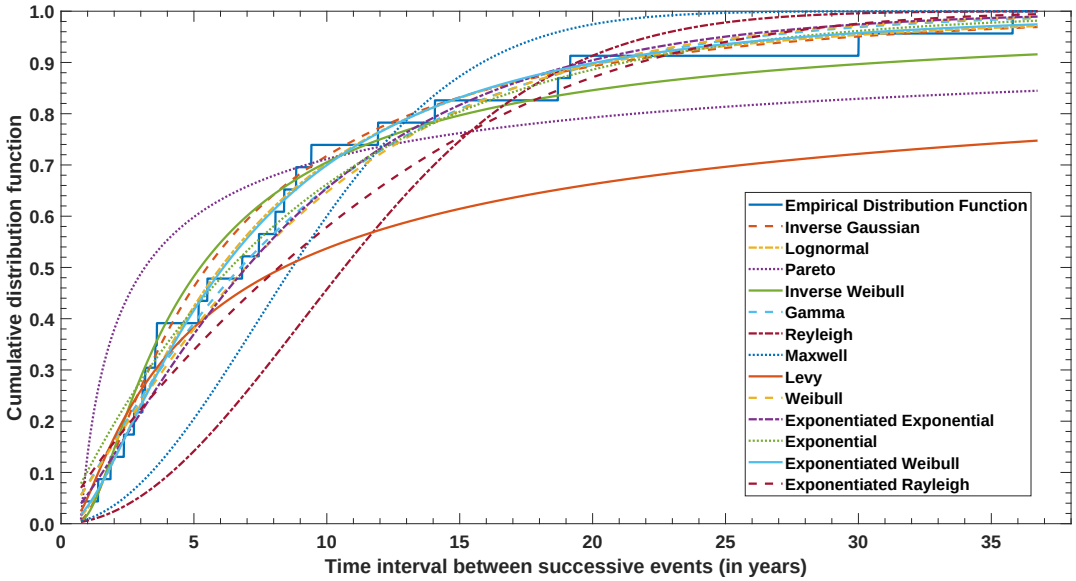

Figure 5.3: Comparison of the CDF of the tested distributions against EDF through K-S plots.

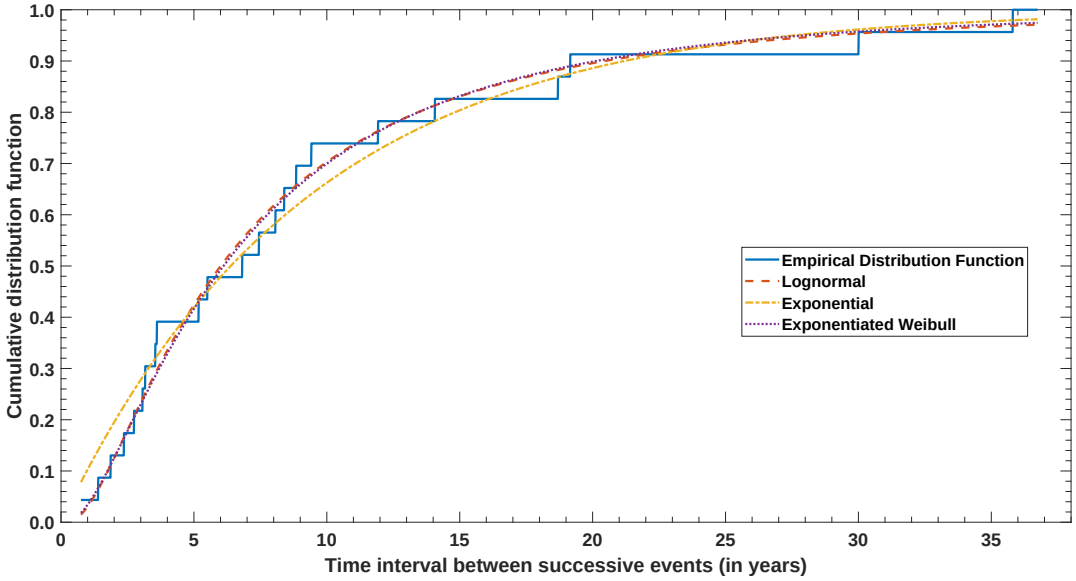

Figure 5.4: Comparison of the best performed CDF of the tested distributions against EDF through K-S plots.

exponentiated Weibull, though there is a noticeable difference between exponential and lognormal. Overall, the proximity or farness among these best-fit distributions motivate researchers to further investigate model efficacy in domain-specific practical applications [191, 308, 310].

Table 5.5: Model selection results using three goodness-of-fit tests and criteria

Distribution	Maximum Likelihood		K-S Min. Distance	Chi-square Values
	$-\ln L$	AIC		χ^2
Exponential	74.0622	150.1244	0.0986	0.6027
Gamma	73.6671	151.3342	0.1076	0.6151
Lognormal	72.8443	149.6886	0.0940	0.3015
Weibull	73.8034	151.6069	0.1168	2.0045
Levy	79.1114	160.2229	0.2573	9.4251
Maxwell	95.1974	192.3949	0.2787	0.5438
Pareto	81.2759	166.5518	0.2954	0.5114
Rayleigh	83.0731	168.1462	0.3206	7.8372
Inverse Gaussian	72.9758	149.9515	0.1045	0.2920
Inverse Weibull	74.6454	153.2907	0.1134	0.3760
Exponentiated exponential	73.5119	151.0238	0.1259	0.3916
Exponentiated Weibull	72.8330	151.6659	0.0997	0.1236
Exponentiated Rayleigh	75.2871	154.5743	0.1846	2.3391

5.2.3 Occurrence probabilities of large earthquakes

After analyzing the performance of the reference distributions, the successive task is to assess long-term earthquake occurrence probabilities in the study region. For this, the best fit lognormal distribution is used to compute cumulative probability and a series of conditional probabilities for different elapsed times (time elapsed since the last large earthquake) and residual times (time to a future large earthquake). The conditional probability values are often represented in terms of hazard function curves of the best performed model (Figure 5.5) for scientific, public and commercial purposes [13, 292]. The conditional probability of a future event in the time window $(\tau, \tau+v)$ for a given elapsed time τ and prospective residual time v can be mathematically defined as [274]:

$$P(V \leq \tau+v|V \leq v) = \frac{F(\tau+v)F(\tau)}{1-F(\tau)}, (v>0) \tag{5.2.4}$$

To note, the cumulative probability describes the occurrence of a future event within a certain time from the last earthquake, whereas the conditional probability determines the chance of an earthquake in the interval $(\tau, \tau+v)$, knowing that there has been no large event in the last τ years. Using the most suitable lognormal distribution, it is found that

the estimated cumulative probability of a $M_w \geq 6.5$ event in the Kumaun-Nepal Himalaya reaches 0.90–0.95 by 2035–2045, whereas the conditional probability reaches 0.90–0.95 by 2048–2059. These probability values are alarmingly high to draw attention of the disaster management authorities in the study area.

Table 5.6: Estimated conditional probabilities for an elapsed time of 8 years (i.e., April 2023) in the study area

Residual time	Year	Lognormal	Exponential	Exponentiated Weibull[a]
1	2024	0.12 (0.07–0.28)	0.10 (0.07–0.17)	0.12
6	2029	0.51 (0.32–0.85)	0.48 (0.37–0.67)	0.52
11	2034	0.70 (0.48–0.96)	0.70 (0.57–0.87)	0.71
16	2039	0.81 (0.59–0.99)	0.82 (0.71–0.95)	0.82
21	2044	0.87 (0.66–0.99)	0.90 (0.80–0.98)	0.88
26	2049	0.91 (0.72–0.99)	0.94 (0.87–0.99)	0.92
31	2054	0.93 (0.76–0.99)	0.97 (0.91–0.99)	0.94
36	2059	0.95 (0.80–0.99)	0.98 (0.94–0.99)	0.96
41	2064	0.96 (0.82–0.99)	0.99 (0.96–0.99)	0.97

[a] absolute conditional probability values are presented, as parametric model uncertainties is unknown.

As the last large earthquake in study area occurred on April 25, 2015, the elapsed time as of today is $\tau = 8$ years (i.e., April 25, 2023). Therefore, for $\tau = 8$ years and $v = 1, 6, 11, \ldots, 41$ years, conditional probabilities and their 95% confidence bounds (Table 5.6) are computed using all the three best performed models, namely the lognormal, exponential, and exponentiated Weibull. Results show that the conditional probabilities according to all distributions reach 0.95 in about 16–36 years from now (2049–2059). Similarly, varying both elapsed time ($\tau = 8, 10, 15, \ldots, 35$ years) and residual time, a series of conditional probabilities are calculated (Figure 5.5) to examine hazard for large earthquakes in the study region. The curves in Figure 5.5 show a consistent pattern for lognormal and exponentiated Weibull distributions, though the exponential exhibits a relatively higher conditional probability value. To investigate more, conditional probabilities (Table 5.7) computed from the best-fit lognormal distribution corresponding to $\tau = 8(2023), 10(2025), 15(2030), 20(2035), 25(2040), 30(2045), 35(2050)$ and $v = 1, 2, \ldots, 15$. It is noted that unlike the exponential distribution that provides

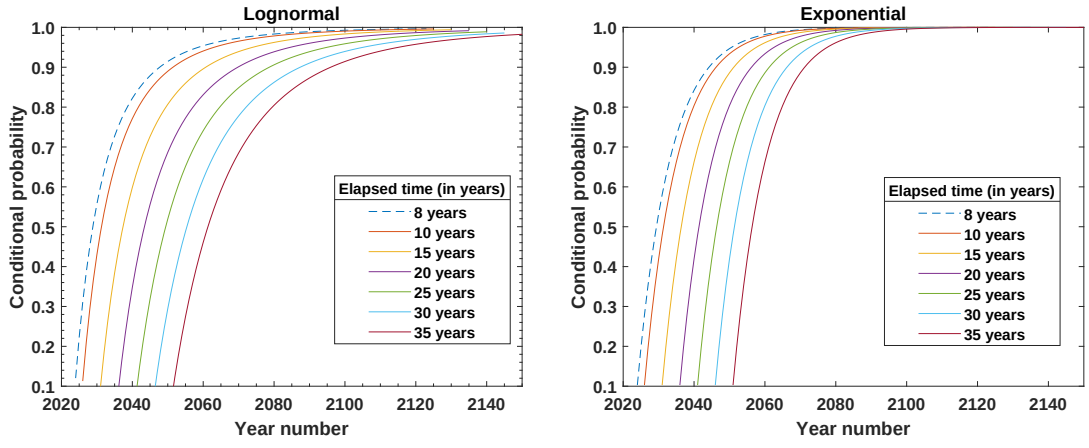

(a)

(b)

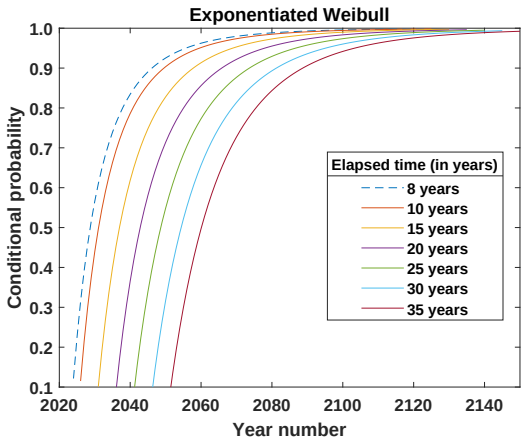

(c)

Figure 5.5: Hazard function curves for various elapsed times ($\tau = 8, 10, 15, 20, 25, 30, 35$ years) as computed from (a) lognormal, (b) exponential, and (c) exponentiated Weibull for $M_w \geq 6.5$ events in the Kumaun-Nepal Himalaya. The dot-line represents the hazard curve corresponding to an elapsed time of 8 years (since the last large Gorkha earthquake in April, 2015).

conditional probability independent of the elapsed time, the conditional probabilities corresponding to the lognormal decrease with increasing elapsed times.

In summary, the estimated cumulative probability of a $M_w \geq 6.5$ event in the Kumaun-Nepal Himalaya reaches 0.90–0.95 by 2035–2045, whereas the conditional probability reaches 0.90–0.95 by 2048–2059. Overall, these findings empower governments and societies to make informed decisions and take proactive measures to enhance resilience

Table 5.7: The estimated conditional probabilities (from lognormal model) that an earthquake with magnitude $M_w \geq 6.5$ will occur in next v years (residual time), given that no $M_w \geq 6.5$ event has occurred in last τ years (elapsed time) since the last Gorkha event in April 2015

	Elapsed Time (τ)						
Residual time (v)	8 (2023)	10 (2025)	15 (2030)	20 (2035)	25 (2040)	30 (2045)	35 (2050)
1	0.12	0.11	0.10	0.09	0.08	0.07	0.06
2	0.22	0.21	0.18	0.16	0.15	0.13	0.12
3	0.31	0.29	0.26	0.23	0.21	0.19	0.18
4	0.39	0.37	0.33	0.29	0.27	0.25	0.23
5	0.45	0.43	0.38	0.35	0.32	0.29	0.27
6	0.51	0.49	0.44	0.40	0.37	0.34	0.32
7	0.56	0.53	0.48	0.44	0.41	0.38	0.36
8	0.60	0.58	0.53	0.48	0.45	0.42	0.39
9	0.64	0.62	0.56	0.52	0.49	0.46	0.43
10	0.67	0.65	0.60	0.56	0.52	0.49	0.46
11	0.70	0.68	0.63	0.59	0.55	0.52	0.49
12	0.73	0.71	0.66	0.62	0.58	0.55	0.52
13	0.75	0.73	0.68	0.64	0.60	0.57	0.54
14	0.77	0.75	0.71	0.66	0.63	0.60	0.57
15	0.79	0.77	0.73	0.69	0.65	0.62	0.59

and minimize the impact of future earthquakes.

After exploring earthquake interevent time modeling in the Kumaun-Nepal Himalaya, the next section is focuses on earthquake nowcasting at 30 major city regions of the study area.

5.3 Earthquake nowcasting along the Kumaun-Nepal Himalaya

This section provides a comprehensive account of earthquake nowcasting in the study area, encompassing detailed descriptions of the earthquake dataset, methodology, and results.

5.3.1 Earthquake data

To carry out nowcasting based Natrural Time Analysis (NTA) in the Kumaun-Nepal Himalaya, a part of earthquake data (i.e., from 1965–2023) obtained in Chapter 2 is re-considered. In this sub-catalog, there are a total of 3397 events ($3.6 \leq M_w \leq 7.8$) with their focal depths 0–100 km. This catalog includes 26 "large" events with $M_w \geq 6.0$, providing 25 seismic cycles. In nowcasting analysis, it is assumed that earthquakes within the study region have a perfect correlation, though they are considered to be unaffected by earthquakes occurring outside the region [277, 282]. Figure 5.7 provides a pictorial summary of the catalog in terms of frequency-magnitude plot and magnitude-time graph. It is observed that the magnitude completeness threshold based on the least-squares linear regression equation turns out to be $\sim$3.6, and the completeness threshold is largely homogeneous over time. Figure 5.8 displays a dependence plot comparing the average counts N_α (the average cumulative count of $4.0 \leq M_w < 6.0$ earthquakes) and N_β (the average cumulative count of $M_w \geq 6.0$ earthquakes) to analyze potential linear dependencies between them. It is evident from Figure 5.8 that there exists a linear relationship between N_α and N_β.

5.3.2 Formulation

Occurrence of earthquakes are random, though they are observed to appear quasi-periodically in seismic cycles [191, 316]. The irregularity in seismic "cycles" in a large geographic area has resulted into the formulation of different statistical measures based on a space-time organization of events [191, 282, 317]. The proposed method considers the ensemble statistics of recurring "natural times", intermittent small earthquake counts, to estimate the current level of seismic progression in terms of earthquake potential score (EPS). This empirical method is known as earthquake nowcasting [282].

To illustrate the nowcasting idea, let us consider a geographic region of area A and two magnitude thresholds (small and large) M_α and M_β. Let N_α and N_β denote the average cumulative count of earthquakes having magnitudes greater than M_α and M_β, respectively.

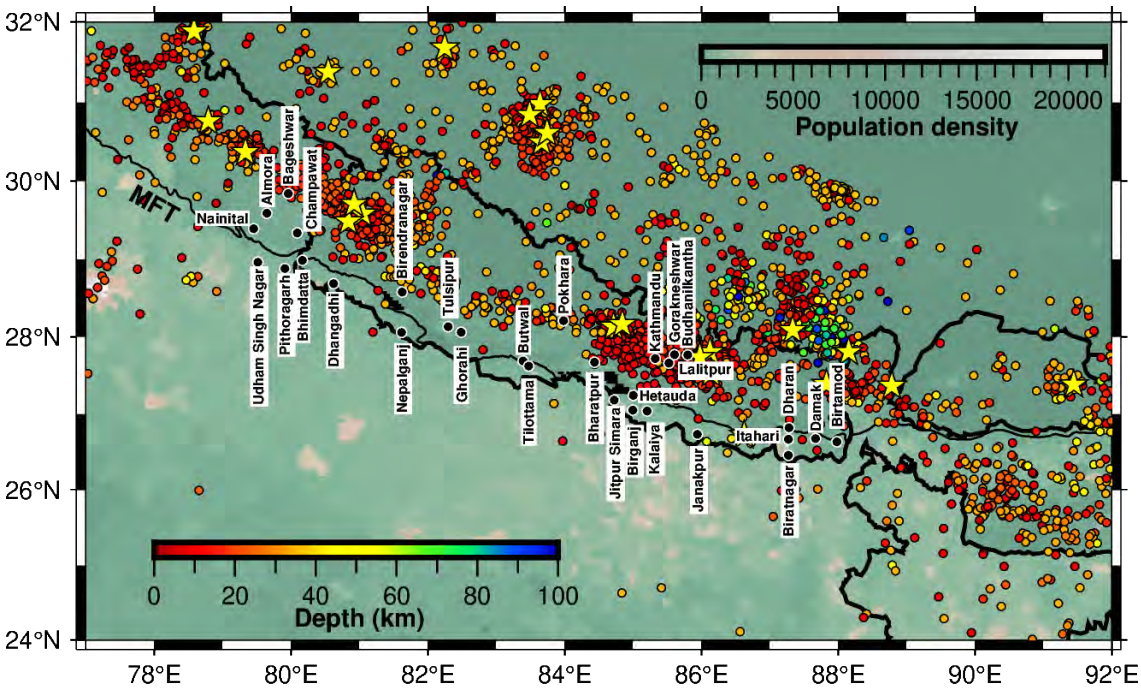

Figure 5.6: Seismotectonic map of Kumaun-Nepal Himalaya and surrounding regions. The background color indicates the population density of persons per 5km^2 area [315]. Earthquakes with magnitude $M_w \geq 6.0$ are represented by yellow stars. The black circles indicate the geographic center of 30 major cities in the study area. The colored circles represent seismicity ($3.5 \leq M_w < 6.0$) in the study region.

Using Gutenberg-Richter scaling relation, the cumulative event count turns out to be $N_\alpha = 10^{a-bM_\alpha}$ and $N_\beta = 10^{a-bM_\beta}$, respectively, for some constants a and b. Thus, the average number (N) of interevent small earthquakes (natural times) in a seismic cycle can be defined as:

$$N = \frac{N_\alpha - N_\beta}{N_\beta} = 10^{\,b(M_\beta - M_\alpha)} \tag{5.3.1}$$

The above equation shows that (i) the NTA is independent to the productivity (a) of a spatial region, be it dominated by aftershocks or triggering events; (ii) natural time count scales exponentially with the difference of the threshold magnitudes; (iii) particularly, with the assumption that b-value remains constant in time and space, the natural time (N) scales exponentially to the magnitude of large earthquakes, as the small magnitude threshold M_α, often deduced from the magnitude of completeness in a catalog (Figure 5.7), remains

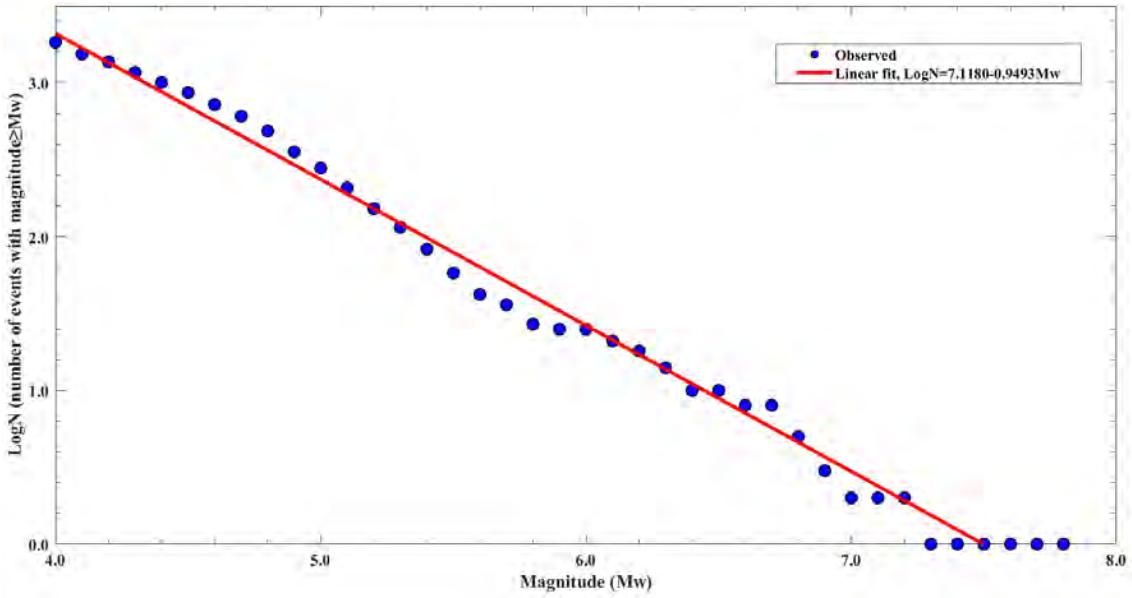

(a)

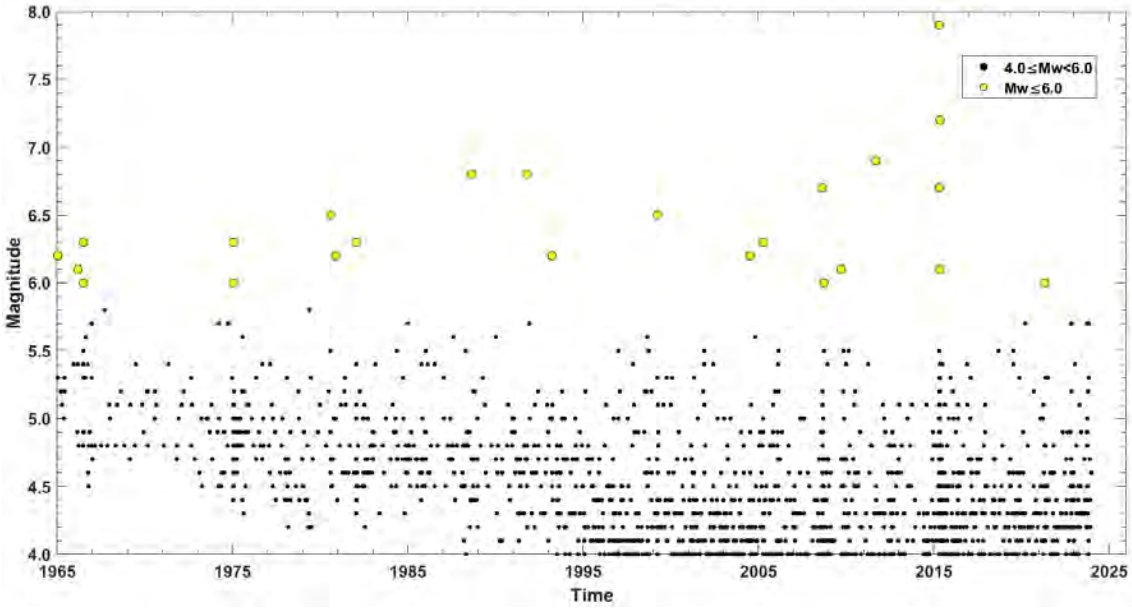

(b)

Figure 5.7: (a) Frequency-magnitude and (b) magnitude-time plots for the present earthquake catalog in the Kumaun-Nepal Himalaya.

unchanged [191, 282]. As a consequence, unlike conventional hazard assessment methods, in nowcasting analysis, (i) dependent events have an equal opportunity to contribute to the analysis and (ii) the fault "segmentation" concept can be dropped to account for

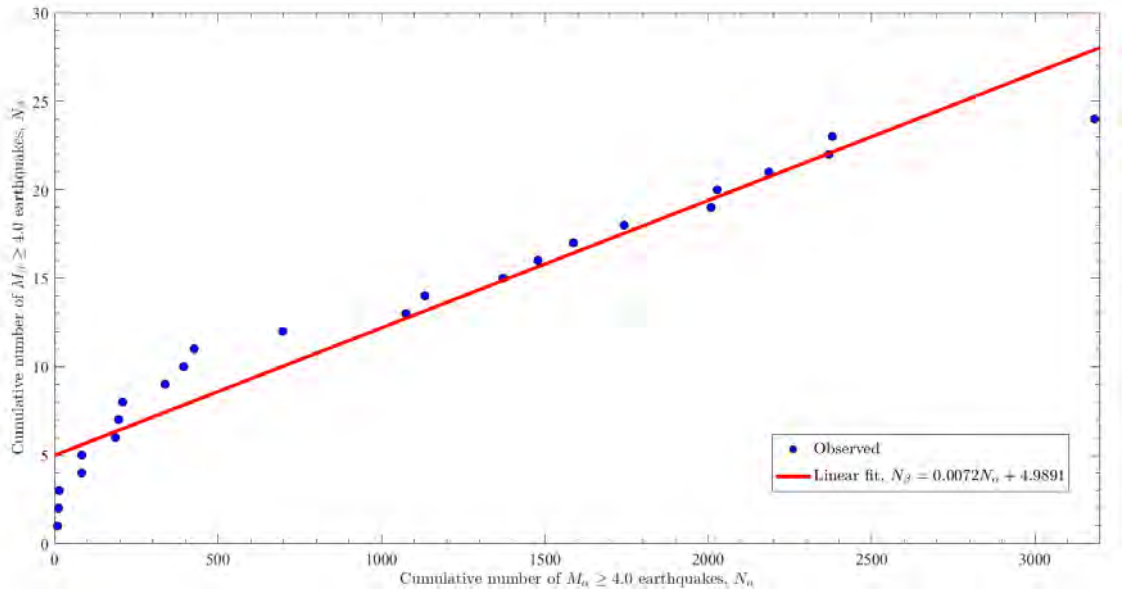

Figure 5.8: Dependence plot between the cumulative number of small earthquake counts N_α and cumulative number of large earthquake counts N_β.

a combined space-time interactions among a miscellany of faults and their associated "seismic cycles" [278, 282, 318].

To develop ensemble seismicity statistics for a given region A based on observed natural times (say, $N_1, N_2, ..., N_C$) corresponding to C number of earthquakes cycles, a group of reference probability distributions is employed to select the right data-derived CDF. Assuming that the natural time statistics remains invariant in space and time, the EPS for several local regions (say, $A_i, i = 1, 2, ..., k, A_i \subseteq A$) can be computed as $EPS_i \equiv F_N(m_i(t)) = P\{N \leq m_i(t)\}$ where $F_N(.)$ is the distribution of natural times and $m_i(t)$ is the current count of small events in the region A_i at clock (calendar) time t [282]. It may be noted that ergodic principle in the statistical mechanics of earthquake physics provides a theoretical ground for the above assumption in nowcasting analysis [282, 317]. Besides, it may be emphasized that earthquake nowcasting conceptually differs from earthquake forecasting (i.e., earthquake interevent modeling) in which the probability of a future event is estimated [282].

The methodology adopted in a nowcasting analysis consists of three broad steps: preparing data (natural times) for the study region, deriving seismicity statistics of natural

times, and computing earthquake potential score (nowcast scores) for a number of cities embedded in the study region. While the description of "small" (say, $4.0 \leq Mw < 6.0$) and "large" (say, $M \geq 6.0$) events in data preparation (Step-1) usually comes from the notion of magnitude completeness threshold (Figure 5.7) and societal destruction, deriving natural time statistics (Step-2) requires probability model description, parameter estimation, and model selection. Using the best-fit cumulative distribution of natural times in the entire study region (in Step-2), the nowcast values for several circular city regions are computed to measure their current state of earthquake hazards. A simple flowchart of the earthquake nowcasting approach is illustrated in Figure 5.9.

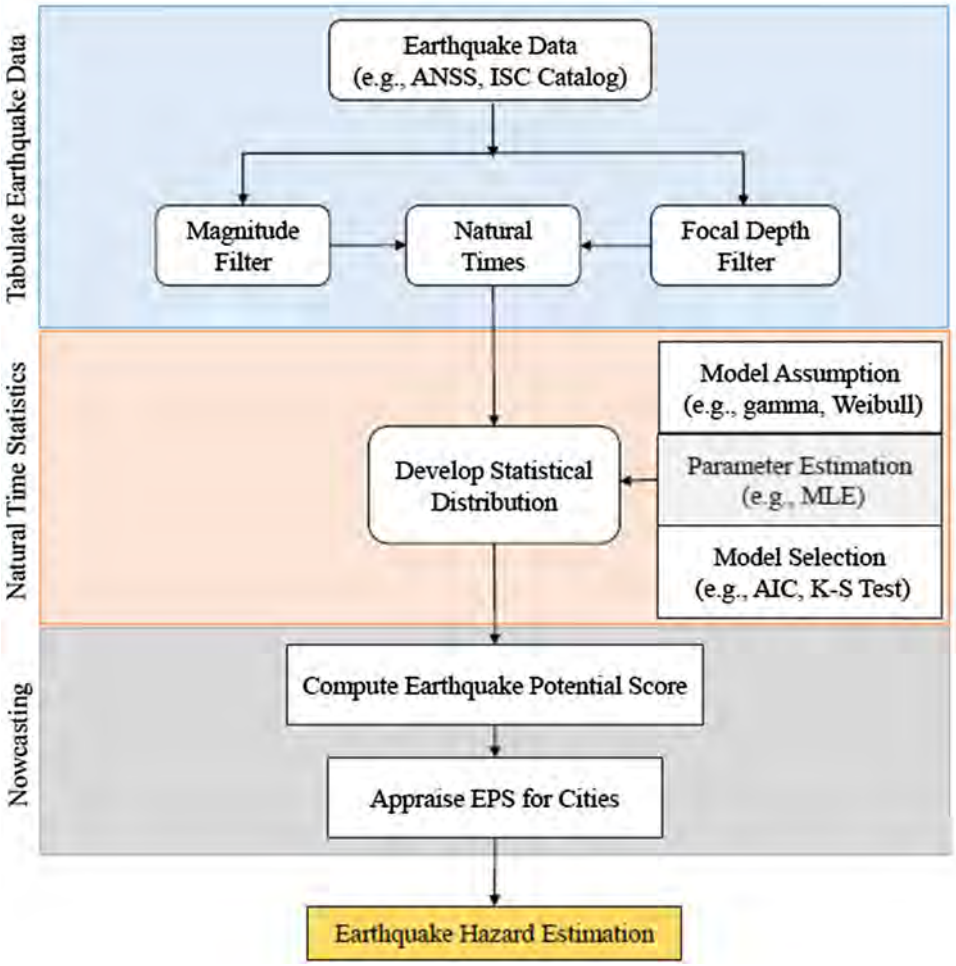

Figure 5.9: Flowchart of the nowcasting approach for earthquake hazard estimation [274].

To perform NTA on the earthquake dataset, a parametric family of five probability

Table 5.8: Estimated parameter values and goodness-of-fit measures of selected probability distribution

Distribution	Statistical Inference	
	MLE	K-S
Exponential	$\hat{\alpha}$= 69.7500	0.1336
Gamma	$\hat{\alpha}$= 100.2030	0.0972
	$\hat{\beta}$= 0.6961	
Weibull	$\hat{\alpha}$= 65.3160	0.0892
	$\hat{\beta}$= 0.8772	
Exponentiated Exponential	$\hat{\alpha}$= 79.7828	0.0915
	$\hat{\beta}$= 0.8171	
Exponentiated Weibull	$\hat{\alpha}$= 56.3087	0.1285
	$\hat{\beta}$= 0.8091	
	$\hat{\gamma}$= 1.3039	

distributions is employed having positive real line as their domain. Since natural time count scales exponentially with the difference of the threshold magnitudes (Equation 5.3.1) it is reasonable to consider exponential distribution and its primary variants gamma, Weibull, and exponentiated exponential in developing the data-derived cumulative distribution function (CDF) and associated earthquake potential score (EPS) computation (Table 5.2). Using the maximum likelihood method and the non-parametric Kolmogorov-Smirnov (K-S) statistic, model parameters are estimated and the best-fit distribution is determined for the observed event counts [294]. While the maximum likelihood technique involves maximizing the likelihood function of the unknown population parameters for a given set of observations, the non-parametric K-S procedure ranks candidate probability models based on their (minimum) vertical distances between the two distribution functions: empirical data distribution and the reference cumulative distribution. It is found that the Weibull distribution provides the best representation to the observed natural times for the Kumaun-Nepal Himalaya (Table 5.8).

5.3.3 Results

Considering the small event magnitude threshold M_α to be $M_w = 4.0$, large event magnitude threshold M_β to be $M_w = 6.0$, and the radius of circular city region $R = 250$ km, the

nowcast score of 30 cities from Kumaun-Nepal Himalaya is calculated. Nevertheless, in a later part of this chapter, a sensitivity analysis of these input parameter is discussed.

5.3.3.1 EPS at several city regions

As mentioned above, the nowcasting method produces EPS, a numerical value (between 0% and 100%), that can serve as a yardstick to examine the current level of seismic cycle progression in a defined region. The EPS is calculated according to small and

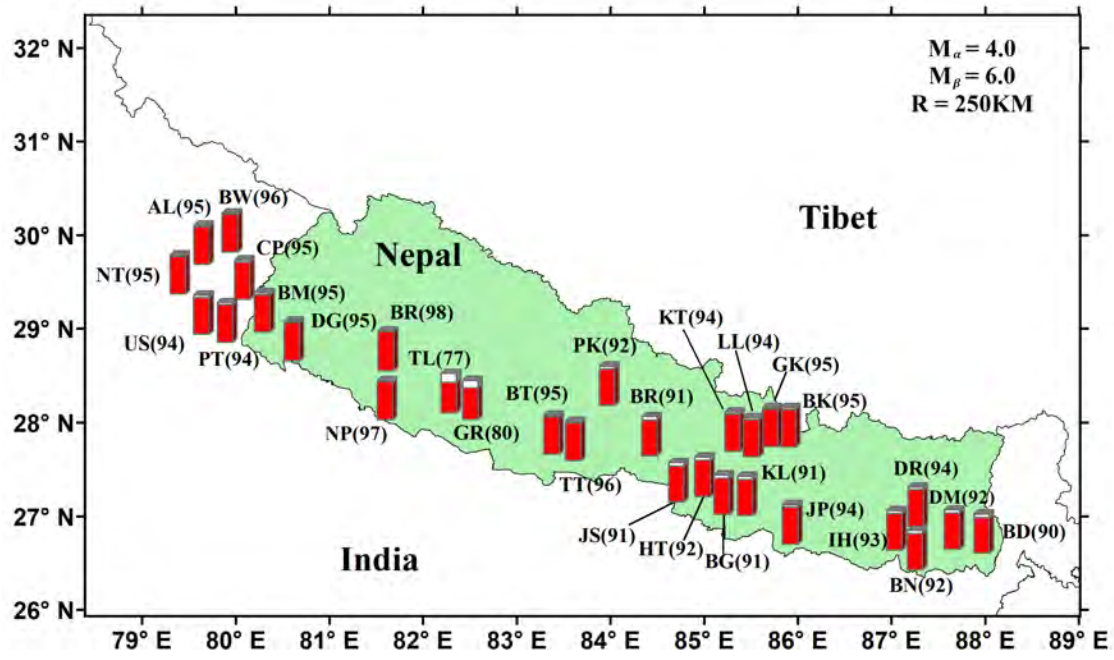

Figure 5.10: Earthquake potential scores for $M_w \geq 6.0$ events at 30 major cities in the Kumaun-Nepal Himalaya for $M_a = 4.0$ and $R = 250$ km are shown by solid bars. Abbreviations for city-names are as follows: BP, Bharatpur; BM, Bhimdatta; BN, Biratnagar; BR, Birendranagar; BG, Birganj; BD, Birtamod; BK, Budhanilkantha; BT, Butwal; DM, Damak; DG, Dhangadhi; DR, Dharan; GR, Ghorahi; GK, Gokarneshwar; HT, Hetauda; IT, Itahari; JK, Janakpur; JS, Jitpur Simara; KL, Kalaiya; KT, Kathmandu; LT, Lalitpur; NP, Nepalgunj; PK, Pokhara; TT, Tilottama; TL, Tulsipur; PT, Pithoragarh; BW, Bageshwar; AL, Almora; CP, Champawat; NT, Nainital; US, Udham Singh Nagar.

large magnitude thresholds of $M_w = 4.0$ and $M_w = 6.0$, respectively. As on December 31, 2023, the EPS corresponding to $M_w \geq 6.0$ events at 30 major cities in Kumaun-Nepal Himalaya ranges between 77% and 98% with the following ranking in decreasing order: Birendranagar (98%), Nepalgunj (97%), Tilottama (96%), Bageshwar (96%), Bhimdatta

Table 5.9: Earthquake potential scores for $M_w \geq 6.0$ events in 30 major cities along the Kumaun-Nepal Himalaya corresponding to $M_a = 4.0$ and $R = 250$ km

City	City centre		Date of last	Magnitude of last	Current	EPS
	Lat (°N)	Lat (°E)	large event	large event	count	(%)
Bharatpur	27.6706	84.4385	12-05-2015	7.3	182	91
Bhimdatta	28.9873	80.1652	28-03-1999	6.6	223	95
Biratnagar	26.4525	87.2718	12-05-2015	7.3	193	92
Birendranagar	28.5776	81.6254	29-07-1980	6.5	308	98
Birganj	27.0449	84.8672	12-05-2015	7.3	176	91
Birtamod	26.6293	87.9825	12-05-2015	7.3	168	90
Budhanilkantha	27.7654	85.3653	12-05-2015	7.3	221	95
Butwal	27.6866	83.4323	25-04-2015	7.8	236	95
Damak	26.6717	87.6680	12-05-2015	7.3	192	92
Dhangadhi	28.6852	80.6216	28-03-1999	6.6	227	95
Dharan	26.8143	87.2797	12-05-2015	7.3	210	94
Ghorahi	28.0588	82.4861	25-04-2015	7.8	114	80
Gokarneshwar	27.7668	85.4066	12-05-2015	7.3	224	95
Hetauda	27.4368	85.0026	12-05-2015	7.3	190	92
Itahari	26.6646	87.2718	12-05-2015	7.3	203	93
Janakpur	26.7271	85.9407	12-05-2015	7.3	213	94
Jitpur Simara	27.1775	84.7237	12-05-2015	7.3	178	91
Kalaiya	27.0323	85.0078	12-05-2015	7.3	179	91
Kathmandu	27.7172	85.3240	12-05-2015	7.3	218	94
Lalitpur	27.6588	85.3247	12-05-2015	7.3	216	94
Nepalgunj	28.0548	81.6145	29-07-1980	6.5	277	97
Pokhara	28.2096	83.9856	12-05-2015	7.3	190	92
Tilottama	27.6193	83.4750	25-04-2015	7.8	242	96
Tulsipur	28.1309	82.2972	25-04-2015	7.8	102	77
Pithoragarh	28.5829	80.2182	28-03-1999	6.6	214	94
Bageshwar	29.8404	79.7694	28-03-1999	6.6	244	96
Almora	29.5892	79.6467	28-03-1999	6.6	232	95
Champawat	29.3361	80.0910	28-03-1999	6.6	237	95
Nainital	29.3924	79.4534	28-03-1999	6.6	220	95
Udham Singh Nagar	28.9610	79.5154	28-03-1999	6.6	209	94

(95%), Budhanilkantha (95%), Butwal (95%), Dhangadhi (95%), Gokarneshwar (95%), Almora (95%), Champawat (95%), Nainital (95%), Dharan (94%), Janakpur (94%), Kathmandu (94%), Lalitpur (94%), Pithoragarh (94%), Udham Singh Nagar (94%), Itahari (93%), Biratnagar (92%), Damak (92%), Hetauda (92%), Pokhara (92%), Bharatpur (91%), Birganj (91%), Jitpur Simara (91%), Kalaiya (91%), Birtamod (90%), Ghorahi (80%), and

Tulsipur (77%) (Figure 5.10 and Table 5.9). Physically, this result indicates, for example, that the capital city Kathmandu has progressed about 94% of the way through its cycle of magnitude 6.0 or higher events. Overall, it is noted that, the EPS scores for all major cities in the study area lie in the range of 77% and 98%. The high EPS scores indicate that these cities have reached to their rear end in the seismic cycle of large earthquakes. These EPS values are alarmingly high to draw attention of the disaster management authorities in Kumaun-Nepal Himalaya.

5.3.3.2 Sensitivity analysis

As the time-dependent nowcast scores for $M_w \geq 6.0$ events are obtained for a particular choice of small magnitude threshold and city region, a sensitivity testing of the parameters is desirable to improve reliability (Rundle et al. 2016; Pasari 2022). Therefore, the sensitivity analysis in a two-fold style is performed: (i) changing city radius $R = 200, 250, 300$ km with fixed small magnitude threshold $M_w = 4.0$ and (ii) changing small magnitude threshold $M_w = 4.0$ and $M_w = 3.6$ with fixed $R = 250$ km.

For each of the above cases, the EPS values are re-computed and visually depicted in Figures 5.11 to 5.13. Several observations are made from the sensitivity testing: (i) a steady increase in the city radius often yields a steady increase in EPS scores, though there are a few cases (Birendranagar and Tulsipur) where the inclusion of the most recent large event in the enlarged city area leads to decreased EPS values; (ii) the EPS score for Ghorahi within a 200 km city radius can not be calculated due to the absence of any large events within this range; (iii) a lower value of small magnitude threshold $M_w = 3.6$ yields a slight change ($\pm$2%–3%) in observed EPS scores. Therefore, the EPS values are largely consistent with the variations in threshold magnitude and city area in the seismically active Kumaun-Nepal Himalaya.

In summary, most of the cities have reached to their rear end in the seismic cycle of large earthquakes indicating a potential catastrophic to the human population in the Kumaun-Nepal Himalaya.

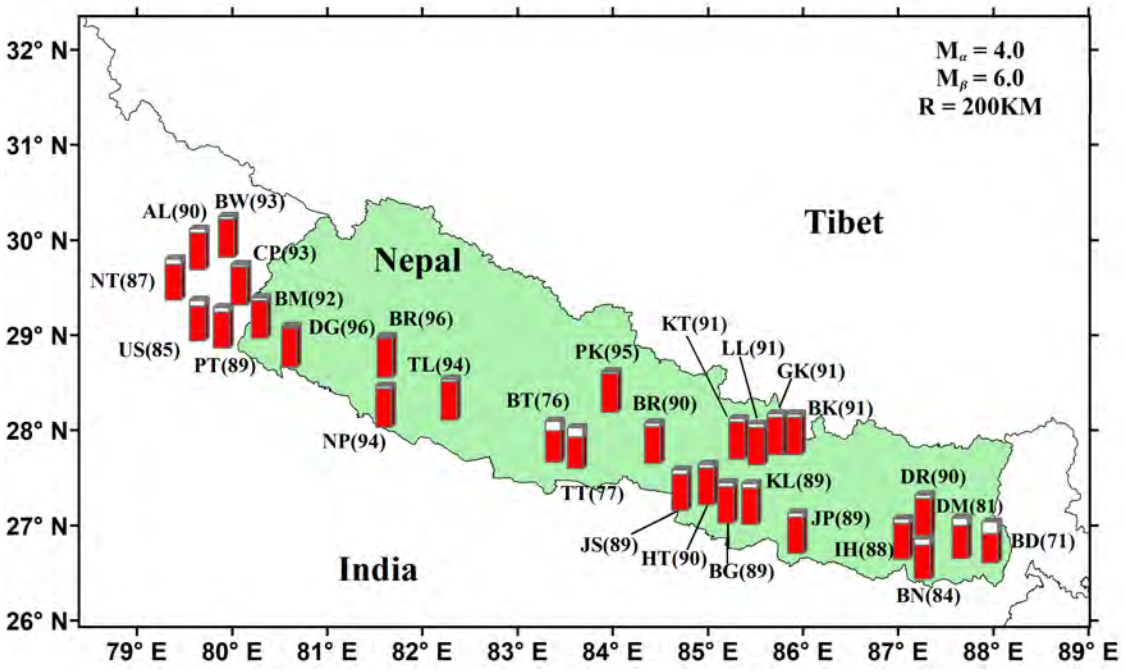

(a)

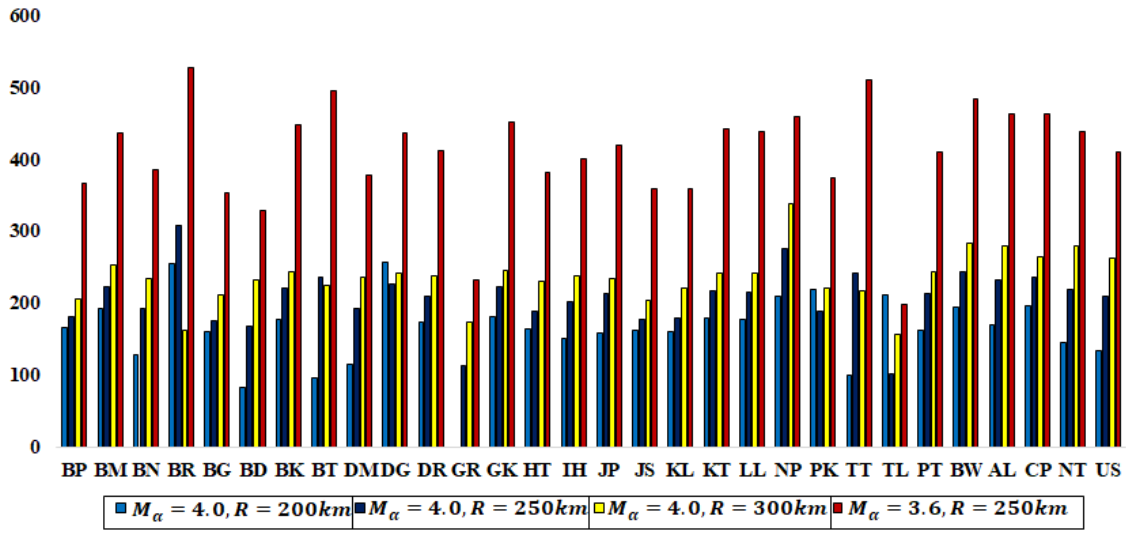

(b)

Figure 5.11: (a) Earthquake potential scores for $M_w \geq 6.0$ events at 30 major cities in the Kumaun-Nepal Himalaya for $M_a = 4.0$ and $R = 200$ km are shown by solid bars. The stacked bar-chart in the lower panel (b) of the figure shows a comparison of the current number of small event counts at several city areas. Abbreviations align with the Figure 5.10.

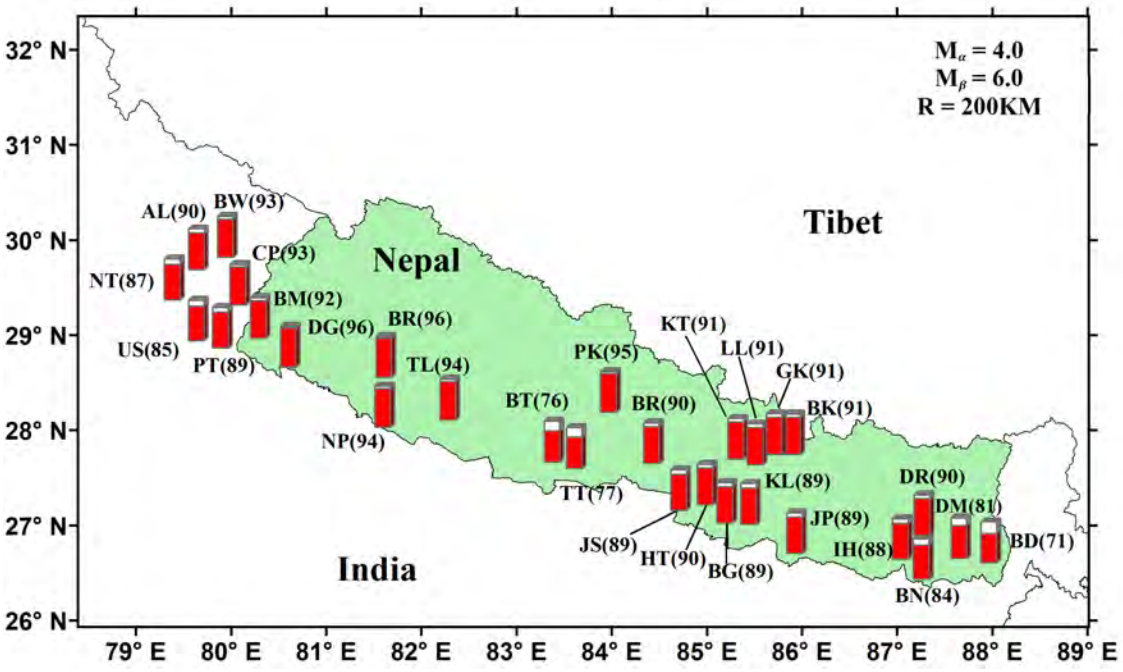

Figure 5.12: Earthquake potential scores for $M_w \geq 6.0$ events at 30 major cities in the Kumaun-Nepal Himalaya for $M_a = 4.0$ and $R = 300$ km are shown by solid bars. Abbreviations align with the Figure 5.10.

5.4 Validation of EPS score

The nowcast scores, interpreted as a way of assessing tectonic stress build-up at the current time, also yield useful information for strategic planning. However, it is important to keep in mind that in NTA or any statistical data-driven analysis, early failures (much more before than the "expected number of natural time counts") are inevitable phenomena, reflecting the variability in natural time statistics [120, 214]. To provide a validation, EPS scores (%) for five cities prior to the 2015 M_w 7.8 Gorkha earthquake are calculated. Prior to the 2015 earthquake, the present analysis would assign EPS scores as Bharatpur (81%), Birganj (79%), Kathmandu (86%), Lalitpur (85%), and Pokhara (64%). In addtion, to investigate more, the EPS scores corresponding of several city regions ptior to 1999 Mw 6.5 Chamoli earthquake and 1991 Mw 6.8 Uttarkashi earthquake are estimated. Prior to the 1999 event, the EPS scores are as follows: Bhimdatta (59%), Dhangadhi (78%), Pithoragarh (78%), Bageshwar (63%), Almora (63%), Champawat (62%), Nainital (60%),

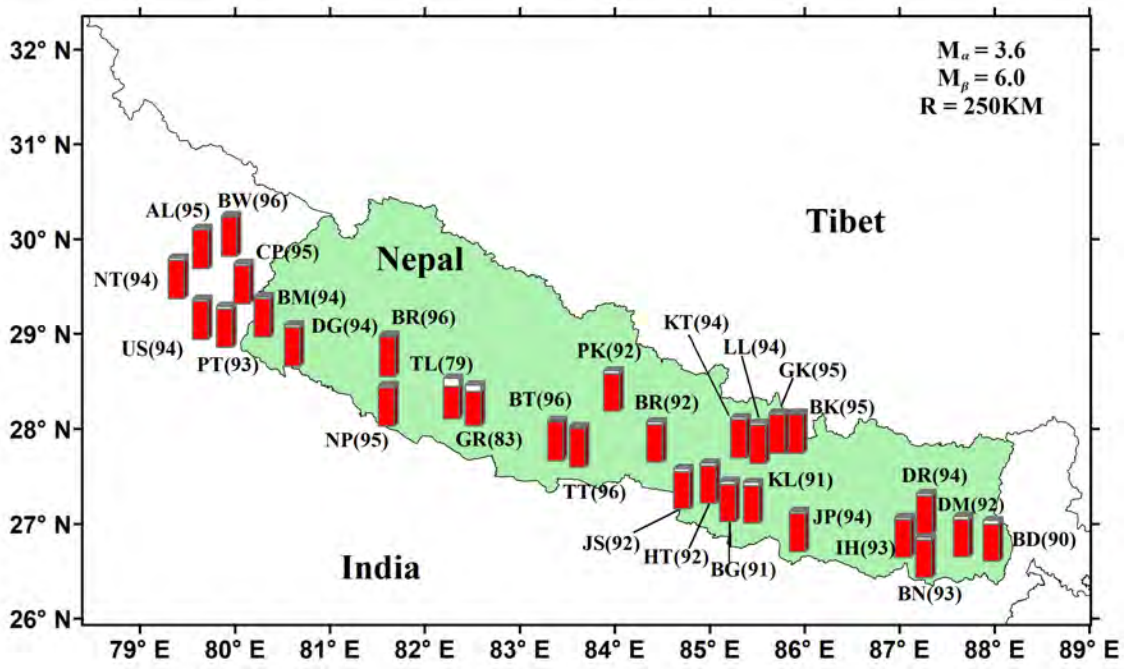

Figure 5.13: Earthquake potential scores for $M_w \geq 6.0$ events at 30 major cities in the Kumaun-Nepal Himalaya for $M_a = 3.6$ and $R = 250$ km are shown by solid bars. Abbreviations align with the Figure 5.10.

and Udham Singh Nagar (57%). Similarly, prior to the 1991 event, the present analysis would assign EPS scores for cities as Bhimdatta (61%), Bageshwar (65%), Almora (64%), Champawat (64%), Nainital (64%), and Udham Singh Nagar (59%). The EPS scores mentioned prior to the 1991, 1999, and 2015 events show high values for the majority of city regions, indicating the validation of the nowcasting method across the study area. Consequently, apart from a few instances of "infant mortality," the expected nowcast scores clearly demonstrate their usefulness.

5.5 Seismic hazard analysis through combined geodetic and statistical approaches

The current study conducted a thorough seismic hazard assessment employing geodetic techniques (Chapters 2 to 4) and statistical methodologies (Chapter 5). While the geodetic analysis focused on evaluating seismic hazard through an examination of underlying crustal structure, strain distribution, fault kinematics, and earthquake potential based on

seismic moment budget within the study region, statistical methods were utilized for earthquake inter-event time analysis and earthquake nowcasting in the same area. Both approaches revealed that each segment of the study area demonstrates elevated EPS scores, indicating the potential for significant to severe earthquakes in the future. Consequently, the integration of these two methodologies offers insight into high seismic hazard zones across the study area.

5.6 Summary

The present chapter focuses on analyzing the seismic hazards along the Kumaun-Nepal Himalaya based on an area-based statistical approach. For this, probabilistic earthquake recurrence modeling and natural time analysis are carried out to estimate the conditional probability of large-sized earthquakes and the current state of developing earthquake cycles at several city regions, respectively. The analysis leads to the following remarks:

1. The best-performed distributions are the lognormal, exponential, and exponentiated Weibull to the observed inter-arrival times of large events ($M_w \geq 6.5$) in the Kumaun-Nepal Himalaya.

2. The best-fit exponentiated lognormal model shows that the estimated cumulative and conditional probability of a $M_w \geq 6.5$ event in the study region reach 0.90–0.95 in the 2035–2045 and 2048–2059, respectively.

3. To analyze the current state of developing earthquake cycles in the study region through natural time counts, the best-fit model turns out to be Weibull.

4. The EPS scores calculated from the best-performed Weibull distribution for all major cities in the study area are high and lie in the range of 77% and 98%.

5. These EPS values are alarmingly high to draw attention of the disaster management authorities in the Kumaun-Nepal Himalaya.

In summary, to examine a comprehensive seismic hazard in Kumaun and Nepal Himalaya, two approaches namely, theory-driven physical models (i.e., fault and/or area

based models) and data-driven statistical models (i.e., area based models) are implemented. The physical models have focused on the spatial distribution of the contemporary seismic moment budget, fault kinematics and associated earthquake potential using the geodetic and earthquake data (in Chapters 2 to 4), whereas the latter data-driven statistical models, namely the earthquake forecasting and nowcasting, have aimed to provide a synoptic statistical view of earthquake hazard in terms of conditional probabilities of large sized earthquake and earthquake potential score in the study area, respectively (in Chapter 5). The estimated results not only enable researchers to understand the seismic hazard analysis but also have several end-user applications. The next chapter will summarize the entire thesis work along with a few recommendations.

Chapter 6

Conclusions and Future Scope

"Earthquakes remind us how small we really are and how temporary everything is."

— Greg Lake

The present thesis has provided a contemporary seismic hazard analysis using a combination of GPS, InSAR, and earthquake data along the Kumaun and Nepal Himalaya. For this, Chapter 1 has provided an overview and rationale of the thesis, along with the primary objective and scope of the thesis. Chapter 2 has outlined the study area and various datasets including GPS velocity field, InSAR velocity field, integrated velocity field, and earthquake data. Chapters 3 and 4 have respectively provided an area-based and fault-based earthquake potential of different segments using geodetic approach of the study area, whereas, Chapter 5 has carried out probabilistic earthquake recurrence modeling along with earthquake nowcasting analysis. Finally, the present chapter (Chapter 6) summarizes research outcomes of the thesis accompanying with relevant future scopes. The overall content of this chapter is provided below.

Contents

6.1 Summary of work done

The current thesis offers a present-day seismic hazard analysis by integrating GPS, InSAR, and earthquake data across the Kumaun and Nepal Himalaya. The primary objective of this thesis involves evaluating the ongoing crustal deformation during the interseismic period and consequently to re-evaluate the contemporary seismic hazards in the Kumaun and Nepal Himalaya. To accomplish this objective, a high-resolution integrated velocity field from the combination of GPS and InSAR data was derived. The estimated integrated velocity field was subsequently employed to obtain the strain distribution within the Kumaun and Nepal Himalaya. The resulting strain rate distribution and compiled earthquake dataset enabled the seismic moment budget along the Kumaun and Nepal Himalaya. Additionally, the high-resolution integrated velocity field was used for the computation of the MHT's fault kinematics, slip rate distribution, and corresponding earthquake potential within the study region. Furthermore, probabilistic earthquake recurrence modeling and natural time analysis were conducted to estimate the conditional probability of large-sized earthquakes and the current state of developing earthquake cycle at several city regions, respectively. A consolidated summary of work done across previous chapters is presented below.

6.1.1 High-resolution integrated velocity field

After a theoretical overview of the Himalayan arc in Chapter 1, the high-resolution integrated velocity field along the Kumaun-Nepal Himalaya was derived in Chapter 2 through a number of successive tasks, such as the GPS velocity field estimation, InSAR LOS velocity derivation, and integration of derived GPS and InSAR velocities. The GPS data of the regional network in Kumaun was processed using the GAMIT-GLOBK suite of post-processing software and the GPS velocity vectors along with daily position time-series plots were derived. To improve the spatial resolution of the GPS velocity field across the study region, an updated set of GPS velocity data obtained from NGL and published sources was utilized. On the other hand, InSAR based ascending and descending LOS velocities were calculated from "COMET-LiCS Sentinel-1 InSAR" portal using the

LiCSBAS processing toolbox. Then, the derived GPS and InSAR based velocities were combined to obtain a high-resolution velocity field. It was observed that the northern part of the study region shows a southward deformation ranging from 9 mm/yr to 15 mm/yr, while the southern part experiences relatively lower deformation due to the ongoing north-south convergence between the Indian and Eurasian plates.

6.1.2 Strain rate distribution and seismic moment budget

The derived integrated velocity field in Chapter 2 was utilized in Chapter 3 to calculate the contemporary seismic moment budget in the Kumaun Himalaya and three spatial sections along the Nepal Himalaya using the state-of-the-art high-resolution integrated velocity field. For this, (i) three types of geodetic strains, namely dilatational, maximum shear, and rotational strains were calculated; then, (ii) geodetic and seismic moment rates were computed using the estimated strain tensor and compiled earthquake data, respectively; and, (iii) a section-wise seismic moment budget was estimated through an area-based approach by comparing geodetic and seismic moment rates over the study region. It was observed that the compressional strain rates are dominant because of the India-Eurasia tectonic collision, though there are some patches of extensional strain rates in southern Tibet. Higher dilatational and maximum shear strain rates were inferred along the MCT region. The rotation rates reflected the general pattern of the surface velocity field along the study region. Additionally, earthquake potentials of M_w 8.1 in the Kumaun Himalaya, M_w 8.5 in western Nepal, M_w 7.9 in central Nepal, and M_w 8.1 in eastern Nepal were determined by comparing geodetic and seismic moment rates in each respective section.

6.1.3 Fault kinematics and slip-rate distribution of the megathrust MHT

In Chapter 4, to characterize fault parameters and associated earthquake potential of the MHT along the Kumaun-Nepal region, (i) the derived integrated velocity field and compiled earthquake data were re-considered from Chapter 2; then, (ii) twenty arc-normal profiles to the MHT were selected across the study region based on the velocity pattern;

subsequently, (iii) the spatial distribution of slip rates and fault geometry for the MHT was determined from a two-dimensional Bayesian inversion model; then, (iv) a section-wise slip deficit rate, moment deficit rate, and associated earthquake potential were computed based on the estimated slip rate and seismic energy release; finally, (v) these fault-based moment deficit rates and associated earthquake potential were compared with their corresponding area-based values as mentioned in Chapter 3. The long-term slip rate along the MHT was determined to be 19.1 mm/yr in the Kumaun Himalaya, 15.5 mm/yr in the western Nepal Himalaya, 13.8 mm/yr in the central Nepal Himalaya, and 12.4 mm/yr in the eastern Nepal Himalaya. Furthermore, earthquake potentials were estimated to be M_w 8.2 in the Kumaun Himalaya, M_w 8.4 in the western Nepal Himalaya, M_w 8.2 in the central Nepal Himalaya, and M_w 8.3 in the eastern Nepal Himalaya based on the observed slip-rate distribution.

6.1.4 Seismicity statistics in the study area

After estimating the seismic moment budget, fault kinematics, and associated earthquake potential along the Kumaun-Nepal Himalaya through a geodetic based approach in Chapters 3 and 4, the second state-of-the-art approach, namely the statistical area-based earthquake nowcasting and forecasting method, was utilized in Chapter 5. For this, (i) the compiled earthquake data was re-considered from Chapter 2; then, (ii) the interevent time of successive large events ($M_w \geq 6.5$) was calculated from several competitive probability distributions to examine various properties of inter-occurrence times in the study area; subsequently, (iii) the conditional probability plots and their implications for future earthquakes were described; and, (iv) the current progression of contemporary earthquake cycle of different city regions in terms of earthquake potential score (EPS) was estimated based on statistical approach. From interevent modeling, it was calculated that the cumulative and conditional probability of a $M_w \geq 6.5$ event in the study region reach 0.90–0.95 in the next 08–22 years (2030–2045) and 25–36 years (2048–2059), respectively. Additionally, the estimated EPS scores are above 90% at most of the cities in the study region (including capital city Kathmandu), indicating that these cities have reached their rear end in the seismic cycle of large earthquakes.

Seismic hazard analysis using the above area and fault based methods are all related to the concept of elastic rebound. While the geodetic approach has provided a long-term prospective of moment build-up, the proposed intervent and nowcasting approach have evaluated the conditional probability of large-sized earthquakes and the current state of developing earthquake cycle at several city regions, respectively. A combination of these physical and empirical methods have provided a snapshot of high seismic hazard areas along the Kumaun-Nepal Himalaya.

In summary, the present thesis work has better characterized the seismic hazard in terms of the updated high-resolution velocity field, strain rate patterns, seismic moment budget, fault kinematics of the megathrust MHT, and earthquake nowcasting and forecasting along the Kumaun-Nepal Himalaya. The findings will provide invaluable inputs to the time-dependent seismic hazard analysis of the study region.

6.2 Major findings of the thesis

The major findings of the present thesis are outlined as follows:

1. The high-resolution integrated velocities from the combination of GPS and InSAR indicate that the northern part of the study area exhibits deformation towards the south at a rate ranging from 9 mm/yr to 15 mm/yr, while the deformation in the southern part is relatively smaller.

2. The strain rate is not homogeneous over the Kumaun and Nepal Himalaya. Particularly, along the MCT, higher strain rates are observed and minimal strain rate is observed along the MBT and MFT, indicating the locking behavior of these faults in the study region.

3. The calculated moment deficit rates using an "area-based" approach in different sections of the study area are as follows: 7.64×10^{18} Nm/yr in Kumaun, 12.13×10^{18} Nm/yr in western Nepal, 4.74×10^{18} Nm/yr in central Nepal, and 5.33×10^{18} Nm/yr in eastern Nepal. These rates imply earthquake potentials of M_w 8.1, M_w 8.5, M_w 7.9, M_w 8.1 in Kumaun, western Nepal, central Nepal, and eastern Nepal, respectively.

4. The Bayesian inversion fault model reveals a long-term slip rate for the MHT of 19.1 mm/yr in the Kumaun Himalaya, 15.5 mm/yr in the western Nepal Himalaya, 13.8 mm/yr in the central Nepal Himalaya, and 12.4 mm/yr in the eastern Nepal Himalaya.

5. This determined slip rate of the MHT corresponds to a slip deficit of 16.5 mm/yr in the Kumaun Himalaya, 13.3 mm/yr in the western Nepal Himalaya, 11.3 mm/yr in the central Nepal Himalaya, and 10.9 mm/yr in the eastern Nepal Himalaya, along with associated earthquake potentials of M_w 8.3, M_w 8.5, M_w 8.2, and M_w 8.0 through a "fault-based" approach, respectively.

6. To analyze interevent time, the best performed models are the lognormal, exponential, and exponentiated Weibull. The best-fit lognormal distribution shows that the estimated cumulative and conditional probability of a $M_w \geq 6.5$ event in the study region reaches 0.90–0.95 in the next 12–22 years (2035–2045) and 25–36 years (2048–2059), respectively.

7. To analyze the current state of developing earthquake cycles in the study region through natural time counts, the best-fit model turns out to be Weibull. The EPS from the best-performed model corresponding to $M_w \geq 6.0$ events at 30 major cities in Kumaun-Nepal Himalaya ranges between 77% and 98% with the following ranking in decreasing order: Birendranagar (98%), Nepalgunj (97%), Tilottama (96%), Bageshwar (96%), Bhimdatta (95%), Budhanilkantha (95%), Butwal (95%), Dhangadhi (95%), Gokarneshwar (95%), Almora (95%), Champawat (95%), Nainital (95%), Dharan (94%), Janakpur (94%), Kathmandu (94%), Lalitpur (94%), Pithoragarh (94%), Udham Singh Nagar (94%), Itahari (93%), Biratnagar (92%), Damak (92%), Hetauda (92%), Pokhara (92%), Bharatpur (91%), Birganj (91%), Jitpur Simara (91%), Kalaiya (91%), Birtamod (90%), Ghorahi (80%), and Tulsipur (77%).

The applied physical and statistical approaches in this thesis revealed that each segment

Table 6.1: Slip rate, earthquake occurrence rate and earthquake potential along the Kumaun and Nepal Himalaya

Section	Slip rate of MHT	Slip-deficit rate of MHT	Earthquake potential	
	(mm/yr)	(mm/yr)	Area based (M_w)	Fault based (M_w)
Kumaun	19.1	16.5	8.1	8.3
Western Nepal	15.5	13.3	8.5	8.5
Central Nepal	13.8	11.3	7.9	8.2
Eastern Nepal	12.4	10.9	8.1	8.0

of the study area has the potential for significant earthquake(s) in the future. Consequently, the integration of these two methodologies offers insight into high seismic hazard zones across the study area.

6.3 Contributions through this research

The present research has following contributions towards a better understanding of the contemporary seismic hazard in the Kumaun-Nepal Himalaya using geodetic and earthquake data:

1. The present work combines GPS and InSAR observations to obtain a state-of-the-art high-resolution integrated velocity field in the Kumaun-Nepal Himalaya.

2. The thesis provides spatial distribution of seismic moment budget and associated earthquake potential along the Kumaun and three various sections of the Nepal Himalaya using an "area-based" comparison method.

3. The Bayesian inversion fault model enables fault characteristics and slip distributions of the megathrust MHT along the study region. Essentially, the estimated slip rates provide an earthquake potential in each section of the study area using a "fault-based" comparison method.

4. The area-based probabilistic earthquake recurrence modeling and natural time analysis provide the conditional probability of large-sized earthquakes and the current

state of developing earthquake cycles at several city regions, respectively. Emanated conditional probability curves (hazard function curves) for different elapsed times and residual times reveal long-term seismic hazard, whereas the EPS scores from the nowcasting approach serve as a yardstick for a ranking of the major cities based on their current seismic exposure.

5. Finally, the integrated velocity field, strain distribution, fault characteristics, slip distribution, seismic moment budget, earthquake recurrence modeling, and natural time analysis enable researchers to understand the contemporary seismic hazard in the Kumaun and Nepal Himalaya, consequently aiding in social policy-making, insurance strategies, urban planning, and various other practical applications for end-users.

6.4 Future scope of the research

Below are several potential research avenues that could be developed and/or integrated to advance the current thesis work.

1. **Enhancing InSAR precision:** Certainly, considering the challenges in phase unwrapping and coherence in InSAR data, incorporating techniques such as installing high-coherence fixed objects or artificial reflectors on the ground could be an excellent future scope for enhancing the precision and reliability. This can highlight the potential for improving data quality and accuracy in InSAR applications, particularly in areas where natural reflectors might be limited or less effective.

2. **Estimating seismic budget through consideration of aseismic strain in analysis:** Activities that occur aseismically along a fault, unlike the locked behavior of the fault, are generally viewed as less prone to causing significant earthquakes due to the absence of prolonged strain buildup. Thus, creating models and measuring the aseismic aspect within the overall strain buildup will offer a more practical assessment of stored energy, crucial in gauging the current earthquake potential along the Himalayan arc.

3. **Modeling coupling rates of the megathrust MHT using high-resolution integrated velocity field:** Modeling the coupling rate of the Main Himalayan Thrust (MHT) from an improved high-resolution integrated velocity field involves delving into the quantification of the interseismic coupling along the MHT. This could encompass refining models that estimate the degree to which the tectonic plates are interlocked or coupled, thus providing insights into areas prone to seismic release or potential earthquake generation. Additionally, such advancements will contribute to enhancing seismic hazard assessments by enabling a more detailed understanding of regions experiencing greater or lesser coupling rates, thereby aiding in more accurate earthquake forecasting and risk assessments.

4. **Integration of seismic and geodetic data for fault kinematics:** In the present thesis, only geodetic-based results were considered to constrain fault parameters. While geodetic data provides valuable insights into surface deformation, it has limitations in revealing the geometry and behavior of faults at greater depths. Geodetic measurements alone may not fully capture the complexities of fault structure, particularly in the deeper parts of the area. Therefore, integrating seismic data that can provide information about the subsurface fault geometry and slip distribution would be beneficial. This comprehensive approach would allow for a more detailed calculation of fault kinematics, including a precise mapping of the fault.

5. **Integration of geological and geodetic data with field investigation for fault kinematics:** While geodetic data offers precise surface deformation measurements, geological data, including rock samples and stratigraphic information, provides context about the fault's history and structural characteristics. Field investigations, such as mapping fault traces, studying outcrops, and analyzing sediment deposits, can reveal past earthquake events and the physical properties of fault zones. By combining these approaches, researchers can develop more accurate models of fault slip behavior, including both the shallow and deeper parts of the fault system. This comprehensive analysis would improve our understanding of the fault's mechanical

properties, help refine slip rate estimates, and provide a clearer picture of the seismic hazard posed by these faults.

6. **Enhancing earthquake interevent time-modeling**: This thesis explores modeling the interevent time of large earthquakes using thirteen reference probability distributions. Apart from the studied probability distributions that include conventional (e.g. exponential, gamma, lognormal, Weibull, and Rayleigh), heavy-tailed (e.g. Frechet, lognormal, Pareto, Levy, and Weibull), and exponentiated groups (e.g. exponentiated exponential, exponentiated Weibull, and exponentiated Rayleigh), beta-group of distributions such as the beta-exponential, beta-Weibull, beta-Frechet, beta-Maxwell, beta-exponentiated exponential, and others can be implemented to examine their suitability for the present earthquake catalogs of the Himalayan region. Additionally, the present research derives hazard function curves for various elapsed times and residual times, with potential future investigations focusing on functions like the survival function and reverse hazard function for a more comprehensive analysis of interevent times in the Himalaya.

7. **Understanding the physical implications of the nowcasting methodology:** The empirical nowcasting approach relies on a model rooted in "short-term fault memory," assuming the total release of accumulated strain in a single seismic event. This stands in contrast to the emerging idea of "earthquake supercycles" observed in major earthquakes, displaying "long-term fault memory" and potentially leaving residual stress. Exploring this discrepancy further, along with a detailed physical interpretation of the empirical nowcasting method, could be a focus for future investigation.

8. **Enhansing seismic hazard using combined geodetic and statistical methods:** Future research can focus on combining geodetic results, such as crustal deformation, strain measurements with statistical methods to enhance our understanding about earthquake potential, interoccurrence times, and earthquake potential scores. By

integrating these data sources, researchers can refine the estimation of earthquake potential and improve predictions for future seismic activity. This interdisciplinary approach will lead to more accurate and comprehensive seismic hazard assessments, aiding in better risk mitigation and preparedness strategies.

9. **Understanding the role of seasonal variations in seismicity modulation:** Several studies, such as Bollinger et al. (2007) [319] and Bettinelli et al. (2008) [320] propose that the seasonal fluctuations in seismic activity in the Himalayas will result from added compression in the region due to reduced pressure in the Indo-Gangetic plains during winter. To truly comprehend how seasonal mass changes impact seismicity, a precise measurement of stress alteration on the MHT is needed. Additionally, delving into the mechanisms influencing seasonal changes in surface deformation across the Himalayas will contribute significantly to understanding these seismic fluctuations.

10. **Combining GPS and InSAR data to achieve high-resolution crustal deformation mapping across the entire Himalayan arc:** In the future, integrating GPS and InSAR data could open avenues for comprehensive, high-resolution crustal deformation mapping across the entire Himalayan arc. This integration might enable a more detailed understanding of the complex tectonic processes in this region. Further, this approach can offer an enhanced perspective on seismic hazard assessment and active tectonics along the whole Himalaya.

11. **Exploring the impact of subducting ridges and rifts on Himalayan tectonics remains a significant pursuit:** Investigating how these features potentially constrain the scope of large earthquakes and studying their influence on fault geometry and strain accumulation through GPS and/or InSAR observations is crucial. This exploration would contribute significantly to a more accurate evaluation of future seismic hazards in the region.

12. **Seismic risk mapping:** The insights gained from this thesis can contribute sig-

nificantly to seismic hazard analysis along the Kumaun and Nepal Himalaya. A prospective avenue for future work involves generating seismic risk maps by considering vulnerability factors and other pertinent aspects.

Bibliography

[1] P. Molnar and P. Tapponnier. “Relation of the tectonics of eastern China to the India-Eurasia collision: Application of slip-line field theory to large-scale continental tectonics”. *Geology* 5.4 (1977), pp. 212–216.

[2] A. Yin. “Cenozoic tectonic evolution of the Himalayan orogen as constrained by along-strike variation of structural geometry, exhumation history, and foreland sedimentation”. *Earth-Science Reviews* 76.1-2 (2006), pp. 1–131.

[3] N. Ambraseys and D. Jackson. “A note on early earthquakes in northern India and southern Tibet”. *Current Science* (2003), pp. 570–582.

[4] R. Bilham. “Earthquakes in India and the Himalaya: Tectonics, geodesy and history”. *Annals of Geophysics* 47 (2004), pp. 839–858.

[5] R. Bilham. “Himalayan earthquakes: A review of historical seismicity and early 21st century slip potential”. *Geological Society, London, Special Publications* 483.1 (2019), pp. 423–482.

[6] N. Ambraseys and J. Douglas. “Magnitude calibration of north Indian earthquakes”. *Geophysical Journal International* 159.1 (2004), pp. 165–206.

[7] R. Bilham, V. K. Gaur, and P. Molnar. “Himalayan seismic hazard”. *Science* 293.5534 (2001), pp. 1442–1444.

[8] S. Sapkota, L. Bollinger, Y. Klinger, P. Tapponnier, Y. Gaudemer, and D. Tiwari. “Primary surface ruptures of the great Himalayan earthquakes in 1934 and 1255”. *Nature Geoscience* 6.1 (2013), pp. 71–76.

[9] H. Verma, S. Pasari, and Y. Sharma. “Tectonic deformation along the Delhi-Haridwar Ridge revealed by InSAR observations: Preliminary results”. In: *2021 IEEE International India Geoscience and Remote Sensing Symposium (InGARSS)*. IEEE. 2021, pp. 181–184.

[10] Y. Sharma, S. Pasari, K.-E. Ching, O. Dikshit, T. Kato, J. N. Malik, C.-P. Chang, and J.-Y. Yen. “Spatial distribution of earthquake potential along the Himalayan arc”. *Tectonophysics* 791 (2020), p. 228556.

[11] E. O. Lindsey, R. Almeida, R. Mallick, J. Hubbard, K. Bradley, L. L. Tsang, Y. Liu, R. Burgmann, and E. M. Hill. “Structural control on downdip locking extent of the Himalayan megathrust”. *Journal of Geophysical Research: Solid Earth* 123.6 (2018), pp. 5265–5278.

[12] T. Ader, J.-P. Avouac, J. Liu-Zeng, H. Lyon-Caen, L. Bollinger, J. Galetzka, J. Genrich, M. Thomas, K. Chanard, S. N. Sapkota, et al. “Convergence rate across the Nepal Himalaya and interseismic coupling on the Main Himalayan Thrust: Implications for seismic hazard”. *Journal of Geophysical Research: Solid Earth* 117.B4 (2012), B04403.

[13] S. Pasari and O. Dikshit. “Three-parameter generalized exponential distribution in earthquake recurrence interval estimation”. *Natural Hazards* 73.2 (2014), pp. 639–656.

[14] S. Pasari and A. Mehta. “Nowcasting earthquakes in the northwest Himalaya and surrounding regions”. *The International Archives of the Photogrammetry, Remote Sensing and Spatial Information Sciences* 42 (2018), pp. 855–859.

[15] J. B. Rundle and A. Donnellan. “Nowcasting earthquakes in southern California with machine learning: Bursts, swarms, and aftershocks may be related to levels of regional tectonic stress”. *Earth and Space Science* 7.9 (2020), e2020EA001097.

[16] R. Bilham, K. Larson, and J. Freymueller. “GPS measurements of present-day convergence across the Nepal Himalaya”. *Nature* 386.6620 (1997), pp. 61–64.

[17] J. Champenois, B. Fruneau, E. Pathier, B. Deffontaines, K.-C. Lin, and J.-C. Hu. "Monitoring of active tectonic deformations in the longitudinal valley (eastern Taiwan) using Persistent Scatterer InSAR method with ALOS PALSAR data". *Earth and Planetary Science Letters* 337 (2012), pp. 144–155.

[18] M. Lazeckỳ, K. Spaans, P. J. González, Y. Maghsoudi, Y. Morishita, F. Albino, J. Elliott, N. Greenall, E. Hatton, A. Hooper, et al. "LiCSAR: An automatic InSAR tool for measuring and monitoring tectonic and volcanic activity". *Remote Sensing* 12.15 (2020), p. 2430.

[19] X. Xu, D. T. Sandwell, E. Tymofyeyeva, A. González-Ortega, and X. Tong. "Tectonic and anthropogenic deformation at the Cerro Prieto geothermal step-over revealed by Sentinel-1A InSAR". *IEEE Transactions on Geoscience and Remote Sensing* 55.9 (2017), pp. 5284–5292.

[20] M. C. Garthwaite, H. Wang, and T. J. Wright. "Broadscale interseismic deformation and fault slip rates in the central Tibetan Plateau observed using InSAR". *Journal of Geophysical Research: Solid Earth* 118.9 (2013), pp. 5071–5083.

[21] M. Nyst and W. Thatcher. "New constraints on the active tectonic deformation of the Aegean". *Journal of Geophysical Research: Solid Earth* 109.B11 (2004), B11406.

[22] H. Billiris, D. Paradissis, G. Veis, P. England, W. Featherstone, B. Parsons, P. Cross, P. Rands, M. Rayson, P. Sellers, et al. "Geodetic determination of tectonic deformation in central Greece from 1900 to 1988". *Nature* 350.6314 (1991), pp. 124–129.

[23] E. Gunawan and S. Widiyantoro. "Active tectonic deformation in Java, Indonesia inferred from a GPS-derived strain rate". *Journal of Geodynamics* 123 (2019), pp. 49–54.

[24] Y. Bock and D. Melgar. "Physical applications of GPS geodesy: A review". *Reports on Progress in Physics* 79.10 (2016), p. 106801.

[25] R. Gens and J. L. Van Genderen. “Review article SAR interferometry–issues, techniques, applications”. *International Journal of Remote Sensing* 17.10 (1996), pp. 1803–1835.

[26] H. Verma, Y. Sharma, and S. Pasari. “Synthetic aperture radar interferometry to measure earthquake-related deformation: A case study from Nepal”. In: *Disaster Management in the Complex Himalayan Terrains*. Springer, 2022, pp. 133–140.

[27] H Wang and T. Wright. “Satellite geodetic imaging reveals internal deformation of western Tibet”. *Geophysical Research Letters* 39.7 (2012), p. L07303.

[28] C. Pagli, H. Wang, T. J. Wright, E. Calais, and E. Lewi. “Current plate boundary deformation of the Afar rift from a 3-D velocity field inversion of InSAR and GPS”. *Journal of Geophysical Research: Solid Earth* 119.11 (2014), pp. 8562–8575.

[29] Z. Shen and Z. Liu. “Integration of GPS and InSAR data for resolving 3-dimensional crustal deformation”. *Earth and Space Science* 7.4 (2020), e2019EA001036.

[30] X. Tong, D. Sandwell, and B. Smith-Konter. “High-resolution interseismic velocity data along the San Andreas Fault from GPS and InSAR”. *Journal of Geophysical Research: Solid Earth* 118.1 (2013), pp. 369–389.

[31] X. Song, Y. Jiang, X. Shan, W. Gong, and C. Qu. “A fine velocity and strain rate field of present-day crustal motion of the northeastern Tibetan Plateau inverted jointly by InSAR and GPS”. *Remote Sensing* 11.4 (2019), p. 435.

[32] P. Patriat and J. Achache. “India–Eurasia collision chronology has implications for crustal shortening and driving mechanism of plates”. *Nature* 311.5987 (1984), pp. 615–621.

[33] P. Molnar and P. Tapponnier. “The collision between India and Eurasia”. *Scientific American* 236.4 (1977), pp. 30–41.

[34] M. Searle, R. I. Corfield, B. Stephenson, and J. McCarron. “Structure of the north Indian continental margin in the Ladakh–Zanskar Himalayas: Implications for the timing of obduction of the Spontang ophiolite, India–Asia collision and deformation events in the Himalaya”. *Geological Magazine* 134.3 (1997), pp. 297–316.

[35] M. K. Clark. “Continental collision slowing due to viscous mantle lithosphere rather than topography”. *Nature* 483.7387 (2012), pp. 74–77.

[36] A. Copley, J.-P. Avouac, and J.-Y. Royer. “India-Asia collision and the Cenozoic slowdown of the Indian plate: Implications for the forces driving plate motions”. *Journal of Geophysical Research: Solid Earth* 115.B3 (2010), B03410.

[37] D. B. Rowley. “Age of initiation of collision between India and Asia: A review of stratigraphic data”. *Earth and Planetary Science Letters* 145.1-4 (1996), pp. 1–13.

[38] C. M. Powell and P. Conaghan. “Plate tectonics and the Himalayas”. *Earth and Planetary Science Letters* 20.1 (1973), pp. 1–12.

[39] K. V. Hodges. “Tectonics of the Himalaya and southern Tibet from two perspectives”. *Geological Society of America Bulletin* 112.3 (2000), pp. 324–350.

[40] M. P. Coward, D. C. Rex, M. A. Khan, B. F. Windley, R. D. Broughton, I. W. Luff, M. G. Petterson, and C. J. Pudsey. “Collision tectonics in the NW Himalayas”. *Geological Society, London, Special Publications* 19.1 (1986), pp. 203–219.

[41] J. Ni and M. Barazangi. “Seismotectonics of the Himalayan collision zone: Geometry of the underthrusting Indian plate beneath the Himalaya”. *Journal of Geophysical Research: Solid Earth* 89.B2 (1984), pp. 1147–1163.

[42] P. Bettinelli, J.-P. Avouac, M. Flouzat, F. Jouanne, L. Bollinger, P. Willis, and G. R. Chitrakar. “Plate motion of India and interseismic strain in the Nepal Himalaya from GPS and DORIS measurements”. *Journal of Geodesy* 80.8 (2006), pp. 567–589.

[43] A. Gansser. *Geology of the Himalayas*. Wiley Interscience, 1964.

[44] K. Valdiya. “Lesser Himalayan geology: Crucial problems and controversies”. *Current Science* (1983), pp. 839–857.

[45] L. Seeber and J. G. Armbruster. “Great detachment earthquakes along the Himalayan arc and long-term forecasting”. *Earthquake Prediction: An International Review* 4 (1981), pp. 259–277.

[46] K. Valdiya. “Reactivation of terrane-defining boundary thrusts in central sector of the Himalaya: Implications”. *Current Science* 81.11 (2001), pp. 1418–1431.

[47] T. Nakata. “Geomorphic history and crustal movement of the foot-hills of the Himalayas”. *Science Report Tohoku Univ. 7th series (Geography)* 22 (1972), pp. 39–177.

[48] T. Nakata. “Active faults of the Himalaya of India and Nepal”. *Tectonics of the Western Himalayas* 232 (1989), pp. 243–264.

[49] K. S. Valdiya. “The Main Boundary Thrust zone of the Himalaya, India”. *Annales Tectonicae* 6 (1992), pp. 54–84.

[50] A. Macfarlane, R. B. Sorkhabi, and J. Quade. *Himalaya and Tibet: Mountain Roots to Mountain Tops*. Vol. 328. Geological Society of America, 1999.

[51] P. Saklani and V. Bahugana. “Thrust tectonics of Garwhal Himalaya”. In: *Himalayan Thrusts and Associated Rocks*. 1986, pp. 1–25.

[52] K. Valdiya. “Himalayan transverse faults and folds and their parallelism with subsurface structures of north Indian plains”. *Tectonophysics* 32.3-4 (1976), pp. 353–386.

[53] L. P. Paudel and K. Arita. “Tectonic and polymetamorphic history of the Lesser Himalaya in central Nepal”. *Journal of Asian Earth Sciences* 18.5 (2000), pp. 561–584.

[54] C. Tripathi. “Siwaliks of the Indian subcontinent”. *Journal of the Palaeontological Society of India* 31 (1986), pp. 1–8.

[55] C. Karunakaran. “Status of exploration for hydrocarbons in the Himalayan region: Contributions to stratigraphy and structure”. *Geological Survey of India, Miscellaneous Publications* 41 (1976), pp. 1–66.

[56] S. Arora and J. N. Malik. “Overestimation of the earthquake hazard along the Himalaya: Constraints in bracketing of medieval earthquakes from paleoseismic studies”. *Geoscience Letters* 4 (2017), pp. 1–15.

[57] S. Mukherjee. “A review on out-of-sequence deformation in the Himalaya”. *Special Publications* 412.1 (2015), pp. 67–109.

[58] W. R. Dickinson. *Tectonics and Sedimentation*. SEPM Society for Sedimentary Geology, 1974.

[59] P. Molnar. “Structure and tectonics of the Himalaya: Constraints and implications of geophysical data”. *Annual Review of Earth and Planetary Sciences* 12.1 (1984), pp. 489–516.

[60] P. Gupta. “The geology and geomorphology of the Indo-Gangetic Plain and the emergence of the Harappan culture”. *Mankind Quarterly* 25.4 (1985), p. 371.

[61] A. Yin, C. Dubey, T. Kelty, G. Gehrels, C. Chou, M. Grove, and O Lovera. “Structural evolution of the Arunachal Himalaya and implications for asymmetric development of the Himalayan orogen”. *Current Science* (2006), pp. 195–206.

[62] R. Quittmeyer and K. Jacob. “Historical and modern seismicity of Pakistan, Afghanistan, northwestern India, and southeastern Iran”. *Bulletin of the Seismological Society of America* 69.3 (1979), pp. 773–823.

[63] P. Le Fort. “Himalayas: The collided range. Present knowledge of the continental arc”. *American Journal of Science* 275.1 (1975), pp. 1–44.

[64] R. Carosi, C. Montomoli, and S. Iaccarino. “20 years of geological mapping of the metamorphic core across central and eastern Himalayas”. *Earth-Science Reviews* 177 (2018), pp. 124–138.

[65] G. Fuchs. *Contributions to the Geology of the North-Western Himalayas*. Geologische Bundesanstalt, 1975.

[66] P. M. Powers, R. J. Lillie, and R. S. Yeats. "Structure and shortening of the Kangra and Dehra Dun reentrants, sub-Himalaya, India". *Geological Society of America Bulletin* 110.8 (1998), pp. 1010–1027.

[67] S. Kumar and A. Mahajan. "Seismotectonics of the Kangra region, northwest Himalaya". *Tectonophysics* 331.4 (2001), pp. 359–371.

[68] J. N. Malik and C. Mohanty. "Active tectonic influence on the evolution of drainage and landscape: Geomorphic signatures from frontal and hinterland areas along the Northwestern Himalaya, India". *Journal of Asian Earth Sciences* 29.5-6 (2007), pp. 604–618.

[69] V. Raiverman, A. Srivastava, and D. Prasad. "On the foothill thrust of northwestern Himalaya". *Journal of Himalayan Geology* 4.2 (1993), pp. 237–256.

[70] V. Gahalaut and B. Kundu. "Possible influence of subducting ridges on the Himalayan arc and on the ruptures of great and major Himalayan earthquakes". *Gondwana Research* 21.4 (2012), pp. 1080–1088.

[71] F. Jouanne, J.-L. Mugnier, J. Gamond, P. Le Fort, M. Pandey, L. Bollinger, M Flouzat, and J.-P. Avouac. "Current shortening across the Himalayas of Nepal". *Geophysical Journal International* 157.1 (2004), pp. 1–14.

[72] J. Lavé and J.-P. Avouac. "Active folding of fluvial terraces across the Siwaliks Hills, Himalayas of central Nepal". *Journal of Geophysical Research: Solid Earth* 105.B3 (2000), pp. 5735–5770.

[73] V. Stevens and J. Avouac. "Interseismic coupling on the Main Himalayan Thrust". *Geophysical Research Letters* 42.14 (2015), pp. 5828–5837.

[74] J. Lavé, D. Yule, S. Sapkota, K. Basant, C. Madden, M. Attal, and R. Pandey. "Evidence for a great medieval earthquake ($\sim$1100 AD) in the central Himalayas, Nepal". *Science* 307.5713 (2005), pp. 1302–1305.

[75] I. Pierce and S. G. Wesnousky. “On a flawed conclusion that the 1255 AD earthquake ruptured 800 km of the Himalayan Frontal Thrust east of Kathmandu”. *Geophysical Research Letters* 43.17 (2016), pp. 9026–9029.

[76] D. Schelling and K. Arita. “Thrust tectonics, crustal shortening, and the structure of the far-eastern Nepal Himalaya”. *Tectonics* 10.5 (1991), pp. 851–862.

[77] L. Bollinger, P. Tapponnier, S. Sapkota, and Y. Klinger. “Slip deficit in central Nepal: Omen for a repeat of the 1344 AD earthquake?” *Earth, Planets and Space* 68.1 (2016), pp. 1–12.

[78] I. BIS. “Indian standard criteria for earthquake resistant design of structures”. *Bureau of Indian Standards, New Delhi* (2002).

[79] J. Kayal, S. Arefiev, S. Barua, D. Hazarika, N. Gogoi, A. Kumar, S. Chowdhury, and S. Kalita. “Shillong plateau earthquakes in northeast India region: Complex tectonic model”. *Current Science* 91.1 (2006), pp. 109–114.

[80] D. Nandy. *Geodynamics of Northeastern India and the Adjoining Region*. Scientific Book Centre, 2017.

[81] C. Wobus, A. Heimsath, K. Whipple, and K. Hodges. “Active out-of-sequence thrust faulting in the central Nepalese Himalaya”. *Nature* 434.7036 (2005), pp. 1008–1011.

[82] W. Zhao, K. Nelson, J. Che, J. Quo, D. Lu, C. Wu, and X. Liu. “Deep seismic reflection evidence for continental underthrusting beneath southern Tibet”. *Nature* 366.6455 (1993), pp. 557–559.

[83] R. S. Yeats and R. J. Lillie. “Contemporary tectonics of the Himalayan frontal fault system: Folds, blind thrusts and the 1905 Kangra earthquake”. *Journal of Structural Geology* 13.2 (1991), pp. 215–225.

[84] V. Thakur, M. Joshi, D. Sahoo, N. Suresh, R. Jayangondapermal, and A. Singh. "Partitioning of convergence in northwest Sub-Himalaya: Estimation of late Quaternary uplift and convergence rates across the Kangra reentrant, north India". *International Journal of Earth Sciences* 103 (2014), pp. 1037–1056.

[85] M. Ponraj, S. Miura, C. Reddy, S. Prajapati, S. Amirtharaj, and S. Mahajan. "Estimation of strain distribution using GPS measurements in the Kumaun region of Lesser Himalaya". *Journal of Asian Earth Sciences* 39.6 (2010), pp. 658–667.

[86] B. Mukhopadhyay. "Clusters of moderate size earthquakes along Main Central Thrust (MCT) in Himalaya". *International Journal of Geosciences* 2.03 (2011), p. 318.

[87] K. D. Nelson, W. Zhao, L. Brown, J. Kuo, J. Che, X. Liu, S. Klemperer, Y. Makovsky, R. Meissner, J. Mechie, et al. "Partially molten middle crust beneath southern Tibet: Synthesis of project INDEPTH results". *Science* 274.5293 (1996), pp. 1684–1688.

[88] H. Gupta and V. Gahalaut. "Seismotectonics and large earthquake generation in the Himalayan region". *Gondwana Research* 25.1 (2014), pp. 204–213.

[89] M. Ponraj, S. Amirtharaj, P. Sunil, A. P. Saji, K. V. Kumar, S. Arora, C. Reddy, and S. Begum. "An assessment of present-day crustal deformation in the Kumaun Himalaya from GPS observations". *Journal of Asian Earth Sciences* 176 (2019), pp. 274–280.

[90] R. K. Yadav, V. K. Gahalaut, A. K. Bansal, S. Sati, J. Catherine, P. Gautam, K. Kumar, and N. Rana. "Strong seismic coupling underneath Garhwal-Kumaun region, NW Himalaya, India". *Earth and Planetary Science Letters* 506 (2019), pp. 8–14.

[91] P. Banerjee and R. Bürgmann. "Convergence across the northwest Himalaya from GPS measurements". *Geophysical Research Letters* 29.13 (2002), pp. 30–1.

[92] P. K. Gautam, V. Gahalaut, S. K. Prajapati, N. Kumar, R. K. Yadav, N. Rana, and C. P. Dabral. “Continuous GPS measurements of crustal deformation in Garhwal-Kumaun Himalaya”. *Quaternary International* 462 (2017), pp. 124–129.

[93] V. Stevens and J.-P. Avouac. “Millenary Mw$>$ 9.0 earthquakes required by geodetic strain in the Himalaya”. *Geophysical Research Letters* 43.3 (2016), pp. 1118–1123.

[94] H. F. Reid. “The mechanism of the earthquake, the California earthquake of April 18, 1906”. *Report of the Research Senatorial Commission, Carnegie Institution, Washington, DC* 2 (1910), pp. 16–18.

[95] H. Gupta and V. Gahalaut. “Can an earthquake of $M_w \sim 9$ occur in the Himalayan region?” *Geological Society, London, Special Publications* 412.1 (2015), pp. 43–53.

[96] K. Khattri and A. Tyagi. “Seismicity patterns in the Himalayan plate boundary and identification of the areas of high seismic potential”. *Tectonophysics* 96.3-4 (1983), pp. 281–297.

[97] K. Khattri. “Great earthquakes, seismicity gaps and potential for earthquake disaster along the Himalaya plate boundary”. *Tectonophysics* 138.1 (1987), pp. 79–92.

[98] H. N. Srivastava, M. Verma, B. K. Bansal, and A. K. Sutar. “Discriminatory characteristics of seismic gaps in Himalaya”. *Geomatics, Natural Hazards and Risk* 6 (2015), pp. 224–242.

[99] S. Kannaujiya, R. K. Yadav, T. Sarkar, G. Sharma, P. Chauhan, S. K. Pal, P. N. Roy, P. K. Gautam, A. K. Taloor, A. Yadav, et al. “Unraveling seismic hazard by estimating prolonged crustal strain buildup in Kumaun-Garhwal, northwest Himalaya using GPS measurements”. *Journal of Asian Earth Sciences* 223 (2022), p. 104993.

[100] C. P. Rajendran and K. Rajendran. “The status of central seismic gap: A perspective based on the spatial and temporal aspects of the large Himalayan earthquakes”. *Tectonophysics* 395 (2005), pp. 19–39.

[101] S. S. Negi, A. Paul, S. Cesca, M. Kriegerowski, P. Mahesh, S. Gupta, et al. “Crustal velocity structure and earthquake processes of Garhwal-Kumaun Himalaya: Constraints from regional waveform inversion and array beam modeling”. *Tectonophysics* 712 (2017), pp. 45–63.

[102] R. A. Prasath, A. Paul, and S. Singh. “Upper crustal stress and seismotectonics of the Garhwal Himalaya using small-to-moderate earthquakes: Implications to the local structures and free fluids”. *Journal of Asian Earth Sciences* 135 (2017), pp. 198–211.

[103] G. Rawat, B. Arora, and P. Gupta. “Electrical resistivity cross-section across the Garhwal Himalaya: Proxy to fluid-seismicity linkage”. *Tectonophysics* 637 (2014), pp. 68–79.

[104] C. Rajendran, B. John, and K. Rajendran. “Medieval pulse of great earthquakes in the central Himalaya: Viewing past activities on the frontal thrust”. *Journal of Geophysical Research: Solid Earth* 120.3 (2015), pp. 1623–1641.

[105] C. Rajendran, B. John, K. Anandasabari, J. Sanwal, K. Rajendran, P. Kumar, and S. Chopra. “On the paleoseismic evidence of the 1803 earthquake rupture (or lack of it) along the frontal thrust of the Kumaun Himalaya”. *Tectonophysics* 722 (2018), pp. 227–234.

[106] S. Kumar, S. G. Wesnousky, T. K. Rockwell, R. W. Briggs, V. C. Thakur, and R. Jayangondaperumal. “Paleoseismic evidence of great surface rupture earthquakes along the Indian Himalaya”. *Journal of Geophysical Research: Solid Earth* 111.B3 (2006), B03304.

[107] Y. Kumahara and R. Jayangondaperumal. “Paleoseismic evidence of a surface rupture along the northwestern Himalayan Frontal Thrust (HFT)”. *Geomorphology* 180 (2013), pp. 47–56.

[108] K. Sreejith, P. Sunil, R. Agrawal, A. P. Saji, A. Rajawat, and D. Ramesh. “Audit of stored strain energy and extent of future earthquake rupture in central Himalaya”. *Scientific Reports* 8.1 (2018), pp. 1–9.

[109] B. Neupane, Y. Ju, C. M. Allen, P. D. Ulak, and K. Han. “Petrography and provenance of Upper Cretaceous–Palaeogene sandstones in the foreland basin system of central Nepal”. *International Geology Review* 60.2 (2018), pp. 135–156.

[110] O. Bhargava and B. P. Singh. “Geological evolution of the Tethys Himalaya”. *Episodes Journal of International Geoscience* 43.1 (2020), pp. 404–416.

[111] K. M. Larson, R. Bürgmann, R. Bilham, and J. T. Freymueller. “Kinematics of the India-Eurasia collision zone from GPS measurements”. *Journal of Geophysical Research: Solid Earth* 104.B1 (1999), pp. 1077–1093.

[112] R. Bilham and V. Gaur. “Buildings as weapons of mass destruction”. *Science* 341.6146 (2013), pp. 618–619.

[113] R. Bilham and N. Ambraseys. “Apparent Himalayan slip deficit from the summation of seismic moments for Himalayan earthquakes, 1500-2000”. *Current Science* 88.10 (2005), pp. 1658–1663.

[114] H. Bungum, C. D. Lindholm, and A. K. Mahajan. “Earthquake recurrence in NW and central Himalaya”. *Journal of Asian Earth Sciences* 138 (2017), pp. 25–37.

[115] S. Li, Q. Wang, S. Yang, X. Qiao, Z. Nie, R. Zou, K. Ding, P. He, and G. Chen. “Geodetic imaging mega-thrust coupling beneath the Himalaya”. *Tectonophysics* 747 (2018), pp. 225–238.

[116] R. Jayangondaperumal, J. Mugnier, and A. Dubey. “Earthquake slip estimation from the scarp geometry of Himalayan Frontal Thrust, western Himalaya: Implications for seismic hazard assessment”. *International Journal of Earth Sciences* 102 (2013), pp. 1937–1955.

[117] S. Jade. “Estimates of plate velocity and crustal deformation in the Indian subcontinent using GPS geodesy”. *Current Science* 86.10 (2004), pp. 1443–1448.

[118] S. Jade, B. Bhatt, Z. Yang, R. Bendick, V. Gaur, P. Molnar, M. Anand, and D. Kumar. “GPS measurements from the Ladakh Himalaya, India: Preliminary tests of plate-like or continuous deformation in Tibet”. *Geological Society of America Bulletin* 116.11-12 (2004), pp. 1385–1391.

[119] S. Jade, M. Mukul, V. Gaur, K. Kumar, T. Shrungeshwar, G. Satyal, R. K. Dumka, S. Jagannathan, M. Ananda, P. D. Kumar, et al. “Contemporary deformation in the Kashmir-Himachal, Garhwal and Kumaon Himalaya: Significant insights from 1995–2008 GPS time series”. *Journal of Geodesy* 88 (2014), pp. 539–557.

[120] M. Ponraj, S. Miura, C. Reddy, S. Amirtharaj, and S. Mahajan. “Slip distribution beneath the central and western Himalaya inferred from GPS observations”. *Geophysical Journal International* 185.2 (2011), pp. 724–736.

[121] R. K. Dumka, B. S. Kotlia, K. Kumar, G. S. Satyal, and L. M. Joshi. “Crustal deformation revealed by GPS in Kumaun Himalaya, India”. *Journal of Mountain Science* 11 (2014), pp. 41–50.

[122] R. K. Dumka, B. S. Kotlia, K. Kumar, and G. S. Satyal. “Quantification of crustal strain rate in Kumaun Himalaya (India) using GPS measurements of crustal deformation”. *Himalayan Geology* 35.2 (2014), pp. 146–155.

[123] R. K. Dumka, B. S. Kotlia, G. C. Kothyari, J. Paikrey, and S. Dimri. “Detection of high and moderate crustal strain zones in Uttarakhand Himalaya, India”. *Acta Geodaetica et Geophysica* 53.3 (2018), pp. 503–521.

[124] R. K. Yadav, V. K. Gahalaut, and A. K. Bansal. “Tectonic and non-tectonic crustal deformation in Kumaun Garhwal Himalaya”. *Quaternary International* 585 (2021), pp. 171–182.

[125] Y. Sharma, S. Pasari, K.-E. Ching, H. Verma, and N. Choudhary. “Kinematics of crustal deformation along the central Himalaya”. *Acta Geophysica* 72 (2024), pp. 553–564.

[126] R. Bilham, F. Blume, R. Bendick, and V. K. Gaur. “Geodetic constraints on the translation and deformation of India: Implications for future great Himalayan earthquakes”. *Current Science* 74.3 (1998), pp. 213–229.

[127] R. Burgmann, K. Larson, and R. Bilham. “Model inversion of GPS and leveling measurements across the Himalaya: Implications for earthquake hazards and future geodetic networks”. *Himalayan Geology* 20 (1999), pp. 59–72.

[128] Q. Chen, J. T. Freymueller, Z. Yang, C. Xu, W. Jiang, Q. Wang, and J. Liu. “Spatially variable extension in southern Tibet based on GPS measurements”. *Journal of Geophysical Research: Solid Earth* 109.B9 (2004), B09401.

[129] R. Grandin, M.-P. Doin, L. Bollinger, B. Pinel-Puysségur, G. Ducret, R. Jolivet, and S. N. Sapkota. “Long-term growth of the Himalaya inferred from interseismic InSAR measurement”. *Geology* 40.12 (2012), pp. 1059–1062.

[130] Y. Li, X. Song, X. Shan, C. Qu, and Z. Wang. “Locking degree and slip rate deficit distribution on MHT fault before 2015 Nepal Mw 7.9 earthquake”. *Journal of Asian Earth Sciences* 119 (2016), pp. 78–86.

[131] F. Jouanne, J. L. Mugnier, S. N. Sapkota, P. Bascou, and A. Pecher. “Estimation of coupling along the Main Himalayan Thrust in the central Himalaya”. *Journal of Asian Earth Sciences* 133 (2017), pp. 62–71.

[132] F. Diao, R. Wang, Y. Zhu, and X. Xiong. “Revisiting the fault locking of the Central Himalayan Thrust with a viscoelastic earthquake-cycle deformation model”. *Seismological Society of America* 93.1 (2022), pp. 193–200.

[133] B. Hofmann-Wellenhof, H. Lichtenegger, and J. Collins. *Global Positioning System: Theory and Practice*. Springer Science & Business Media, 2012.

[134] M. S. Grewal, L. R. Weill, and A. P. Andrews. *Global Positioning Systems, Inertial Navigation, and Integration*. John Wiley & Sons, 2007.

[135] X. He, J.-P. Montillet, R. Fernandes, M. Bos, K. Yu, X. Hua, and W. Jiang. "Review of current GPS methodologies for producing accurate time series and their error sources". *Journal of Geodynamics* 106 (2017), pp. 12–29.

[136] G. T. French. *Understanding the GPS–An Introduction to the Global Positioning System Bethesda, MD 20814: GeoResearch*. Inc. USA, 1996.

[137] F. S. T. Van Diggelen. *A-GPS: Assisted GPS, GNSS, and SBAS*. Norwood, USA: Artech House, 2009.

[138] L. H. Estey and C. M. Meertens. "TEQC: The multi-purpose toolkit for GPS/-GLONASS data". *GPS Solutions* 3.1 (1999), pp. 42–49.

[139] T. Herring, R. King, S. McClusky, et al. *Introduction to GAMIT/GLOBK*. Massachusetts Institute of Technology, Cambridge, Massachusetts, 2010.

[140] F. Leberl. *Observations and Least Squares*. New York, NY: Elsevier, 1978.

[141] T. Van Dam, J. Wahr, P. Milly, A. Shmakin, G. Blewitt, D. Lavallée, and K. Larson. "Crustal displacements due to continental water loading". *Geophysical Research Letters* 28.4 (2001), pp. 651–654.

[142] Z. Altamimi, L. Métivier, and X. Collilieux. "ITRF2008 plate motion model". *Journal of Geophysical Research: Solid Earth* 117.B7 (2012), B07402.

[143] G. Blewitt and D. Lavallée. "Effect of annual signals on geodetic velocity". *Journal of Geophysical Research: Solid Earth* 107.B7 (2002), ETG–9.

[144] S. Jade, T. Shrungeshwara, K. Kumar, P. Choudhury, R. K. Dumka, and H. Bhu. "India plate angular velocity and contemporary deformation rates from continuous GPS measurements from 1996 to 2015". *Scientific Reports* 7.1 (2017), pp. 1–16.

[145] S. K. Mondal, A. Borghi, P. Roy, and A. Aoudia. “GPS, scaling exponent and past seismicity for seismic hazard assessment in Garhwal–Kumaun, Himalayan region”. *Natural Hazards* 80 (2016), pp. 1349–1367.

[146] J. P. Pappachen, R. Sathiyaseelan, P. K. Gautam, and S. K. Pal. “Crustal velocity and interseismic strain-rate on possible zones for large earthquakes in the Garhwal–Kumaun Himalaya”. *Scientific Reports* 11.1 (2021), p. 21283.

[147] C. Mitsakaki, A. Agatza-Balodimou, and K. Papazissi. “Geodetic reference frames transformations”. *Survey Review* 38.301 (2006), pp. 608–618.

[148] G. Blewitt, C. Kreemer, W. C. Hammond, and J. Gazeaux. “MIDAS robust trend estimator for accurate GPS station velocities without step detection”. *Journal of Geophysical Research: Solid Earth* 121.3 (2016), pp. 2054–2068.

[149] P Banerjee, R Bürgmann, B Nagarajan, and E Apel. “Intraplate deformation of the Indian subcontinent”. *Geophysical Research Letters* 35.18 (2008), p. L18301.

[150] J. Paul, R. Bürgmann, V. Gaur, R. Bilham, K. Larson, M. Ananda, S. Jade, M. Mukal, T. Anupama, G. Satyal, et al. “The motion and active deformation of India”. *Geophysical Research Letters* 28.4 (2001), pp. 647–650.

[151] C. Kreemer, G. Blewitt, and E. C. Klein. “A geodetic plate motion and global strain rate model”. *Geochemistry, Geophysics, Geosystems* 15.10 (2014), pp. 3849–3889.

[152] H. Zhang, S. Van Der Lee, and Z. Ge. “Multiarray rupture imaging of the devastating 2015 Gorkha, Nepal, earthquake sequence”. *Geophysical Research Letters* 43.2 (2016), pp. 584–591.

[153] A. Berger, F. Jouanne, R. Hassani, and J. L. Mugnier. “Modelling the spatial distribution of present-day deformation in Nepal: How cylindrical is the Main Himalayan Thrust in Nepal?” *Geophysical Journal International* 156.1 (2004), pp. 94–114.

[154] R. K. Dumka, D. SuriBabu, K. Malik, S. Prajapati, and P. Narain. “PS-InSAR derived deformation study in the Kachchh, western India”. *Applied Computing and Geosciences* 8 (2020), p. 100041.

[155] A. Yhokha, C.-P. Chang, P. K. Goswami, J.-Y. Yen, and S.-I. Lee. “Surface deformation in the Himalaya and adjoining piedmont zone of the Ganga Plain, Uttarakhand, India: Determined by different radar interferometric techniques”. *Journal of Asian Earth Sciences* 106 (2015), pp. 119–129.

[156] T. Kobayashi, Y. Morishita, and H. Yarai. “Detailed crustal deformation and fault rupture of the 2015 Gorkha earthquake, Nepal, revealed from ScanSAR-based interferograms of ALOS-2”. *Earth, Planets and Space* 67.1 (2015), pp. 1–13.

[157] X. Zhou, N.-B. Chang, and S. Li. “Applications of SAR interferometry in earth and environmental science research”. *Sensors* 9.3 (2009), pp. 1876–1912.

[158] Y. Morishita, M. Lazecky, T. J. Wright, J. R. Weiss, J. R. Elliott, and A. Hooper. “LiCSBAS: An open-source InSAR time series analysis package integrated with the LiCSAR automated Sentinel-1 InSAR processor”. *Remote Sensing* 12.3 (2020), p. 424.

[159] A. Radutu, I. Nedelcu, and C. Gogu. “An overview of ground surface displacements generated by groundwater dynamics, revealed by InSAR techniques”. *Procedia Engineering* 209 (2017), pp. 119–126.

[160] V. Gahalaut, R. K. Yadav, K. Sreejith, K. Gahalaut, R. Bürgmann, R. Agrawal, S. Sati, and A. Bansal. “InSAR and GPS measurements of crustal deformation due to seasonal loading of Tehri reservoir in Garhwal Himalaya, India”. *Geophysical Journal International* 209.1 (2017), pp. 425–433.

[161] K. Sreejith, R. Agrawal, and A. Rajawat. “Crustal deformation studies using synthetic aperture interferometry”. *Proceedings of the Indian National Science Academy* 82.3 (2016), pp. 737–746.

[162] A. Ferretti, A. Monti-Guarnieri, C. Prati, and F. Rocca. *InSAR principles: Guidelines for SAR interferometry processing and interpretation, 19 vols*. The Netherlands: ESA Publications, 2007.

[163] D. Massonnet and K. L. Feigl. "Radar interferometry and its application to changes in the Earth's surface". *Reviews of Geophysics* 36.4 (1998), pp. 441–500.

[164] R. Bürgmann, P. A. Rosen, and E. J. Fielding. "Synthetic aperture radar interferometry to measure Earth's surface topography and its deformation". *Annual Review of Earth and Planetary Sciences* 28.1 (2000), pp. 169–209.

[165] P. A. Rosen, S. Hensley, I. R. Joughin, F. K. Li, S. N. Madsen, E. Rodriguez, and R. M. Goldstein. "Synthetic aperture radar interferometry". *Proceedings of the IEEE* 88.3 (2000), pp. 333–382.

[166] H. A. Zebker, P. A. Rosen, and S. Hensley. "Atmospheric effects in interferometric synthetic aperture radar surface deformation and topographic maps". *Journal of Geophysical Research: Solid Earth* 102.B4 (1997), pp. 7547–7563.

[167] C. Yu, N. T. Penna, and Z. Li. "Generation of real-time mode high-resolution water vapor fields from GPS observations". *Journal of Geophysical Research: Atmospheres* 122.3 (2017), pp. 2008–2025.

[168] C. Yu, Z. Li, and N. T. Penna. "Interferometric synthetic aperture radar atmospheric correction using a GPS-based iterative tropospheric decomposition model". *Remote Sensing of Environment* 204 (2018), pp. 109–121.

[169] C. Yu, Z. Li, N. T. Penna, and P. Crippa. "Generic atmospheric correction model for interferometric synthetic aperture radar observations". *Journal of Geophysical Research: Solid Earth* 123.10 (2018), pp. 9202–9222.

[170] P. López-Quiroz, M.-P. Doin, F. Tupin, P. Briole, and J.-M. Nicolas. "Time series analysis of Mexico city subsidence constrained by radar interferometry". *Journal of Applied Geophysics* 69.1 (2009), pp. 1–15.

[171] M.-P. Doin, S. Guillaso, R. Jolivet, C. Lasserre, F. Lodge, G. Ducret, and R. Grandin. “Presentation of the small baseline NSBAS processing chain on a case example: The Etna deformation monitoring from 2003 to 2010 using Envisat data”. In: *Proceedings of the Fringe Symposium*. ESA SP-697, Frascati, Italy. 2011, pp. 3434–3437.

[172] B. Efron and R. Tibshirani. “Bootstrap methods for standard errors, confidence intervals, and other measures of statistical accuracy”. *Statistical Science* 1.1 (1986), pp. 54–75.

[173] F. De Zan, M. Zonno, and P. Lopez-Dekker. “Phase inconsistencies and multiple scattering in SAR interferometry”. *IEEE Transactions on Geoscience and Remote Sensing* 53.12 (2015), pp. 6608–6616.

[174] E. Hussain, T. J. Wright, R. J. Walters, D. P. Bekaert, R. Lloyd, and A. Hooper. “Constant strain accumulation rate between major earthquakes on the North Anatolian Fault”. *Nature Communications* 9.1 (2018), pp. 1–9.

[175] J. R. Weiss, R. J. Walters, Y. Morishita, T. J. Wright, M. Lazecky, H. Wang, E. Hussain, A. J. Hooper, J. R. Elliott, C. Rollins, et al. “High-resolution surface velocities and strain for Anatolia from Sentinel-1 InSAR and GNSS data”. *Geophysical Research Letters* 47.17 (2020), e2020GL087376.

[176] R. Walters, B. Parsons, and T. Wright. “Constraining crustal velocity fields with InSAR for eastern Turkey: Limits to the block-like behavior of eastern Anatolia”. *Journal of Geophysical Research: Solid Earth* 119.6 (2014), pp. 5215–5234.

[177] H. Wang, T. J. Wright, J. Liu-Zeng, and L. Peng. “Strain rate distribution in south-central Tibet from two decades of InSAR and GPS”. *Geophysical Research Letters* 46.10 (2019), pp. 5170–5179.

[178] M. Desbrun, M. Meyer, P. Schröder, and A. H. Barr. “Implicit fairing of irregular meshes using diffusion and curvature flow”. In: *Proceedings of the 26th Annual Conference on Computer Graphics and Interactive Techniques*. 1999, pp. 317–324.

[179] B. Parsons, T. Wright, P. Rowe, J. Andrews, J. Jackson, R. Walker, M. Khatib, M. Talebian, E. Bergman, and E. Engdahl. “The 1994 Sefidabeh (eastern Iran) earthquakes revisited: New evidence from satellite radar interferometry and carbonate dating about the growth of an active fold above a blind thrust fault”. *Geophysical Journal International* 164.1 (2006), pp. 202–217.

[180] L. Bollinger, J. Avouac, R. Cattin, and M. Pandey. “Stress buildup in the Himalaya”. *Journal of Geophysical Research: Solid Earth* 109.B11 (2004), B11405.

[181] R. Cattin and J. Avouac. “Modeling mountain building and the seismic cycle in the Himalaya of Nepal”. *Journal of Geophysical Research: Solid Earth* 105.B6 (2000), pp. 13389–13407.

[182] M. R. Pant. “A step toward a historical seismicity of Nepal”. *Adarsa* 2 (2002), pp. 29–60.

[183] R. Yadav, Y. Bayrak, J. Tripathi, S. Chopra, A. Singh, and E. Bayrak. “A probabilistic assessment of earthquake hazard parameters in NW Himalaya and the adjoining regions”. *Pure and Applied Geophysics* 169 (2012), pp. 1619–1639.

[184] S. Pasari. “Stochastic modelling of earthquake interoccurrence times in northwest Himalaya and adjoining regions”. *Geomatics, Natural Hazards and Risk* 9.1 (2018), pp. 568–588.

[185] E. Scordilis. “Empirical global relations converting MS and mb to moment magnitude”. *Journal of Seismology* 10 (2006), pp. 225–236.

[186] A. Pancha, J. G. Anderson, and C. Kreemer. “Comparison of seismic and geodetic scalar moment rates across the basin and range province”. *Bulletin of the Seismological Society of America* 96.1 (2006), pp. 11–32.

[187] M. A. Goudarzi, M. Cocard, and R. Santerre. “GeoStrain: An open source software for calculating crustal strain rates”. *Computers & Geosciences* 82 (2015), pp. 1–12.

[188] M. Hackl, R. Malservisi, and S. Wdowinski. “Strain rate patterns from dense GPS networks”. *Natural Hazards and Earth System Sciences* 9.4 (2009), pp. 1177–1187.

[189] M. Palano, P. Imprescia, A. Agnon, and S. Gresta. “An improved evaluation of the seismic/geodetic deformation-rate ratio for the Zagros Fold-and-Thrust collisional belt”. *Geophysical Journal International* 213.1 (2018), pp. 194–209.

[190] F. Sparacino, B. G. Galuzzi, M. Palano, M. Segou, and C. Chiarabba. “Seismic coupling for the Aegean-Anatolian region”. *Earth-Science Reviews* 228 (2022), p. 103993.

[191] C. Scholz. *The mechanics of earthquakes and faulting*. Cambridge University Press, 1990.

[192] P. Bird, D. D. Jackson, Y. Y. Kagan, C. Kreemer, and R. Stein. “GEAR1: A global earthquake activity rate model constructed from geodetic strain rates and smoothed seismicity”. *Bulletin of the Seismological Society of America* 105.5 (2015), pp. 2538–2554.

[193] P. Molnar. “Earthquake recurrence intervals and plate tectonics”. *Bulletin of the Seismological Society of America* 69.1 (1979), pp. 115–133.

[194] C. Rollins and J.-P. Avouac. “A geodesy-and seismicity-based local earthquake likelihood model for central Los Angeles”. *Geophysical Research Letters* 46.6 (2019), pp. 3153–3162.

[195] S. G. Wesnousky, C. H. Scholz, and K. Shimazaki. “Deformation of an island arc: Rates of moment release and crustal shortening in intraplate Japan determined from seismicity and Quaternary fault data”. *Journal of Geophysical Research: Solid Earth* 87.B8 (1982), pp. 6829–6852.

[196] Z.-K. Shen, D. D. Jackson, and B. X. Ge. “Crustal deformation across and beyond the Los Angeles basin from geodetic measurements”. *Journal of Geophysical Research: Solid Earth* 101.B12 (1996), pp. 27957–27980.

[197] D. L. Turcotte and G. Schubert. *Geodynamics*. Cambridge University Press, 2002.

[198] A. Haines and W. Holt. "A procedure for obtaining the complete horizontal motions within zones of distributed deformation from the inversion of strain rate data". *Journal of Geophysical Research: Solid Earth* 98.B7 (1993), pp. 12057–12082.

[199] C. Kreemer, J. Haines, W. E. Holt, G. Blewitt, and D. Lavallee. "On the determination of a global strain rate model". *Earth, Planets and Space* 52.10 (2000), pp. 765–770.

[200] R. W. Allmendinger, R. Reilinger, and J. Loveless. "Strain and rotation rate from GPS in Tibet, Anatolia, and the Altiplano". *Tectonics* 26.3 (2007), TC3013.

[201] K. Chousianitis, A. Ganas, and C. P. Evangelidis. "Strain and rotation rate patterns of mainland Greece from continuous GPS data and comparison between seismic and geodetic moment release". *Journal of Geophysical Research: Solid Earth* 120.5 (2015), pp. 3909–3931.

[202] M. Pandey, R. Tandukar, J. Avouac, J. Vergne, and T. Heritier. "Seismotectonics of the Nepal Himalaya from a local seismic network". *Journal of Asian Earth Sciences* 17.5-6 (1999), pp. 703–712.

[203] D. Hatzfeld, J. Martinod, G. Bastet, and P. Gautier. "An analog experiment for the Aegean to describe the contribution of gravitational potential energy". *Journal of Geophysical Research: Solid Earth* 102.B1 (1997), pp. 649–659.

[204] C. Faccenna, O. Bellier, J. Martinod, C. Piromallo, and V. Regard. "Slab detachment beneath eastern Anatolia: A possible cause for the formation of the North Anatolian fault". *Earth and Planetary Science Letters* 242.1-2 (2006), pp. 85–97.

[205] K. Regenauer-Lieb, G. Rosenbaum, and R. F. Weinberg. "Strain localisation and weakening of the lithosphere during extension". *Tectonophysics* 458.1-4 (2008), pp. 96–104.

[206] C. Klootwijk, P. Conaghan, and C. M. Powell. “The Himalayan Arc: Large-scale continental subduction, oroclinal bending and back-arc spreading”. *Earth and Planetary Science Letters* 75.2-3 (1985), pp. 167–183.

[207] K. Ansari. “Crustal deformation and strain analysis in Nepal from GPS time-series measurement and modeling by ARMA method”. *International Journal of Earth Sciences* 107.8 (2018), pp. 2895–2905.

[208] C. Angelica, A. Bonforte, G. Distefano, E. Serpelloni, and S. Gresta. “Seismic potential in Italy from integration and comparison of seismic and geodetic strain rates”. *Tectonophysics* 608 (2013), pp. 996–1006.

[209] S. N. Ward. “On the consistency of earthquake moment rates, geological fault data, and space geodetic strain: The United States”. *Geophysical Journal International* 134.1 (1998), pp. 172–186.

[210] J. C. Savage and R. W. Simpson. “Surface strain accumulation and the seismic moment tensor”. *Bulletin of the Seismological Society of America* 87.5 (1997), pp. 1345–1353.

[211] G. R. Jiracek, V. M. Gonzalez, T. G. Caldwell, P. E. Wannamaker, and D. Kilb. “Seismogenic, electrically conductive, and fluid zones at continental plate boundaries in New Zealand, Himalaya, and California, USA”. *Geophysical Monograph-American Geophysical Union* 175 (2007), p. 347.

[212] J. Kayal. *Microearthquake Seismology and Seismotectonics of South Asia*. Vol. 503. Springer, 2008.

[213] H. Kanamori. “The energy release in great earthquakes”. *Journal of Geophysical Research* 82.20 (1977), pp. 2981–2987.

[214] Y. Sharma. “Measuring and modeling crustal deformation along the Himalayan arc”. *PhD Thesis, BITS Pilani, Pilani Campus* (2021).

[215] Neha. “Earthquake cycle deformation in New Zealand using spatio-temporal techniques”. *PhD Thesis, BITS Pilani, Pilani Campus* (2023).

[216] P. Bird and Y. Y. Kagan. “Plate-tectonic analysis of shallow seismicity: Apparent boundary width, beta, corner magnitude, coupled lithosphere thickness, and coupling in seven tectonic settings”. *Bulletin of the Seismological Society of America* 94.6 (2004), pp. 2380–2399.

[217] Z. Tian, Z. Yang, R. Bendick, J. Zhao, S. Wang, X. Wu, and Y. Shi. “Present-day distribution of deformation around the southern Tibetan Plateau revealed by geodetic and seismic observations”. *Journal of Asian Earth Sciences* 171 (2019), pp. 321–333.

[218] K.-E. Ching, R.-J. Rau, K. M. Johnson, J.-C. Lee, and J.-C. Hu. “Present-day kinematics of active mountain building in Taiwan from GPS observations during 1995–2005”. *Journal of Geophysical Research: Solid Earth* 116.B9 (2011), B09405.

[219] Y.-J. Hsu, S.-B. Yu, M. Simons, L.-C. Kuo, and H.-Y. Chen. “Interseismic crustal deformation in the Taiwan plate boundary zone revealed by GPS observations, seismicity, and earthquake focal mechanisms”. *Tectonophysics* 479.1-2 (2009), pp. 4–18.

[220] L. Dal Zilio, Y. Dinther, T. Gerya, and J.-P. Avouac. “Bimodal seismicity in the Himalaya controlled by fault friction and geometry”. *Nature Communications* 10.1 (2019), pp. 1–11.

[221] R. Bilham and W. Szeliga. “Interaction between the Himalaya and the flexed Indian plate–Spatial fluctuations in seismic hazard in India in the past Millennium?” In: *AIP Conference Proceedings*. Vol. 1020. American Institute of Physics. 2008, pp. 224–231.

[222] C. Schiffman, B. S. Bali, W. Szeliga, and R. Bilham. “Seismic slip deficit in the Kashmir Himalaya from GPS observations”. *Geophysical Research Letters* 40.21 (2013), pp. 5642–5645.

[223] B. Mukhopadhyay. “An estimation of probable seismic hazard in the active deformation front of the Himalayan arc”. *Journal of Earth System Science* 130 (2021), pp. 1–18.

[224] N. Goswami, S. C. Gupta, and A. Kumar. “Estimation of quality factor, seismic moment, and stress drop of local earthquakes along the MCT in Chamoli region, India”. *Arabian Journal of Geosciences* 14.13 (2021), p. 1236.

[225] P. Hazarika and M. R. Kumar. “Seismicity and source parameters of moderate earthquakes in Sikkim Himalaya”. *Natural hazards* 62 (2012), pp. 937–952.

[226] V. K. Gahalaut. “Great and major earthquakes in the Himalayan arc”. *Journal of the Geological Society of India* 97 (2021), pp. 1327–1330.

[227] J.-P. Avouac. “Mountain building, erosion, and the seismic cycle in the Nepal Himalaya”. *Advances in Geophysics* 46 (2003), pp. 1–80.

[228] J.-L. Mugnier, A. Gajurel, P. Huyghe, R. Jayangondaperumal, F. Jouanne, and B. Upreti. “Structural interpretation of the great earthquakes of the last millennium in the central Himalaya”. *Earth-Science Reviews* 127 (2013), pp. 30–47.

[229] P. Kumar, X. Yuan, R. Kind, and J. Ni. “Imaging the colliding Indian and Asian lithospheric plates beneath Tibet”. *Journal of Geophysical Research: Solid Earth* 111.B6 (2006), B06308.

[230] L. Bollinger, S. N. Sapkota, P. Tapponnier, Y. Klinger, M. Rizza, J. Van Der Woerd, D. Tiwari, R. Pandey, A. Bitri, and S. Bes De Berc. “Estimating the return times of great Himalayan earthquakes in eastern Nepal: Evidence from the Patu and Bardibas strands of the Main Frontal Thrust”. *Journal of Geophysical Research: Solid Earth* 119.9 (2014), pp. 7123–7163.

[231] R. Bilham, D. Mencin, R. Bendick, and R. Bürgmann. “Implications for elastic energy storage in the Himalaya from the Gorkha 2015 earthquake and other incomplete ruptures of the Main Himalayan Thrust”. *Quaternary International* 462 (2017), pp. 3–21.

[232] A. Hooper. “A multi-temporal InSAR method incorporating both persistent scatterer and small baseline approaches”. *Geophysical Research Letters* 35.16 (2008), p. L16302.

[233] J. Hu, Z. Li, X. Ding, J. Zhu, L. Zhang, and Q. Sun. “Resolving three-dimensional surface displacements from InSAR measurements: A review”. *Earth-Science Reviews* 133 (2014), pp. 1–17.

[234] C. Milliner, A. Donnellan, S. Aati, J.-P. Avouac, R. Zinke, J. F. Dolan, K. Wang, and R. Bürgmann. “Bookshelf kinematics and the effect of dilatation on fault zone inelastic deformation: Examples from optical image correlation measurements of the 2019 Ridgecrest earthquake sequence”. *Journal of Geophysical Research: Solid Earth* 126.3 (2021), e2020JB020551.

[235] S. Atzori, I. Hunstad, M. Chini, S. Salvi, C. Tolomei, C. Bignami, S. Stramondo, E. Trasatti, A. Antonioli, and E. Boschi. “Finite fault inversion of DInSAR coseismic displacement of the 2009 L’Aquila earthquake (central Italy)”. *Geophysical Research Letters* 36.15 (2009), p. L15305.

[236] R. Jolivet, C. Lasserre, M.-P. Doin, S. Guillaso, G. Peltzer, R. Dailu, J. Sun, Z.-K. Shen, and X. Xu. “Shallow creep on the Haiyuan fault (Gansu, China) revealed by SAR interferometry”. *Journal of Geophysical Research: Solid Earth* 117.B6 (2012), B06401.

[237] A. Kaverina, D. Dreger, and E. Price. “The combined inversion of seismic and geodetic data for the source process of the 16 October 1999 Mw 7.1 Hector Mine, California, earthquake”. *Bulletin of the Seismological Society of America* 92.4 (2002), pp. 1266–1280.

[238] D. J. Wald and R. W. Graves. “Resolution analysis of finite fault source inversion using one-and three-dimensional Green’s functions: 2. Combining seismic and geodetic data”. *Journal of Geophysical Research: Solid Earth* 106.B5 (2001), pp. 8767–8788.

[239] W. Xu. “Finite-fault slip model of the 2016 Mw 7.5 Chiloé earthquake, southern Chile, estimated from Sentinel-1 data”. *Geophysical Research Letters* 44.10 (2017), pp. 4774–4780.

[240] X. Xu, X. Tong, D. T. Sandwell, C. W. Milliner, J. F. Dolan, J. Hollingsworth, S. Leprince, and F. Ayoub. “Refining the shallow slip deficit”. *Geophysical Journal International* 204.3 (2016), pp. 1867–1886.

[241] H. Yue, T. Lay, L. Rivera, Y. Bai, Y. Yamazaki, K. F. Cheung, E. M. Hill, K. Sieh, W. Kongko, and A. Muhari. “Rupture process of the 2010 Mw 7.8 Mentawai tsunami earthquake from joint inversion of near-field hr-GPS and teleseismic body wave recordings constrained by tsunami observations”. *Journal of Geophysical Research: Solid Earth* 119.7 (2014), pp. 5574–5593.

[242] B. Schurr, G. Asch, S. Hainzl, J. Bedford, A. Hoechner, M. Palo, R. Wang, M. Moreno, M. Bartsch, Y. Zhang, et al. “Gradual unlocking of plate boundary controlled initiation of the 2014 Iquique earthquake”. *Nature* 512.7514 (2014), pp. 299–302.

[243] F. Jouanne, J. Mugnier, M. Pandey, J. Gamond, P. Le Fort, C. Serrurier L .and Vigny, and J. Avouac. “Oblique convergence in the Himalayas of western Nepal deduced from preliminary results of GPS measurements”. *Geophysical Research Letters* 26.13 (1999), pp. 1933–1936.

[244] S. Li, Q. Wang, G. Chen, P. He, K. Ding, Y. Chen, and R. Zou. “Interseismic Coupling in the central Nepalese Himalaya: Spatial correlation with the 2015 Mw 7.9 Gorkha Earthquake”. *Pure and Applied Geophysics* 176 (2019), pp. 3893–3911.

[245] J.-P. Avouac. “From geodetic imaging of seismic and aseismic fault slip to dynamic modeling of the seismic cycle”. *Annual Review of Earth and Planetary Sciences* 43 (2015), pp. 233–271.

[246] M. Chlieh, J.-P. Avouac, K. Sieh, D. H. Natawidjaja, and J. Galetzka. “Heterogeneous coupling of the Sumatran megathrust constrained by geodetic and paleogeodetic measurements”. *Journal of Geophysical Research: Solid Earth* 113.B5 (2008), B05305.

[247] M. Moreno, D. Melnick, M. Rosenau, J. Bolte, J. Klotz, H. Echtler, J. Baez, K. Bataille, J. Chen, M. Bevis, et al. “Heterogeneous plate locking in the south–central Chile subduction zone: Building up the next great earthquake”. *Earth and Planetary Science Letters* 305.3-4 (2011), pp. 413–424.

[248] J. Kayal. “Himalayan tectonic model and the great earthquakes: An appraisal”. *Geomatics, Natural Hazards and Risk* 1.1 (2010), pp. 51–67.

[249] Y. Sharma, S. Pasari, K.-E. Ching, H. Verma, T. Kato, and O. Dikshit. “Interseismic slip rate and fault geometry along the northwest Himalaya”. *Geophysical Journal International* 235.3 (2023), pp. 2694–2706.

[250] Y. Okada. “Surface deformation due to shear and tensile faults in a half-space”. *Bulletin of the Seismological Society of America* 75.4 (1985), pp. 1135–1154.

[251] K.-E. Ching, J. R. Gourley, Y.-H. Lee, S.-C. Hsu, K.-H. Chen, and C.-L. Chen. “Rapid deformation rates due to development of diapiric anticline in southwestern Taiwan from geodetic observations”. *Tectonophysics* 692 (2016), pp. 241–251.

[252] M. Bagnardi and A. Hooper. “Inversion of surface deformation data for rapid estimates of source parameters and uncertainties: A Bayesian approach”. *Geochemistry, Geophysics, Geosystems* 19.7 (2018), pp. 2194–2211.

[253] S. G. Wesnousky. “Great pending Himalaya earthquakes”. *Seismological Research Letters* 91.6 (2020), pp. 3334–3342.

[254] S. Kumar, S. G. Wesnousky, R. Jayangondaperumal, T. Nakata, Y. Kumahara, and V. Singh. “Paleoseismological evidence of surface faulting along the northeastern Himalayan front, India: Timing, size, and spatial extent of great earthquakes”. *Journal of Geophysical Research: Solid Earth* 115.B12 (2010), B12422.

[255] R. Jayangondaperumal, S. G. Wesnousky, and B. Choudhuri. “Near-surface expression of early to late Holocene displacement along the northeastern Himalayan frontal thrust at Marbang Korong Creek, Arunachal Pradesh, India”. *Bulletin of the Seismological Society of America* 101.6 (2011), pp. 3060–3064.

[256] K. Johnson, P. Segall, and S. Yu. “A viscoelastic earthquake cycle model for Taiwan”. *Journal of Geophysical Research: Solid Earth* 110.B10 (2005), B10404.

[257] J. Fukuda and K. M. Johnson. “A fully Bayesian inversion for spatial distribution of fault slip with objective smoothing”. *Bulletin of the Seismological Society of America* 98.3 (2008), pp. 1128–1146.

[258] J. Sun, K. M. Johnson, Z. Cao, Z. Shen, R. Bürgmann, and X. Xu. “Mechanical constraints on inversion of coseismic geodetic data for fault slip and geometry: Example from InSAR observation of the 6 October 2008 Mw 6.3 Dangxiong-Yangyi (Tibet) earthquake”. *Journal of Geophysical Research: Solid Earth* 116.B1 (2011), pp. 1–20.

[259] R. Amey, A. Hooper, and R. Walters. “A Bayesian method for incorporating self-similarity into earthquake slip inversions”. *Journal of Geophysical Research: Solid Earth* 123.7 (2018), pp. 6052–6071.

[260] J. Kruschke. *Doing Bayesian Data Analysis: A Tutorial with R, JAGS, and Stan*. Academic Press, 2014.

[261] G. L. Jones and Q. Qin. “Markov Chain Monte Carlo in practice”. *Annual Review of Statistics and Its Application* 9 (2022), pp. 557–578.

[262] C. P. Robert, G. Casella, and G. Casella. *Monte Carlo Statistical Methods*. Vol. 2. Springer, 1999.

[263] J.-L. Mugnier, P. Huyghe, A. P. Gajurel, and D Becel. “Frontal and piggy-back seismic ruptures in the external thrust belt of western Nepal”. *Journal of Asian Earth Sciences* 25.5 (2005), pp. 707–717.

[264] S. G. Wesnousky, Y. Kumahara, D. Chamlagain, I. K. Pierce, A. Karki, and D. Gautam. “Geological observations on large earthquakes along the Himalayan frontal fault near Kathmandu, Nepal”. *Earth and Planetary Science Letters* 457 (2017), pp. 366–375.

[265] Z. Li, J. Ren, and S. Qin. “Contemporary kinematic models and moment deficit of Chinese mainland”. *Geodesy and Geodynamics* 8.3 (2017), pp. 181–186.

[266] A Kijko and M. Sellevoll. “Triple exponential distribution, a modified model for the occurrence of large earthquakes”. *Bulletin of the Seismological Society of America* 71.6 (1981), pp. 2097–2101.

[267] C. H. Cramer, M. D. Petersen, and M. S. Reichle. “A Monte Carlo approach in estimating uncertainty for a seismic hazard assessment of Los Angeles, Ventura, and Orange Counties, California”. *Bulletin of the Seismological Society of America* 86.6 (1996), pp. 1681–1691.

[268] R. Yadav, P. Bormann, B. Rastogi, M. Das, and S. Chopra. “A homogeneous and complete earthquake catalog for northeast India and the adjoining region”. *Seismological Research Letters* 80.4 (2009), pp. 609–627.

[269] J. W. Baker. *An Introduction to Probabilistic Seismic Hazard Analysis (PSHA)*. Vol. 1. White paper, version, 2008.

[270] C. A. Cornell. “Engineering seismic risk analysis”. *Bulletin of the Seismological Society of America* 58.5 (1968), pp. 1583–1606.

[271] U. Tokuji. “Estimation of parameters for recurrence models of earthquakes”. *Bulletin of the Earthquake Research Institute, Tokyo* 59 (1984), pp. 53–66.

[272] Y. Y. Kagan and D. D. Jackson. “Long-term earthquake clustering”. *Geophysical Journal International* 104.1 (1991), pp. 117–133.

[273] O. Mangira, C. Kourouklas, D. Chorozoglou, A. Iliopoulos, and E. Papadimitriou. “Modeling the earthquake occurrence with time-dependent processes: A brief review”. *Acta Geophysica* 67 (2019), pp. 739–752.

[274] S. Pasari. “Understanding Himalayan tectonics from geodetic and stochastic modeling”. *PhD Thesis, Indian Institute of Technology Kanpur* 376 (2015).

[275] P. Varotsos, N. Sarlis, H. Tanaka, and E. Skordas. “Some properties of the entropy in the natural time”. *Physical Review E* 71.3 (2005), p. 032102.

[276] P. Varotsos, N. V. Sarlis, and E. S. Skordas. *Natural Time Analysis: The New View of Time: Precursory Seismic Electric Signals, Earthquakes and Other Complex Time Series*. Springer Science & Business Media, 2011.

[277] J. R. Holliday, W. R. Graves, J. B. Rundle, and D. L. Turcotte. “Computing earthquake probabilities on global scales”. *Pure and Applied Geophysics* 173 (2016), pp. 739–748.

[278] S. Pasari. “Nowcasting earthquakes in the Bay of Bengal region”. *Pure and Applied Geophysics* 176.4 (2019), pp. 1417–1432.

[279] S. Pasari and Y. Sharma. “Contemporary earthquake hazards in the west-northwest Himalaya: A statistical perspective through natural times”. *Seismological Research Letters* 91.6 (2020), pp. 3358–3369.

[280] I. A. Parvez and A. Ram. “Probabilistic assessment of earthquake hazards in the north-east Indian peninsula and Hindukush regions”. *Pure and Applied Geophysics* 149 (1997), pp. 731–746.

[281] J. B. Rundle, A. Donnellan, G. Fox, J. P. Crutchfield, and R. Granat. “Nowcasting earthquakes: Imaging the earthquake cycle in California with machine learning”. *Earth and Space Science* 8.12 (2021), e2021EA001757.

[282] J. B. Rundle, D. Turcotte, A Donnellan, L Grant Ludwig, M. Luginbuhl, and G. Gong. “Nowcasting earthquakes”. *Earth and Space Science* 3.11 (2016), pp. 480–486.

[283] M. Luginbuhl, J. B. Rundle, and D. L. Turcotte. “Natural time and nowcasting induced seismicity at the Groningen gas field in the Netherlands”. *Geophysical Journal International* 215.2 (2018), pp. 753–759.

[284] M. Luginbuhl, J. B. Rundle, A. Hawkins, and D. L. Turcotte. “Nowcasting earthquakes: A comparison of induced earthquakes in Oklahoma and at the Geysers, California”. *Pure and Applied Geophysics* 175 (2018), pp. 49–65.

[285] M. Luginbuhl, J. B. Rundle, and D. L. Turcotte. “Natural time and nowcasting earthquakes: Are large global earthquakes temporally clustered?” *Earthquakes and Multi-hazards Around the Pacific Rim, Vol. II* (2019), pp. 137–146.

[286] S. Pasari, A. V. Simanjuntak, A. Mehta, Neha, and Y. Sharma. “The current state of earthquake potential on Java Island, Indonesia”. *Pure and Applied Geophysics* 178 (2021), pp. 2789–2806.

[287] S. Pasari, A. V. Simanjuntak, A. Mehta, Neha, and Y. Sharma. “A synoptic view of the natural time distribution and contemporary earthquake hazards in Sumatra, Indonesia”. *Natural Hazards* 108 (2021), pp. 309–321.

[288] J. Gardner and L. Knopoff. “Is the sequence of earthquakes in southern California, with aftershocks removed, Poissonian?” *Bulletin of the Seismological Society of America* 64.5 (1974), pp. 1363–1367.

[289] R. Uhrhammer. “Characteristics of northern and central California seismicity”. *Earthquake Notes* 57.1 (1986), p. 21.

[290] F. Mulargia and S. Tinti. “Seismic sample areas defined from incomplete catalogues: An application to the Italian territory”. *Physics of the Earth and Planetary Interiors* 40.4 (1985), pp. 273–300.

[291] R. B. S. Yadav, J. N. Tripathi, B. K. Rastogi, M. C. Das, and S. Chopra. “Probabilistic assessment of earthquake recurrence in northeast India and adjoining regions”. *Pure and Applied Geophysics* 167 (2010), pp. 1331–1342.

[292] R. B. S. Yadav, J. N. Tripathi, B. K. Rastogi, and S. Chopra. “Probabilistic assessment of earthquake hazard in Gujarat and adjoining region of India”. *Pure and Applied Geophysics* 165 (2008), pp. 1813–1833.

[293] T. M. Bantidi. “Inter-occurrence time statistics of successive large earthquakes: Analyses of the global CMT dataset”. *Acta Geophysica* 70.6 (2022), pp. 2603–2619.

[294] S. Pasari and O. Dikshit. “Distribution of earthquake interevent times in north-east India and adjoining regions”. *Pure and Applied Geophysics* 172.10 (2015), pp. 2533–2544.

[295] S. Pasari and O. Dikshit. “Earthquake interevent time distribution in Kachchh, northwestern India”. *Earth, Planets and Space* 67.1 (2015), p. 129.

[296] S. Bajaj and M. L. Sharma. “Modeling earthquake recurrence in the Himalayan seismic belt using time-dependent stochastic models: Implications for future seismic hazards”. *Pure and Applied Geophysics* 176 (2019), pp. 5261–5278.

[297] C. Kourouklas, G. Tsaklidis, E. Papadimitriou, and V. Karakostas. “Analyzing the correlations and the statistical distribution of moderate to large earthquakes interevent times in Greece”. *Applied Sciences* 12.14 (2022), p. 7041.

[298] T. Utsu. “Aftershocks and earthquake statistics (IV)”. *Journal of the Faculty of Science, Hokkaido University. Series 7, Geophysics* 4.1 (1972), pp. 1–42.

[299] Y. Hagiwara. “Probability of earthquake occurrence as obtained from a Weibull distribution analysis of crustal strain”. *Tectonophysics* 23.3 (1974), pp. 313–318.

[300] T. Rikitake. “Recurrence of great earthquakes at subduction zones”. *Tectonophysics* 35.4 (1976), pp. 335–362.

[301] S. Abaimov, D. Turcotte, R. Shcherbakov, J. B. Rundle, G. Yakovlev, C. Goltz, and W. I. Newman. “Earthquakes: Recurrence and interoccurrence times”. In: *Earthquakes: Simulations, Sources and Tsunamis*. Springer, 2008, pp. 777–795.

[302] A. Corral. “Local distributions and rate fluctuations in a unified scaling law for earthquakes”. *Physical Review E* 68.3 (2003), p. 035102.

[303] A. Corral. “Long-term clustering, scaling, and universality in the temporal occurrence of earthquakes”. *Physical Review Letters* 92.10 (2004), p. 108501.

[304] Y. Y. Kagan and L. Knopoff. “Statistical short-term earthquake prediction”. *Science* 236.4808 (1987), pp. 1563–1567.

[305] M. V. Matthews, W. L. Ellsworth, and P. A. Reasenberg. “A Brownian model for recurrent earthquakes”. *Bulletin of the Seismological Society of America* 92.6 (2002), pp. 2233–2250.

[306] M. Pal, M. M. Ali, and J. Woo. “Exponentiated Weibull distribution”. *Statistica* 66.2 (2006), pp. 139–147.

[307] S. Foss, D. Korshunov, and S. Zachary. *An Introduction to Heavy-tailed and Subexponential Distributions*. Vol. 6. Springer, 2011.

[308] N. L. Johnson, S. Kotz, and N. Balakrishnan. *Continuous Multivariate Distributions*. Vol. 7. Wiley New York, 1972.

[309] G. S. Mudholkar and D. K. Srivastava. “Exponentiated Weibull family for analyzing bathtub failure-rate data”. *IEEE Transactions on Reliability* 42.2 (1993), pp. 299–302.

[310] R. D. Gupta and D. Kundu. “Theory & methods: Generalized exponential distributions”. *Australian & New Zealand Journal of Statistics* 41.2 (1999), pp. 173–188.

[311] M. Mahmoud and M. Ghazal. “Estimations from the exponentiated Rayleigh distribution based on generalized Type-II hybrid censored data”. *Journal of the Egyptian Mathematical Society* 25.1 (2017), pp. 71–78.

[312] R. Hogg, J. Mckean, and A. Craig. *Introduction to Mathematical Statistics*. Vol. 6. PRC Press, 2005.

[313] R. E. Quandt. “Old and new methods of estimation and the Pareto distribution”. *Metrika* 10 (1964).

[314] D. Sornette and L. Knopoff. “The paradox of the expected time until the next earthquake”. *Bulletin of the Seismological Society of America* 87.4 (1997), pp. 789–798.

[315] F. Ciesin. “Gridded population of the world, version 4: population count grid”. *Center for International Earth Science Information Network (CIESIN)* (2020).

[316] N. Kuehn, S. Hainzl, and F. Scherbaum. “Non-Poissonian earthquake occurrence in coupled stress release models and its effect on seismic hazard”. *Geophysical Journal International* 174.2 (2008), pp. 649–658.

[317] J. B. Rundle, J. R. Holliday, W. R. Graves, D. L. Turcotte, K. F. Tiampo, and W. Klein. “Probabilities for large events in driven threshold systems”. *Physical Review E* 86.2 (2012), p. 021106.

[318] J. B. Rundle, A. Giguere, D. L. Turcotte, J. P. Crutchfield, and A. Donnellan. “Global seismic nowcasting with Shannon information entropy”. *Earth and Space Science* 6.1 (2019), pp. 191–197.

[319] L. Bollinger, F Perrier, J.-P. Avouac, S. Sapkota, U. Gautam, and D. Tiwari. “Seasonal modulation of seismicity in the Himalaya of Nepal”. *Geophysical Research Letters* 34.8 (2007), p. L08304.

[320] P. Bettinelli, J.-P. Avouac, M. Flouzat, L. Bollinger, G. Ramillien, S. Rajaure, and S. Sapkota. “Seasonal variations of seismicity and geodetic strain in the Himalaya induced by surface hydrology”. *Earth and Planetary Science Letters* 266.3-4 (2008), pp. 332–344.

List of Research Publications

Journal Publication

- **H. Verma**, S. Pasari, Y. Sharma, K. E. Ching. "High-resolution velocity and strain rate fields in the Kumaun Himalaya: An implication for seismic moment budget". *Journal of Geodynamics* 160 (2024), p. 102023 (SCI).

- S. Pasari, **H. Verma.** "Recurrence Statistics of M≥6 Earthquakes in the Nepal Himalaya: Formulation and Relevance to Future Earthquake Hazards". *Natural Hazards* 120 (2024), pp. 7725–7748 (SCIE).

- S. Pasari, **H. Verma**, Y. Sharma, and N. Choudhary. "Spatial distribution of seismic cycle progression in northeast India and Bangladesh regions inferred from natural time analysis". *Acta Geophysica* 71.1 (2023), pp. 89–100 (SCIE).

- Y. Sharma, S. Pasari, K. E. Ching, **H. Verma**, T. Kato, and O. Dikshit. Interseismic slip rate and fault geometry along the northwest Himalaya. *Geophysical Journal International* 235.3 (2023), pp. 2694–2706 (SCI).

- Y. Sharma, S. Pasari, K. E. Ching, **H. Verma**, and N. Choudhary. Kinematics of crustal deformation along the central Himalaya. *Acta Geophysica* 72 (2024), pp. 553–564 (SCIE).

- **H. Verma**, Y. Sharma, K. E. Ching, S. Pasari. "Contemporary seismic moment budget along the Nepal Himalaya derived from high-resolution InSAR and GPS velocity field". *Acta Geophysica* (2024) (In print, SCIE).

- **H. Verma**, S. Pasari, Y. Sharma, K. E. Ching. "Spatial Distribution of Fault Dynamics in the Nepal Himalaya: Seismic Hazard Insights" (Under preparation).

- **H. Verma**, S. Pasari, Y. Sharma, K. E. Ching. "Kinematics of crustal deformation along the Kumaun Himalaya derived from high-resolution InSAR and GPS velocity field" (Under preparation).

Conference Proceedings/Book Chapters

- **H. Verma**, S. Pasari, and Y. Sharma. "Tectonic deformation along the Delhi-Haridwar Ridge revealed by InSAR observations: Preliminary results". In: *2021 IEEE International India Geoscience and Remote Sensing Symposium (InGARSS)*. IEEE, 2021, pp. 181–184 (Scopus).

- Neha, S. Mehrotra, **H. Verma**, and S. Pasari. "Iterative Empirical Orthogonal Function in Gap Filling of GPS and InSAR Data". In: *2021 IEEE International India Geoscience and Remote Sensing Symposium (InGARSS)*. IEEE, 2021, pp. 496–499 (Scopus).

- **H. Verma**, Y. Sharma, and S. Pasari. "Synthetic aperture radar interferometry to measure earthquake-related deformation: A case study from Nepal". In: *Disaster Management in the Complex Himalayan Terrains.* Springer, 2022, pp. 133–140.

- A. K. Agrawal, **H. Verma**, and S. Pasari. "InSAR Data Analysis using Deep Neural Networks". In: *IOP Conference Series: Earth and Environmental Science.* IOP Publishing, 2022, p. 012025 (Scopus).

- A. Kumar, S. Pasari, A. Mehta, and **H. Verma**. "Impact of directional effect of strong ground motion on scenario-based earthquake hazards: preliminary results". In: *IOP Conference Series: Earth and Environmental Science.* IOP Publishing, 2022, p. 012042 (Scopus).

- R. Ranjan, S. Pasari, S. Devi, and **H. Verma**. "A Novel Framework for Building Vulnerability Assessment for the 2015 Nepal Earthquake". In: *International Conference on Advances in Computing, Communication and Applied Informatics (ACCAI).* IEEE, 2023, pp. 1–5 (Scopus).

List of Attended Conferences/Workshops/Schools

Presented works in international conferences

1. Presented paper entitled "Tectonic deformation along the Delhi-Haridwar Ridge revealed by InSAR observations: Preliminary results" in 2021 IEEE International India Geoscience and Remote Sensing Symposium (InGARSS), Ahmedabad (India), December 06–10, 2021.

2. Presented paper entitled "Strain Rate Deformation Parameters: Formulation and Application to Crustal Analysis" in International Conference on Advances in Mechanics, Modelling, Computing and Statistics (ICAMMCS 2022), organized by the Department of Mathematics, BITS Pilani, Pilani Campus, Rajasthan, March 19–21, 2022.

3. Presented poster entitled "Contemporary seismic moment budget along the Nepal Himalaya derived from high-resolution InSAR and GPS velocity field" in 2022 Taiwan-Japan-New Zealand Seismic Hazard Assessment Meeting, Taiwan, October 31–November 4, 2022.

4. Presented paper entitled "A Novel Framework for Building Vulnerability Assessment for the 2015 Nepal Earthquake" in 2nd International Conference on Advances in Computing, Communication and Applied Informatics (ACCAI-2023), organized by St. Joseph's College of Engineering, Chennai, India, May 25–26, 2023.

5. Presented poster entitled "Strain rate and associated seismic moment budget along the Nepal Himalaya" in International Conference on Geomatics in Civil Engineering, organized by Civil Engineering Department, Indian Institute of Technology Roorkee, March 11–12, 2024.

Attended conferences/workshops/schools

1. Attended “Winter School on Physical Geodesy and Its Applications”, organized by the National Centre in Geodesy (NCG) at IIT Kanpur, February 15–24, 2021.

2. Attended “International Workshop on Recent Advancements in Data Envelopment Analysis and Applications (IWRADEAA-2021)”, organized by the Department of Mathematics, BITS Pilani, Pilani Campus, July 07–11, 2021.

3. Attended “1st Short-Term course on Introduction to GNSS and its Applications”, organized by the National Centre in Geodesy (NCG) at IIT Kanpur, November 08–19, 2021.

4. Attended “2nd International Conference on Advances in Earth and Environmental Studies (AEES 2022)”, organized by Department of Applied Geology, National Institute of Technology Raipur, February 25–26, 2022.

5. Attended “5-day short term course titled Training on InSAR: Theory, Processing and Applications”, organized by GIS Cell, MNNIT, Allahabad, March 27–31, 2022.

Biography of the Candidate

Mr. Himanshu Verma received his B.A. in Mathematics from Chaudhary Devi Lal University, Sirsa, in 2016 and later completed his M.Sc. in Mathematics at the Department of Mathematics, Guru Jambheshwar University of Science & Technology, Hisar, in 2018. He has successfully qualified for the CSIR-UGC based Junior Research Fellowship (JRF) and National Eligibility Test (NET) in Mathematical Sciences twice, in December 2018 and June 2019. Currently, he is working towards a Ph.D. degree from Birla Institute of Technology and Science Pilani, Pilani Campus. His research interests lie primarily in the areas of crustal deformation, active tectonics, and seismic hazard analysis using geodetic and statistical-based approaches. He has 11 research publications in peer-reviewed journals and conference proceedings. He has attended ten international conferences, short-term courses, and international workshops during his Ph.D. tenure. He has attended ten international conferences, short-term courses, and international workshops during his Ph.D. tenure. Additionally, he received the best poster presentation award at the ICGCE-2024 conference held at IIT Roorkee. During his Ph.D., he had the privilege of conducting research at NCKU Taiwan for three months in 2022 and participating in the 2022 Taiwan-Japan-New Zealand Seismic Hazard Assessment Meeting, Taitung (Taiwan).

Biography of the Supervisor

Prof. Sumanta Pasari is an Associate Professor in the Department of Mathematics at Birla Institute of Technology and Science, Pilani (Pilani Campus). He completed his Ph.D. in Civil Engineering, specializing in Geoinformatics, from the Indian Institute of Technology, Kanpur (IITK). Before his doctorate, he obtained his Masters in Mathematics from IITK as well. His research area includes crustal deformation and active tectonics from geodetic techniques, statistical seismology, and renewable energy modeling. His contributions include numerous publications in esteemed journals and proceedings, showcasing his expertise and commitment to advancing these fields. Recently, Prof. Pasari successfully supervised Dr. Yogendra Sharma, Dr. Neha, and Dr. Sarita, who obtained their Ph.D. degrees under his guidance. Six Ph.D. scholars are currently conducting research on various topics of crustal deformation, machine learning in geosciences, and renewable energy prediction under his supervision.

Biography of the Co-supervisor

Prof. Kuo-En Ching is an Associate Professor in the Department of Geomatics at National Cheng Kung University (NCKU), Taiwan. He completed his Ph.D. in 2007 from the Department of Earth Sciences at NCKU, Taiwan. Following his Ph.D., he held several postdoctoral positions, including at the Department of Earth Sciences at NCKU, Taiwan (Feb. 2008–Jul. 2008), the Department of Geological Sciences at Indiana University, USA (Aug. 2009–Jul. 2010), and the Institute of Earth Sciences at Academia Sinica, Taiwan (Aug. 2010–Jan. 2011). Prof. Ching is an accomplished geodetic researcher specializing in crustal deformation, earthquake-related analysis, mud diapirism, seismic hazard assessment, volcanic deformation, semi-dynamic geodetic datum construction, and land subsidence. He is working in several seismically active regions of the world, such as Taiwan, Himalaya, Philippines, Indonesia, etc. He has participated in several international and national conferences in Taiwan and abroad, and visited many reputed universities/institutes in Taiwan, USA, India, Japan, Phillippines, etc. His dedication to advancing the field is evident through numerous publications in esteemed journals and proceedings. Prof. Ching successfully supervised 15 Masters students, and currently, four Masters students, four Ph.D. scholars, and one post-doc scholar are conducting research in his group.